

**THE MICROSTRUCTURE AND PROPERTIES
OF POWDER HIPPED NICKEL-BASED
SUPERALLOY CM247LC**

QINQIN ZHANG

A thesis submitted to
The UNIVERSITY OF BIRMINGHAM
For the degree of
DOCTOR OF PHILOSOPHY

School of Metallurgy and Materials
College of Engineering and Physical Sciences
The University of Birmingham
January 2011

UNIVERSITY OF
BIRMINGHAM

University of Birmingham Research Archive

e-theses repository

This unpublished thesis/dissertation is copyright of the author and/or third parties. The intellectual property rights of the author or third parties in respect of this work are as defined by The Copyright Designs and Patents Act 1988 or as modified by any successor legislation.

Any use made of information contained in this thesis/dissertation must be in accordance with that legislation and must be properly acknowledged. Further distribution or reproduction in any format is prohibited without the permission of the copyright holder.

Synopsis

The response of powder of the Nickel-based superalloy CM247LC to a range of Hot Isostatic Pressing (HIPping) conditions and post-HIP heat treatments has been investigated as a preliminary step in the assessment of net shape HIPping as a possible process-route for component production.

A HIPping pressure of 150MPa was used at temperatures of 1100°C, 1200°C, 1260°C and 1320°C. 1260°C as-HIPped specimens had the best tensile and HCF fatigue properties at both room temperature and 750 °C; the influence of post-HIP solution treatment conditions and of subsequent ageing on the properties of samples which had been HIPped at 1260 °C was thus investigated. A solution treatment at 1100 °C for 1h followed by forced air cooling and ageing at 870 °C for 16h resulted in the optimum tensile, high cycle fatigue at both room temperature and 750 °C. The optimized microstructure consists of a 'necklace' structure of coarse γ' particles along the grain boundaries; cuboidal γ' distributed inside grains with hyper-fine γ' precipitated in γ channels; and fine carbides homogeneously disperse in the matrix. The properties of samples with this microstructure were comparable with those of cast, directionally solidified CM247LC. Solution treatment at 1260 °C gives better creep resistance at 760 °C/ 350MPa. It was also concluded that with gas-atomised powder, solution treatment must be carried out below the HIP temperature to minimise porosity.

Analytical scanning electron microscopy showed that Hf-rich inclusions, some of which had alumina cores, initiated failure in almost all tensile samples and in all fatigue samples. It was shown that this type of inclusion can be avoided by removal of Hf from the alloy; but the removal of Hf – which is added to the alloy to improve castings – degrade the creep

properties over the temperature range of 700 °C to 950 °C and the stress range of 150 MPa to 550 MPa. Further work is required to assess the influence on the tensile and fatigue properties.

This thesis is dedicated to the memory of my father,

Wenfu Gong

1958 - 2010

Acknowledgements

I wish to express my sincere gratitude to my supervisors, Prof. Xinhua Wu and Dr. Junfa Mei, for their continuous support, encouragement, and guidance which they provided during my PhD. Special thanks must go to Prof. Michael H. Loretto for many helpful discussions. I also wish to thank the School of Metallurgy and Materials and the ORS Committee for a scholarship and Rolls- Royce plc for additional financial support.

Thanks also to Prof. P. Bowen for the provision of research facilities. I am grateful to Dr. D. Hu his help over the PhD. years. I would like to thank Dr R. Morrell from the National Physical Library for his help with the creep tests and for useful discussions; Dr C. Martin and Dr R. Bradley from the University of Manchester for their help with X-ray tomography analysis; Dr. T. Doel and Dr. H. Li for help in carrying out the mechanical tests. I am greatly obliged to Mr. J. Shurvinton and Mr. M. Glynn for their help with the powder HIPping. Also thanks to D. Price, P. Stanley, M. Chu, T. Morris and J. Singh for their technical assistance and co-operation. I would also like to thank my friends and colleagues, both past and present, for their support and assistance.

Finally, I wish to thank my dearest family especially my grandfather Ruqing Zhang for their belief in me and encouraging me to pursue my Ph.D. I could never have completed my study without them.

Table of Contents

Chapter 1 Introduction	- 1 -
Chapter 2 Literature Review	- 5 -
2.1 Nickel-base superalloys	- 5 -
2.2 γ' hardened nickel-based superalloy.....	- 16 -
2.3 Hot isostatic pressing	- 40 -
2.3 Properties and application of CM247LC	- 48 -
2.4 Aim of the project.....	- 59 -
Chapter 3 Experimental Methods.....	- 61 -
3.1 Materials and their processing	- 61 -
3.2 Microstructural characterisation.....	- 66 -
3.3 Chemical composition analysis.....	- 68 -
3.4 Physical characteristics	- 69 -
3.5 X-ray Tomography	- 71 -
3.6 Mechanical testing	- 73 -
Chapter 4 Microstructure and Mechanical Properties of HIPped CM247LC	- 80 -
4.1 Powder assessment and analysis	- 80 -
4.2 Microstructure and properties of as-HIPped CM247LC.....	- 98 -

4.3 Microstructure and properties of HIP+Solution-treated+Aged CM247LC	- 126 -
4.4 Comparison of Hf-containing and Hf-free HIPped CM247LC	- 154 -
Chapter 5 Discussion	- 172 -
5.1 The response of powder to HIPping.....	- 172 -
5.2 The influence of HIPping temperature on microstructure and mechanical properties	- 180 -
5.3 The role of inclusions on initiation of failure.....	- 192 -
5.4 Recommendations on powder HIPping of nickel-base alloys	- 201 -
Chapter 6 Conclusions and Future Work	- 204 -
6.1 Conclusions	- 204 -
6.2 Future work	- 205 -
Appendices.....	- 207 -
Appendix 1 Notch test.....	- 207 -
Appendix 2 Diffusion layer.....	- 212 -
Appendix 3 Jominy Curve T (t)	- 214 -
Appendix 4 X-ray tomography	- 215 -
References.....	- 249 -

Chapter 1 Introduction

Nickel-base alloys are used at temperatures in excess of 550 °C in components including turbine blades, discs, combustion chambers, etc. These components are manufactured from bar, sheet, large forgings and castings and have specific property requirements. The principal reason for the use of nickel-base superalloys in gas turbines is their outstanding strength and oxidation resistance over the temperature range encountered. Nickel-base alloys have a fully austenitic face centred cubic (FCC) structure which has the capability of maintaining good tensile, rupture and creep properties to much higher temperatures than body centred cubic (BCC) systems. The superalloys can be used to 0.9 T_m (melting point) or for times up to 100,000 h at somewhat lower temperatures.

High temperature components, for example, combustion chambers are conventionally fabricated from sheet materials and the necessary design complexity requires good welding characteristics. Early combustion chambers were fabricated either by casting or by thermomechanical processing of ingots in simple solid solution strengthened austenitic alloys such as Nimonic 75 [Lefebvre 1983]. These alloys are relatively easy to manipulate, but they were found to have inadequate strength in later designs. Precipitation-hardening superalloys were then introduced, but they require complex and lengthy manufacturing sequences, involving powder-production from an ingot, so that segregation is effectively eliminated, and HIPping (Hot Isostatic Pressing) of the powder to produce consolidated billets, followed by thermomechanical processing in order that highly stressed components can be produced to an acceptable and reproducible standard. This is however a complex expensive manufacturing route and if the obvious benefit of using powder, the reduction of segregation, is to be taken advantage of, a lower cost powder processing must be developed.

Net Shape HIPping is just such a process. In this technology the superalloy is atomised and produced to the desired shape by HIPping the powder in a capsule which is designed, via modelling, so that the HIPped product is close to the required final shape and extensive machining is not required. The capsule is usually made of mild steel which is cheap and easy to remove. If this process is to be developed it is essential that the response of the powder to HIPping be understood, that optimum HIPping conditions be identified and any post-HIP heat treatment required is optimised. This approach has been followed in the present research using the nickel-based superalloy CM247LC.

CM247LC is a modified superalloy derived in late 1978 from the MarM247 composition, specifically designed for directionally solidified blade and vane applications [*Harris et al. 1984*] which have higher temperature capabilities than the wrought alloys currently used for combustor support casing and combustor liner. This material was evaluated for combustor liner applications that require an increased temperature capability beyond the current liner material, C263 [*Andrews 1999*]. CM247LC, as one of modern superalloys of general type, contains large amounts of secondary phase γ' and complex carbides in a γ matrix which contribute significantly to its high temperature properties. The presence of these constituents, however, has made it exceedingly difficult to form subsequent to casting. It is obviously not practical to cast and machine it into the thin-walled combustion casing which involves complex design skin-cooling structures. A novel manufacturing procedure is required in order to take the advantage of CM247LC in combustion casings.

This project investigates the HIPping process on argon-atomised CM247LC nickel-base superalloy powders. These HIPped materials have potential application for engine casings. A systematic study on the effect of HIPping variables (HIPping temperature, HIPping procedure and powder type) and heat treatment temperature on microstructure, tensile

Chapter 1 Introduction

properties, fatigue properties, creep properties and fracture mechanisms has been carried out in the work reported in this thesis.

Chapter 2 presents the literature review which starts with the general introduction and classification of nickel-base superalloys followed by a summary of the mechanical properties and applications of these alloys. Structure control is achieved through composition selection/modification and by processing; thus two sections will focus on reviewing the influence of compositional elements and the processing parameters on the microstructure of γ' hardened nickel-base superalloys. Processing methods, especially details of the HIPping process are described. Following this, a brief review on the findings of other researchers on the microstructural behaviour and mechanical responses of HIPped nickel-base super alloys is given. Finally, the main aims of the research project are summarised.

Chapter 3 describes the experimental methods used in this investigation, which include descriptions of powder materials used and HIPping procedure. Details on the specimen preparation and microstructural analyses of as-received powders and of as-HIPped samples utilising well-established metallographic and analytical electron microscopy techniques are given. Mechanical testing and fracture analyses methods of the tested HIPped samples are also presented.

The results are given in Chapter 4 in four sections. In section 4.1, the details of microstructure and morphology of as-received CM247LC powders are given. Heat treatment and trial HIPping was conducted to obtain the critical HIPping conditions for the densification of CM247LC powder and factors that influence the sintering process. Following this, four sets of HIPping conditions were chosen. The microstructure and properties of as-HIPped samples of CM247LC powder are presented in section 4.2 and the microstructure and morphology of HIPped samples are compared. The effect of HIPping

temperature on mechanical properties was assessed under different test temperatures. Moreover, the fracture surface features are analysed in order to understand the fracture mechanisms. The optimum set of HIPping conditions was chosen for heat treatment study in section 4.3. Several temperatures below or above the γ' solvus were used to solution treat the as-HIPped CM247LC samples. The details of the response of the material to the solution temperature and cooling rate are presented.

Chapter 5 discusses issues in four aspects. Firstly in section 5.1, the HIPpability of the gas-atomized CM247LC powder is analysed by the response of powder to different temperature, the densification mechanism and bonding behaviour. The relation between the HIPping + heat treatment parameters and mechanical properties is proposed in section 5.2. The main problem of the HIPped CM247LC, which is the presence of inclusions is indicated and its source is traced in section 5.3. Finally recommendations on the powder HIPping of nickel-base superalloys are given in section 5.4.

Chapter 6 summarises the main findings and conclusions in this study. Some future work that should be carried out is also proposed in order to obtain further understanding in this research area.

Chapter 2 Literature Review

This chapter begins with a brief overview of nickel-base alloys including the market demand and the main applications, followed by the classification and different fields of their applications. As the main concern of this thesis, precipitation hardened nickel-base superalloys will then be covered in more detail including the strengthening mechanisms and aspects that affects their microstructure hence mechanical properties. The science and technology background to hot isostatic pressing (HIPping) is then given. The choice of HIPping conditions and their influence on the microstructure of P/M nickel-base alloys are summarized as well as problems encountered plus suggestions to overcome these problems. The material investigated, CM247LC, is introduced by its applications and its typical microstructures and mechanical properties when manufactured using various methods. Finally, the research areas covered in this thesis are described using areas identified in the literature review to put the work in perspective. The main thrust of the research is in the area of net shape manufacture using HIPping of powder CM247LC and thus as noted above, much of the literature review covers these areas, but other relevant background areas are also covered.

2.1 Nickel-base superalloys

2.1.1 Background

Superalloys are a group of metallic alloys which can be used at high temperatures, often in excess of 0.7 of their absolute melting temperature. They were initially developed for use in aircraft piston engine turbo superchargers, and their development over the last 70 years has

been paced by the demands of advancing gas turbine engine technology. Superalloys can be based on iron-nickel, cobalt or nickel, the latter being best suited for aero engine applications. The vast majority of use by tonnage of nickel-base superalloy is found in turbines, both for aerospace applications and for land-based power generation.

Nickel-base superalloys are used primarily in turbine blades, turbine disks, combustion casings, and vanes in modern engines. Fig. 2-1 illustrates the materials used in the Trent 800 engine, which is the Rolls-Royce engine used in the Boeing 777 - the most common aircraft seen in civil aviation service since 1996. The titanium alloys are highly favoured in aerospace applications for their marvellous strength to weight ratio. But their applications are limited to before the combustion takes place in the engine, where the service temperature is up to 550 °C. Nickel-base superalloys currently constitute over 50 % of the weight of advanced engines. The widespread use of superalloys in turbine engines, coupled with the fact that the thermodynamic efficiency of turbine engines is increased with increasing turbine inlet temperatures has, in part, provided the motivation for increasing the maximum-use temperature of superalloys. The environmental operating temperatures of these components range from the relatively mild temperature of 150 °C to almost 1500 °C. Additionally, several components experience large temperature gradients; for example, turbine disks range from 150 °C at the centre to 550 °C at the rim where the blades are attached. In addition to the high temperature they must endure, the blades are also subject to an extremely corrosive environment – namely, the products of combustion. The primary loading, which results mainly from centripetal acceleration of the rotating blades and disc, in conjunction with the high temperature, leads to creep-deformation. Finally, fatigue cycles result from each engine start-up and shutdown as the load changes from zero to maximum and back to zero. For some military engines, thrust settings are varied so greatly that they

can also be considered as a fatigue cycle. These are considered as LCF (low cycle fatigue) in engine design. Vibratory loading at high frequencies can lead to catastrophic failure in rotating engine components because of the very high number of HCF (High cycle fatigue) cycles which can be encountered in very short times; therefore it is imperative to remain below the stress conditions corresponding to the onset of crack growth due to HCF. [Frost et al. 1974]

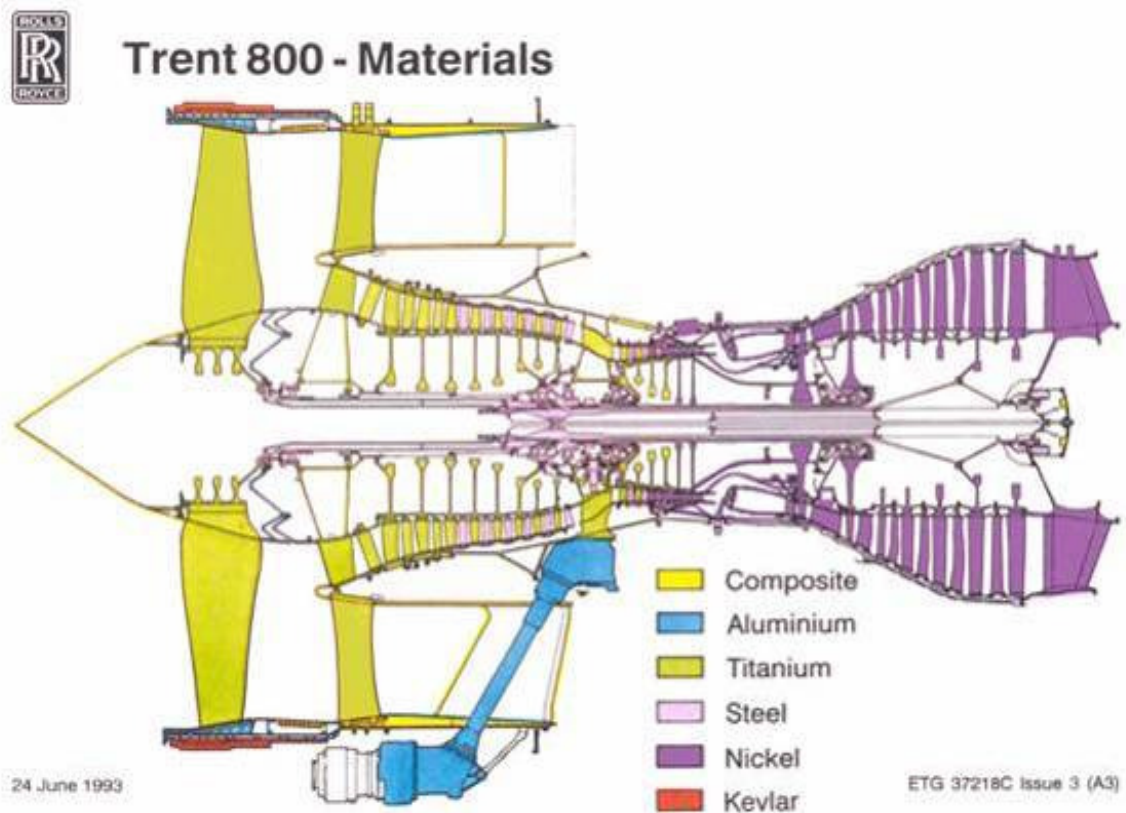


Fig. 2-1 Illustration of material usage in the Trent 800 engine. Note the Ni-based alloys are all in the combustor and turbine. (Courtesy of Rolls-Royce.)

Turbine components thus experience thermomechanical loading and fatigue as well as creep-fatigue interactions. These applications require a material with high strength, good creep and fatigue resistance, good corrosion resistance and the ability to be operated continuously at elevated temperatures; among which creep and oxidation resistance are the prime design criteria. The good combination of strength and toughness, as well as unusual yield behaviour (in which the yield strength increases with increased temperature up to about 700 °C), continues to make nickel-base superalloys the material of choice for high performance, high temperature applications.

2.1.2 Alloy classification and applications

2.1.2.1 Why are nickel-base alloys preferred to other alloys?

There are several reasons why nickel is the best base of high temperature materials. First, it is reported [*Brown et al. 1980*] that FCC metals display the lowest diffusivity relative to their melting point and highest normalised activation energy(Q/RT) for diffusion among the various crystal classes of transition metals. These two properties make FCC metals display better creep properties than other crystal structures such as HCP and BCC [*Fost et al. 1982*], thus the FCC crystal structure is the first choice for high temperature applications. Nickel is FCC and is thus both tough and ductile, due to a considerable cohesive energy arising from the bonding provided by the outer *d* electrons [*Betteridge 1984*]. Furthermore, nickel is FCC from room temperature to its melting point, so that there are no phase transformations to cause expansions and contractions which might complicate its use for high temperature components. Other metals in the transition metal series, the platinum group metals, display this crystal structure. Pt-based superalloys have been studied in recent years. It was found

that their potential application temperature would be around 1300 °C [Fairbank 2003; Cornish et al. 2009]. But they are both dense and very expensive.

Low rates of thermally activated creep require low rates of diffusion – as suggested by the correlation between the activation energies for self-diffusion and creep in the pure metals. Diffusion rates for FCC metals such as Ni are low; hence, considerable microstructural stability is imparted at elevated temperatures. Finally, considering other elements which possess different crystal structures; of the HCP metals, only Co displays an acceptable density and cost; Re and Ru are platinum group metals and are therefore expensive; Os has an oxide which is poisonous; and Tc is radioactive. Co-based superalloys are, in fact, used for high-temperature applications; however, they tend to be more expensive than nickel-based superalloys. The BCC metals such as Cr have relatively low activation energies for diffusion, are prone to brittleness, and there is a ductile/brittle transition which means that the toughness decreases significantly with decreasing temperature [Reed 2006].

2.1.2.2 Classification of nickel-base superalloys

Nickel-base high temperature alloys are basically of three types: solid-solution strengthened, precipitation hardened, and oxide-dispersion strengthened (ODS).

Solid-solution strengthened alloys, such as Hastelloy X, Haynes 625, Haynes 188, are used in applications requiring only modest strength [Matthews 1976]. They contain little or no aluminium, titanium, or niobium. In the most demanding applications, such as hot sections of gas turbine engines, a precipitation-strengthened alloy is required.

The precipitation-hardened alloys contain several percent aluminium and titanium, and a few contain substantial amounts of niobium; they are strengthened by γ' precipitation, by the

addition of aluminium and titanium, by carbides, and by solid-solution alloying. The nature of the γ' is of primary importance in obtaining optimum high temperature properties. Compositionally, the aluminium and titanium contents and the aluminium/titanium ratio are very important, as is heat treatment. Increasing the aluminium/titanium ratio improves high temperature properties. The volume fraction, size and the spacing of γ' are important parameters and must be controlled to optimise properties.

The ODS alloys contain a small amount of fine, 10 to 100nm, oxide particles (0.5 to 1% Y_2O_3) and are produced by powder metallurgy techniques. The dispersion strengthening with yttria allows the strength to be maintained to much higher temperatures. For example, at 1093 °C, the 1000h rupture strength of MA6000 is twice that of conventional nickel-base superalloys [*Bhadeshia 1997*].

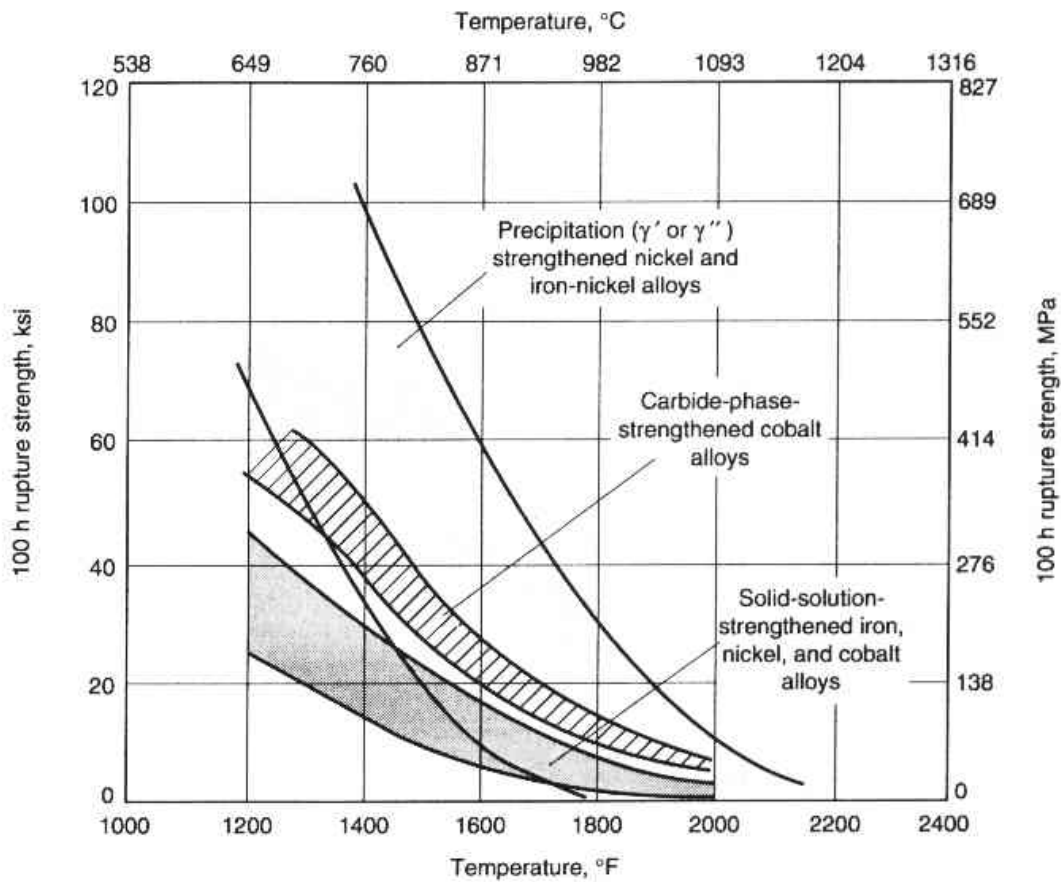


Fig. 2-2 Stress rupture characteristics of wrought superalloys [Davis 1997]

As illustrated in Fig. 2-2, precipitation-hardening alloys have considerably higher strength values than solid-solution strengthened alloys. For the most demanding of elevated temperature applications, γ' strengthened alloys are preferred. Solid-solution strengthened alloys are preferred, when service conditions allow their use, because of their ease of fabrication, especially weldability. γ' strengthening is most effective in the medium temperature range between 600 °C and 800 °C. It compensates for the steep drop of the yield strength, found in solid solution strengthened Nimonic 75 and in oxide dispersion strengthened PM 1000 due to the transition from (glide controlled) low temperature to (climb-controlled) high temperature deformation mechanisms [Nabarro et al. 1995].

However, at temperatures above 1000 °C the effect of γ' strengthening on yield strength disappears due to unavoidable diffusion-controlled changes in the γ' particle microstructure. Then, dispersion strengthening is left over as the only significant contributor to high temperature strength [Nganbe et al. 2004]. Combining oxide dispersion and γ' precipitation strengthening in nickel-base superalloys provides the greatest strength advantage in the temperature range of 600°C and 850°C, as both the strength and the fatigue life of PM 3030 (ODS plus γ' -strengthened) were improved over PM 1000 (solely strengthened by ODS) [Nganbe et al. 2009]. However, the Al_2O_3 in MA 6000 [Nazmy et al. 1985] or Y_2O_3 in PM 3000 [Nganbe and Heilmaier 2009], present in the ODS material are detrimental to the ductility of the materials.

2.1.3 Development of superalloys - processing and composition

Superalloy components are produced by three distinct processing routes: casting, powder metallurgy processes and conventional wrought (deformation) processing.

Over the latter part of the twentieth century, a concerted period of alloy and process development enabled the performance of superalloys to be improved dramatically. Although further improvements are being actively pursued, it is important to recognise this historical context, since much can be learned from it. Fig.2-3 provides a perspective for the alloy and process development which has occurred since the first alloys began to appear in the 1940s; the data relate to the materials and processes for turbine blading, so that the creep performance (here taken as the highest temperature at which rupture occurs in 1000h, at 137 MPa) is a suitable measure of the progress which has been made. Various points emerge from a study of the figure. First, one can see that, for the blading application, cast rather than wrought materials are now preferred since the very best creep performance is then conferred.

However, the first aerofoils were produced in wrought form. During this time, alloy development work – which saw the development of the first Nimonic alloys – enabled the performance of the blading to be improved considerably; the vacuum induction casting technologies which were introduced in the 1950s [*Craw et al. 1956*] helped with this since the quality and cleanliness of the alloys were improved dramatically. Second, the introduction of improved casting methods, and later the introduction of processing by directional solidification, enabled significant improvements to be made; this was due to the columnar microstructures that were produced in which the transverse grain boundaries were absent. Once this development occurred, it was quite natural to remove the grain boundaries completely such that monocrystalline (single-crystal) superalloys were produced. This allowed, in turn, the removal of grain-boundary strengthening elements such as boron and carbon which had traditionally been added; this enabled better heat treatments to reduce microsegregation and eutectic content induced by casting, whilst avoiding incipient melting during heat treatment. The fatigue life is then improved. Nowadays, single-crystal alloys are being used in increasing quantities in the gas turbine engine; if the very best creep properties are required, then the turbine engineers turn to them, although it should be recognised that the use of castings in the columnar and equiaxed forms is still practised in many instances [*Lund et al. 1972; Zhang 2005*].

Powder techniques have been used extensively in superalloy production ever since the 1970s [*Allen et al. 1975*]. Principally, high strength gas-turbine disk alloy compositions such as IN-100 [*Menzies et al. 1982*], which are difficult or impractical to forge by conventional methods, have been powder processed. Inert atmospheres are used in the production of powders, often by gas atomization, and the powders are consolidated by extrusion or hot isostatic pressing (HIP). HIP has been used recently to produce some near net shape

components directly for final limited machining [Seliverstov et al. 1999]. More traditionally HIP has been used to consolidate billets for subsequent thermo-mechanical processing. Minimal segregation, reduced inclusion sizes, ability to use very high γ' -content compositions, and ease of grain size control are significant advantages of powder processing. Powder techniques also have been used to produce turbine blade/vane ODS alloys since 1980s [Tien et al. 1982]. Mechanical alloying is the principal technique for introducing the requisite oxide/strain energy combination to achieve maximum properties.

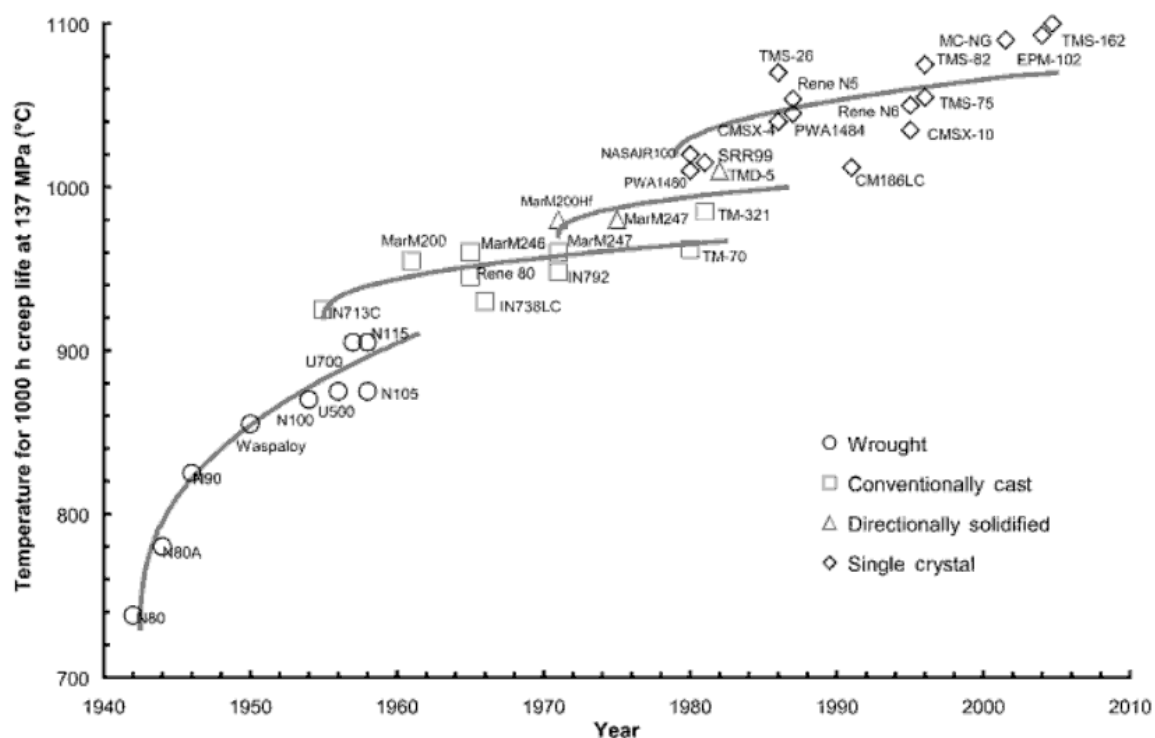


Fig. 2-3 Evolution of the high temperature capability of the superalloys over a 70 year period since their emergence in the 1940s. From [Reed 2006]

As many as 14 different alloying additions are added in nickel-base superalloys, but they vary depending on whether the material is designed for cast or wrought. Changes in alloy compositions are likely to be required if components are to be made directly by net shape

HIPping. Using such powder metallurgical techniques, alloy design can be extended to more complex, higher alloy systems, without the macrosegregation problems associated with conventional cast materials. This aspect will be discussed in this thesis.

The so called first –generation cast alloys were single-crystal superalloys, such as PWA1480, Rene N4 and SRR99, which contain appreciable quantities of the γ' hardening elements Al, Ti and Ta; the grain-boundary-strengthening elements C and B, which were added routinely to the earlier directionally solidified alloys, are no longer present. Second-generation alloys, such as PWA1484, CMSX-4 and Rene N5, are characterised by a 3 wt% concentration of Re, which is increased to about 6 wt% for the third-generation alloys such as CMSX-10 and Rene N6. Generally speaking, the modern alloys are characterised by significantly lower concentrations of Cr and higher concentrations of Al and Re. Concentrations of Ti and Mo are now at very modest levels. The period since 2000 has seen the emergence of the fourth-generation single-crystal superalloys, such as MC-NG, EPM-102 and TMS-162, which are characterised by additions of ruthenium.

Wrought superalloys are employed therefore in polycrystalline form. When their chemical compositions are compared with those of the cast superalloys, various points emerge. The concentrations of the γ' hardening elements Al and Ti are generally lower. Appreciable quantities of Fe are sometimes employed, and quantities of Nb are present. The Cr content is usually at least 15 wt%, higher than for the cast alloys. Furthermore, additions such as Re and Ta are not generally made.

2.2 γ' hardened nickel-based superalloy

The principal microstructural variables of γ' hardened nickel-based superalloys are: the precipitate amount and its morphology; grain size and shape; carbide distribution. This section is an introduction to the morphology of these phases and their contribution to mechanical properties, followed by the ways to control them by adjusting compositional elements and processing method. The name of the processing methods of nickel-base alloys may vary from DS, wrought or PM, etc, but the influence of detailed processing parameters such as temperature and cooling rate may have some effects in common. Understanding these aspects could be important guidance to optimizing the HIPping parameters in this project.

2.2.1 Phases in γ' hardened nickel-base superalloys

Gamma matrix (γ) and gamma prime (γ')

The essential solutes in nickel-based superalloys are aluminium and/or titanium, with a total concentration which is typically less than 10 atomic percent. This generates a two-phase equilibrium microstructure, consisting of gamma (γ) and the ordered phase, gamma-prime (γ'). It is the γ' which is largely responsible for the elevated-temperature strength of the material and its incredible resistance to creep deformation. The amount of γ' depends on the chemical composition and temperature, as illustrated in the ternary phase diagrams in Fig.2-4.

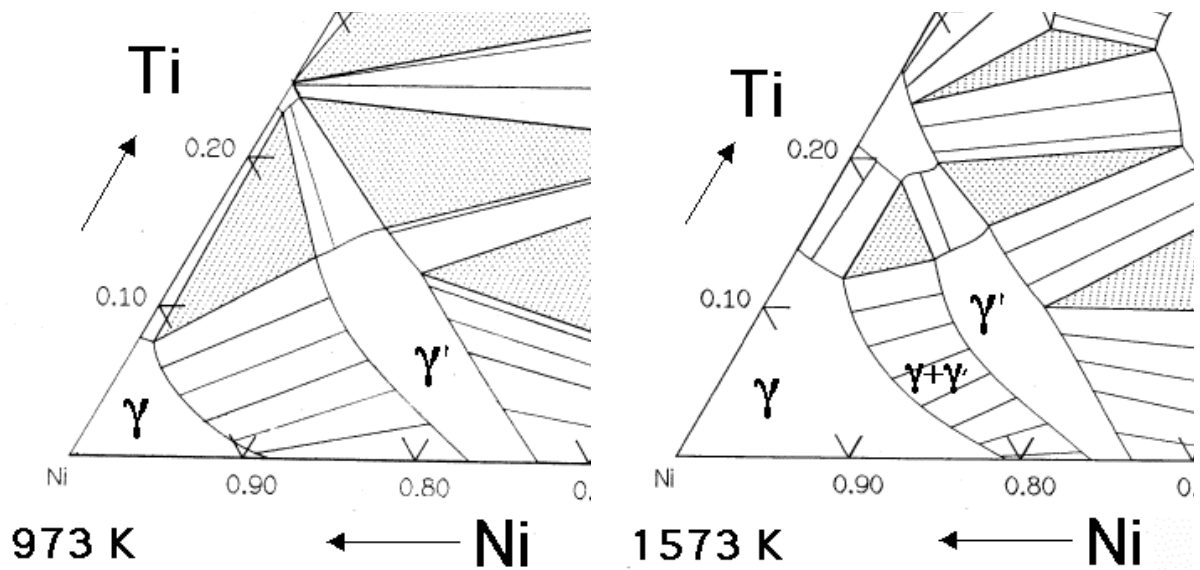


Fig. 2-4 The isothermal cross sections of the Ni-Al-Ti ternary phase diagrams show the γ and γ' phase field. For a given chemical composition, the fraction of γ' decreases as the temperature is increased. This phenomenon is used in order to dissolve the γ' at a sufficiently high temperature (a solution treatment) followed by ageing at a lower temperature in order to generate a uniform and fine dispersion of strengthening precipitates. From [Bhadeshia 2003]

As shown in Fig. 2-5 a), the γ -phase is a solid solution with a FCC (face-centred cubic) lattice and a random distribution of the different species of atoms. By contrast, γ' has a $L1_2$ cubic-P (primitive cubic) lattice in which the nickel atoms are at the face-centres and the aluminium or titanium atoms at the cube corners, shown in Fig.2-5 b). This atomic arrangement has the chemical formula Ni_3Al , Ni_3Ti or $Ni_3(Al,Ti)$. However, as can be seen from the $(\gamma+\gamma')/\gamma'$ phase boundary on the ternary sections of the Ni, Al, Ti phase diagram, the phase is not strictly stoichiometric. An excess of vacancies may exist on one of the sublattices which leads to deviations from stoichiometry; alternatively, some of the Ni atoms might occupy the Al sites and vice-versa. In addition to aluminium and titanium, niobium, hafnium and tantalum partition preferentially into γ' . [Sims et al. 1987]

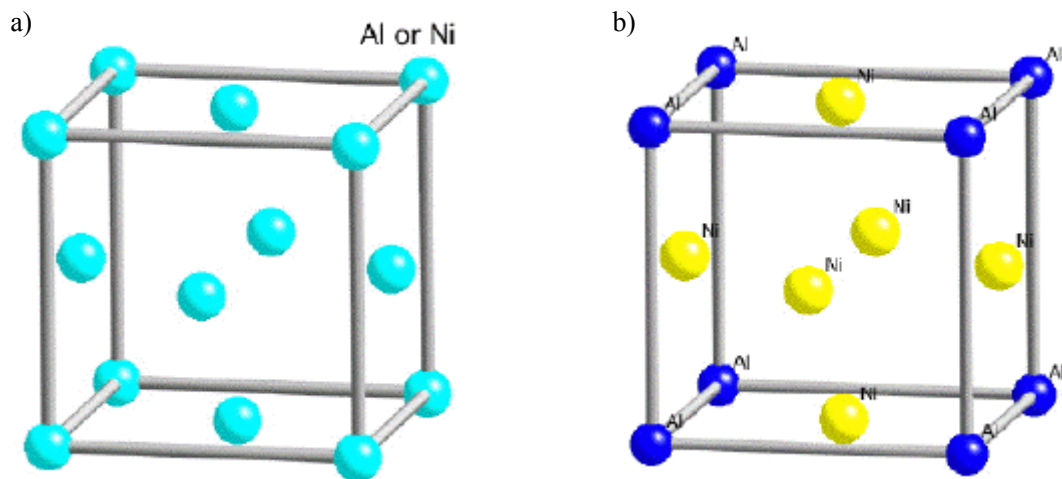


Fig. 2-5 Crystal structures of a) γ and b) γ' . From [Bhadeshia 2003]

Carbides

Carbides, in which carbon that is added in amounts of about 0.02 to 0.2 wt% combines with reactive elements, such as titanium, tantalum, hafnium, and niobium, to form metal carbides. The common nickel-base alloy carbides are MC, $M_{23}C_6$, and M_6C .

MC carbides, FCC in structure, usually exhibit a coarse, random cubic or script morphology (see Fig.2-6); they occur as discrete particles distributed randomly throughout the alloy, both in intergranular and transgranular positions, often interdendritically. They occur from simple combinations of carbon with reactive and refractory metals, classically possessing a formula such as TiC or TaC. The preferred order of formation in superalloys for these carbides is HfC, TaC, NbC, and TiC in order of decreasing stability.

$M_{23}C_6$ shows a marked tendency to precipitate on grain boundaries (see Fig. 2-6); it usually occurs as irregular discontinuous blocky particles, although plates and regular geometric forms have been observed. $M_{23}C_6$ carbides are profuse in alloys with moderate to high chromium content. They form during lower temperature heat treatment and service that is

760-980 °C, both from degeneration of MC and from soluble carbides residual in the alloy matrix. When molybdenum or tungsten are present, the approximate composition is $\text{Cr}_{21}(\text{Mo}, \text{W})_2\text{C}_6$ and generally appears fixed as such. M_{23}C_6 carbides have a significant effect on nickel alloy properties. Their critical location at grain boundaries promotes a significant effect on rupture strength, apparently through inhibition of grain boundary sliding. Eventually, however, rupture failure can initiate either by fracture of their same grain boundary M_{23}C_6 particles or by decohesion of the M_{23}C_6 interface.

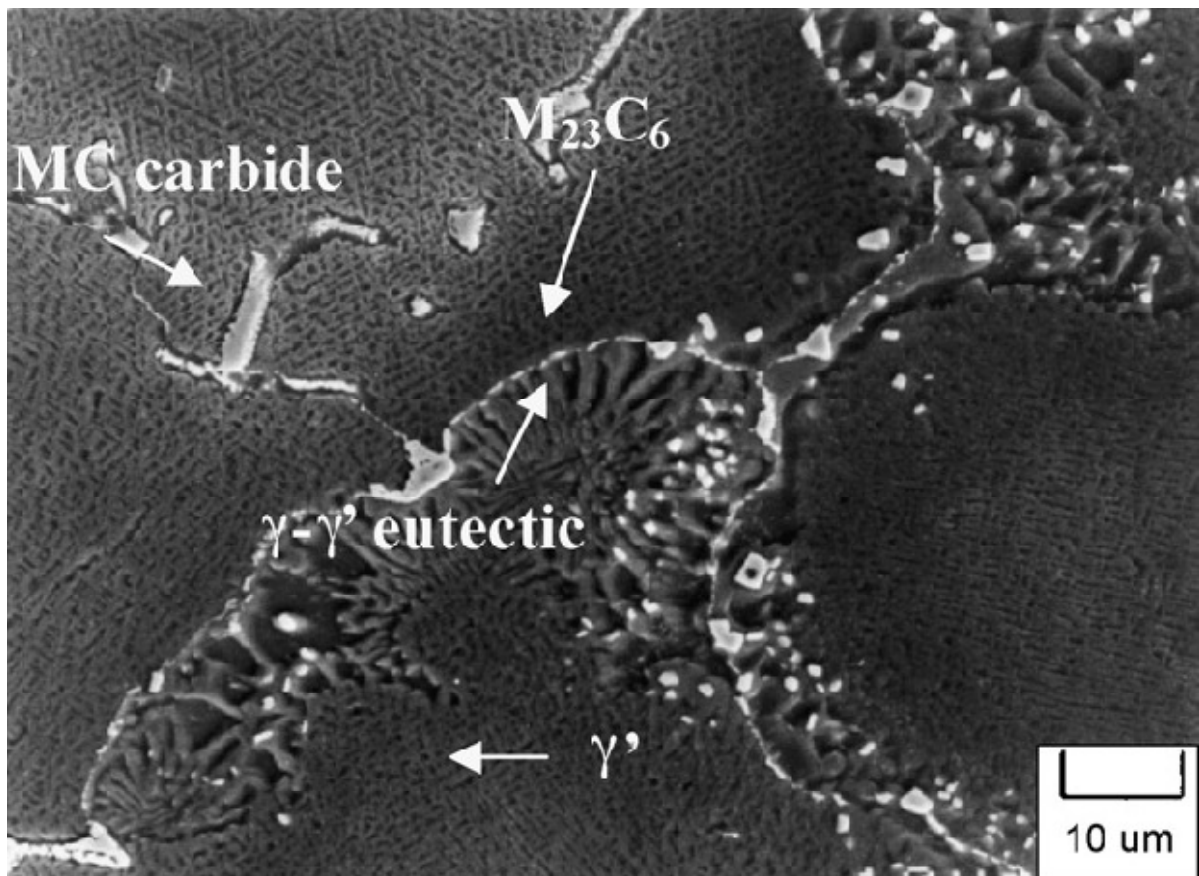
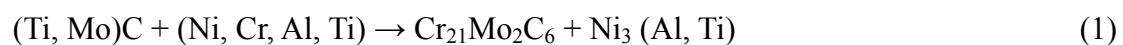


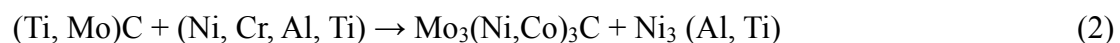
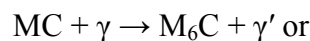
Fig.2-6 Secondary electron SEM of etched cast MarM247 showing morphology of Script-like MC carbides and grain boundary M_{23}C_6 carbides. From [Bor et al. 2008].

M_6C can also precipitate in blocky form in grain boundaries and more rarely in a Widmanstätten intragranular morphology. M_6C carbides have a complex cubic structure and form at slightly higher temperatures, 815-980 °C, than $M_{23}C_6$. They are formed when the molybdenum and/or tungsten content is high. Typical formulae for M_6C are $(Ni, Co)_3Mo_3C$ and $(Ni, Co)_2W_4C$. Since M_6C carbides are more stable at higher temperatures than $M_{23}C_6$ carbides, M_6C is more beneficial as a grain boundary precipitate to control grain size in processing wrought alloys. Although data are insufficient for precise correlation, it is apparent that continuous and/or denuded grain boundary $M_{23}C_6$ and Widmanstätten M_6C are to be avoided for best ductility and rupture life.

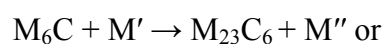
MC carbides are a major source of carbon in most nickel-base superalloys below 980 °C. However, MC decomposes slowly during heat treatment and service, releasing carbon for several important reactions. [Youdelis et al. 1983] The principal carbide reaction in many alloys is believed to be the formation of $M_{23}C_6$:



The carbide M_6C can form in a similar manner.



Also, M_6C and $M_{23}C_6$ interact, forming one from the other:





These reactions lead to carbide precipitation in various locations, but typically at grain boundaries. Perhaps the most beneficial reaction (for high creep resistance applications), that is controlled in many heat treatments, is that shown in reaction (1). Both the blocky carbides and the γ' produced are important in that they may inhibit grain-boundary sliding. In many cases, the γ' generated by this reaction coats the carbides [Sims, Stoloff et al. 1987], and the grain boundary becomes a relatively ductile, creep-resistant region. Recent findings in In718, GTD111, K452 served at intermediate temperature or long term exposure stated that the primary MC decomposed in the form of $\text{MC} + \gamma \rightarrow \text{M}_{23}\text{C}_6 + \eta$ [Lvov 2004; Qin et al. 2008]. η is a phase of HCP structure, the formula is Ni_3Ti and no solubility for other elements. It is commonly found in alloys with high titanium/aluminium ratios after extended exposure, may form intergranularly in a cellular form or intragranularly as acicular platelets in a Widmanstätten pattern. Thus the decomposition of MC is considered detrimental to material properties. However, modern alloys with high niobium and tantalum contents contain MC carbides that do not break down easily during solution treatment at, for instance, 1200-1260 °C.

Other phases

- Borides

Boron is an essential element to improve creep resistance in polycrystalline alloys by small additions. Borides are hard particles, blocky to half moon in appearance, that are observed at grain boundaries, where they block the onset of grain boundary tearing under creep rupture loading.

- TCP (Topologically Close-Packed) Phases

In some alloys where composition is not carefully controlled, undesirable phases can form either during heat treatment or more commonly during service. These precipitates, known as TCP phases, are composed of close packed layers of atoms parallel to $\{111\}$ planes of the γ matrix. Usually harmful, they may appear as thin linear plates, which generally nucleate on grain boundary carbides. Nickel alloys are especially prone to the formation of σ and μ . The formula for σ is $(\text{Fe, Mo})_x(\text{Ni, Co})_y$, where x and y can vary from 1 to 7. Alloys containing a high level of BCC (Body-Centred Cubic) transition metals (tantalum, niobium, chromium, tungsten, and molybdenum) are most susceptible to TCP formation.

The σ hardness and its plate-like morphology cause premature cracking, leading to low-temperature brittle failure, although yield strength is unaffected. However, the major effect is on elevated-temperature rupture strength. As reported in Udimet 700 [Johnson 1967], sigma formation must deplete refractory metals in the γ matrix, causing loss of strength of the matrix. Also, high temperature fracture can occur along σ plates rather than along the normal intergranular path, resulting in sharply reduced rupture life.

Plate-like μ can form also, but little is known about its detrimental effects. A general formula for μ is $(\text{Fe, Co})_7(\text{Mo, W})_6$. Nickel can substitute for part of the iron or the cobalt.

Laves phase has an MgZn_2 hexagonal crystal structure with a composition of AB_2 type. Typical examples include Fe_2Ti , Fe_2Nb , and Fe_2Mo , but a more general formula is $(\text{Fe, Cr, Mn, Si})_2(\text{Mo, Ti, Nb})$. They are most commonly observed in the iron-nickel-base alloys as coarse intergranular particles. Silicon and niobium promote formation of Laves phase in Inconel 718. Excessive amounts will impair room-temperature tensile ductility and creep properties.

2.2.2 Strengthening of γ' hardened alloy

The major contribution to the strength of γ' hardened nickel-base superalloys is provided by the amount and morphology of γ' . Other phases in single crystal alloys, for example, borides and carbides, provide little additional strengthening at low temperatures due to the small volume fractions present. However, the usable strength in polycrystalline alloys is determined by the condition of the grain boundaries, particularly as affected by the carbide phase morphology and distribution. Satisfactory properties are achieved by optimizing the γ' volume fraction and morphology (not necessarily independent characteristics) in conjunction with securing a dispersion of discrete globular carbides along the grain boundaries.

Strengthening by γ'

The γ phase forms the matrix in which the γ' precipitates. The phases both have a cubic lattice with similar lattice parameters and the γ' precipitates in a cube-cube orientation relationship with the γ [Sims, Stoloff et al. 1987]. This means that its cell edges are exactly parallel to corresponding edges of the γ phase. Furthermore, because their lattice parameters are similar, the γ' is coherent with the γ when the precipitate size is small. Dislocations in the γ nevertheless find it difficult to penetrate γ' , partly because the γ' is an atomically ordered phase. The order interferes with dislocation motion and hence strengthens the alloy. It is now generally accepted that small γ' precipitates are cut by paired $\frac{1}{2}\langle 110 \rangle$ dislocations and that large γ' precipitates are bypassed by Orowan looping [Reppich et al. 1986].

The volume fraction of γ' clearly influences alloy strength. Early superalloys contained less than 25 vol% of γ' . Most wrought nickel-base superalloys contain between 20 and 45 vol% of γ' . Gamma prime contents above approximately 45% render the alloy difficult to deform

by hot or cold rolling. Nickel-base cast superalloys contain approximately 60 vol% γ' . This increased level of γ' results in greater alloy creep strength.(see Fig. 2-7)

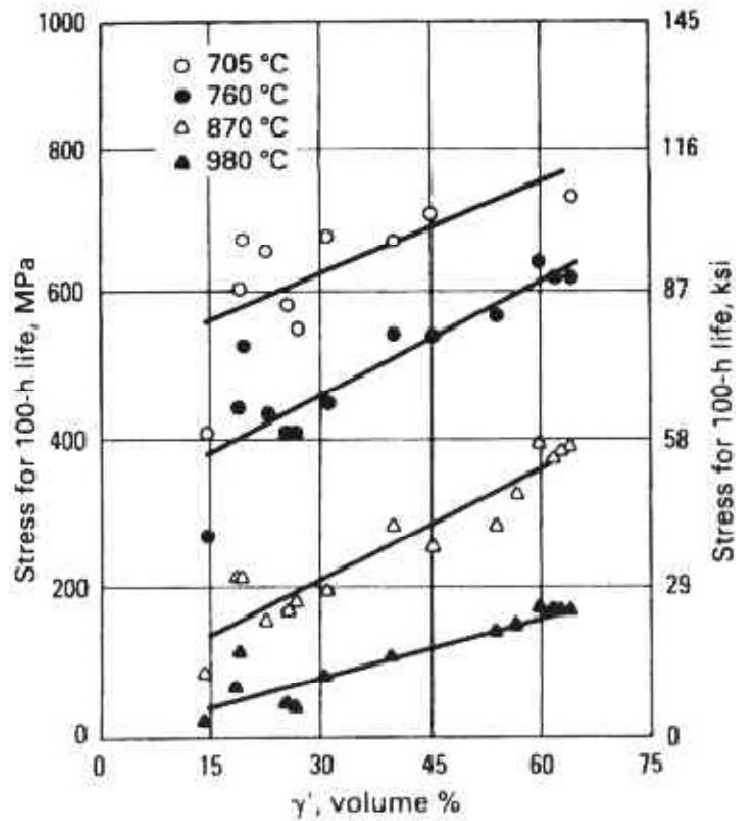


Fig.2-7 The relationship between γ' volume fraction and stress-rupture strength for nickel-base superalloys. From [Decker et al. 1969]

The 0.2% proof stress and ultimate tensile strength increased with increasing gamma prime - particle size up to a peak value and then decreased with further increase in particle size (see Fig. 2-8). The proof stress peaks occurred at critical particle sizes in the range of 15-20 μm . The change in ductility with strength followed the normal behaviour, i.e., as the peak strength was approached the ductility decreased [Rifai et al. 1985]. Later research found that for the same material, the specimens having smaller γ' precipitates showed higher strength

and creep resistance, because dislocation motion was significantly suppressed due to the small mean surface-to-surface spacing between precipitates. [Kakehi 1999].

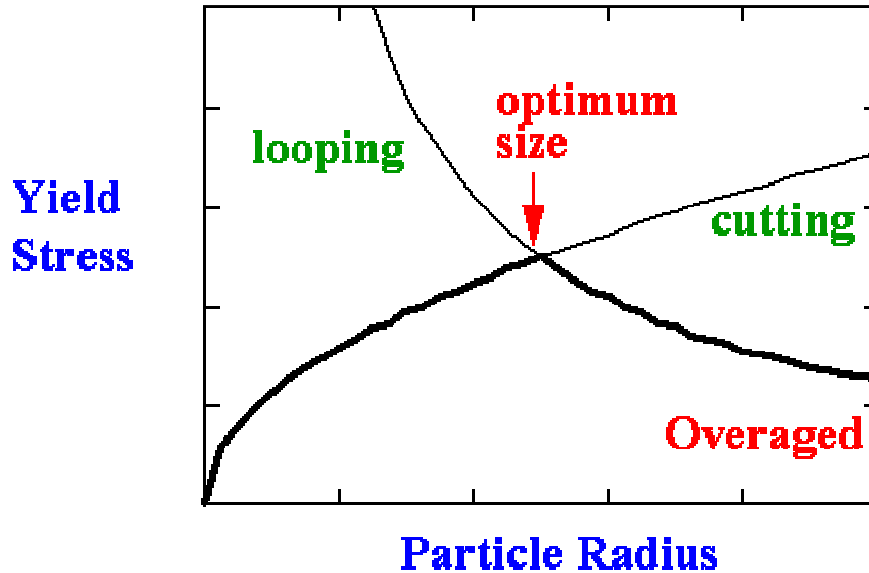


Fig. 2-8 Consideration of the critical stresses for cutting and looping shows that there is an optimum particle size for precipitate hardening. [Rifai, Abdou et al. 1985]

The coherent precipitation of the ordered $L1_2$ γ' structure in a disordered γ matrix gives rise to coherency strains between the two phases, due to their different lattice parameters. The magnitude of the strengthening effect of γ' is influenced by the mismatch in lattice parameters between the γ' and the γ matrix, which is given by Eq.2.1

$$\delta = 2 \frac{(a_{\gamma'} - a_{\gamma})}{(a_{\gamma'} + a_{\gamma})} \quad (2.1)$$

Where δ is the mismatch and a is the lattice parameter of γ' or γ , respectively. The small misfit between the γ and γ' lattices is important for two reasons. Firstly, when combined with the cube-cube orientation relationship, it ensures a low γ/γ' interfacial energy. The ordinary mechanism of precipitate coarsening is driven entirely by the minimization of total

interfacial energy. A coherent or semi-coherent interface therefore makes the microstructure stable, a property which is useful for elevated temperature applications.

The magnitude and sign of the misfit also influences the development of microstructure under the influence of a stress at elevated temperatures, e.g. the 'rafting' of γ' which is a hardening process during creep [Kakehi 1999; Ma et al. 2005]. The misfit is said to be positive when the γ' has a larger lattice parameter than γ . The morphology of γ' is correlated with magnitude of the γ/γ' mismatch [Ricks et al. 1983]. It is observed that γ' occurs as spheres for 0 to 0.2% mismatches, becomes cubic for mismatches of 0.5 to 1%, and is plate-like at mismatches above about 1.25% [Davis 1997]. This applies to both positive and negative misfit alloys.

Alloys with relatively large negative lattice misfits (-0.2% to -0.5%) create dense interfacial networks of edge dislocations in the γ of the sense that effectively removes atomic planes in the gamma. As these networks form, matrix dislocations are drawn to the γ/γ' interface to relieve the misfit stress; these networks at γ/γ' interfaces were not well developed in positive misfit alloys as a compressive hydrostatic stress in vicinity to the precipitate particles will tend to repel matrix dislocations [Ricks, Porter et al. 1983]. The alloys with large, negative values of lattice mismatch exhibited superior creep properties as deformation is more often limited to the γ matrix [Harada 2001; Zhang et al. 2005]. Furthermore, the rafts formed on planes normal to the tensile stress axis under a negative misfit tend to improve creep properties [MacKay et al. 1990; Nabarro and Villiers 1995]. The γ' precipitates are stronger and resist the dislocation movement; the weak matrix γ provides the softer characteristics necessary for the ductility, thus giving the high temperature creep strength to the alloy.

In addition, it is well known that the $L1_2$ ordered structure displays an anomalous yield stress versus temperature behaviour (see Fig.2-9). The most widely accepted mechanism is that the flow stress increase involves cross slip of screw dislocations from $\{111\}$ slip planes to the $\{010\}$ planes where the dislocations are locked and assumed to be immobile [Thornton et al. 1970]. This interaction can result in unusual behaviour where the high temperature (e.g.600 °C) yield strength is higher than the room temperature value even though the strength of the γ phase decreases with increasing temperature. At even higher temperatures, diffusional mechanisms start to unlock the dislocations and the strength of the γ' drops rapidly and with it the overall strength of the material decreases. Therefore below the peak strength temperature, i.e. in the regime where the yield strength increases with rising temperature, the active slip systems are predominantly $\{111\}\langle 110\rangle$, where above the peak temperature $\{100\}\langle 110\rangle$ slip is dominant [Stantonbevan et al. 1975]. The driving force for the change of slip mode with increasing temperature is provided both by the anisotropy of the anti-phase boundary (APB) on the different planes and by the resolved shear stress on the $\{100\}\langle 110\rangle$ system. It was illustrated by a number of researchers [Koehler et al. 1947; Taunt et al. 1974] that at high temperature, dislocations have a lower energy on the $\{010\}$ planes than on the $\{111\}$ planes because the APB energy is at a minimum on the $\{010\}$ planes and the $\frac{1}{2}\langle 110\rangle$ dislocations are further apart. Further studies in this area showed that Shockley partials form during high temperature deformation, which cause the critical resolved shear stress (CRSS) of grains orientated near $\langle 001\rangle$ and $\langle 111\rangle$ to be directionally dependent [Lall et al. 1979; Shah et al. 1980]. Experimental evidence of the change of the slip mode in γ' has been achieved by in situ TEM studies on single crystal alloy [Clement et al. 1991] and also detected in polycrystalline alloys using neutron diffraction [Daymond et al. 2007; Preuss et al. 2008].

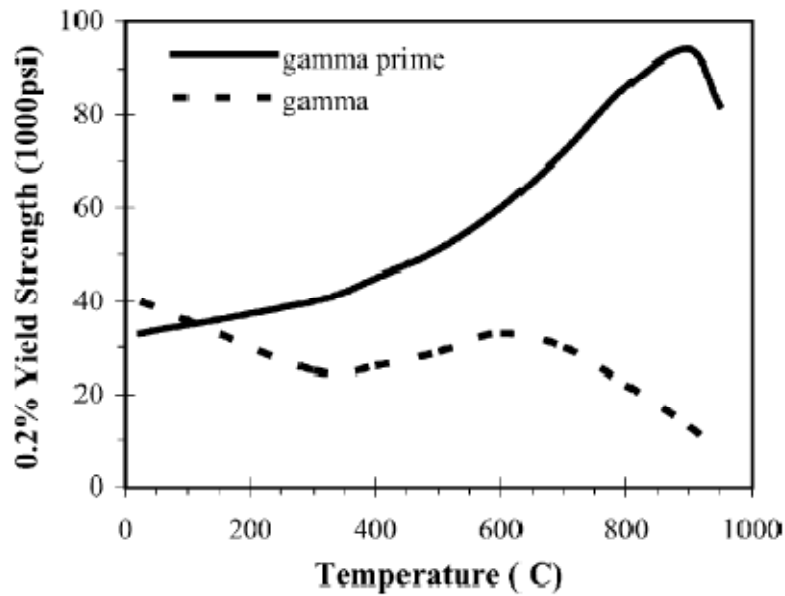


Fig. 2-9 0.2% yield strength variations of single-phase γ and γ' alloys with temperature.

From [Sajjadi et al. 2004]

Carbide distribution

Beside γ' , carbide particles also play an important role in nickel-based superalloys. They serve three principal functions. Firstly grain-boundary carbides, when properly formed, strengthen the grain boundary, preventing or retarding grain-boundary sliding. Secondly, if fine carbides are precipitated in the matrix, strengthening results. Thirdly carbides can tie up certain elements that would otherwise promote phase instability during service. Their volume fraction, size and morphology have very important effects on the mechanical properties. For example, the MC carbides usually have blocky or script-like morphology, and are often located at grain boundaries. They have been observed to fracture during tensile straining, and during thermal-fatigue experiments, and in each case were thought to be instrumental in crack initiation leading to grain-boundary failure. Similarly, pre-cracked MC

carbides have been found to initiate slip and fatigue cracking in tests carried out at room temperature and elevated temperatures. Fatigue life was found to be a strong function of carbide size at high stress levels and at low or intermediate (760 °C) temperatures. Fatigue life was observed to vary inversely with carbide size [Gell *et al.* 1968]. The removal of large carbide particles or defects prevents crack initiation at these locations in the structure. The delay of this initiation step can improve HCF strength by 15 to 20%. In some alloys, removal of carbides larger than 1 µm has also increased LCF life [Decker 1973]. However, small equiaxed MC carbides can have a beneficial effect as obstacles to fatigue-crack propagation [Chen *et al.* 1998].

Grain size and grain boundary

Work in the first half of the twentieth century by Hall and Petch gave rise to the general relationship relating yield stress and other mechanical properties to grain size based on the idea that grain boundaries act as barriers to dislocation motion [Calister 2005]. Although later work emphasized the role of grain boundaries as dislocation sources, experimental observations confirmed the general relationship between decreased grain size and increased yield strength. A balance must be struck to avoid excessively fine grains, which decrease creep and rupture strength, and excessively large grains which lower tensile strength (but conversely have good rupture strength).

Besides the grain size, the morphology of grain boundaries is also a key aspect of structure-property relationship. Serration of grain boundaries (Fig.2-10) are observed in many superalloys [Larson 1976; Koul *et al.* 1983; Henry *et al.* 1993; Danflou *et al.* 1996; Mitchell *et al.* 2009]. Further work investigated the effect of these serrations on mechanical properties, especially in a PM nickel-based superalloy [Danflou *et al.* 1992]. Results from this work showed no clear change in tensile properties between the serrated and straight

boundary material. However, creep-fatigue crack growth rates were found to be significantly slower for the serrated material. The crack propagation mode was consistently intergranular but crack paths were more complex following the rough surface of serrated grain boundaries and thereby retarding crack growth.

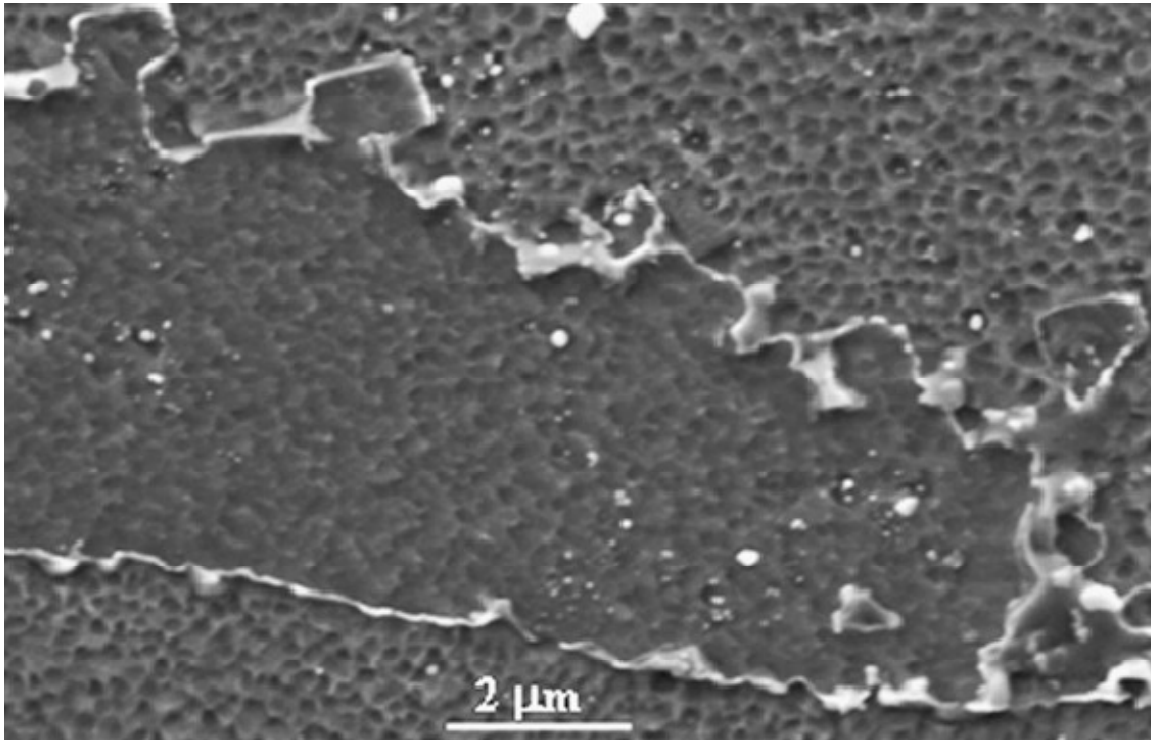


Fig.2-10 Secondary electron SEM micrograph showing the grain boundary serration caused by coarse secondary γ' particles in RR1000. From [Mitchell, Li et al. 2009]

The serrated grain boundary formation as a function of cooling rate has been studied in a number of nickel-based superalloys, e.g. IN738, Nimonic 115 and Nimonic 105. The mechanism is related to γ' precipitation in these alloys and a higher γ' solvus temperature than the $M_{23}C_6$ solvus temperature appears to be a pre-requisite for the development of serrations [Koul and Morphy 1983]. The mechanism of formation of the serrated grain

boundaries will be discussed in more detail in § 2.2.4.

2.2.3 The phase control of γ' hardened alloy by compositional elements

Most nickel-based alloys contain 10-20% Cr, up to 8% Al and Ti, 5-10% Co, and small amounts of B, Zr, and C. Other common additions are Mo, W, Ta, Hf, and Nb. In broad terms, the elemental additions in Ni-base superalloys can be categorized as being i) γ formers and strengtheners - elements that tend to partition to the γ matrix, ii) γ' formers and strengtheners - elements that partition to the γ' precipitate, iii) carbide formers, and iv) elements that segregate to the grain boundaries. Elements that are commonly used in nickel-base superalloys are shown in Fig. 2-11. Elements which are considered γ formers are Group V, VI, and VII elements such as Co, Cr, Mo, W and Fe. The atomic diameters of these alloys are only 3-13% different from that of Ni (the primary matrix element). γ' formers come from group III, IV, and V elements and include Al, Ti, Nb, Ta and Hf. The atomic diameters of these elements differ from Ni by 6-18%. The main carbide formers are Cr, Mo, W, Nb, Ta and Ti. The primary grain boundary elements are B, C, Zr and Hf. Their atomic diameters are 21-27% different from that of Ni. Re and Ru have the effect of increasing the liquidus and solidus temperature of the alloy; they are employed in the new single crystal alloys such as TMS-138 and MC-NG and improved their stability and high temperature mechanical properties significantly [Caron 2000; Ma et al. 2007].

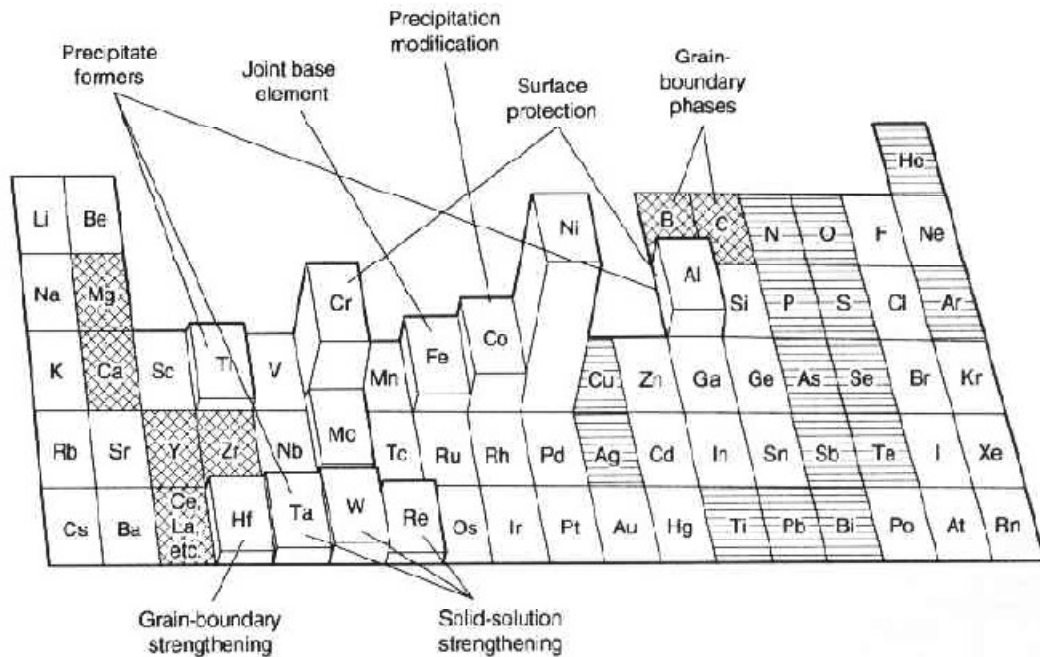


Fig. 2-11 Alloying elements used in nickel-base superalloys. Beneficial trace elements are marked with cross hatching and harmful trace elements are marked with horizontal line hatching. [Sims, Stoloff et al. 1987]

Phase control of γ' by composition

The volume fraction of γ' is mainly adjusted by controlling the percentage of γ' -forming elements such as Al, Ti and Ta [Janowski et al. 1986] in the alloy. The solution of some elements also shifts the temperature and magnitude of the γ' -induced peak of the flow stress (see Fig. 2-12). However, changes of some non- γ' -forming elements may also indirectly influence the volume fraction of γ' . For example, the amount of γ' increases with decreasing C concentration [Miner 1977].

The addition of Hf causes colonies of $\gamma + \gamma'$ with rosette morphology to form and individual γ' platelets exhibit dendritic growth in casting. It was also shown that this morphology of γ' causes grain boundaries to be distorted from planar equilibrium interfaces to a convoluted interlocking configuration (serrated boundaries) [Kotval *et al.* 1972]. As mentioned previously, the interlocking boundaries retard grain boundary sliding and separation during creep and result in higher stress-rupture life for Hf-bearing alloys.

The mismatch between γ and γ' can also be controlled by altering the chemical composition, thus the morphology is controlled. The distribution of elements within the bulk alloy has a significant effect upon the lattice parameter of each phase. Elements such as cobalt, aluminium, titanium and tantalum, which are all present in γ' , may be present in varying quantities in the γ phase, due to effects of cooling rate for example. Nucleation of γ' occurs via an ordering transformation and then is followed by diffusion-controlled growth. Elements that partition to both phases may also contribute to the γ/γ' misfit and to the morphology of the γ' . For example, increasing the Mo-content significantly influences the particle size distributions and decreases the coarsening rate of the γ' cubes, as a result of increasing the magnitude of the lattice mismatch [MacKay and Nathal 1990]; increasing the content of W increases both lattice parameters of γ and γ' , moreover, the misfit γ and γ' was transformed from negative to positive because more W partitions to the γ' phase [Tian *et al.* 2008].

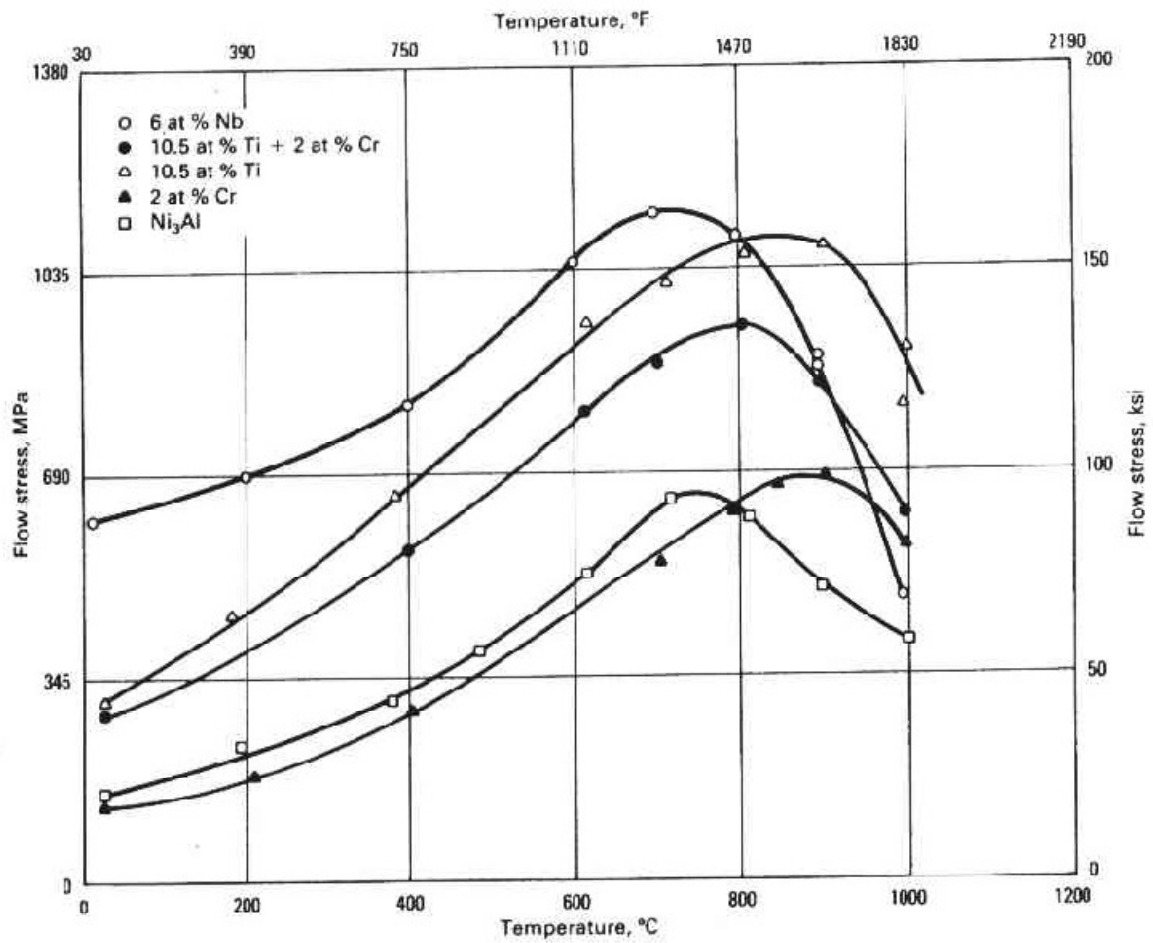


Fig. 2-12 Flow stress peak in γ' and influence of several solutes on the magnitude and temperature of the peak. [Sims, Stoloff et al. 1987]

Phase control of carbides by composition

Slight carbon additions increase grain boundary precipitation, decrease grain size and γ' solvus temperature [Podob 1977]. The carbon content should be carefully controlled to obtain desired properties. A low carbon concentration may cause insufficient pinning of grain boundaries and a high carbon concentration may cause continuous $M_{23}C_6$ carbides to form along boundaries leading to embrittlement of the boundaries. An improved distribution

of $M_{23}C_6$ on serrated grain boundaries in heat treated P/M IN-792 has been obtained at a carbon level of 0.04% [Larson 1976].

HfC is very stable compared with other carbide and its formation is favoured especially when the Hf content is more than 1% [McLean 1983; Sims, Stoloff et al. 1987]. Hafnium additions have been shown to change the carbide morphology from script to nodular in a powder metallurgy superalloy [Kotval, Venables et al. 1972], and to fewer block-shaped MC carbides and more fine $M_{23}C_6$ particles on grain boundaries [Hou et al. 2010]. Tantalum and niobium additions to superalloys altered carbide compositions, but their morphology was not affected [Youdelis and Kwon 1983; Janowski, Heckel et al. 1986].

2.2.4 The phase control of γ' hardened alloy by processing

The main processing parameters that affect the phase fractions, compositions and microstructures in alloys which are hardened by γ' are: (i) the temperatures at which the metal liquid is poured in casting, (ii) the temperatures at which the material is thermo-mechanically worked, (iii) the temperatures at which the metal powders are hot extruded (HE), hot pressed (HP) or hot isostatically pressed (HIP) (iv) the temperatures and holding times applied in heat treatments and (v) the cooling rate from those temperatures. The temperatures chosen are basically related to the alloy's melting point and γ' solvus when fabricating γ' -hardened nickel-base superalloys. The influence of pouring temperatures in casting will not be reviewed here since the work is focussed on solid phase transformations.

The as-processed materials are not directly employed in service due to various factors such as segregation, residual stress etc that downgrade the mechanical properties. These factors and the principal microstructural variables of superalloys - the amount of γ' and its

morphology; the γ grain size and shape; the carbide distribution - are usually controlled by post-process heat treatment.

A relatively common heat treatment consists of three steps: solution treatment at high temperature, stabilization/stress relief at an intermediate temperature, and a low temperature age [Blackburn *et al.* 1977; Sims, Stoloff *et al.* 1987]. Solution temperature is usually in the range of 1040 - 1230 °C, around the γ' solvus, and prepares the matrix for uniform precipitation of γ' on subsequent aging as well as influencing the extent of grain growth. A series of ages are then given to precipitate and to develop the major strengthening γ' phase and sometimes carbides or borides. Some other phases mentioned in §2.2.1 may also be present if the composition is not well controlled.

Early heat treatments consisted principally of only a high temperature solution treatment followed by a low temperature age. This generated good tensile and short time rupture properties but did not stabilize the structure sufficiently to produce optimized long time rupture properties. An additional intermediate temperature age was then added to drive the MC degeneration reaction [eqs.(1) and (2)] forward; grain boundaries with coarse particulate $M_{23}C_6$ embedded in a layer of γ' were developed, resulting in good rupture life and ductility. Thus, the alloy structure was “stabilized”. Fig 2-13 schematically illustrates the morphology of carbides and of γ' , before and after heat treatment, in wrought and cast nickel-base alloys. Solution temperature should not be high enough to dissolve M_6C since this would make the alloy susceptible to subsequent rapid precipitation of a continuous grain boundary $M_{23}C_6$ film [eqs. (3)], which would lead to poor ductility and cracking.

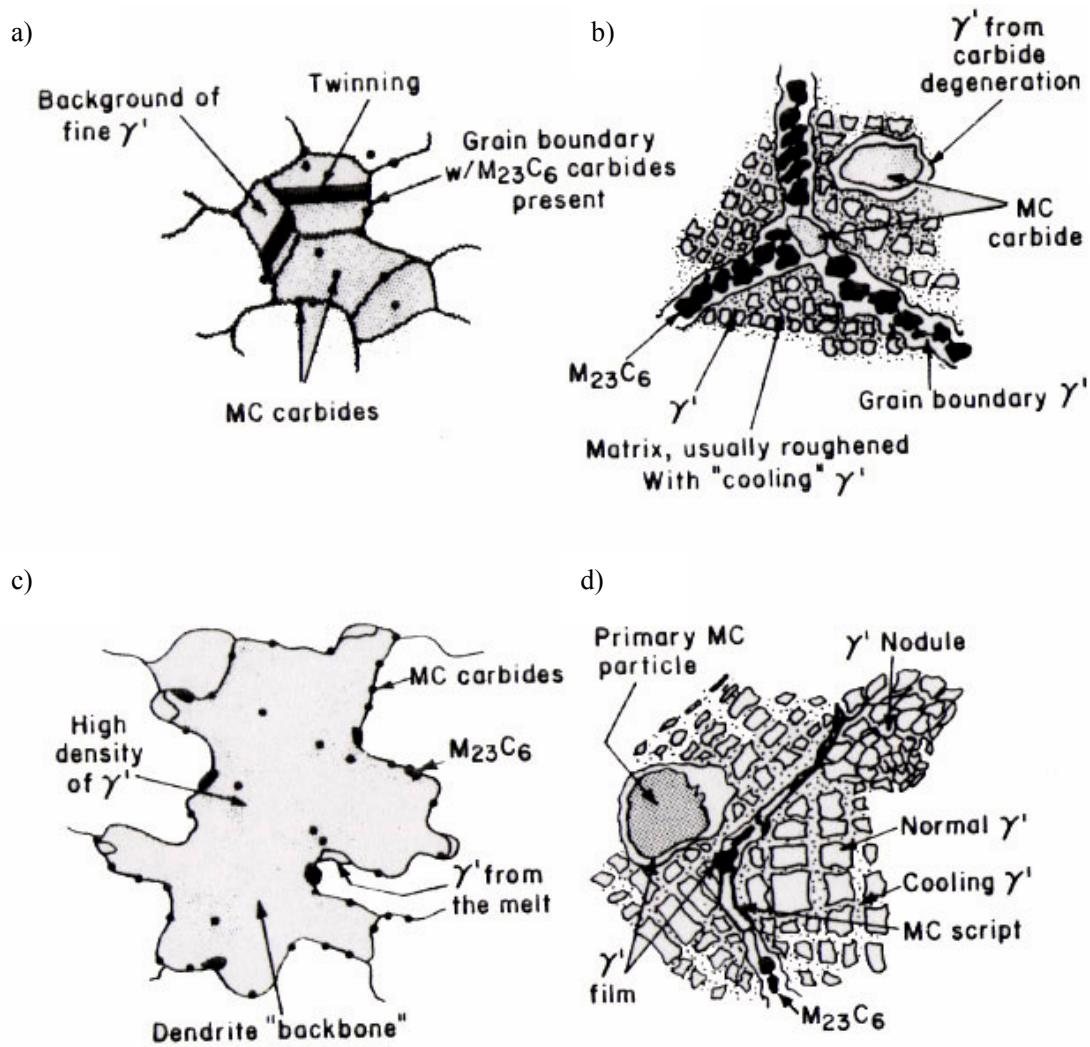


Fig 2-13 Sketch of phase's morphology before and after heat treatment in nickel-base superalloys. a) as- wrought b) as- heat treated wrought c) as-cast d) as-heat treated cast.

From [Sims, Stoloff et al. 1987]

Phase control of γ' by processing

Solution temperatures are selected sometimes above the solvus to completely dissolve primary γ' , not only to rearrange the distribution of γ' , but also to cause grain growth, to improve creep strength. Solution temperatures chosen below the γ' solvus normally aim to

partly dissolve primary γ' and to generate a bimodal distribution of γ' precipitates [Chellman et al. 1976; Balikci et al. 1997].

The cooling rate is responsible for determining the size and distribution of the γ' that forms, in addition to the initial volume fraction [Mitchell et al. 2008]. For fast cooling rates there is little time for particle growth and the γ' distribution is governed by the nucleation event, resulting in a high number of fine γ' being precipitated. At slower cooling rates and smaller volume fractions, precipitate growth dominates and precipitates deviate from spheres as their size increases and their diffusion and strain fields overlap [Ardell 1968].

Cooling rate is also reported to be responsible for the generation of serrated grain boundaries. Early studies by Larson found in IN-792 that fast cooling, e.g. air cooling, through the γ' solvus temperature can develop highly serrated grain boundaries. Serrations were suggested to be the result of γ' initially precipitating at the grain boundaries and the shape of the grain boundaries are influenced by the dendritic development of γ' [Larson 1976]. Later studies reported that it was slow cooling that enhanced the extent of boundary serrations [Henry, Yoo et al. 1993; Danflou, Macia et al. 1996]. Their explanation was that the growth behaviour of the γ' precipitates is determined by the degree of supersaturation maintained in the matrix. Under the condition of high supersaturation and low nucleation rate, which can be obtained either by aging at temperature just below the γ' solvus or by slow cooling after supersolvus solution treatment [Sharpe 2007; Gabb et al. 2008], coherent γ' particles show a strong propensity for dendritic growth. The unbalanced growth of γ' occurs particularly at grain boundaries because of the extent of diffusion of solute atoms from the supersaturated matrix. The asymmetric growth of dendrite arms towards grain boundaries is expected to perturb the grain boundaries on both sides and consequently to produce grain boundary serrations.

It is found that for the subsolvus annealing in powder-formed IN-792, γ' precipitates

coherently with the matrix, for short duration, anneals whereas 2-hour annealing causes precipitation of γ' along grain boundaries [Huda et al. 1990]. This agrees with the previous conclusion that γ' prefers to precipitate at grain boundaries as it is easier to fit the γ/γ' mismatch at grain boundaries.

Phase control of carbides by processing

MC carbides usually form during freezing if manufactured by casting. During heat treatment and service, MC carbides tend to decompose and generate other carbides, such as $M_{23}C_6$ and/or M_6C , which tend to form at grain boundaries. Carbides in nominally solid-solution alloys may form after extended service exposures.

The MC carbide size and distribution is dependent on the type of processing to a large degree and can greatly affect the mechanical properties of superalloys. For the same material, with decreasing MC carbide size, there is an increased tendency for film-like rather than a globular $M_{23}C_6$ at the grain boundaries [Larson 1976]. The P/M material with finer MC carbide distribution exhibits a larger amount of $M_{23}C_6$ at the grain boundaries than the cast material with the coarser carbide distribution. The tendency for a rather thick film-like layer of $M_{23}C_6$ with decreasing MC carbide size is related to kinetics. With small and finely dispersed MC particles, the interfacial area per unit volume is larger and the diffusion distance for carbon to move to the surface of a grain is smaller than for a material containing large, widely dispersed MC carbides. Both these factors tend to accelerate the MC to $M_{23}C_6$ reaction in the material containing fine dispersed MC.

An intermediate heat treatment was initially employed in an attempt to control the formation of $M_{23}C_6$ carbides more effectively. However, in every case this intermediate treatment led to a film-like $M_{23}C_6$ precipitate at grain boundaries. This brittle film-like $M_{23}C_6$ is thought to be

an excellent path for crack propagation and seriously degrades the mechanical properties of superalloys. The most effective way to control the $M_{23}C_6$ precipitation was to develop a serrated grain boundary which promoted the formation of a globular $M_{23}C_6$ precipitate [Larson 1976].

2.3 Hot isostatic pressing

The hot isostatic pressing (HIPping) process was initially developed as a means of diffusion bonding nuclear reactor components and for the removal of porosity in hard materials [Atkinson et al. 1991]. However, the major commercial activity now centres upon the consolidation of metal powders and on the densification of high-performance castings. HIPping is utilized in a wide range of industries including aerospace, marine, and off-shore, power generation, automotive, medical, defence, telecommunications, metal working and mining.

2.3.1 The HIPping Process

HIPping involves the simultaneous application of a high-pressure (usually inert) gas and an elevated temperature in a specially constructed vessel. Fig 2-14 shows the main elements of a HIPping facility. The pressure applied is isostatic because it is developed with a gas, so that, at least as a first approximation, no alteration in component geometry occurs. Gas-free internal pores or defects within a solid body collapse and weld up under these conditions of heat and pressure. Castings, encapsulated powders and sintered components alike are densified and consolidated to give improved mechanical properties and a reduction in the scatter-band of properties [Atkinson et al. 2000].

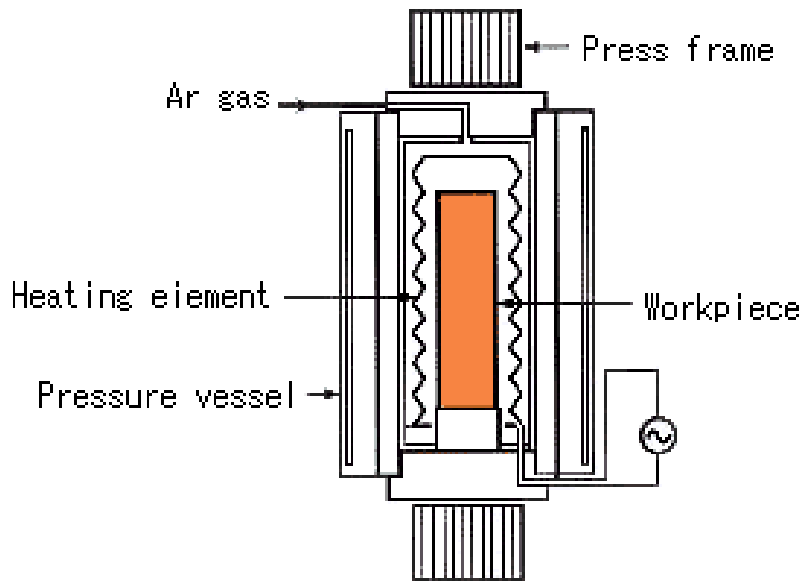


Fig. 2-14 Sketch of a typical HIPping layout

2.2.2 Densification

HIPping is largely concerned with the removal of pores. Pores may originate, for example, from the packing of powder particles or from gas entrapment in powder metallurgy methods. In simple terms the driving force to achieve densification by sintering is associated with the reduction in surface area and hence surface energy of the pores. When pressure is applied in addition to heat, the densification mechanisms are modified. Densification mechanisms are then dependent on the pressure, the temperature, the pore size, the presence of gas within the pores and the location of the pores.

For most metals and ceramics, yield strength decreases with increasing temperature. HIPping conditions are generally chosen so that the gas pressure is greater than the reduced yield point of the material at that temperature. Plastic flow can then occur on a microscopic scale.

Under HIPping conditions, considerable particle shear occurs and creep processes such as Nabarro-Herring creep (diffusion through grain interiors), Coble creep (diffusion around grain boundaries) and dislocation creep operate at very high rates [Helle *et al.* 1985]. Particle shear or extrusion can break up surface films on particles (e.g. oxides), exposing new clean surfaces and hence enhancing surface diffusion rates. Some oxide particles may be retained after HIPping. During the final stages of HIPping densification, when only isolated pores are present, the surface of the pores are not simply pushed together to develop a planar crack. Bonding occurs because atoms diffuse in both directions across the interface. At this stage pore dimensions are small (1µm or less) and the time (1h or longer) is more than adequate to allow complete closure. If there is gas in the pore (as is commonly the case) then the laws relating pressure, temperature and volume of a gas ($PV = nRT$) shows that complete closure is not possible and hence (when reheated) they reopen.

2.2.3 Effect of HIPping on microstructure and composition

As mentioned the major effect of HIPping on the structure of powder compacts is the removal or reduction in the volume fraction of porosity. However, the possible occurrence of secondary effects such as grain growth, changes in precipitate distributions and changes in segregation patterns must be considered. All these processes involve diffusion and are therefore enhanced at high temperatures. In addition, the high temperatures might influence phase transformations, change melting points and crack brittle particles during heating/cooling. Normal grain growth can usually be characterized by the equation [Atkinson and Rickinson 1991]

$$G_t^n - G_0^n = Kt \quad (2.2)$$

where G_t is the grain size at time t , G_0 is the initial grain size, K is a constant at given temperature, t is the time and n is the grain growth exponent (always greater than or equal to 2). K is given by

$$K = C \exp\left(-\frac{Q}{RT}\right) \quad (2.3)$$

where C is another constant, Q the activation energy for grain boundary migration, R the ideal gas constant and T the absolute temperature. Thus, the higher the temperature, the more rapid is boundary migration. Boundaries can be pinned by impurities or by fine distributions of precipitates. However, as the temperature increases, impurity diffusion is enhanced and precipitates may coarsen or dissolve, allowing boundaries to migrate. The effect of precipitates in pinning dislocations is also then reduced, hence decreasing the yield point. All these major processes occur with conventional sintering as well as HIPping, but one advantage of HIPping is that the temperatures required for densification are lower and the times at elevated temperature shorter. Excessive grain growth can then be avoided; thereby retaining the relatively high yield points and toughness which fine grain size confers.

The pressures involved in HIPping (typically 100-200 MPa) are too low in themselves to cause solid-state phase transformations, although there is evidence that phase proportions may be changed in specific case [*Huang et al. 2007; Wang et al. 2009*]. Phase transformations have not therefore been generally regarded as a serious concern in HIPping.

The relationship between cost and HIPping conditions (temperature, pressure and time) is not simple. The shortest cycle is not necessarily the cheapest. In addition, potential effects on microstructure must be taken into account. In general, the processing temperature T is greater than $0.7 T_m$ where T_m is the solidus. In some cases, HIPping may be carried out close

to the solidus. Typical HIPping condition for superalloys is at temperatures between 1100 °C and 1280 °C and pressures between 100 to 200 MPa [Atkinson and Rickinson 1991] .

2.2.4 Advantages and disadvantages of powder HIPping

Conventional cast and wrought nickel-base superalloys, by virtue of their excellent high temperature mechanical properties and corrosion resistance, are the materials of choice for a wide range of gas turbine engine hardware. Among the problems encountered in the manufacture of these parts is a tendency towards elemental segregation in the casting. To an extent, the effects of segregation are reduced by subsequent forging and heat treatment practices. The forging operation necessitates the utilization of a considerably larger preform than the finished component size. Excess material required for adequate hot working of the preform ends up as machining scrap. Both the cost of the excess material and the machining of the material, coupled with an expensive forging operation, increase the cost of the finished product.

Use of advanced powder metallurgy techniques, specifically “Near Net Shape Hot Isostatic Pressing (NSHIPping)” to near finished machined shapes, for the fabrication of these components, is attractive from both a metallurgical and economic approach. High quality pre-alloyed powder produced by several different atomization processes is readily available for commercial use [Hohmann et al. 1990]. Since the cooling kinetics of small molten droplets is extremely fast (10^3 °C/second compared with $10\text{-}10^{-2}$ °C/second for a large casting), both the dendritic arm spacing and volume fraction and particle sizes of secondary phases are small, promoting alloy homogeneity. Hot isostatic pressing nickel-base superalloy powders at proper conditions results in a near 100% dense material which, with suitable heat treatment, may have mechanical properties equivalent to or better than current gas turbine

engine components [Williams 1977]. A direct HIP approach for part manufacture offers potential cost savings since excess material (and machining) and forging is not necessary.

The advantages of NSHIPping are summarized as follows:

- More uniform composition and phase distribution.
- Reduced carbide segregation
- Higher material yields
- Increased flexibility in alloy design
- Material and fabrication savings attainable

However, in addition to cost, several problems arise directly from powder techniques:

- Increased residual gas content
- Carbon contamination
- Ceramic inclusions and general cleanliness control
- Formation of prior particle boundary oxide and/or carbide films
- Entrapped gas if gas is involved in atomization process [Podob 1977]

2.2.5 HIPping of nickel-base superalloys

HIPping is traditionally utilized as a heat treatment method on superalloy castings to eliminate casting porosity [Schweikert et al. 1980; Chang 2009]. Nowadays, more applications of HIPping are investigated in more and more superalloy fabrication fields, such as powder consolidation, diffusion bonding [Larker 1999] and crack healing [Zhao 2009] etc. This section will focus on the techniques and problems encountered in powder HIPping of nickel-base superalloys.

The HIPping temperature was found to influence the morphology of γ' . The shape of γ' was spherical if HIPped below the γ' solvus and changed to cubic when HIPped above the solvus [Podob 1977]. Strengths decrease with increasing HIP temperature, qualitatively in accordance with the Hall-Petch relationship (higher strengths with a fine-grained material). The HIPping pressure, temperature and time should be sufficient to close pores in the powder compact but conditions may be constrained by consideration of the desirability of grain growth. Low pressure processing does not appear desirable for superalloys HIPping such as low carbon P/M Astroloy, as the pores located at triple point of grain boundaries coincident with prior particle boundaries are not collapsed [Price et al. 1977].

A well-known phenomenon in P/M superalloys is the formation of precipitates in the compacted material at prior powder-particle boundaries (PPBs) (see Fig. 2-15). As well as affecting mechanical properties adversely this precipitation can complicate microstructural control e.g. by hindering grain coarsening. Material used for P/M materials are usually optimized in composition to overcome prior particle boundaries. Reduction of the C-content in the material eliminated the problem of continuous films of MC carbides precipitate on PPBs [Williams 1977; Ingesten et al. 1982]. Another possibility of reducing the PPB problem is to add strong carbide formers such as Nb, Ta or Hf [Dahlén et al. 1981]. A literature survey of the existing P/M materials showed that superalloys containing appreciable amounts of Nb and/or Ta do not form MC at PPB [Larson 1976]. This is because when stable carbides are formed in particle interiors, the solubility and thus the redistribution of carbon during the high temperature HIP treatment is reduced. The handling of powder should ensure no contact with oxygen because high energy oxide/metal and oxide/oxide interfaces provide favourable nucleation sites for carbides [Menzies et al. 1980; Dahlén, Ingesten et al. 1981] and the oxides themselves are undesirable. HIPping temperature was

found another solution to PPBs. As for alloy APK1, HIP at temperatures well above the γ' solvus results in a microstructure free from PPB precipitate networks, while HIP at temperature slightly below γ' solvus leads to carbide networks at PPB [Prakash *et al.* 1983]. Heat treatment prior to HIPping can help reduce the PPB net work if sub-solvus HIPping is required, for example, fine grains are expected [Dahlén, Ingesten *et al.* 1981; Prakash, Chari *et al.* 1983].

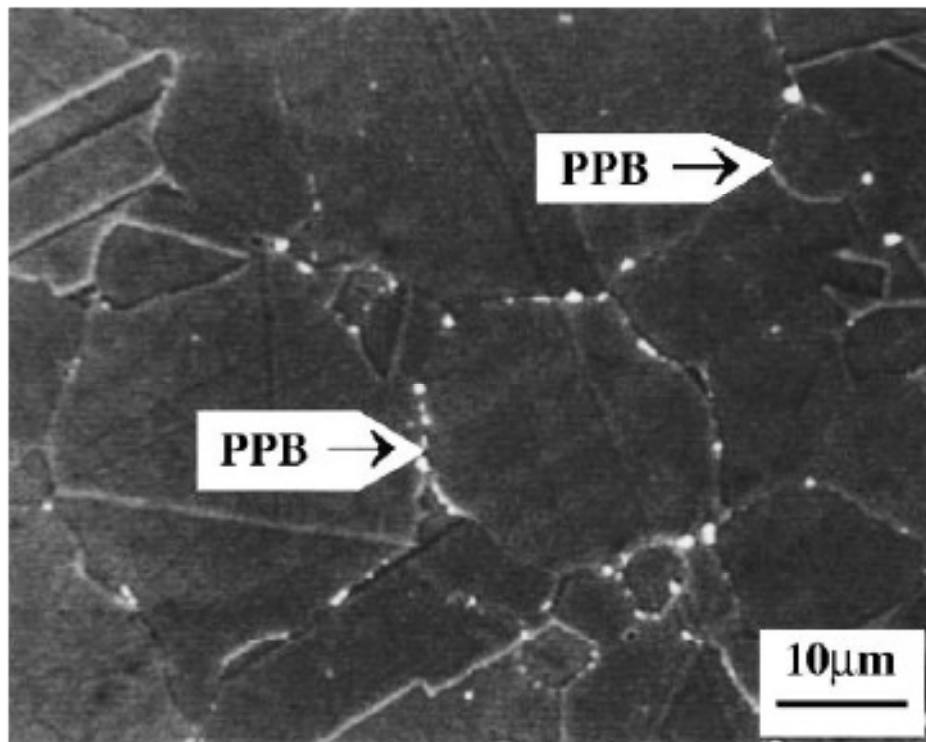


Fig.2-15 Microstructure of as-HIPped superalloy 718 [Rao *et al.* 2006]

In addition to the influence mentioned in §2.2.4, heat treatment after HIPping was found to have some additional affects. The amount of boundary precipitation increases significantly during post-HIP heat treatment [Aubin *et al.* 1980]. The heat treatment parameters are also to be noted. Besides being inconvenient, long treatment times or higher treatment temperatures

may also cause greater argon expansion (thermal induced porosity) [Larson 1976].

Inclusions are commonly found in P/M superalloys [Zhou et al. 2006; Yu 2009]. The various inclusions are rich in Al, Si, Mg, Ca, Zr, Ti, Fe, Cr, and S. Cracks initiate commonly from inclusions and then propagate to failure [Shamblen et al. 1985]. Hence the size and the location of inclusions have great influences on fatigue lives and ductility [Nazmy and Singer 1985] of the specimens.

2.3 Properties and application of CM247LC

2.3.1 Introduction

CM247LC is a typical gamma-prime (γ') strengthened nickel-base superalloy derived from MarM247 with about 62% volume fraction of γ' [Harris et al. 1982; Harris, Ericson et al. 1984] designed for directional solidification (DS). DS CM247LC has cubic γ' precipitates embedded in a softer γ matrix. The nominal chemical composition (wt %) of the alloy is: Ni-9.5W-9.2Co-8.2Cr-5.6Al-3.3Ta-1.4Hf-0.7Ti with a carbon concentration of 0.07wt%. MarM247 is a casting alloy that has a similar composition to MarM002, with CM247LC being the low carbon variant of this alloy. MarM247 is more widely used in the United States, while MarM002 is the alloy of choice in Europe. These two alloys are commonly used for cast blade and vane applications. CM247LC is reported to have a significantly higher incipient melting point than the parent CM247 alloy, whose melting range is 1310-1375 °C.

Table 2.1 Nominal compositions of MarM247 and CM247LC (wt %)

	W	Co	Cr	Al	Ta	Hf	Ti	Mo	C	Zr	B	Ni
MarM247	10.0	10.0	8.4	5.5	3.0	1.5	1.0	0.7	0.15	0.05	0.015	Bal
CM247LC	9.5	9.2	8.1	5.6	3.2	1.4	0.7	0.5	0.07	0.015	0.015	Bal

Table 2.1 lists the chemistry modification of CM247LC from its parent alloy MarM247. The modification is intended to eliminate the DS grain boundary cracking problems. It can be noted that the concentrations of several elements are reduced in CM247LC compared with the parent alloy. First of all, carbon is lowered by half of its original concentration to improve carbide microstructure, carbide stability and room temperature to intermediate temperature ductility. In addition to carbon, the W and Mo are reduced in order to minimize M_6C (M is W, Mo) platelet formation after high temperature solution treatment and subsequent stressed exposure in service. M_6C plates are known to have an adverse effect on fatigue properties, acting as crack initiation points and high propagation-rate crack paths. Zr and Si are known to lead to an increased tendency to DS grain boundary cracking. It is now recognized that very small reductions in Zr and Ti contents, combined with very tight control of Si and S, dramatically reduce the DS grain boundary cracking tendency in MarM247. The major microstructural effect of the lower Ti content in CM247LC, compared to MarM247, is to significantly reduce the size and volume fraction of the γ/γ' eutectic nodules [Harris, Ericson et al. 1982]. This factor is also believed to be significant in reducing the DS grain boundary cracking tendency of CM247LC. The addition of Hf to high strength cast superalloys is also used to combat DS grain boundary cracking problems, with the level of 2% and greater being common. Increasing levels of Hf, unfortunately, increase the occurrence of

HfO inclusions in the DS components usually resulting from Hf/ceramic core/shell reaction [Harris, Ericson et al. 1982; Harris, Ericson et al. 1984]. Hf in CM247LC is retained at a moderate 1.4% level to assist grain boundary strength and ductility without HfO inclusion problems. The Cr is lowered from 8.4% to 8.1% and combined with the lower Ti, W and Mo levels more than compensates for the lower carbon to further ensure CM247LC alloy is free from TCP phases.

2.3.2 Microstructure of CM247LC

The common manufacturing methods of CM247LC are conventional casting (CC) producing equiaxed grains and directional solidification (DS) producing columnar grains aligned in the direction of heat extraction. HIPping is sometimes applied as a step of heat treatment in order to close the shrinkage pores in as-cast ingot. The microstructure of as-cast CM247LC is shown in Fig.2-16, with γ' particles appearing darker. Note that the 'rosette' shape γ/γ' eutectic colonies are commonly found at grain boundaries. This structure was reported to be an aspect causing grain boundary cracking in DS MarM247 [Harris, Ericson et al. 1984] and its presence remarkably reduces the fatigue life [Okazaki 2003]. However, in conventionally cast MarM247, it was found that the ductile γ/γ' eutectic hinders propagation of cracks along grain boundaries. The yield strength increased and the ductility decreased as the amount of γ/γ' eutectic present in the microstructure decreased [Gasko et al. 1988]. Apart from γ/γ' eutectic, coarse and large MC carbides in script shape, attributed to the relatively slow cooling rates during the solidification process, are also present at grain boundaries. They are found to crack easily or to de-bond from the matrix and initiate cracks in tensile, fatigue and creep tests of cast or DS CM247LC [Mishra et al. 1995; Maldini et al. 1996; Osinkolu et al. 1999]. They may also cause the moderate temperature brittleness in nickel-

base superalloys [Fiore 1975; Bor et al. 1997].

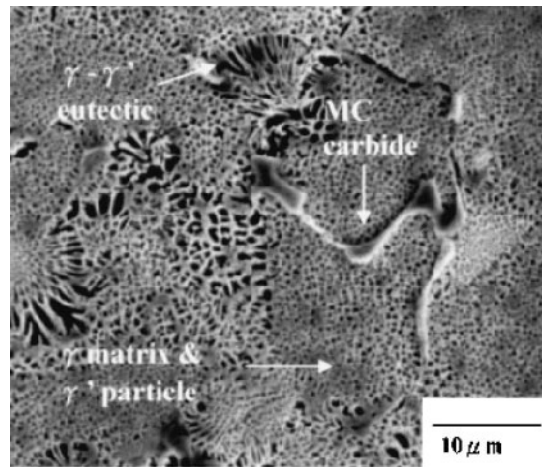


Fig. 2-16 Secondary SEM micrograph showing the as-cast microstructure of fine grain CM 247 LC superalloy. From [Huang et al. 2004]

The heat treatment used for CM247LC of 1260 °C for 2h + 1st aging at 1079 °C for 4h+ 2nd aging at 871 °C for 20h [Kim et al. 2008] is a solution treatment as well as causing grain growth. The γ/γ' eutectic can be dissolved during solution heat treatment. It can be seen in Fig.2-17 a) that after heat treatment, γ/γ' eutectics are partly dissolved and the grain boundary morphology is modified to be decorated by discrete carbides embedded in γ' . The grain interior is occupied by extra fine γ' particles (see Fig.2-17 b)) compared to the as-cast morphology.

Fig. 2-18 demonstrates the typical change in morphology of γ' particles before and after heat treatment. Both conventionally cast and directionally solidified CM247LC are composed of split cube type primary γ' and very fine secondary γ' which precipitates in the matrix channel between the cubic γ' . The formation of the split cube type γ' is explained in the next paragraphs. After solution and two steps of aging, primary γ' particles dissolve or partly

dissolve and re-precipitate during subsequent cooling. The size can be controlled by the aging temperature and time; (the difference of the morphology of the γ' in Fig.2-17 b) and Fig. 2-18 c) is due to different aging conditions.) [Zhao *et al.* 2004].

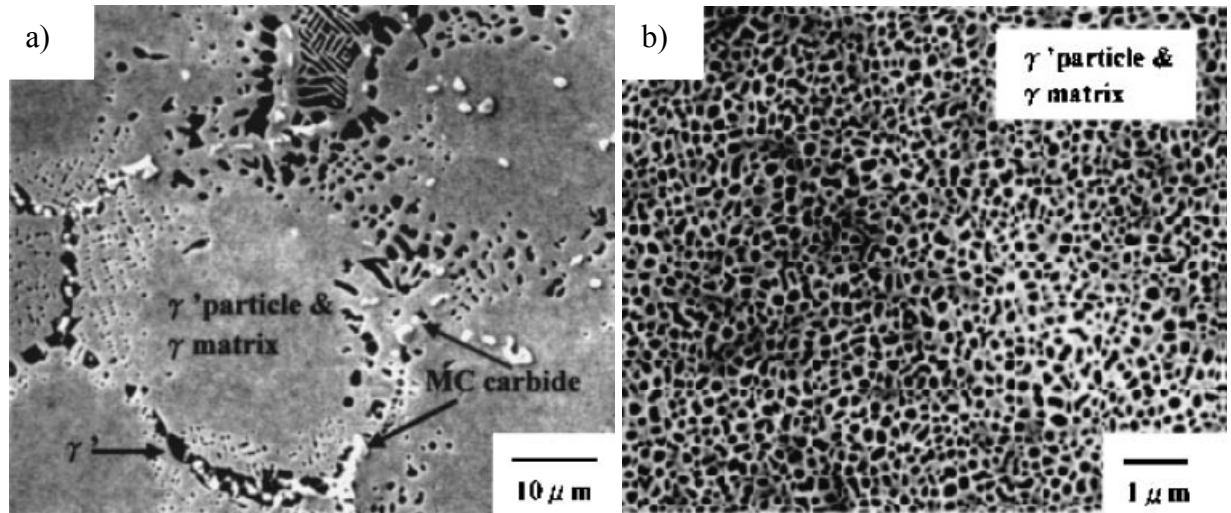


Fig. 2-17 Secondary electron SEM micrographs showing the distribution and size of γ' phase of CM 247 LC superalloy after heat treatment (HIPping + 1221 °C/2 h +771 °C/20 h) and the observation at a) grain boundary, and b) the centre of grain. From [Huang and Koo 2004]

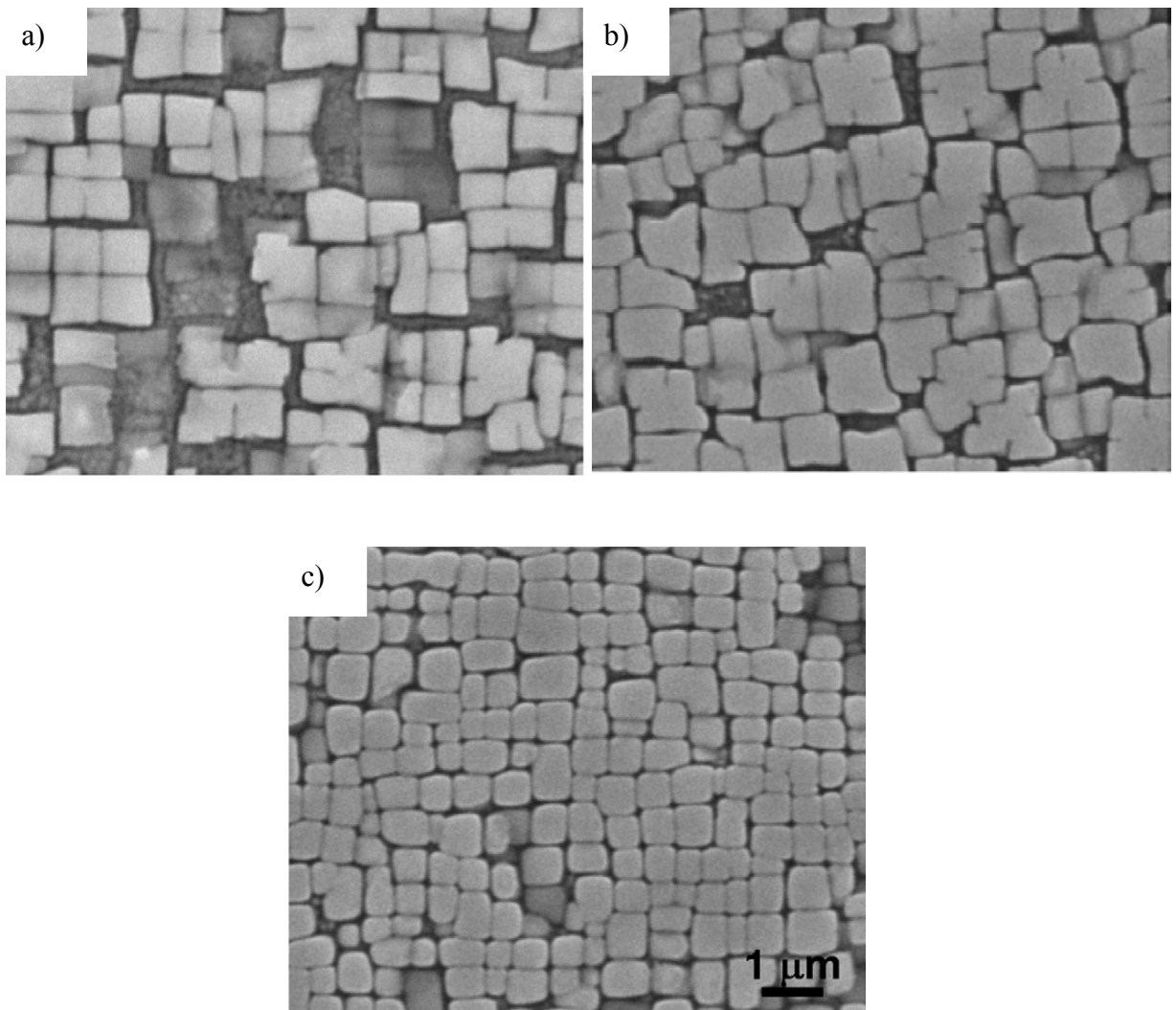


Fig. 2-18 Secondary electron SEM micrographs of heat treated CM247LC a) conventional cast + aged; b) DS+ aged; c) DS + solution treatment + aged. Age treatment is at 871 °C for 20h; solution treatment is at 1260 °C for 2h + 1st age at 1079 °C for 4h. From [Kim, Choi *et al.* 2008]

The shape of individual precipitate and the distribution of precipitates are the two aspects of morphology to be considered in alloy design. During the coarsening of coherent γ' precipitates in nickel-based alloys, the cubical γ' precipitate particle sometimes presents in groups of eight small cubes (i.e. an octad) shown above. The formation of this morphology

has been studied by several researchers [Ricks, Porter et al. 1983; Doi et al. 1984]. Ricks et al. found that the same morphological development occurs in all the alloys in their study in the sequence spheres, cubes, arrays of cubes, solid state dendrites, as shown in Fig. 2-19 a). The driving force of the development is to minimize the misfit energy and the interface energy between γ and γ' . The magnitude of γ/γ' misfit is the key fact to both the size at which the γ' particles depart from a spherical morphology, and the development of cuboidal arrays. The larger the magnitude of the γ/γ' misfit, at the smaller size the shape of γ' become cubic from spherical. However, the morphology of the γ' particles depends not only upon the misfit but also upon the nucleation density, since the size to which particles can grow may be limited by soft impingement. Ricks also stated that the use of the term 'ogdoadically-diced cube' is incorrect since the morphologies observed was actually a central cube joining the group of eight (Fig. 2-19 a) - e).

Later studies by Doi et al. found that the ogdoadically diced cubes were developed by splitting of coarse γ' particles rather than being developed from the corners of the central cube (Fig. 2-19 a) - d). The splitting progress of a γ' particle in an experimental nickel-base alloy is captured in Fig. 2-19 b). The figure suggested that the splitting proceeds as follows: firstly, the centre of each side face (i.e. $\{100\}$) of a γ' cube becomes hollow then each hollow simultaneously extends towards the centre of the cube and widens along $\{100\}$ and finally they split into a group of eight small cubes, i.e. an ogdoad, is complete. The individual coherent precipitate has an energy state which can be expressed by the following equation:

$$E_{total} = E_{str} + E_{surf} + E_{int} \quad (2.4)$$

Where E_{str} is the elastic strain energy due to the lattice mismatch between the precipitate and the matrix, E_{surf} is the interfacial energy of the precipitate and E_{int} is the elastic interaction

Chapter 2 Literature Review

energy between precipitates. The elastic interaction energy results from overlap of the elastic strain fields which accompany coherent precipitate particles when their inter-particle distances become small. They proposed that it was the elastic interaction that governs both the shape of the individual γ' precipitate and the distribution of γ' precipitates. Their calculation results in the conclusion that the elastic interaction between the particles formed by the split compensates for the marked increase in surface energy due to the split.

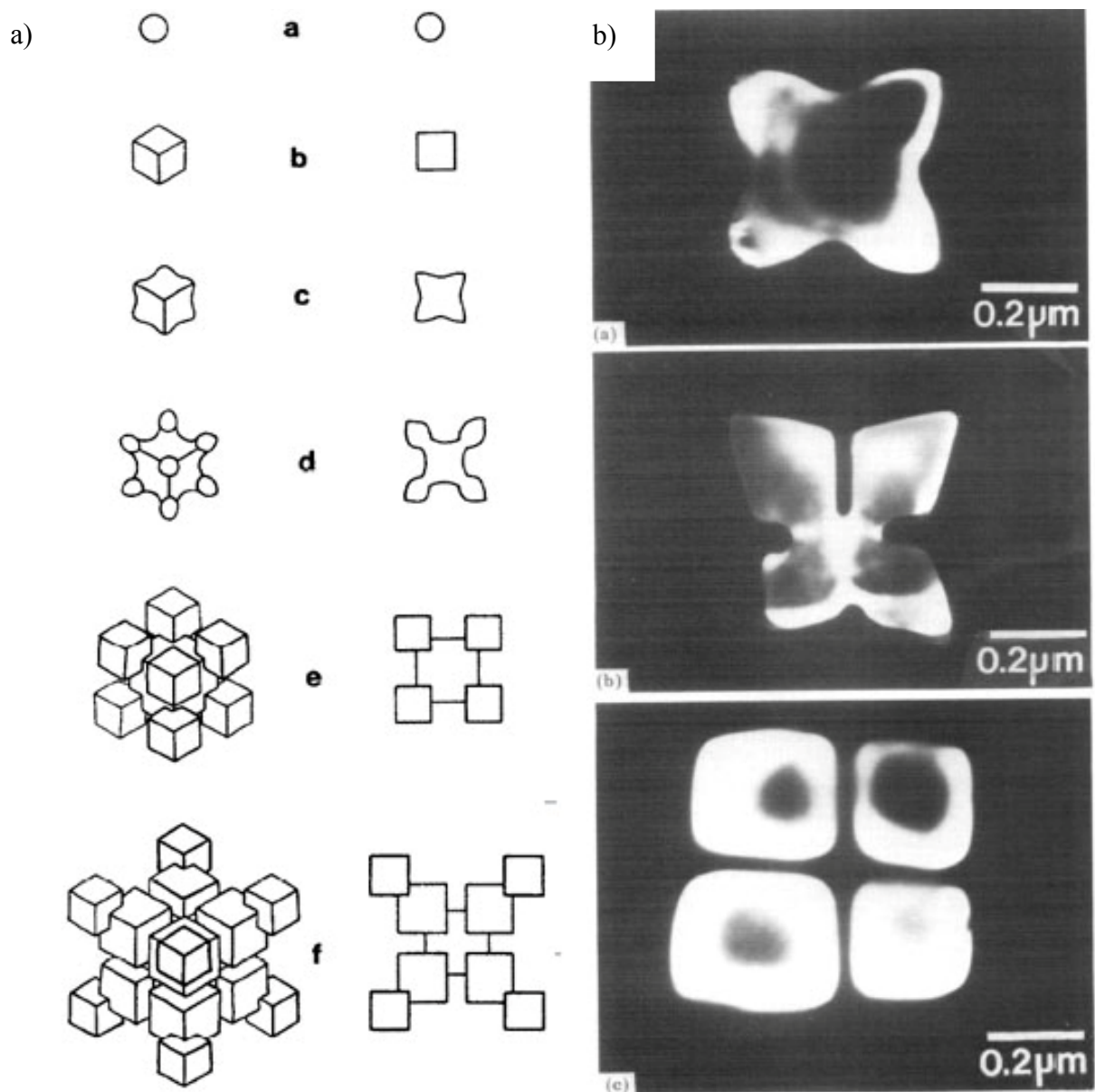


Fig. 2-19 the sequence of γ' coarsening in nickel-base superalloys. a) Schematic diagrams showing the development of strain induced, faceted γ' dendrites in $\langle 111 \rangle$ and $\langle 001 \rangle$ projection. Adapt from [Ricks, Porter et al. 1983]; b) TEM images of the γ' precipitate particles in a nickel alloy illustrating the progressive split of a single cube into eight small cuboids, taken from [Doi, Miyazaki et al. 1984].

2.3.3 Mechanical properties of CM247LC

The mechanical properties of CM247LC depend on the processing method. Table 2.2 demonstrates tensile properties of CM247LC produced by various methods. Low cycle fatigue properties are shown in Fig. 2-20, and the creep properties are shown in Table 2.3.

Table 2.2 Tensile properties of CM247LC produced by various methods

	0.2%PS (MPa)	UTS (MPa)	Elong (%)
Room Temperature	1010 ^[1]	1242 ^[1]	8.1 ^[1]
	772 ^[2]	852 ^[2]	8.8 ^[2]
	928 ^[4]	1355 ^[4]	17.3 ^[4]
750 °C	1016 ^[1]	1200 ^[1]	8.2 ^[1]
	794 ^[3]	1000 ^[3]	8.1 ^[3]
	900 ^[4]	1113 ^[4]	6.5 ^[4]

[1] CM247LC as-cast + HIP at 1185 °C/173MPa/4h + Solution at 1221 °C/2h/GFQ + Age at 771 °C/20h/FC (Grain size 80~90mm). Adapted from [Huang and Koo 2004]

[2] As-cast + aged at 871 °C/20h. Adapted from [Harris, Ericson et al. 1982]

[3] DS longitudinal data, DS + aged at 871 °C/20h. Adapted from [Harris, Ericson et al. 1984]

[4] Vacuum Spray formed CM247LC + HIP at 1185 °C/172MPa + 1260 °C/1h + 1100 °C/1h/cool >= 40 °C + 800 °C/16h. Adapted from [Andrews 1999]

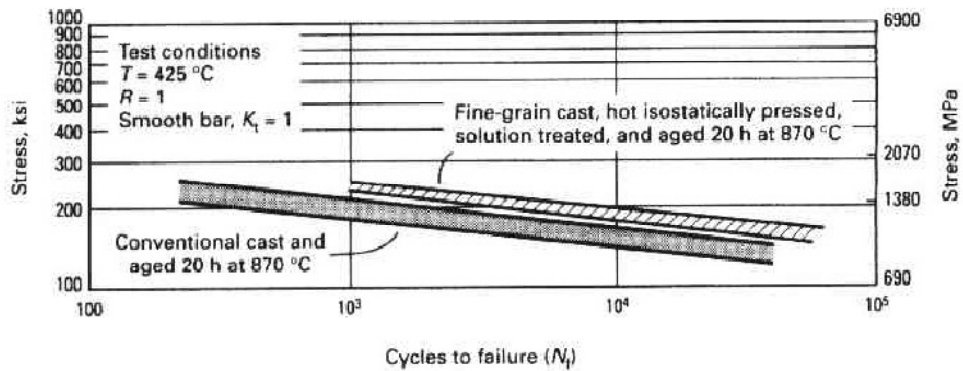


Fig. 2-20 Low cycle fatigue properties of CM247 processed by different methods. Adapted from [Harris, Ericson et al. 1982]

Table 2.3 Creep properties of CM247LC produced by various methods

Processing method	Stress, MPa	Temperature, °C	Creep life, Hours	Time to 1% creep, Hours
	650		1191	--
Vacuum Spray formed CM247LC +	700	700	356	351.7
HIP at 1185 °C/172MPa+1260 °C/1h	130	900	>2321	--
+1100 °C/1h/cool>=40 °C+800 °C/16h.	140		>2321	1495
Adapted from [Andrews 1999]	100	1000	216	127
	120		67	59
	100	1050	1.2	1.1
As-cast + aged at 871 °C/20h.	672	760	84	32
Adapted from [Harris, Ericson et al. 1982]	124	982	770	608

2.4 Aim of the project

CM247LC, as mentioned before, is originally designed for casting. Like many other cast superalloys, it would be difficult to be manufactured via thermal mechanical processing, e.g. rolling. This type of material is not used for the manufacture of thin-walled components e.g. combustion casing, because making thin-walled structure via casting would cause severe material waste plus machining cost. Studies on CM247LC of the microstructure [*Chen, Lee et al. 1998*], tensile and LCF (low cycle fatigue) properties [*Bor, Wei et al. 2008*] are the main focus of early works. The response of the microstructure to creep at various temperatures and stress have been frequently studied in the past forty years [*Mishra, Singh et al. 1995; Engler-Pinto et al. 1996; Maldini, Marchionni et al. 1996; Bor, Chao et al. 1997; Osinkolu, Maldini et al. 1999; Komazaki et al. 2000*]. But those works are mainly based on polycrystalline casting and directional solidification [*Zhang et al. 2002; Kim, Choi et al. 2008*]. Although HIPping was sometimes applied, but it acted as a step of heat treatment and the main purpose was to eliminate the pores formed during casting [*Huang and Koo 2004*]. Data concerning Net Shape HIPped components from CM247LC powder is hardly available. Thus the influence of HIPping conditions plus post heat treatment on the microstructure of the material, consequently on the mechanical properties need to be addressed prior to the manufacturing of real component using this method.

In the light of the above review of the factors that are important in defining the cost of manufacture and the properties/microstructure relationship in components manufactured for aerospace from Ni-based superalloys, the work described in this thesis focuses on optimizing net shape HIPping and post-heat treatment parameters of the material CM247LC by characterising the microstructure including γ and γ' morphology, carbides morphology, grain

boundaries, and evaluating mechanical properties including tensile, HCF (high cycle fatigue; the HCF properties of CM247LC are hardly available in the literature but it is important for engine design) and creep. Furthermore, work has been carried out to identify the problems encountered in the powder HIPping of the material.

Chapter 3 Experimental Methods

3.1 Materials and their processing

3.1.1 CM247LC powder

Gas atomized CM247LC nickel base superalloy powders, with size up to 53 μm , were supplied by Sandvik Osprey LTD. The composition of the received powder and some properties of the powders which are important in HIPping are shown in Table 3.1 and Table 3.2 respectively. (Powders were kept in a vacuum chamber once unsealed.

Table 3.1 Chemical composition of CM247LC (wt %)

W	Co	Cr	Al	Ta	Hf*	Ti	Mo	C	O	Fe	Nb	Cu	Si	Ni
9.1	9.0	8.1	5.4	3.2	1.3	0.88	0.43	0.077	0.008	0.06	0.05	0.02	0.02	Bal

* The Hf level was found lower than the configuration when Osprey was preparing the melt for atomisation. Some pure Hf was added into the liquid to solve this problem before atomization.

Table 3.2 Characterization of CM247LC powders

Tap density (g/cc)	5.90
Density of alloy (g/cc)	8.54
Tap density (% Theoretical)	69.1

A Counter particle size analyser was used to find out the range and particle sizes present. Analysis using scanning electron microscopy was also undertaken to assess the shape and morphology of the powders.

3.1.2 Hot Isostatic Pressing

Consolidation of the powders was achieved by hot isostatic pressing (HIPping). This method involves the application of high temperature and high pressure of Ar gas. The powder needs to be encapsulated in a sealing medium that is deformable at the HIPping conditions to be used, and has good weldability. Mild steel was used as a capsule for all HIPping work and after HIPping the steel was either pickled away using acid or machined off. Cans welded from mild steel tubes with inner diameters ranging from 7 mm to 40 mm and thicknesses of 5 mm were used as capsules for HIPping samples. Before being filled with powders, these capsules were checked by the leak detector with a detectable leak rate of $< 5 \times 10^{-12}$ mbar l/s, as shown in Fig. 3-1. A vacuum furnace (Fig. 3-2) was used to anneal the mild steel cans at 1000°C for 1 hour in order to get rid of impurities inside the cans which could contaminate the powders.

A vibration table was used to increase the flow rate during the process of filling powder into the mild steel cans and also to achieve a consistent tap density. The cans filled with powder were then outgassed at 10^{-5} mbar for 20 h using an outgassing system and were crimp-closed before being welded to ensure vacuum-tightness. The sealed cans were then placed in the HIP furnace.

The pressure and temperature were increased until the final hold conditions were reached. The cooling rate used after the HIP cycle is about 5°C/min. The density of the powder in the can increases as consolidation proceeds during the HIP cycle.

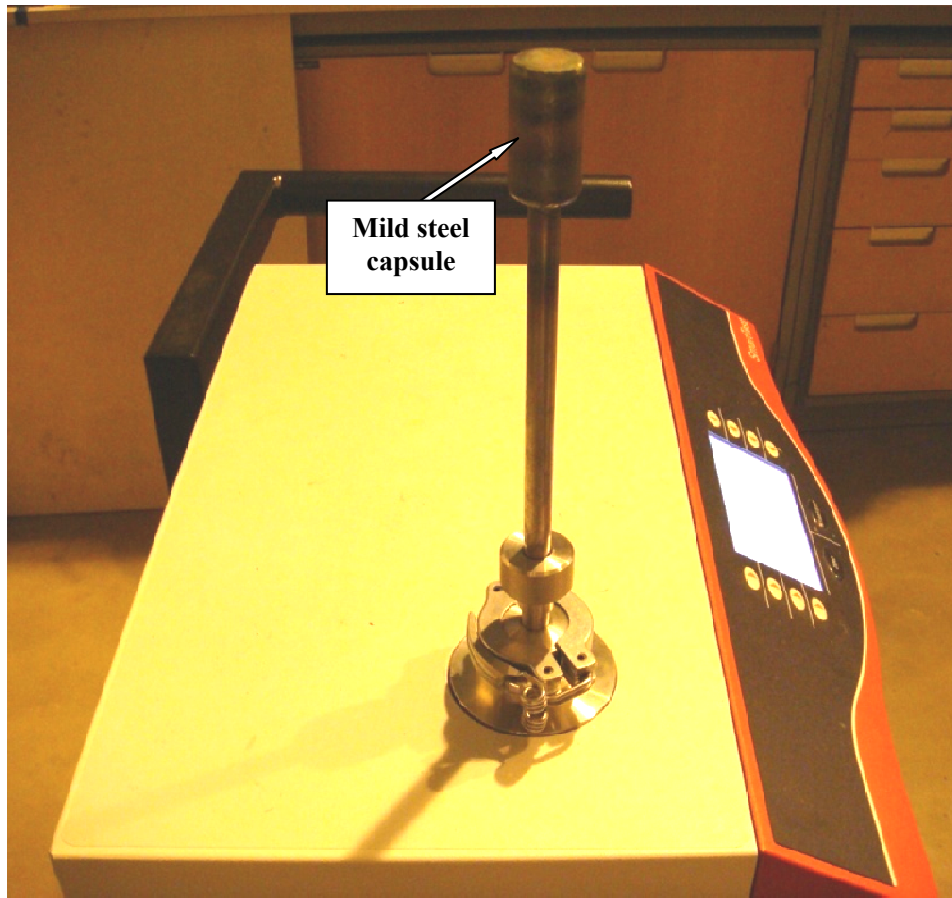


Fig. 3-1 A photograph of leak detector for the checking of capsule's sealing quality.



Fig. 3-2 Vacuum furnace for annealing mild steel cans which are used for powder HIPping to get rid of impurities inside.

The EPSI Lab HIP facility (shown in Fig. 3-3) contains a HIP unit with a maximum operating temperature of 1450 °C and pressure up to 200 MPa. This unit consists of a furnace with molybdenum heating elements, a heat shield, a water-cooled pressure vessel and a gas compressor system. The two-zone molybdenum furnace (see Fig. 3-4) is used to provide the heating, and thermocouples are positioned at the top and bottom of the two hot zones. A computer system is used to monitor the temperature and pressure continuously inside the HIP furnace. Temperature control is within ± 3 °C throughout the working zone.



Fig. 3-3 EPSI Lab HIP facilities.



Fig. 3-4 The two zone molybdenum furnace used for HIPping.

3.1.3 Heat treatment

3.1.3.1 Powder heat treatment

In addition to HIPping, powders they were also heat treated in two ways. In the first method powder was heated in an open crucible in a vacuum furnace which was evacuated at a carefully controlled speed to $\sim 10^{-4}$ mBar before heating up. In the second method powder was sealed in the same type of mild steel can as used for HIPping, and the powder was heated after evacuating the can to a pressure of 10^{-5} mBar. The two different methods were

used to study the influence of the trace oxygen intake if micro leakage occurred. The ramping rate of powder heat treatment was 3°C/min.

3.1.3.2 Heat treatment of HIPped materials

Solution treatment and ageing treatments were conducted in an air furnace. The heating rate was controlled at 8 °C/min. Cooling from the solution temperature was achieved either by pulling the sample from the hot furnace into the air which is called air cooling (AC) in the rest of the thesis; or by forced air cooling (FAC), by using a fan to increase the cooling rate. Cooling from ageing temperature is mentioned as furnace cooling (FC), by isolating the heat elements of the furnace and keeping the samples in the furnace until temperature dropped to room temperature.

3.2 Microstructural characterisation

3.2.1 Specimen preparation

As-received loose powder particles were used directly for surface examination. With respect to the examination of powders' cross sections, individual powder particles were hot mounted in edge protective and conductive Bakelite in an OPAL 400 mounting press. For the microstructural examination of HIPped materials, samples were cut using an electro discharge machine (EDM) from the HIPped bars. The cross sections were cut by a Struers Accutom-5 cutting unit using a SiC cutting wheel and mounted in conductive Bakelite for subsequent metallographic preparation.

Struers DAP-7 and Pedemin S were used for polishing. Polishing routes according to the lab experience for preparing nickel-base alloys are as follows:

1. Struers MD Piano 220 until plane;
2. Struers MD Largo with 9 μm abrasive diamond suspension for ~5 minutes;
3. Struers MD Dac with 3 μm abrasive diamond suspension for ~5 minutes;
4. Struers MD Nap with 1 μm abrasive diamond suspension for ~2 minutes.

For preparation of powder cross sections, step 1 should not be used as no powder particles will remain in the Bakelite bulk. If the samples were polished for SE (secondary electron) imaging, all steps will apply and additionally the sample should be etched by Kalling's reagent (2 gm cupric chloride, 40 ml hydrochloric acid and 60 ml ethanol). Deep etching, by immersing the whole sample in the solution for ~5 seconds, was used to reveal grain boundary information and quick swab-etch was used to reveal γ' morphology. If the samples are to be prepared for EBSD or BSE (backscattered electron) imaging, the final finish method (step 4) would be replaced by 'Struers MD Chem with 50% Struers OP-A (Oxide Polishing- Acidic alumina suspension) + 50% distilled water for 10 minutes.

3.2.2 Microscopy techniques

Secondary electron (SE) imaging of the surface of loose powder particles and back-scattered electron (BSE) imaging of powder particles' and solid specimens' cross sections were carried out using a JEOL 7000. The volume fractions of different phases were analysed utilizing Image-Pro Plus 6.0. Either five SEM images at 1000x were used for each calculation or at least 1000 particles were included in the statistical analysis.

Energy dispersive x-ray (EDX) analyses were done using an Oxford Inca EDX system in the JEOL 7000 to determine the chemical composition of the samples. EDX spectra were acquired using an accelerating voltage of 20 kV and a working distance of 10 mm was used. Wavelength dispersive spectroscopy (WDS), which is also fitted to the JEOL 7000, was used

to analyse C and O levels. The accelerating voltage used for this light element analysis was 5 kV and the probe current at least 10 nA. Analysis was conducted at working distance of 10 mm and magnification over 4000 \times . Pure C and Al₂O₃ compound were chosen as standard material when quantification of carbon and oxygen in discrete particles was needed. For all the quantified results the collected counts were always greater than 1 \times 10⁵ to minimise the statistical error. Electron back scatter diffraction (EBSD) was performed to provide information about the crystallographic orientation in HIPped samples. Ni₃Al was the only phase chosen for the orientation mapping because the lattice parameters of γ and γ' are too close to each other and preliminary experiments showed that complex, uninterpretable patterns were obtained if both phases were selected. The misorientation angles between grains and the grain size in the bulk alloy can be measured by the integrated Oxford INCA software. The EBSD system was an integral part of the JEOL 7000 SEM. The operating parameters were: specimen tilt angle of 70 $^{\circ}$, accelerating voltage of 20 kV, and a working distance of 12~16 mm.

TEM wafers of 3mm diameter were machined by EDM and ground to a thickness of 100 μ m. They were then twin jetted using a solution of 10% perchloric acid in methanol. The voltage was controlled at 20V and the current in the range of 0.5 to 1A. The temperature was controlled to be – 20 $^{\circ}$ C by an ethanol bath, chilled using liquid nitrogen. The samples were examined using a JEOL 2100 TEM at 200KV and spot size of 15nm for EDS analysis.

3.3 Chemical composition analysis

Chemical composition analyses of powder and HIPped samples were performed by IncoTest (Special Metals Wiggin Limited), Hereford, UK. A small solid slice of a HIPped sample with

a weight of at least 5 g was required to analyse interstitial elements (such as O, C) by LEC (LECO inert gas fusion analyser) and other elements by of ICPOES (Inductively Coupled Plasma Optical Emission Spectrometry).

3.4 Physical characteristics

3.4.1 Density

The density of HIPped CM247LC was measured using Archimedes' principle:

$$\rho = \frac{m}{m - m_f} \cdot \rho_f \quad (3.1)$$

Where ρ is the density of the material, m is the weight of material in the air, ρ_f is the density of the fluid and m_f is the apparent immersed weight of the material.

Distilled water was used as the fluid. The pieces to be measured were at least 30 g so that the density could be obtained with acceptable accuracy.

3.4.2 Transition temperatures

A differential scanning calorimeter (NETZSCH DSC 404 C) was used to measure the transition temperatures of CM247LC. Two alumina crucibles were used as container and reference. At least 50 mg material was required for each run. The protective argon flow rate was controlled at 100 ml/min. The temperature was ramped from 800 °C to 1270 °C, at a ramp rate of 5 °C/min. 3 runs are conducted on each sample to validate the reproducibility of the results.

3.4.3 Thermal conductivity

Jominy tests were conducted in order to define the cooling rates obtained when using AC and FAC in heat treatments. A $\varnothing 25 \text{ mm} \times 105 \text{ mm}$ bar was cut from a HIPped cylinder by EDM. Holes of 1.5mm diameter were drilled to the central axis along the bar to hold the thermocouples in position (see Fig.3-6). A tube furnace was heated up to 1260°C prior to the test. The bar was then placed into the furnace and soaked for 1h. A Metaserv end quench unit (see Fig. 3-5) was used to hold the bar when it was taken from the furnace so that one end was cooled directly by the jet of water. Temperatures were monitored at distances of 2mm, 5mm, 10mm, 20mm and 40mm from the water-quenched end using an 8 channel thermocouple data logger during the whole cooling process until the temperature dropped below 200°C .

The bar was aged following the quench. Microstructures of FAC and AC samples were compared with those at known positions and thus at known cooling rates, along the Jominy bar and the relative cooling rates could be determined.



Fig. 3-5 The Metaserv end quench unit



Fig. 3-6 Jominy bar with holes for holding thermocouples

3.5 X-ray Tomography

X-ray Tomography of the distribution of defects in HIPped CM247LC was obtained via an Xradia MicroXCT (as shown in fig. 3-8) in Henry Moseley X-ray Imaging Facility, the Materials Science Centre, the University of Manchester, UK. The Xradia MicroXCT is equipped with 150kV sealed tungsten high-energy micro focus X-ray source, $2k \times 2k$ 16bit high resolution cooled CCD detector and a heavy duty precision 4-axis sample manipulator stage mounted on a granite base and with a 15kg load capacity. Low to high resolution modes are achieved optically with $4\times$, $10\times$, $20\times$ and $40\times$ objective lenses.

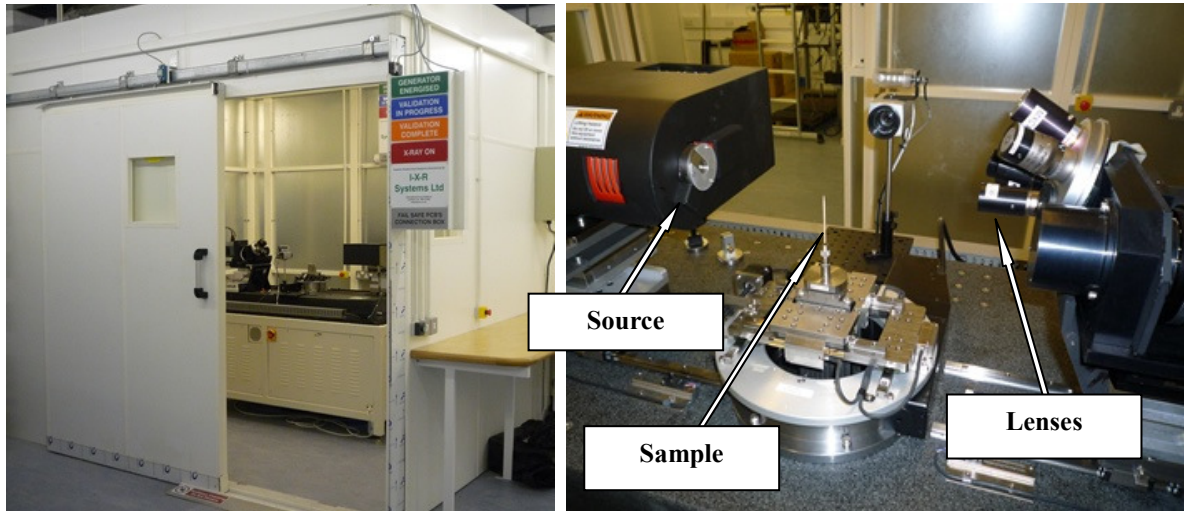


Fig.3-8 Henry Moseley X-Ray Imaging Facility - Xradia MicroXCT

For this study, samples of approximately $1.5\text{mm} \times 1.5\text{mm} \times 40\text{mm}$ were prepared from HIPped cylinders by EDM. Sample surfaces were lightly ground using sand paper. The highest source voltage 150kV and source power 10watt was applied for the X- ray generation. A $10\times$ objective lens which gives up to $\sim 2.6\text{mm}$ field of view with $\sim 1.6\mu\text{m}$ pixel size was used to receive the photons. To achieve best penetration ratio which is about 20%, a quartz filter was used to eliminate the low energy X-rays from the source. Samples were mounted with a source - sample distance of 55 mm and a detector - sample distance of 7 mm. About 2000 images are acquired at angles from $-92^\circ \sim 92^\circ$ for each sample. The exposure time for each image was set to be 30s to ensure at least 1000 counts were obtained from the sample area. The images were reconstructed and exported in pictures of slides that are perpendicular to the sample rotation axis. The generation of 3D images and quantitative analysis were achieved by using the software Avizo Fire 6.1.

3.6 Mechanical testing

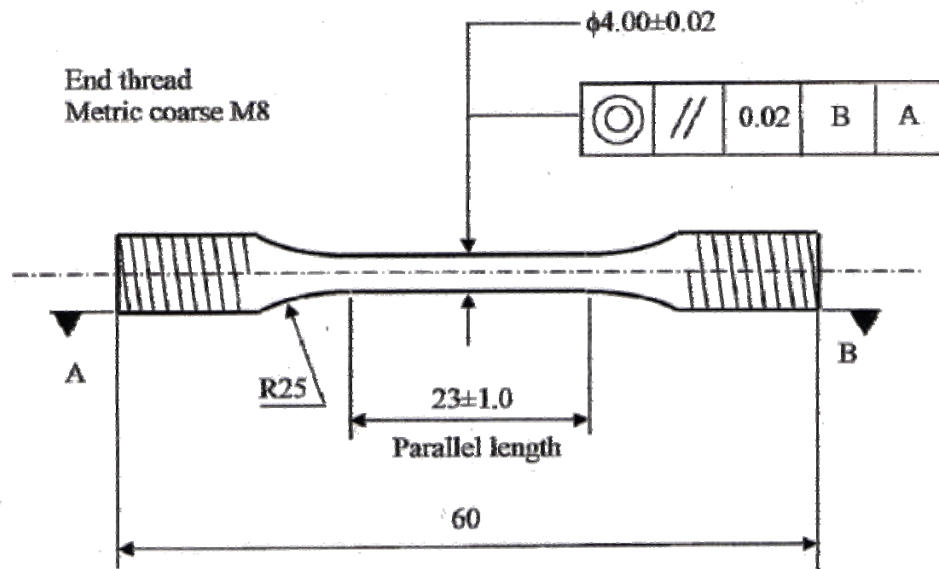
3.6.1 Hammer impact testing

Because standard tensile tests, notched tensile tests, fatigue tests and fracture toughness tests require machined samples, which are all time and resource-consuming to manufacture, some hammer impact tests (samples are broken in an uncontrolled manner using a hammer) were used as a quick way to relate the fracture behaviour to the microstructure in addition to more conventional testing. The fracture surfaces were investigated using a Philips XL30 SEM.

3.6.2 Tensile testing

Cylindrical tensile samples were machined from HIPped compacts. The Ø9mm cylinders were cut out using EDM and sent out to G.T.G Engineering Company Ltd., Leicestershire, UK for finish-machining to the final shape as shown in Fig. 3-9. Tensile tests were carried out using a Zwick Z100 tensile test machine at a strain rate of 10^{-4}s^{-1} in air at room temperature, 700°C and 750°C. When tested at high temperatures, a thermocouple was attached to the sample gauge length. The sample was soaked at the testing temperature for 30 min before the load was applied. The load/displacement curves obtained were converted to nominal stress/nominal strain curves which give tensile strength, yield stress and elongation. The fracture surfaces of tensile failed samples were studied using a Philips XL30 SEM to understand the fracture mechanism.

Elevated temperature (at 900°C, 1050°C and 1200°C) tensile test samples were sent to IncoTest who used testing standard BS EN 10002 PT5. The testing speed was controlled at an initial strain rate of 10^{-4}s^{-1}



Roughness value for machined surfaces to be 1.6 micrometers unless otherwise stated
 All dimensions and tolerances are in mm unless otherwise stated

Fig. 3-9 dimensions for round tensile test pieces.

Notch tensile tests were conducted on some samples using the same testing machine at the same strain rate as used for plain samples. The sample geometry is shown in Appendix 1. A notch of geometric stress concentration factor $K_t = 3.1$ was machined in the middle of the gauge. The specimen was aligned carefully and loaded in tension until fracture occurred. The notch strength is defined as the maximum load divided by the original cross-sectional area at the notch.

3.6.3 Tension-tension fatigue testing

Cylindrical tension-tension fatigue samples were machined from HIPped compacts. The $\square 10$ mm cylinders were cut out using EDM and sent out to G.T.G Engineering Company Ltd., Leicestershire, UK for finish-machining to the final shape according to Rolls-Royce standard

drawing graph number RLH8020.

Fatigue tests were carried out using an Amsler Vibrophore electro-magnetic resonance testing machine (see Fig. 3-10 a)) for fatigue life evaluation. Tests were conducted using sinusoidal waveform at a stress ratio R of 0.1, a frequency of ~95 Hz, and 1.0×10^7 cycles were defined as the run-out life. Fatigue properties at both room temperature and 750 °C were evaluated. Temperatures were monitored by attaching a thermocouple to the gauge length (see fig. 3-10 b)). Samples were soaked at the selected test temperature for about 30 minutes before applying the load. 10 test pieces were prepared for each test temperature for each material. First samples were tested at 70 % of the 0.2 % proof stress of the material. The stress was then increased or decreased at intervals of about 25 MPa until the fatigue limit of the material was reached. Notch fatigue tests were conducted using the same machine and the same method as the plain ones. The sample drawing and interpretation of results are shown in Appendix 1.

Following fatigue tests, fractographic observation of failed samples was carried out using a Philips XL30 SEM. Both halves of the fracture surfaces were assessed for the majority of failed samples.

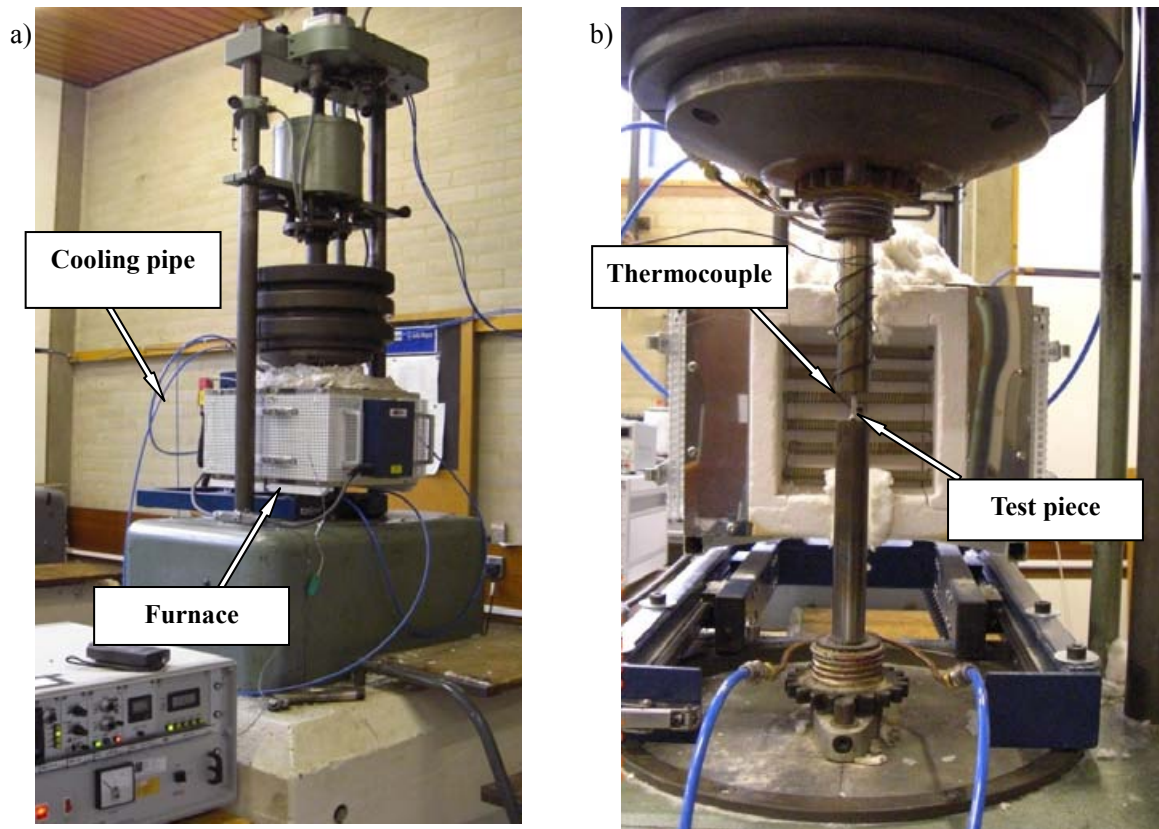


Fig.3-10 a) Amsler Vibrophore electro-magnetic resonance testing machine for fatigue property assessment; b) sample grid and temperature control arrangement.

3.6.4 Flexural creep testing

Flexural creep testing was conducted in the National Physical Laboratory, UK. Flat samples of 3mm×5mm×55mm were machined from HIPped bars by EDM. The flexural creep apparatus used was a Severn Science design using a four-point flexural jig inside an air atmosphere split box furnace (Fig.3-11 a)). The flexural jig was constructed from high-alumina ceramic, using alumina rollers as support and loading contacts (Fig.3-11 c)). In the normal 40 mm span configuration, the support span was on the bottom, and the loading span of 20 mm was provided by a separate block held on the end of a guided alumina ram, which was lever-loaded. The flexural displacement was detected by an extensometer rod passing through a guide hole in the support block and with its tip located at the centre of the loading

span (Fig.3-11 b) and d)). This was connected to a low force displacement transducer. This displacement is recorded between the support point of the test-piece and its centre. Transducer calibration was undertaken using a depth micrometer, incrementing the displacement of the sensing rod in a series of steps and recording the resulting output on a data logger.

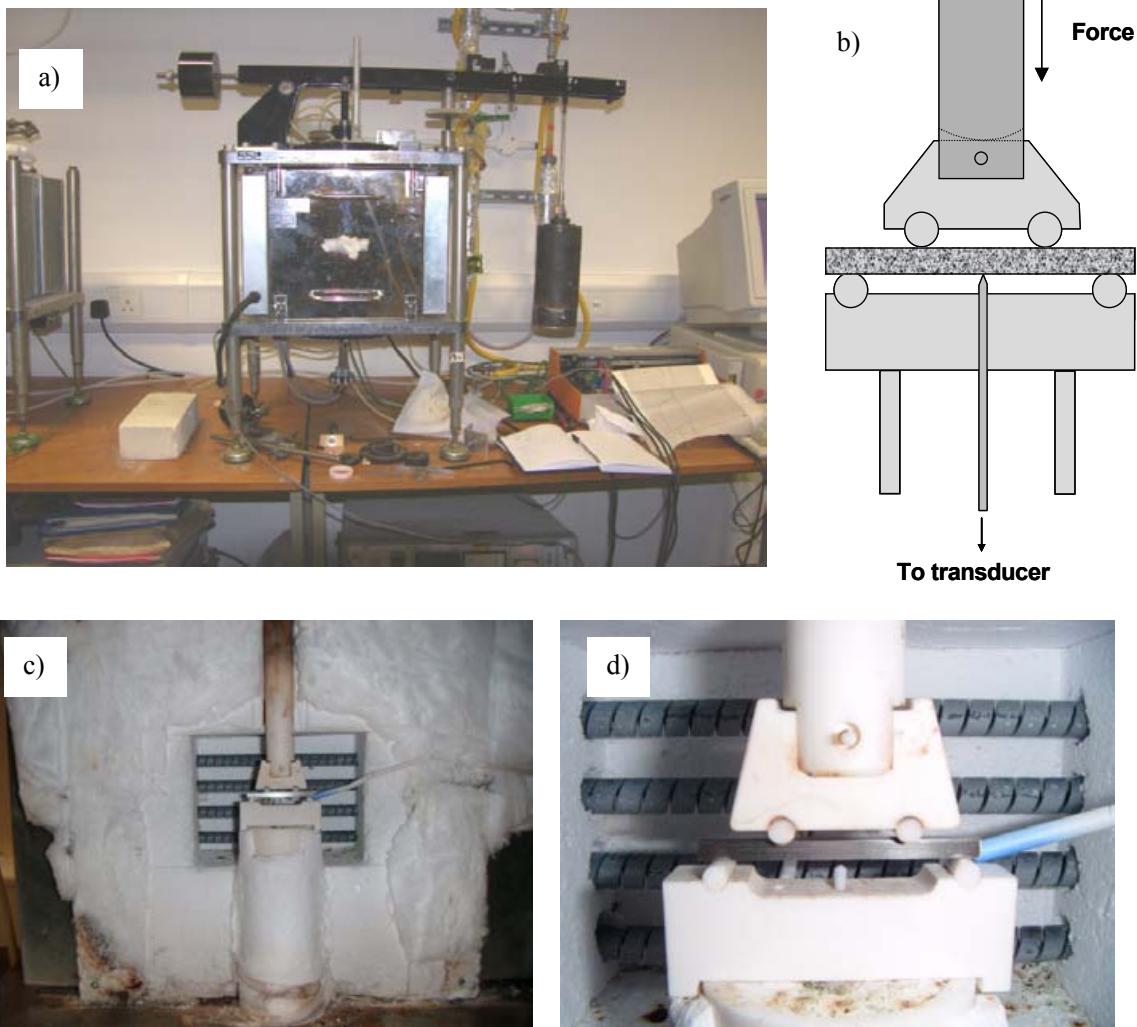


Fig. 3-11 The assembly of creep test. a), c) Severn Science design using a four-point flexural jig inside an air atmosphere split box furnace; b),d) the application of force and detection of displacement via the four-point flexural jig.

Once a test-piece had been positioned in the jig, the guided ram provided approximately 4.5 N force to the system. Under this condition, the test-piece was heated to the required test temperature at 10 °C/min and held for a few minutes before the full required test force was applied through weights on the lever arm. The required test force F was computed from the required stress σ using simple elastic beam theory. The force required was computed as

$$F = \sigma ab^2 / 3d_1 \quad (3.2)$$

where a is width, b is thickness, d_1 is loading arm which is distance between inner and outer rollers. The nominal flexural strain was computed as

$$\varepsilon = \frac{3b\delta}{(2d_1^2 + 6d_1d_2 + 3d_2^2)} \quad (3.3)$$

where δ is the central displacement, $2d_2$ is the inner loading span.

Data from the displacement transducer and the type R thermocouple were recorded at regular intervals (determined by the creep rate expected) on a data-logging computer using Labview software, and converted into nominal flexural strain and temperature using an Excel spreadsheet.

3 tests were conducted for each batch of material. Firstly, a quick creep test was conducted at a constant stress of 350MPa, while the temperature was increased at a rate of 10 °C/min. A creep curve was obtained to observe at what temperature range the material begins to creep. Secondly, a step temperature test at a constant stress of 350MPa was carried out to obtain the steady state creep rate under different temperatures. Lastly, a step stress test under a constant temperature of 760 °C was used to obtain the steady state creep rate under different stress levels.

Chapter 3 Experimental Methods

For step temperature and step stress test, there is always transient behaviour on first loading before the system settles down to creep at a steady rate. The experiments had to be left to settle long enough to be in what looked like a linear creep region in order to reach the steady creep stage so that the creep rate could be defined.

Chapter 4 Microstructure and Mechanical Properties of HIPped CM247LC

4.1 Powder assessment and analysis

Preliminary work has been done on as-received powder to understand the response of CM247LC to HIPping, and also, to define the critical HIPping conditions - temperature, pressure and dwell time at which the material was fully densified. In addition, experiments on the influence of atmosphere on bonding has been studied in order to understand the impact of possible leakage of air into capsules during HIPping which could occur if the cans are not leak proof.

4.1.1 As-received CM247LC powder

As-received CM247LC powder was supplied by Sandvik as below 53 μm . Measurements illustrated in Fig. 4-1 showed that the size varies between ~ 2 to ~ 60 μm with an average diameter of 29.6 μm . It is known that small particles have large surface per unit volume, resulting in high activity during sintering as they possess large surface free energy. In addition for spherical powders (Fig. 4-2), small particles fill the interstices between large ones so that porosity can be further reduced.

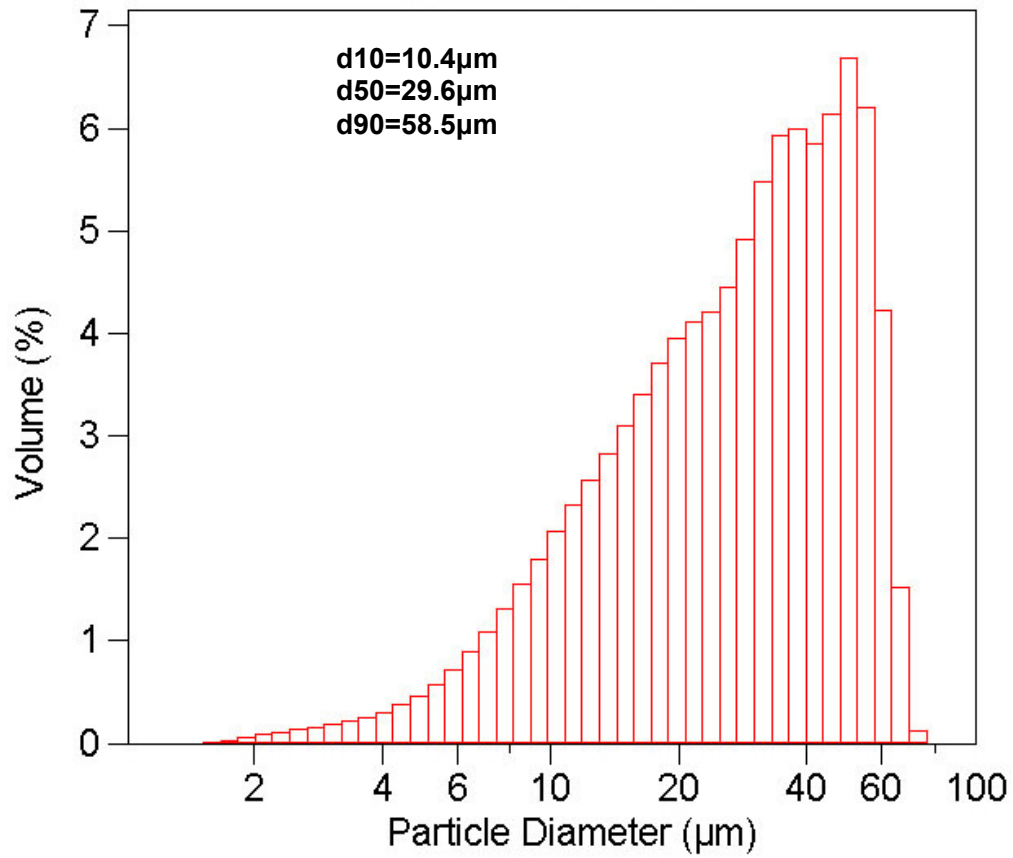


Fig. 4-1 Graph showing the range of particle sizes for gas atomized CM247LC alloy. The definition of d10 is that equivalent diameter where 10 mass-% of the powder has a smaller diameter (and hence the remaining 90% is coarser). The definition of d50 and d90 can be derived similarly.

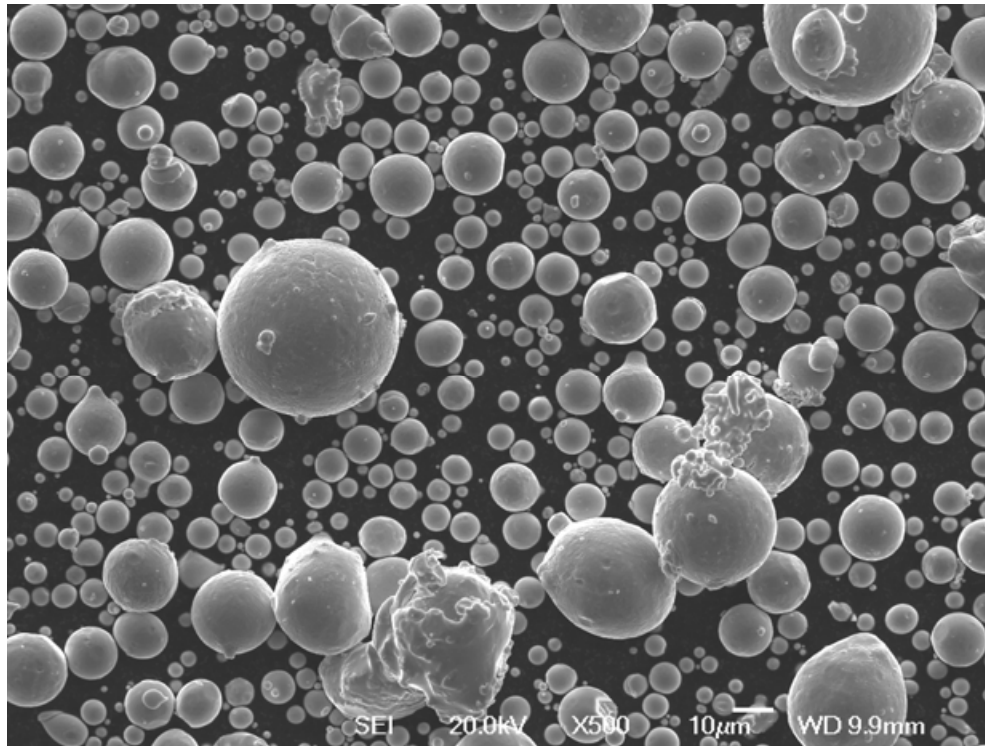


Fig. 4-2 SEM micrograph taken using secondary electrons of the CM247LC gas atomized powder

Examination showed that the as-received powders were not all ideal solid balls and some hollow particles are frequently observed as shown in Fig. 4-3 a). The pores in these hollow particles are present as a result either of entrapped argon or due to shrinkage porosity [Kortovitch *et al.* 1971]. The trapped argon will thus be present in HIPped samples. Fig. 4-3 b) demonstrates that individual powder particles are not homogeneous. Fine crystals, formed during rapid cooling of the molten particles, are surrounded by bright continuous boundaries. No carbides are visible in these SEM images in the as-received particles.

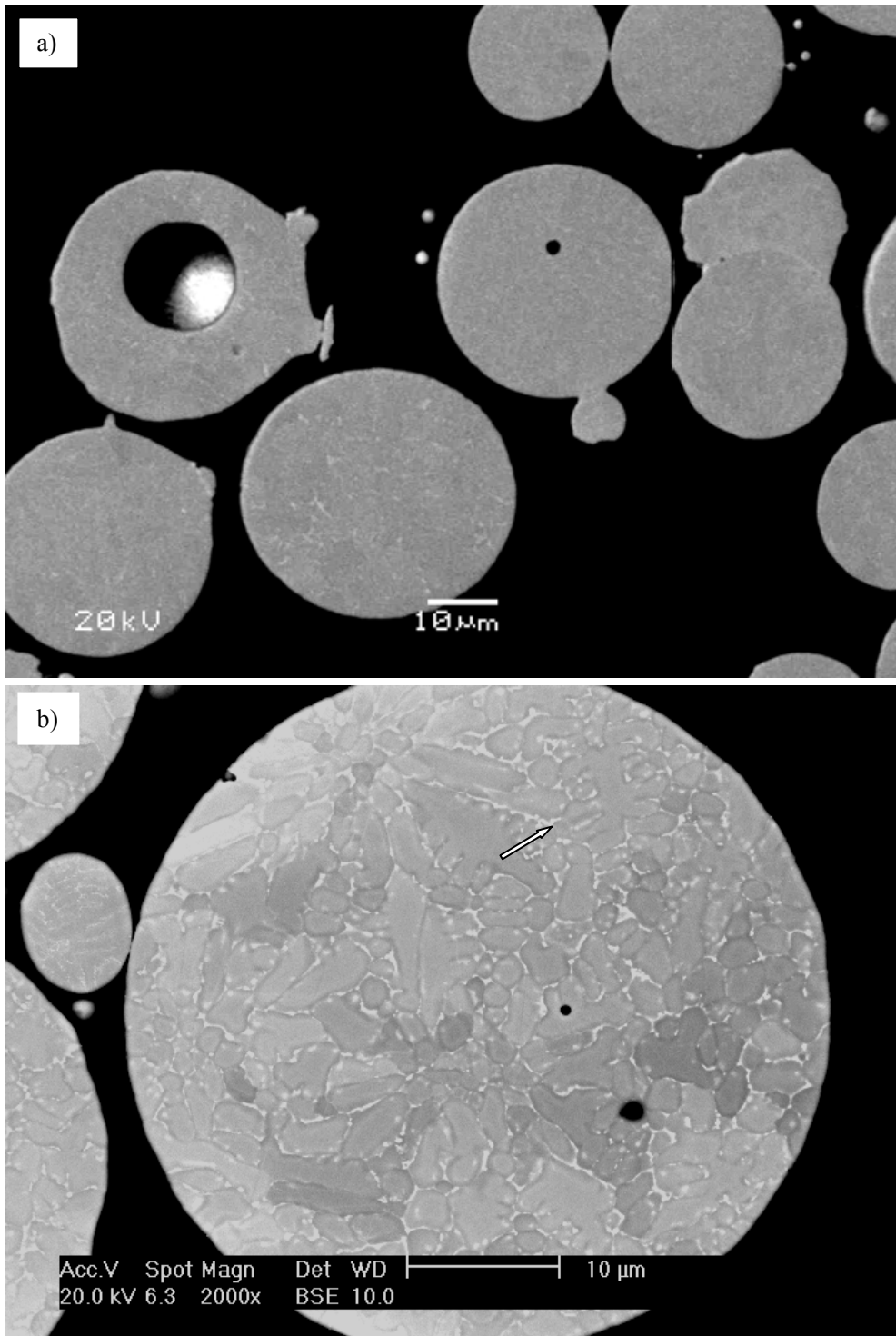


Fig. 4-3 SEM images of as-received CM247LC powder

a) backscattered electron image of hollow powders; b) BSE image of polished powder

4.1.2 Response of powder to temperature

A DSC scan was carried out to obtain an indication of the response of the material to the temperature change. The curves on as-received powder are complicated and not repeatable, presumably due to oxidation at high temperatures and measurements were therefore carried out using solid samples and typical heating and cooling curves are shown in Fig. 4-4. These suggest that the solvus of γ' is at some temperature between 1230°C and 1252 °C which is consistent with the value of 1235°C given by [Sims, Stoloff *et al.* 1987] The temperature difference of the turning point between the heating and cooling curve is caused by superheating and supercooling. The small exothermal peak between 1200 °C and 1220 °C on the cooling curve may be associated with the precipitation behaviour of γ' particles. This curve is not likely to be related to carbides as the solution temperature of carbides is reported to be 1340 °C which is very close to the incipient melting temperature 1345 °C. The microstructural changes in this temperature range could be examined by heating up to 1270C and cooling to a selected temperature at 5C/min to selected temperatures before quenching back to room temperature.

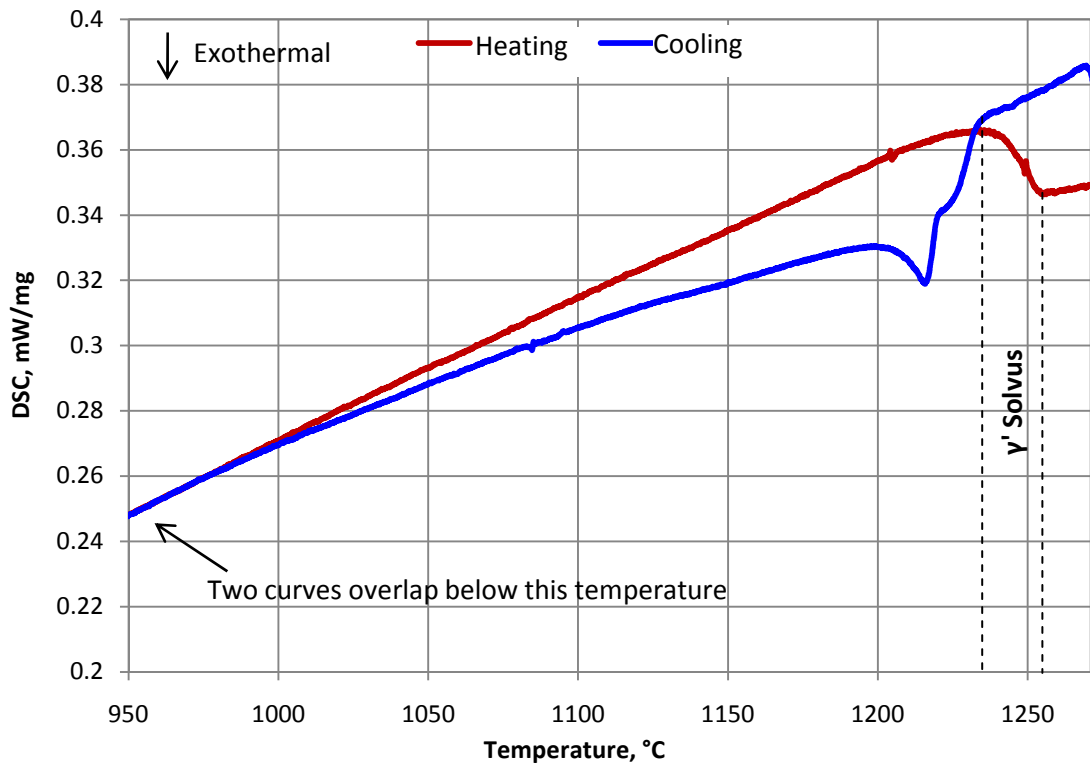


Fig. 4-4 DSC curves of solid CM247LC. The γ' solvus is at a temperature between 1230 °C and 1252 °C. The exothermal peak between 1200 °C and 1220 °C on the cooling curve may be associated to the precipitation behaviour of γ' .

Powder was heat treated below the γ' solvus in a vacuum furnace at 800 °C, 1100 °C and 1200 °C for 2 hours respectively to understand the microstructural response to different temperatures below γ' solvus. Powder surfaces were examined by SEM and typical images are shown in Fig. 4-5.

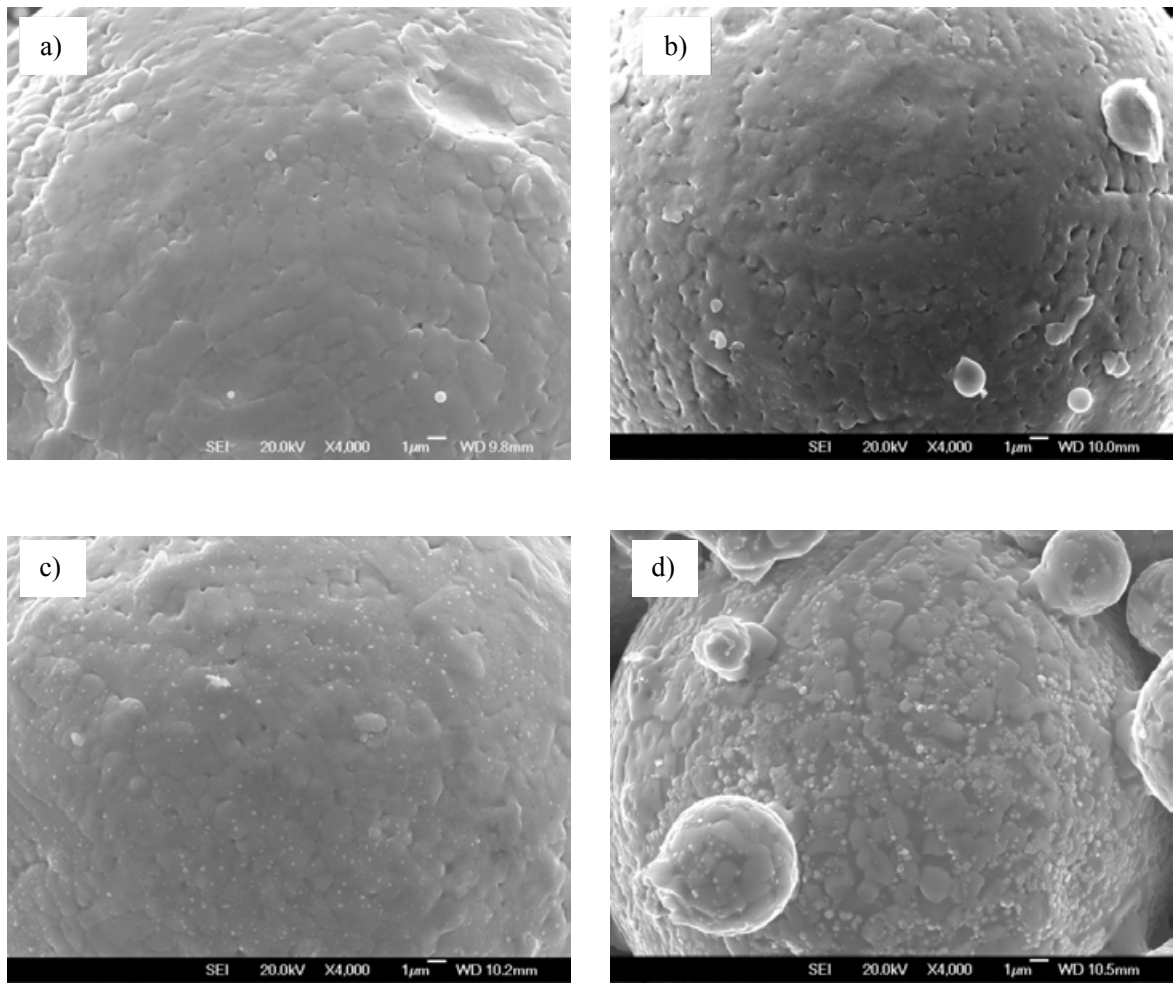


Fig. 4-5 Secondary electron SEM images of powder surfaces of CM247LC.

a) as-received;

b) heat treated at 800 °C for 2h;

c) heat treated at 1100 °C for 2h;

d) heat treated at 1200 °C for 2h.

The surface of the as-received powder shows a dendritic structure with a few bright particles which presumably contain high atomic number elements. As the heat treatment temperature is increased small particles become visible on the powder surface and their density and size increase are highest at 1200°C. The dendrite structure remains unchanged until the temperature reaches 1200°C. At this temperature, sintering necks are also observed.

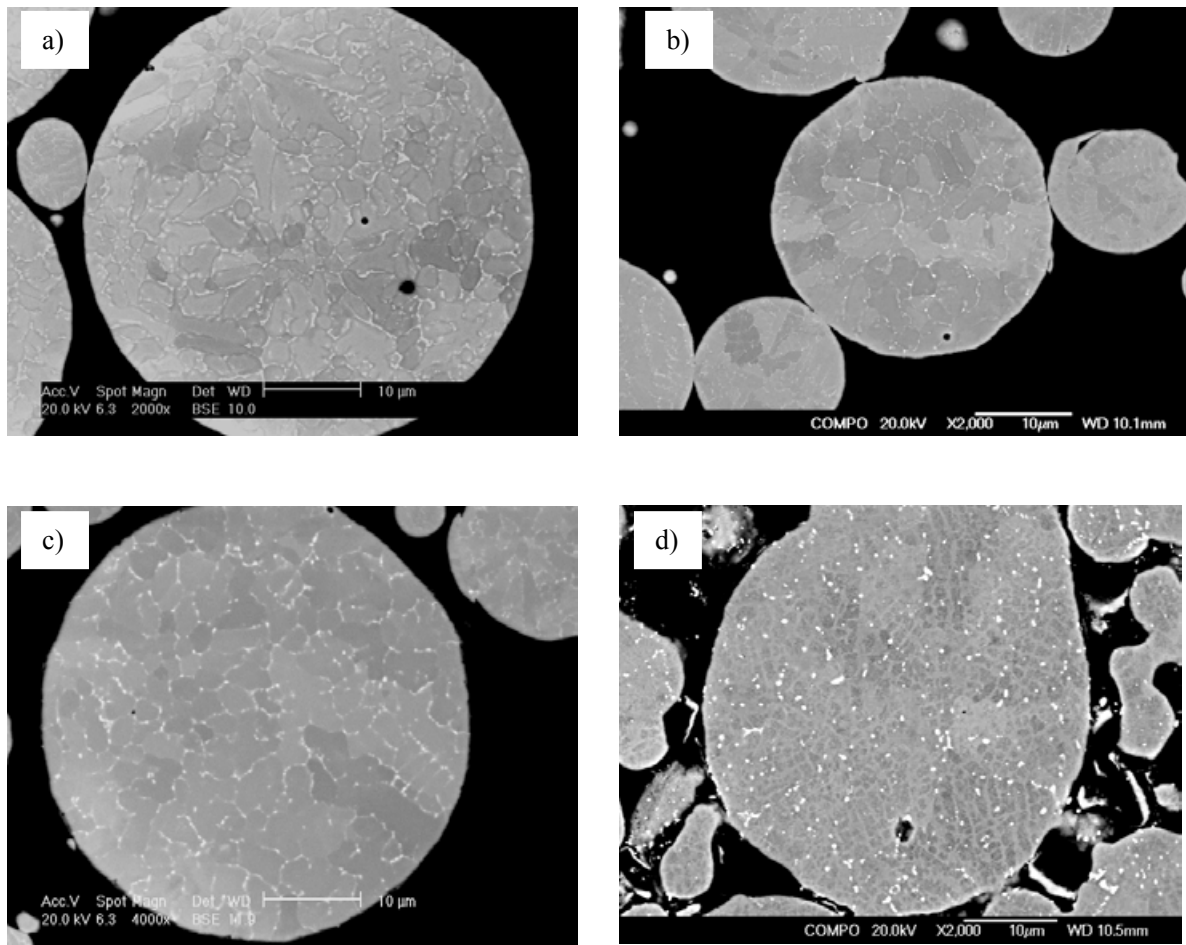


Fig. 4-6 SEM images taken using BSE of cross sections of CM247LC powder.

a) as-received;

b) heat treated at 800 °C for 2h;

c) heat treated at 1100 °C for 2h;

d) heat treated at 1200 °C for 2h.

The cross sectioned powders are shown in Fig.4-6. Again, the subgrain structure remains unchanged until the temperature reaches 1200 °C. The most obvious phenomenon is the formation of the discrete bright particles and the absence of the bright subgrain boundaries in the 1200 °C heat treated sample. In the as-received powder the subgrain boundaries are bright, because of the presence of heavy elements and in samples heat treated at 800 °C and

1100 °C some discrete precipitates can be seen to develop in these bright regions. When the heat treatment temperature is increased to 1200 °C larger bright particles are visible, many of which are apparently within grains rather than only on grain boundaries. Cubic gamma prime particles can also be observed which are darker than the surrounding matrix.

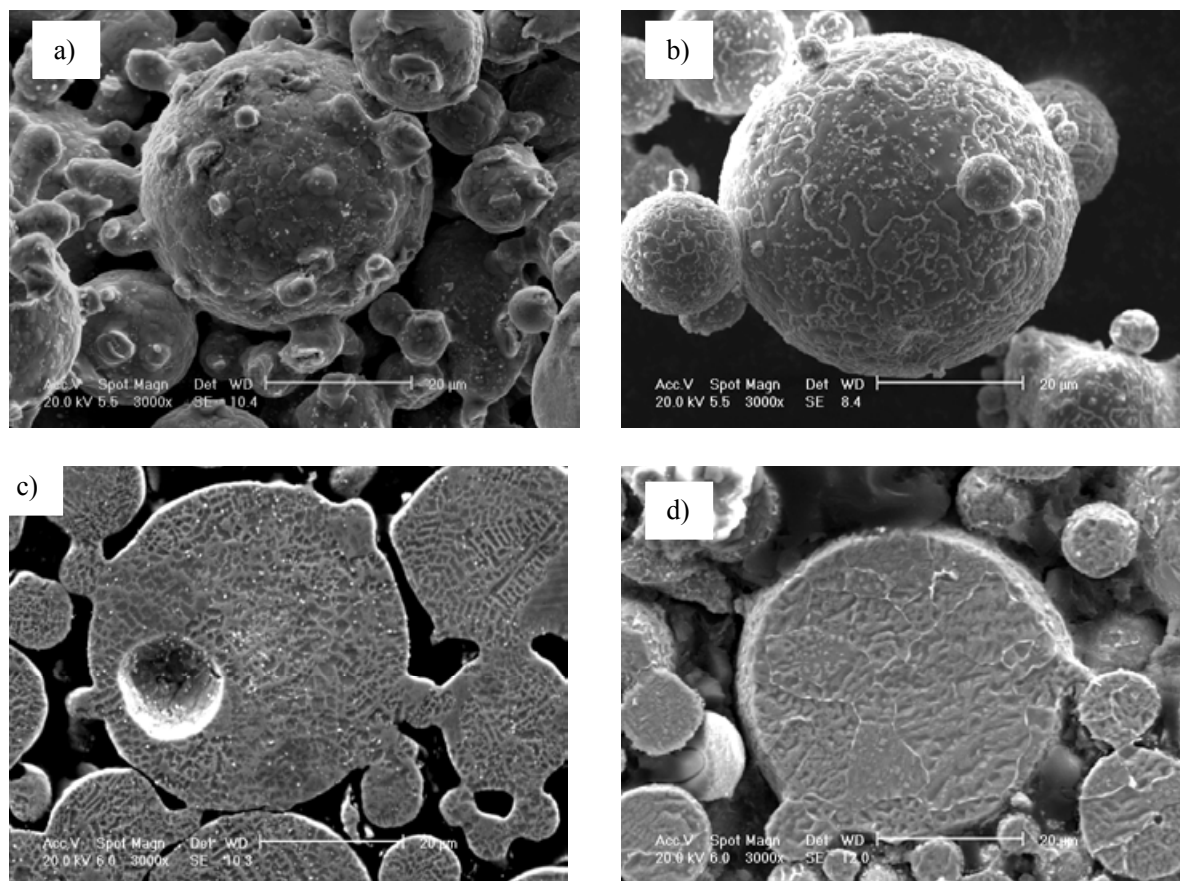


Fig. 4-7 Secondary electron SEM images of CM247LC heat treated at 1200 °C for 2 hours under different vacuum levels.

a) and c) powder heat treated under vacuum level of 10^{-5} mBar;

b) and d) powder heat treated under vacuum level of 10^{-4} mBar.

c) and d) were etched after heat treatment

To further understand the formation of particles and the influence of atmosphere gas that may occur if HIPping cans are not perfectly welded, powder was heat treated at 1200 °C for 2 hours under different vacuum levels of about 10^{-4} mBar and 10^{-5} mBar respectively. Fig. 4-7 a) and c) are surfaces and cross sections of powder heat treated at a vacuum level of 10^{-5} mBar, which is the same as the level of the powders prepared for HIPping. Fig. 4-7 b) and d) are heat treated under a level of 10^{-4} mBar, which would correspond to leakage of air into a capsule during HIPping. Comparison of the surfaces in Fig.4-7 a) and b)) shows that more sintering necks are found in a) and the surface was decorated with discrete particles while hardly any sintering necks are seen and a continuous network of bright lines covered the surface of b). In fact b) remains in form of loose powders rather than a sintered block after heat treatment. The cross sections were etched which showed further differences between samples heat treated at different levels of vacuum. The sample heat treated in a vacuum which corresponded to the HIP condition in the absence of a leak gives a homogenous distribution of particles (Fig. 4-7 c)) as shown earlier in Fig. 4-6 d). The sample heat treated using a poorer vacuum level, no particles are observed and a continuous layer is visible at grain boundaries, as seen in Fig 4-7d).

It should be noted that the formation of particles may not only be the result of dwell-time at temperature but also due to the slow cooling (at the rate of 3 °C/min) from the heat treatment temperature.

4.1.3 Influence of HIPping temperature and time on powder bonding behaviour and bulk density

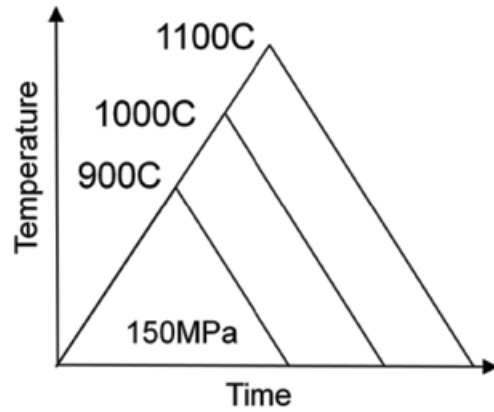
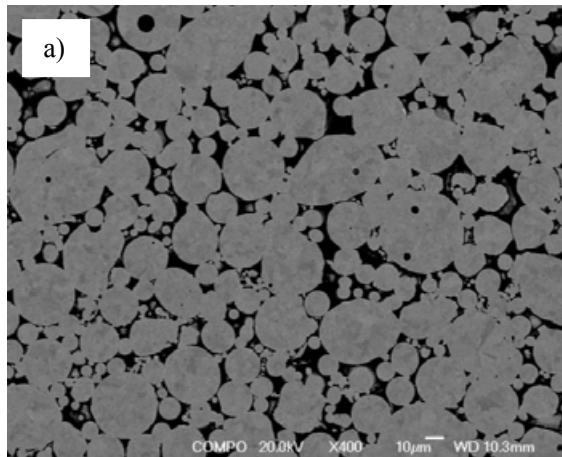
In order to obtain fully dense well-bonded material by powder HIPping, it is important to

know under what conditions the powders begin to bond with each other and when the powder is fully densified. A sample with no porosity and no prior particle boundaries is ideal after HIPping. The variables which can be controlled when HIPping are the temperature, the pressure and the HIPping time. In the present study a pressure of 150Mpa was used during HIPping of the CM247LC on the basis of previous work [Atkinson and Davies 2000] .Thus the influence of pressure on HIPping CM247LC was not studied in this work.

4.1.3.1 Influence of HIPping temperature on powder bonding behaviour

Interrupted HIPping was carried out by heating the sample under the selected HIP pressure of 150MPa to the selected temperature and cooling it to room temperature immediately with no dwell time; the cooling rate from the HIP temperature was 5 °C/min. This method can define the temperature at which the powders begin to bond with each other if the temperature is at the critical value.

Images in Fig. 4-8 shows the overall density of CM247LC powder which had been interrupt-HIPped at 900 °C, 1000 °C and 1100 °C. The densities were measured to be 88.6%, 97.6% and 99.3% respectively of the theoretical value. Pores can be seen in powders in the samples interrupt-HIPped at 900 °C and 1000 °C but can rarely be found when the temperature used was 1100 °C.



Schematic of interrupted HIP schedules

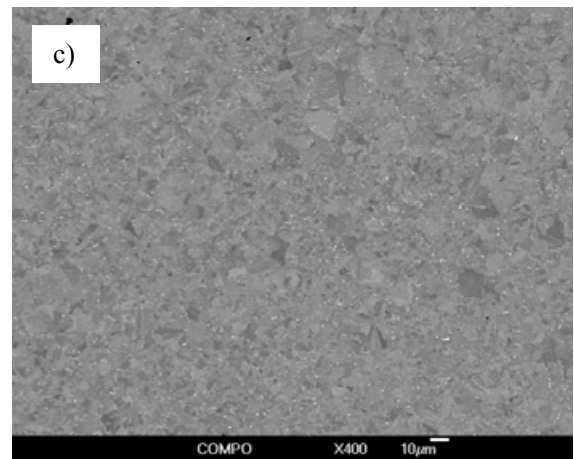
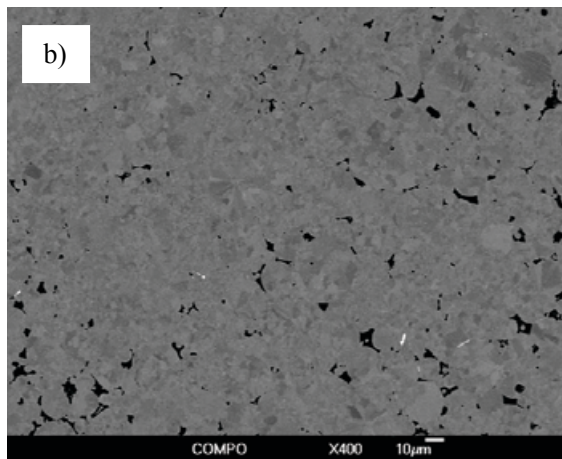


Fig. 4-8 Back scattered SEM low magnification images of samples which had been HIPped using no dwell as illustrated in the inset.

- a) 900 °C at 150MPa, density 88.6%;
- b) 1000 °C at 150MPa, density 97.6%;
- c) 1100 °C at 150MPa, density 99.3%.

The images in Fig. 4-9 show the bonding behaviour of CM247LC powders that occurs during interrupted HIPping at 900 °C, 1000 °C and 1100 °C. The micrographs on the left

were taken using backscatter electron imaging (BSE); and those on the right were taken of the same areas using electron backscatter diffraction (EBSD). Different colours indicate different orientations, that is to say, different grains.

There are two things to be noted from Fig. 4-9 as the temperature is increased from 900°C to 1100°C. One is that the pores are gradually closed; the other is small powders are crushed (in the right part of Fig.4-9 c) and d)) and a recrystallised layer is generated adjacent to large powder particles. It is clear in the EBSD pictures that the critical temperature of the recrystallisation (bonding) is 1000°C. When the temperature reaches 1100°C, the bonding layer is further developed. Grains which have grown across prior particle boundaries can be found (Fig. 4-9 e) and f); an example is arrowed.

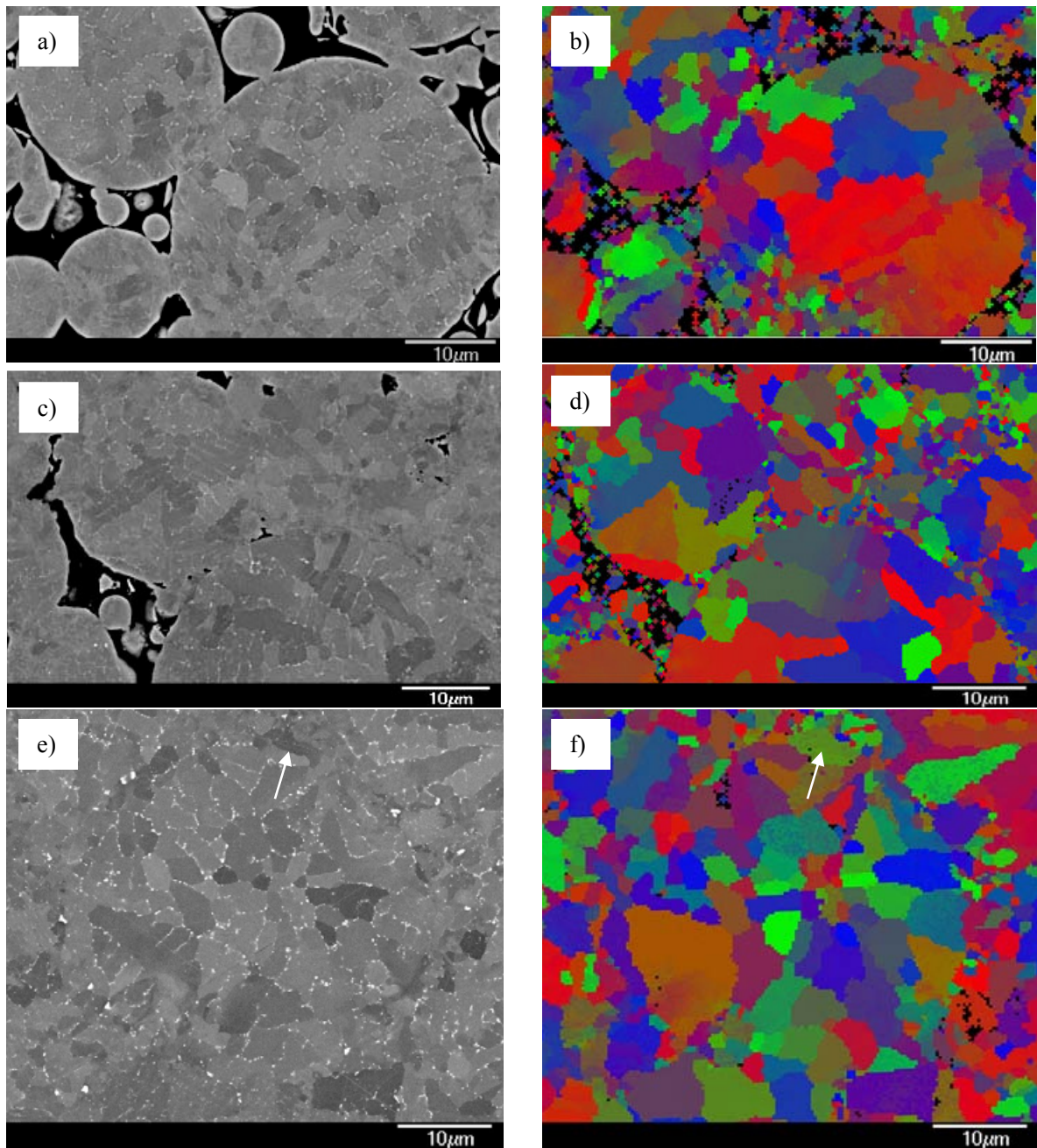


Fig. 4-9 BSE and EBSD images of powder bonding observed in samples which were interrupt-HIPped.

a) 900 °C at 150MPa, BSE ; b) 900 °C at 150MPa, EBSD;

c) 1000 °C at 150MPa, BSE ; d) 1000 °C at 150MPa, EBSD;

e) 1100 °C at 150MPa, BSE ; f) 1100 °C at 150MPa, EBSD; The arrow is pointing at a line of very fine particles at the PPB involved in a recrystallised grain.

4.1.3.2 Influence of dwell time on powder bonding behaviour

In addition to interrupted HIPping, the full HIPping process was applied to CM247LC powder to study the influence of dwell time on powder bonding behaviour. Fig. 4-10 demonstrates the porosity of CM247LC powders HIPped at 800°C, 900°C, 1000°C and 1100°C under the same pressure of 150MPa and dwelt for the same period of 4 hours. Densities are measured to be 84.6%, 96.4%, 99.4% and 99.9% respectively of the theoretical value. Density values of both interrupted HIPping and fully HIPped samples are plotted in Fig. 4-11. The shaded part in the plotting area is the density contributed by the dwell time. It is easy to see that as the temperature is increased, the dwell time plays a less and less important role in densification. When the temperature reaches 1200°C dwell makes hardly any difference in density.

As mentioned before, we are interested not only in the density but also in the bonding strength. 1100 °C and 1200 °C were chosen to understand the influence of dwell time on the extent of bonding, because under these temperatures, the HIPped samples are almost fully densified. Fig. 4-12 a) and b) are cross-sections of samples HIPped at 1100°C. The prior particle boundaries are easily observed to be a thin recrystallisation layer in the interrupted HIPped sample (see Fig 4-12 a)). After 4 hours dwell at the same temperature, this layer grows broader (see Fig 4-12 b)). When the temperature is increased to 1200°C, the interrupted HIPped sample shows an even wider layer of recrystallised grains at the powder boundaries (see Fig 4-12 c)) but still the original powder particles can be easily observed until the sample is dwelt for 4 hours at 1200 °C. Grain boundaries instead of powder boundaries are now more obvious (see Fig. 4-12 d)). The sample was fully recrystallised, and the bonding process finished under this HIPping condition, as judged from the microstructure.

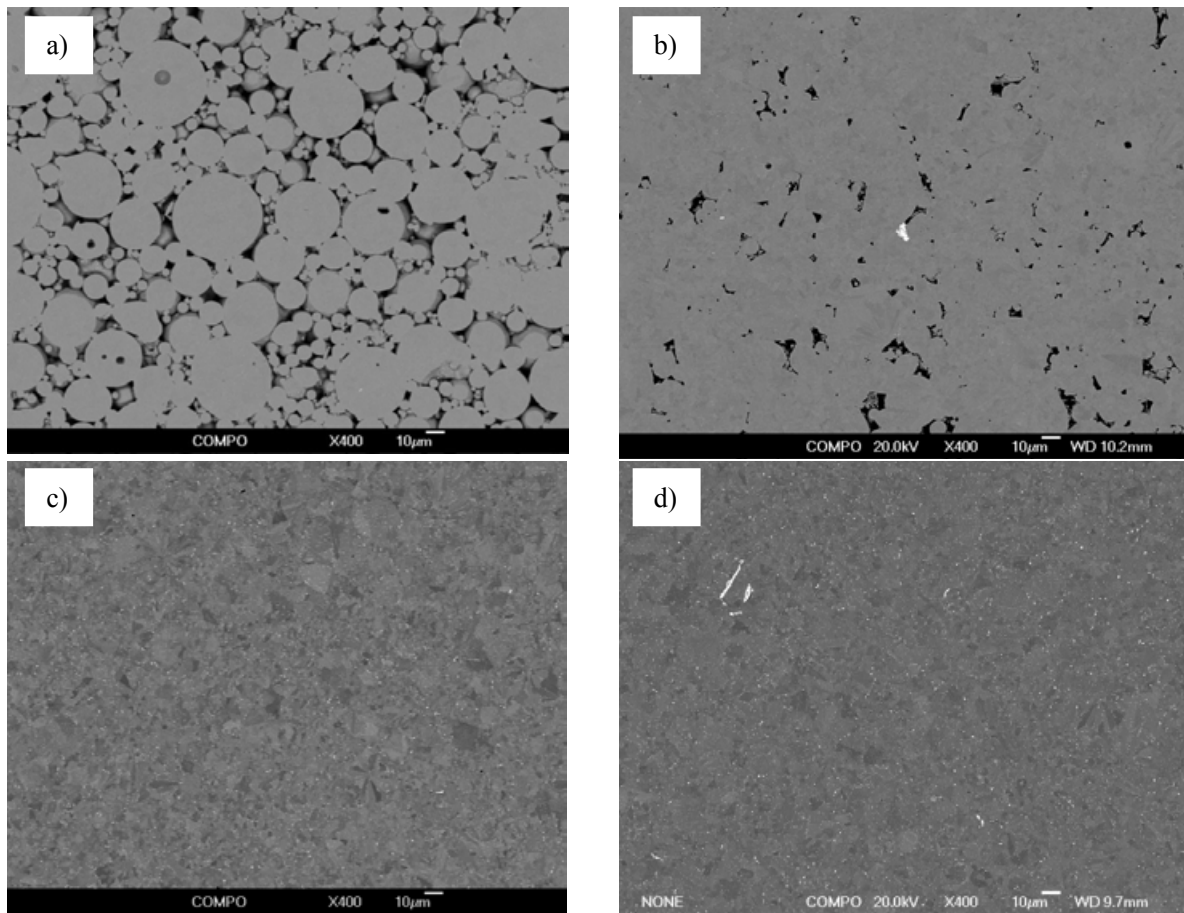


Fig. 4-10 BSE SEM images showing the density of powder HIPped under different conditions

- a) 800 °C at 150MPa for 4 hours, density 84.6%;
- b) 900 °C at 150MPa for 4 hours, density 96.4%;
- c) 1000 °C at 150MPa for 4 hours, density 99.4%;
- d) 1100 °C at 150MPa for 4 hours, density 99.9%;

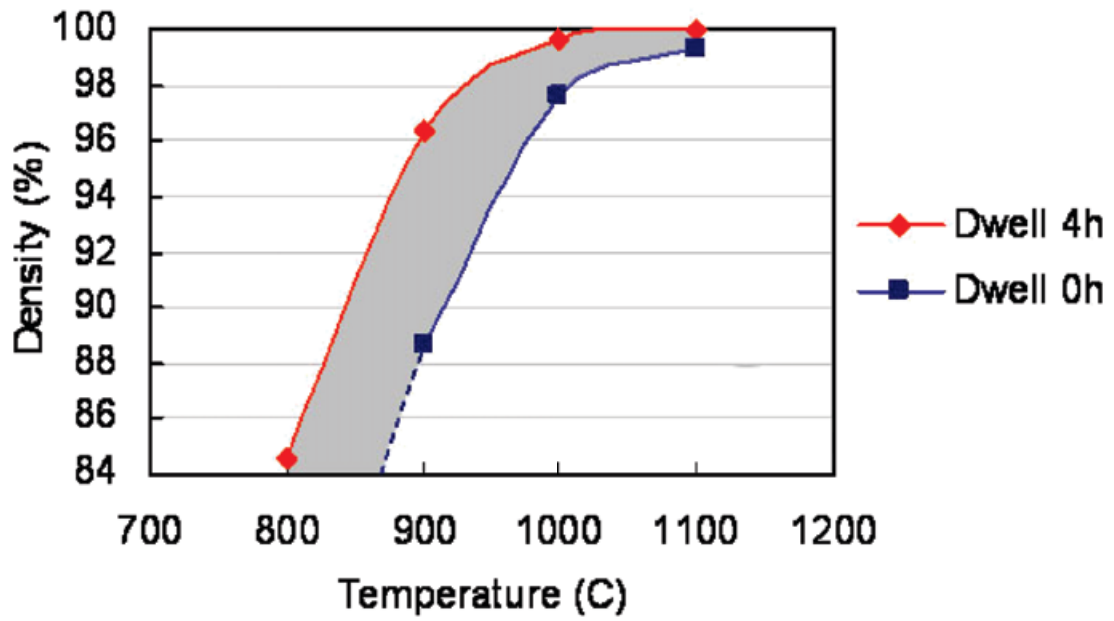


Fig.4-11 Influence of dwell time on the density of CM247LC powder HIPped at a pressure of 150MPa. The grey region is the density increase contributed by 4 hours dwell time.

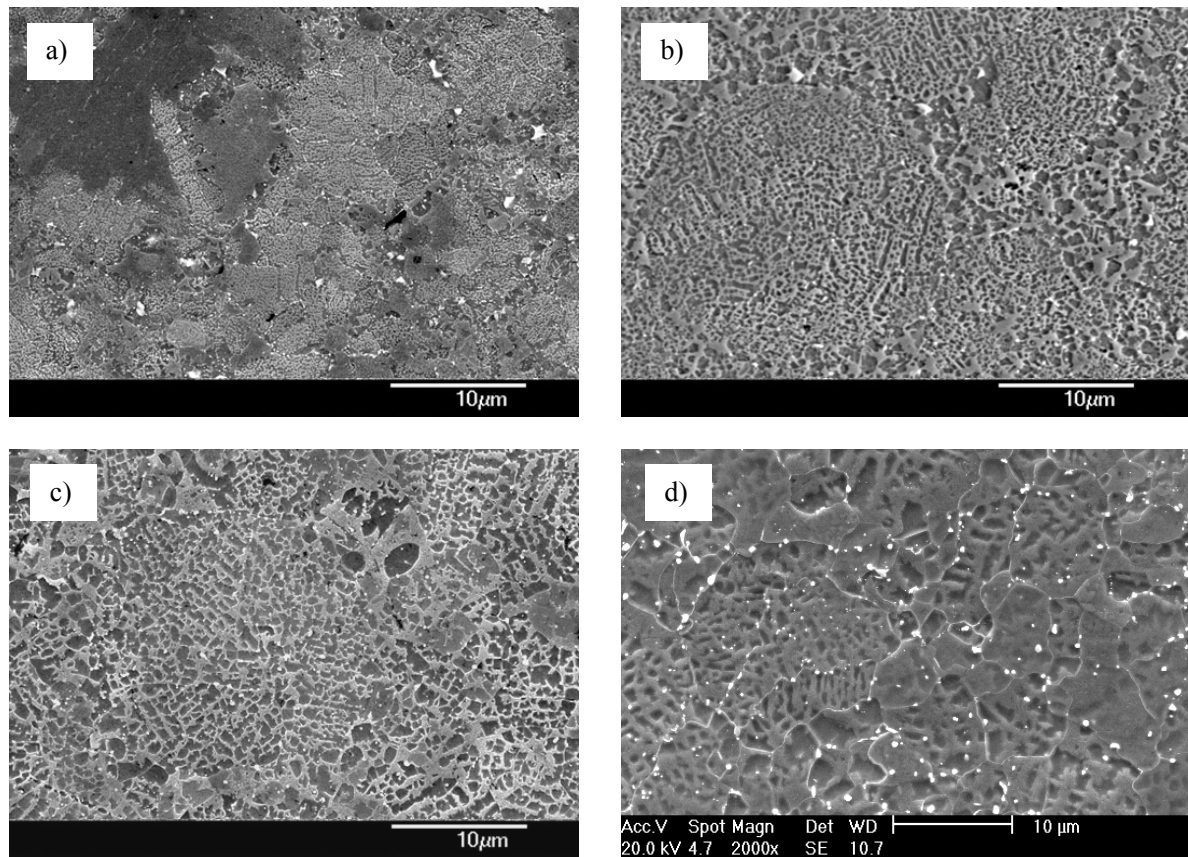


Fig. 4-12 Secondary electron SEM images of etched samples showing the influence of dwell time on development of bonding.

- a) 1100 °C at 150MPa no dwell; b) 1100 °C at 150MPa for 4 hours;
c) 1200 °C at 150MPa no dwell; d) 1200 °C at 150MPa for 4 hours;

4.1.4 Summary

- A significant number of powder particles which contain pores are found in as-received powder. These pores are formed both by entrapment of gas during gas atomisation and by shrinkage. Argon gas will thus be present in HIPped gas-atomised powders;
- The presence of air influences the bonding and surface precipitation behaviour of CM247LC powder during HIPping. This could hinder the sintering process.
- CM247LC powder particles begin to bond with each other at 1000 °C with the assistance

of 150MPa pressure. The density reaches 99% of bulk density when the temperature is over 1100 °C.

- CM247LC powder can be fully densified and fully recrystallised when HIPped at a temperature of 1200 °C, at 150MPa for 4 hours.

4.2 Microstructure and properties of as-HIPped CM247LC

Four sets of HIPping conditions have been investigated in this study and these are shown in Table 4-1. Samples HIPped at temperatures below the γ' solvus (1235 °C) were dwelt for 4 hours while those HIPped above the γ' solvus were dwelt for only 2 hours. The factor concerned to reduce the dwell time is that significant diffusion between the CM247LC powder and the mild steel cans will occur at elevated temperatures. It was found in preliminary work that the thickness of the layer increased with increasing temperature and dwell time (see Appendix 2). The effect of this layer is not yet known. Current work is focused on the material from which the diffusion layer has been removed. The influence of this layer will be investigated in future work.

Table 4-1 HIPping conditions used for CM247LC powder

	Below γ' solvus	Above γ' solvus
Temperature	1100 °C, 1200 °C	1260 °C, 1320 °C
Pressure	150MPa	150MPa
Dwell time	4h	2h
Ramp rate	5 °C/min	5 °C/min

4.2.1 Microstructure of as-HIPped CM247LC

The microstructure of as-HIPped CM247LC has been characterised for the different HIPping conditions by the following parameters: grain boundary morphology, grain size, γ' morphology, carbides and defect densities.

4.2.1.1 Grain boundary

A large volume fraction of γ' dispersed in a γ matrix is expected in the as-HIPped structure. The as-HIPped microstructures shown in Fig. 4-13 consist of two types of γ' particles (γ' particles are darker in contrast than the γ matrix); one is regular in shape and distributed homogeneously within γ grains; the other type is coarser, of irregular shape and distributed differently according to the HIPping temperature used. When HIPped at 1100 °C, the coarse particles are aligned to form the shape of original powder particles, which indicates that the consolidation of CM247LC powder during HIPping begins by the recrystallisation at powder particle boundaries. This γ' will remain at grain boundaries when HIPped above 1200 °C, but its pattern is then not obvious since the size of γ' over the whole sample looks uniform at this

temperature. When the HIPping temperature is above the γ' solvus, another distribution was developed - coarse γ' particles at the γ grain boundaries. This structure, the 'necklace' structure, is reported elsewhere [Kendall et al. 1989] as a stable state for nickel-base superalloys at high temperatures. It is also observed in other P/M nickel- base alloys [Bee et al. 1980; Jeandin et al. 1986; Gao et al. 1996]. A similar microstructure designated 'rosette γ - γ' eutectic' was found in as-cast polycrystalline CM247LC [Huang and Koo 2004] and conventionally cast Mar-M247 [Gasko, Janowski et al. 1988]. Gasko found that the room temperature yield strength increased and the ductility decreased as the amount of γ - γ' eutectic was reduced. Although γ - γ' eutectic is different from the morphology of 'necklace', they both consist of coarser γ' along grain boundaries rather than in the grain interior. The influence of the 'necklace' structure on the mechanical properties might be similar to that of the rosette eutectic because they both contain coarse γ' particles at grain boundaries.

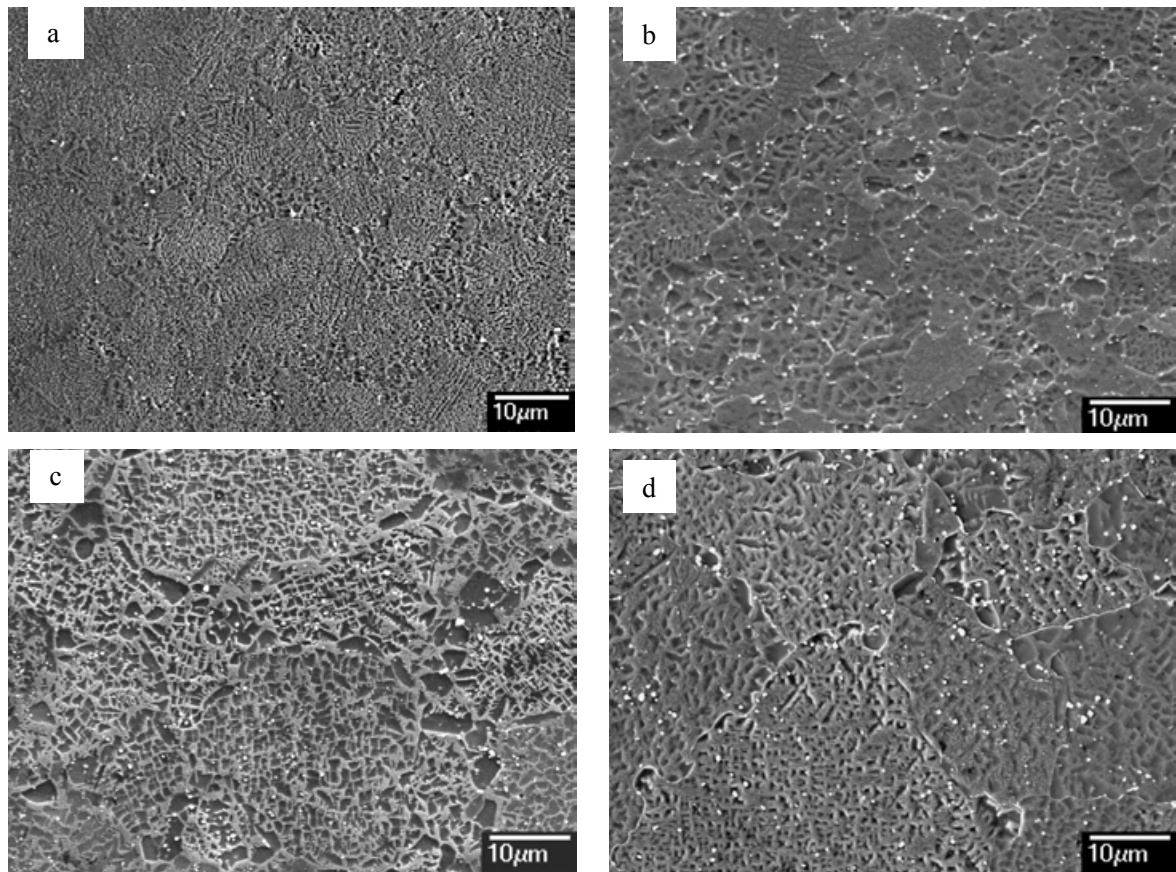


Fig. 4-13 Secondary electron SEM images of etched as-HIPped CM247LC showing the morphology of boundary γ' when HIPped at 150MPa for 4h at a) 1100 °C and b) 1200 °C and at 150Mpa for 2h at c) 1260 °C; d) 1320 °C.

4.2.1.2 Grain size

The EBSD technique is applied to distinguish grains from each other, because the grains in samples HIPped at temperatures below the γ' solvus are not easily seen in SEM images. The orientation maps are shown in Fig. 4-14. Certain magnifications were chosen for different samples so that enough grains are included in the field as well as grain boundaries are clear. No particular colour (i.e. crystallographic direction) is dominant. Typical pole figures (Fig. 4-14 e) of the 1260 °C as-HIPped CM247LC) indicate that the as-HIPped CM247LC

samples have an effectively random texture. Grain boundaries are found to be serrated for all HIPping conditions (as arrowed). This may be due to the presence of Hf in the alloy and the slow cooling rate from the HIPping temperature as mentioned in §2.2.4.

The average grain size is increased significantly with HIPping temperature. Measurement of the grain size was obtained using the integrated INCA software. Three different areas on each sample were scanned using EBSD at an appropriate magnification and at least 1000 grains were measured for the statistical analysis of grain size distribution. The results are shown in Fig. 4-15. The solid line shows the average grain diameter change with the HIPping temperature. The average grain diameter is of the order of 6 μm and this does not change much when the HIPping temperature was below the γ' solvus. When the HIPping temperature was above the γ' solvus, the average diameter of grains was about 17 μm and 29 μm at 1260 °C and 1320 °C respectively. The distribution of grain size also varies for different HIPping temperatures. 1200 °C gives the most uniform grain size. Some grains in the sample HIPped at 1100°C are larger than those in the sample HIPped at 1200 °C, probably because the grains in 1100 °C HIPped sample were inherited from the original powder and not yet recrystallised; while those in the sample HIPped at 1200°C were formed by recrystallisation, starting at powder boundaries. Some large grains, up to 67 μm , which is larger than the biggest powder size used (\sim 53 μm), were found in samples HIPped at 1320 °C, i.e. above the γ' solvus. The grain size of samples HIPped above the γ' solvus could have been even larger if they were held for 4 hours.

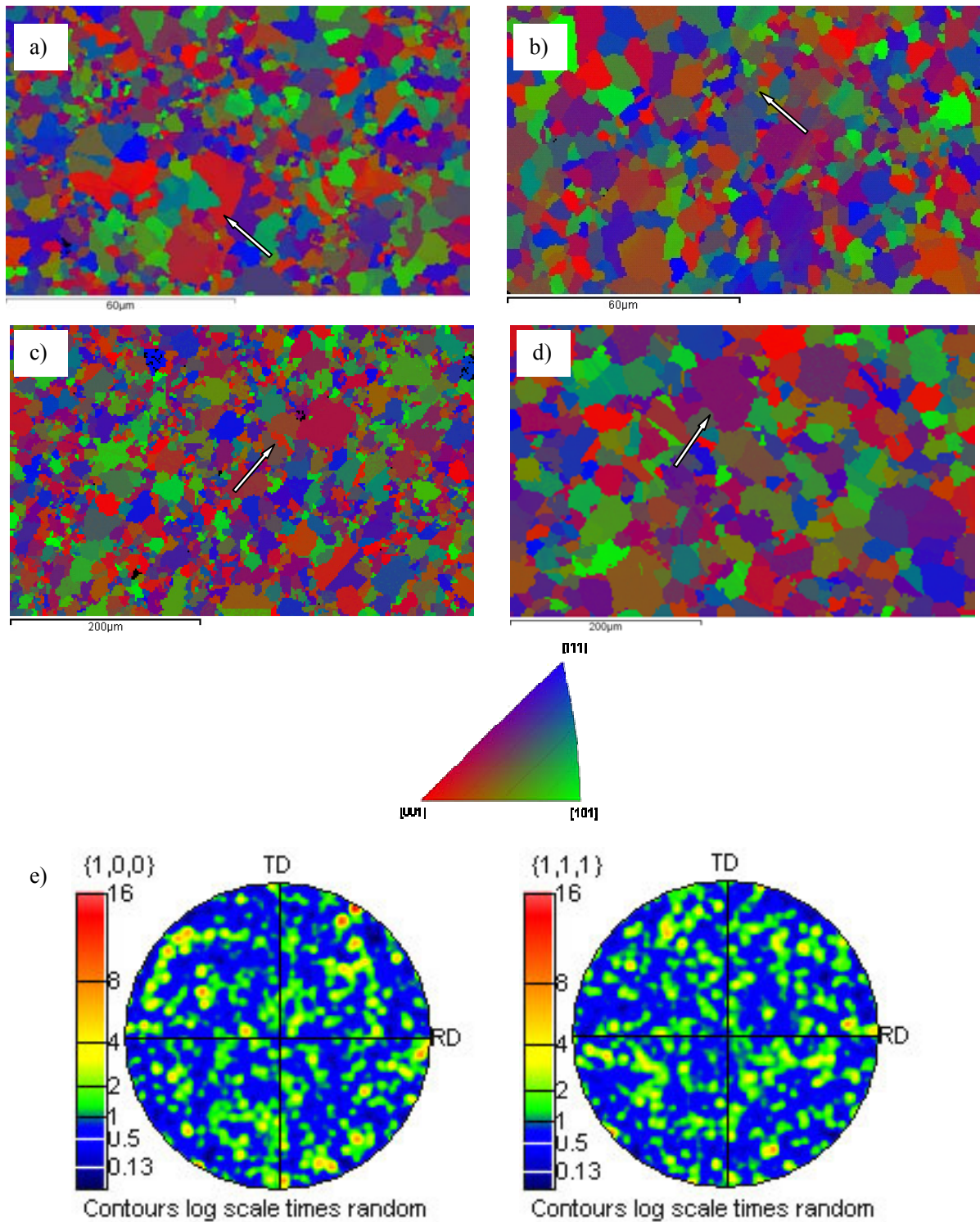


Fig.4-14 Orientation maps of as-HIPped CM247LC showing the change in grain size against HIPping temperature. a) 1100 °C/150MPa/4h; b) 1200 °C/150MPa/4h; c) 1260 °C/150MPa/2h; d) 1320 °C/150MPa/2h; e) pole figures of c), showing random texture. Arrows are pointing at serrated grain boundaries.

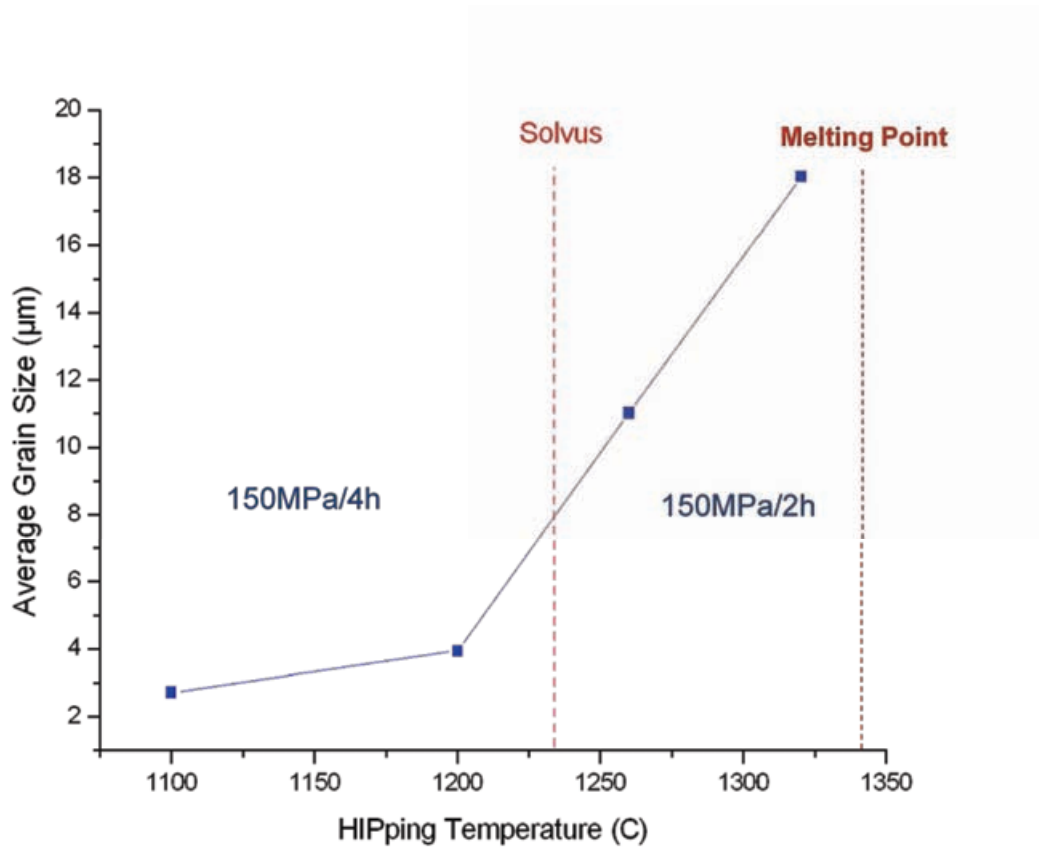


Fig. 4-15 Influence of HIPping temperature on grain size of as-HIPped CM247LC.

4.2.1.3 Gamma prime γ'

The morphology of γ' in grain interiors was investigated using etched samples. Images in Fig.4-16a) – d) are images taken from grains with $\{001\}$ planes parallel to polished sample surfaces. Fig.4-16 a) shows CM247LC powder HIPped at 1100 °C. As mentioned previously, powders are fully densified but not yet completely recrystallised for this HIPping condition. The γ' observed here is formed by coarsening of the original γ' nuclei in powder produced by rapid cooling from the liquid. They are cubic and very fine, up to 0.5 μm in size. The γ' in Fig. 4-16 b) are recrystallised precipitates formed when the HIPping temperature is increased to 1200°C. They are larger than the γ' seen in the sample HIPped at 1100°C and

is not much affected by temperature when HIPped above the solvus (see Fig. 4-16 c) and d)). These γ' particles are cubic and they have straight boundaries and are relatively uniform in size, around 1 μm . The volume fraction of γ' was measured using image analysis and the results are shown in Fig.4-17. The volume fraction of γ' is 54% in 1100 °C as-HIPped CM247LC and of the order of 60% in the rest of the HIPped samples; the value reaches 61% when HIPped at 1320 °C.

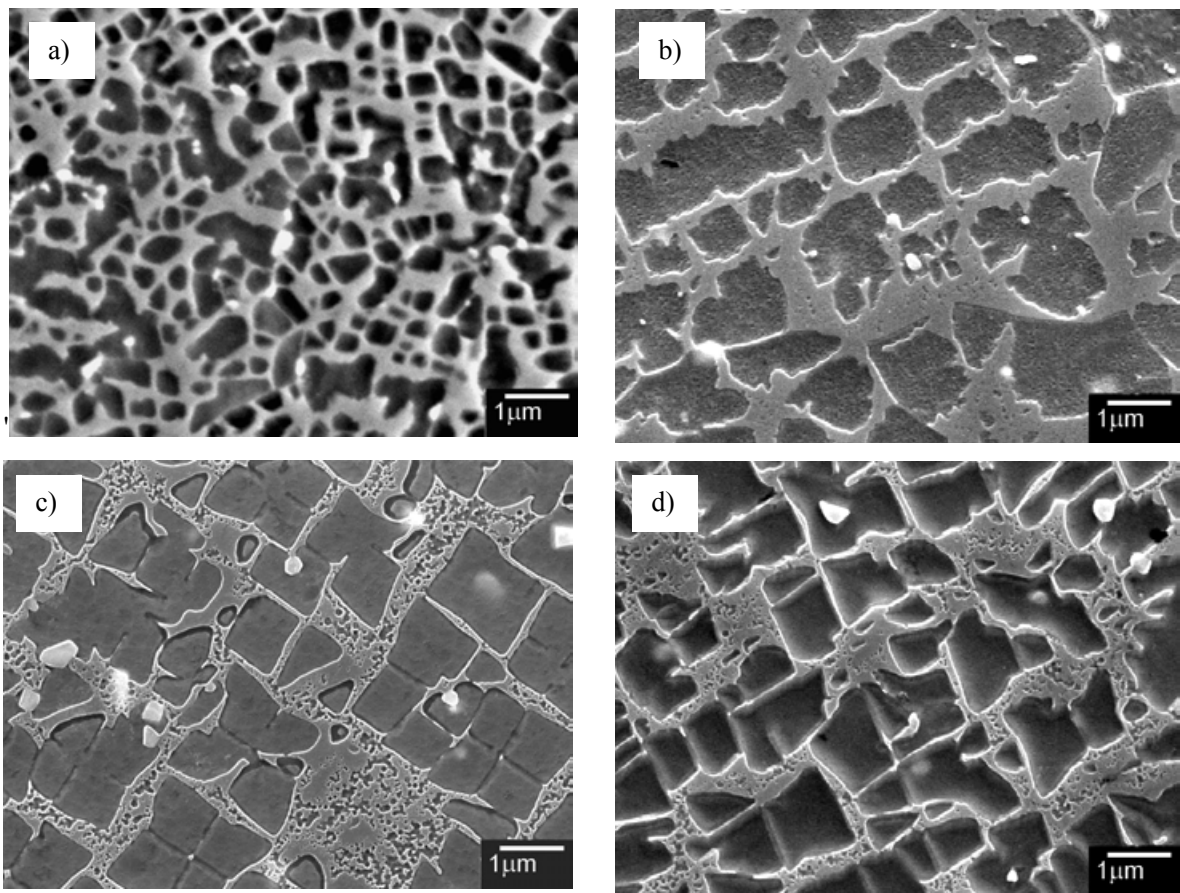


Fig. 4-16 High magnification secondary electron SEM images of etched samples showing the morphology of γ' in grain interiors, imaged in an $\langle 001 \rangle$ direction.

- a) 1100 °C/150MPa/4h; b) 1200 °C/150MPa/4h;
c) 1260 °C/150MPa/2h; d) 1320 °C/150MPa/2h.

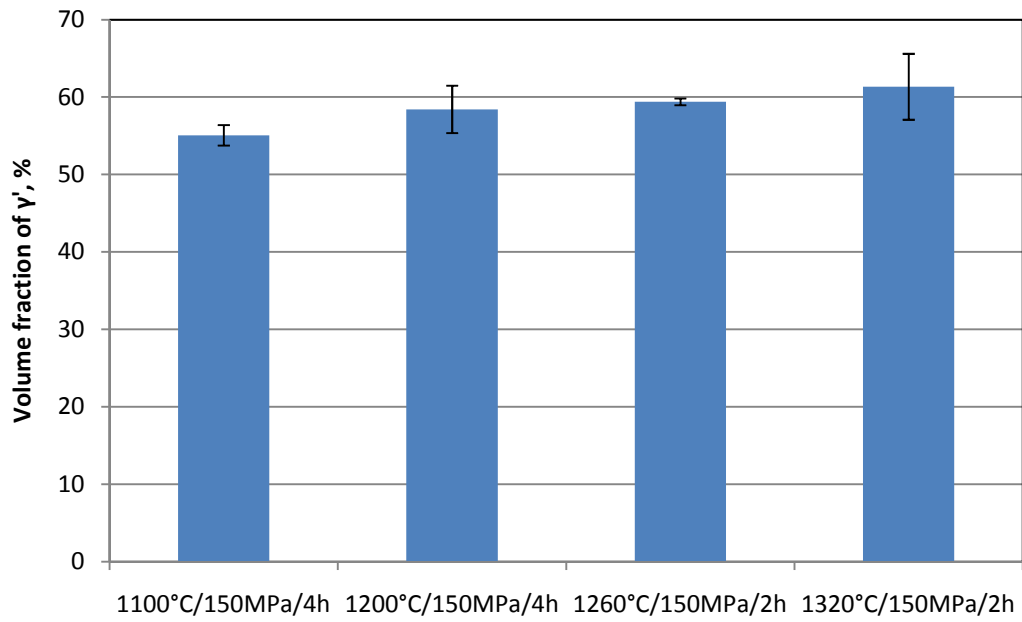


Fig.4-17 Volume fraction of γ' under different HIPping conditions.

4.2.1.4 Carbides

Diamond shape 'white' dots, analysed by EDS in TEM (Table 4-2) were found to be MC carbide which are rich in Hf and Ta. A certain amount of oxygen was also detected which maybe because the Hf and Ta getter oxygen from the matrix.

Table 4-2 EDS analysis of carbides in TEM

Particle			Matrix		
Element	Weight%	Atomic%	Element	Weight%	Atomic%
C	1.8 ± 0.2	14.0	Al	1.8 ± 0.3	4.1
O	1.5 ± 0.2	9.2	Cr	21.3 ± 0.7	25.1
Ti	2.2 ± 0.1	4.5	Co	15.3 ± 0.7	15.9
Cr	4.5 ± 0.1	8.4	Ni	48.2 ± 1.0	50.4
Co	2.6 ± 0.1	4.2	W	13.4 ± 1.3	4.5
Ni	11.7 ± 0.2	19.3			
Hf	37.4 ± 0.6	20.2			
Ta	38.4 ± 0.6	20.4			

They are distributed homogeneously within the whole sample under all HIPping conditions (see Fig. 4-18). Only the distribution of the carbides in the sample HIPped at 1100 °C is different from the rest, apart from some relatively coarse carbide particles, the rest of the carbide distribution is very similar to the ones found in heat treated powder (see Fig. 4-6 c)). Statistical results in Fig. 4-19 show that carbides are fully formed when HIPped above 1200 °C, the size and the volume fraction were not apparently affected by temperature. The morphology of MC carbides is quite different from those script-like MC found in conventionally cast CM247LC. Their fine size and homogeneous distribution would benefit the HIPped material as strengtheners [Chen, Lee et al. 1998] instead of crack initiators as in conventionally cast materials.

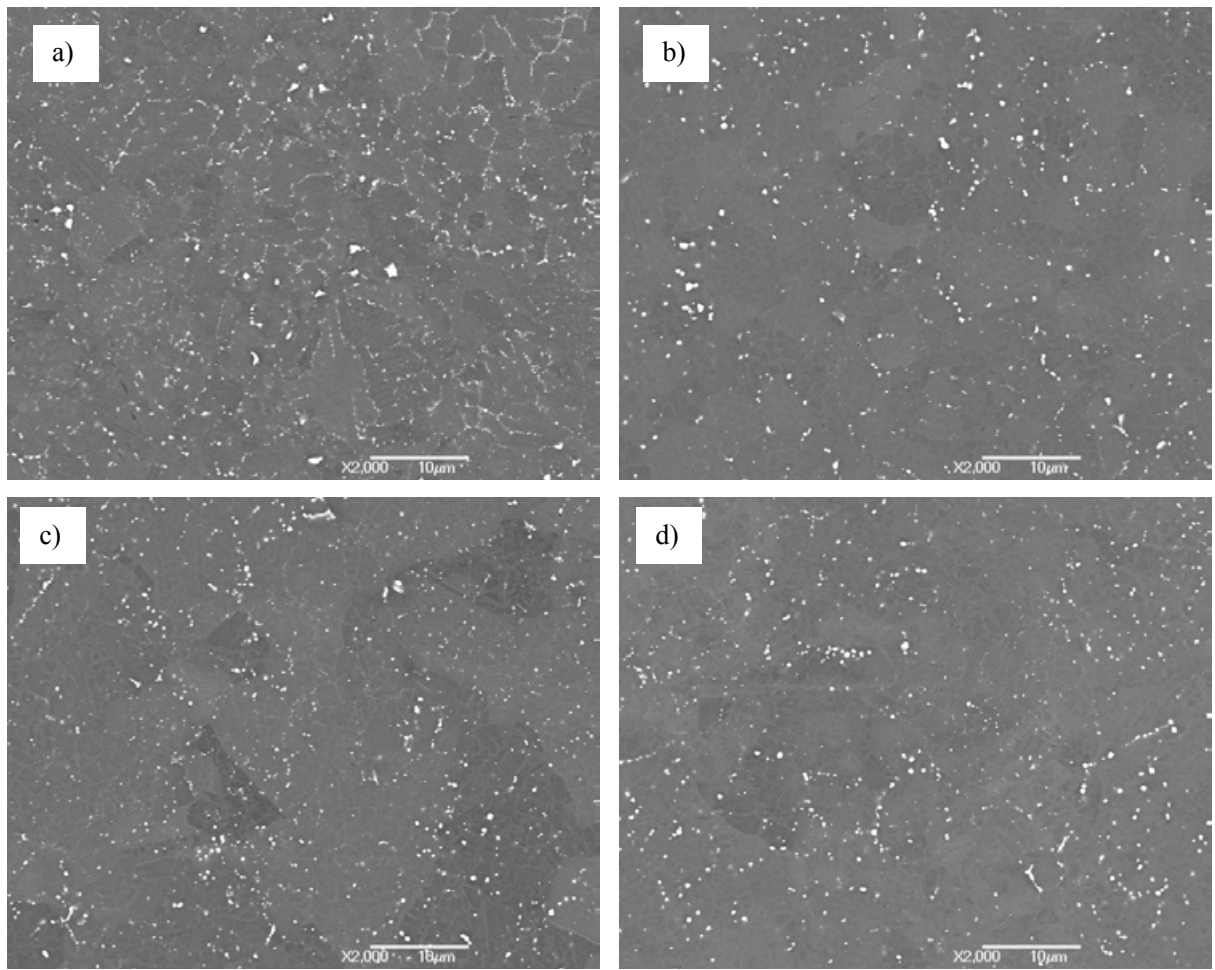


Fig. 4-18 Back scattered SEM images of carbide distribution in powder HIPped CM247LC

a) 1100 °C/150MPa/4h; b) 1200 °C/150MPa/4h;

c) 1260 °C/150MPa/2h; d) 1320 °C/150MPa/2h.

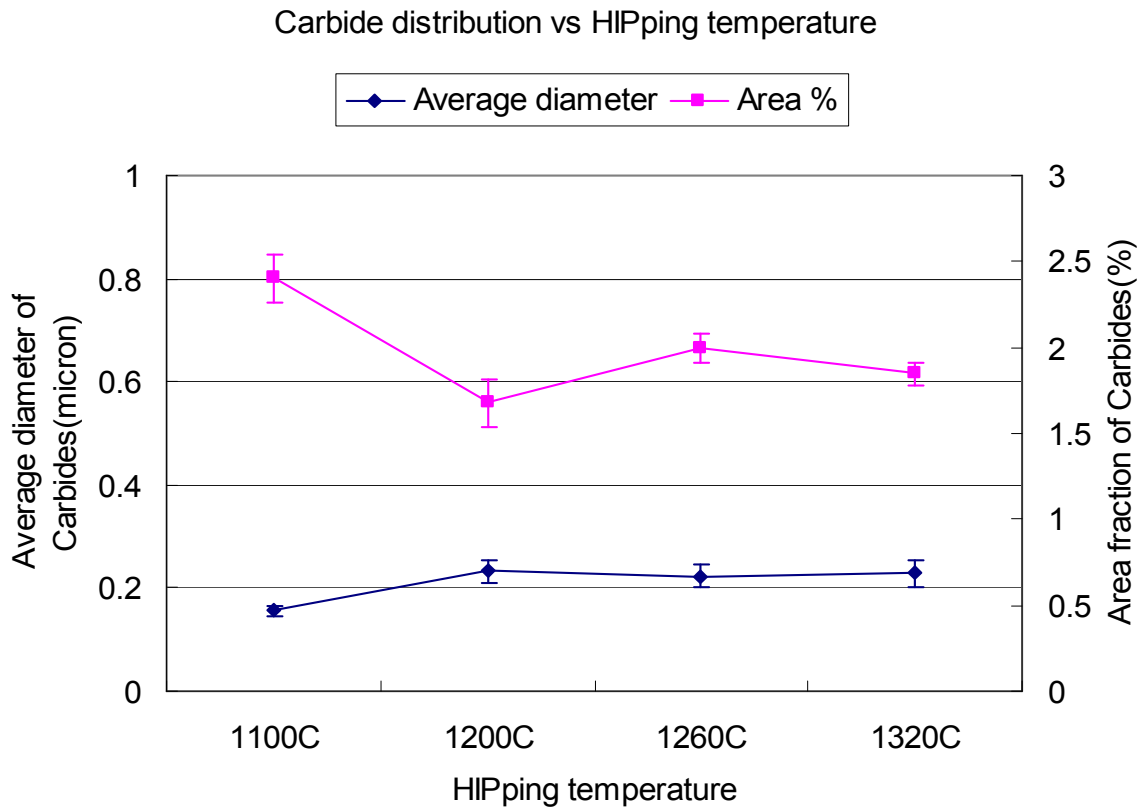


Fig. 4-19 The distribution of carbides in the as-HIPped CM247LC

4.2.1.5 Defects

Apart from carbides of size up to 1 μm , another type of ‘white’ inclusion which shows bright contrast in back scattered electron SEM images was observed for all HIPping conditions (see Fig. 4-20). They are script-like. The size of these particles ranges from 5 μm to $\sim 50 \mu\text{m}$. HIPping temperature does not have much effect on these particles. They look very much like the MC carbides in conventionally cast CM247LC and could degrade the mechanical properties of HIPped material. The identity and the influence of them on the properties of CM247LC will be discussed in detail later in § 4.4.

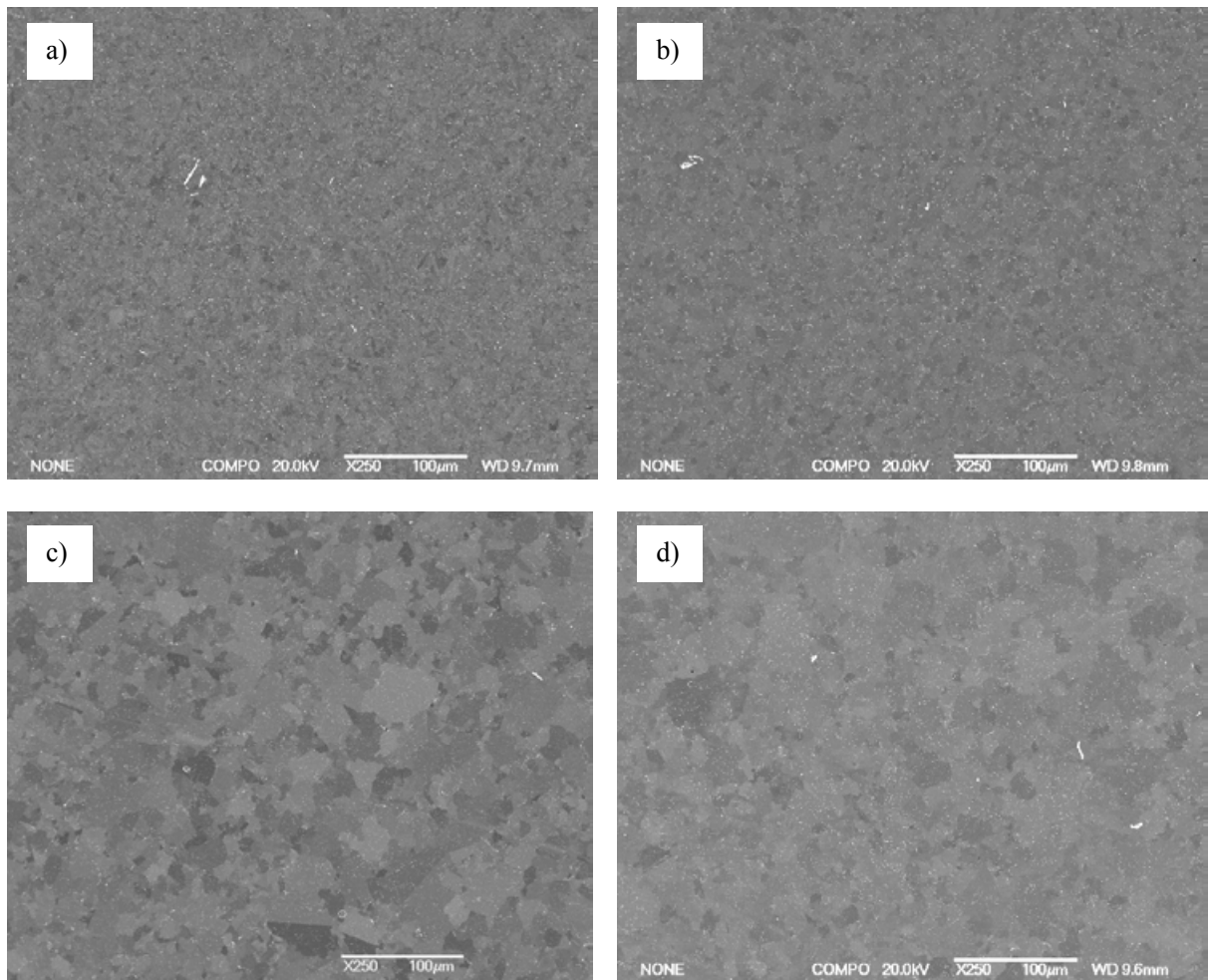


Fig.4-20 Backscattered electron SEM images of inclusions in as-HIPped CM247LC.

a) 1100C/150MPa/4h; b) 1200C/150MPa/4h;
c) 1260C/150MPa/2h; d) 1320C/150MPa/2h.

4.2.2 Mechanical properties of as-HIPped CM247LC

Hammer impact test were conducted on samples HIPped at 1100 °C and 1200 °C to obtain a quick indication of the fracture behaviour of the material HIPped below the γ' solvus. Tensile tests and tension-tension fatigue tests were conducted on samples HIPped at 1200 °C and 1260 °C. Samples as-HIPped at 1320 °C were not tested in this way because they have

similar microstructure to the samples HIPped at 1260 °C.

4.2.2.1 Hammer impact test

This test was carried out on as-HIPped samples which were HIPped at 1100 °C and 1200 °C at the early stage of the project. The fracture surface (Fig. 4-21 a)) of the 1100 °C as-HIPped sample shows dimples in the shape of original powder, while the 1200 °C sample shows transgranular fracture. The fact that cracks tend to propagate along prior powder boundaries in the sample HIPped at 1100 °C indicates that the bonding between powders at 1100 °C is incomplete whereas the powders HIPped at 1200 °C do not fracture along prior particle boundaries indicating good interparticle bonding.

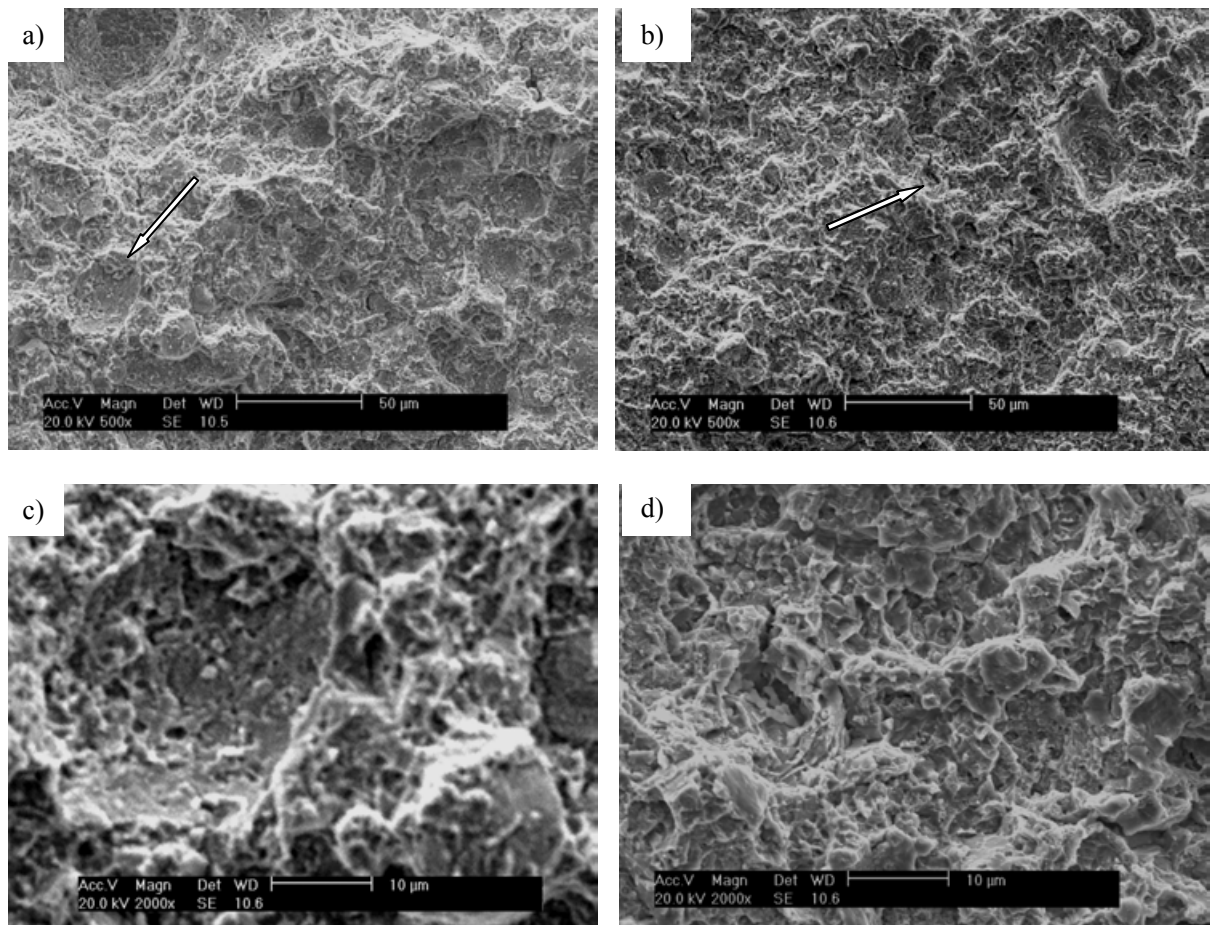


Fig. 4-21 Secondary electron SEM images of fracture surfaces of as-HIPped CM247LC by hammer impact.

a) HIPped at 1100 °C/150MPa/4h, arrow pointing at one of the dimples which indicates cracking from PPBs; b) 1200 °C/150MPa/4h. Ductile mode of fracture. c) and d) are magnified images of arrowed area in a) and b).

4.2.2.2 Tensile properties

1200 °C and 1260 °C as-HIPped samples were selected to undergo the standard tensile test; the test parameters are shown in Table 4-3. Three samples were tested at each temperature for each HIPping condition in order to obtain some indication of the repeatability of the

properties.

Table 4-3 Tensile test parameters of as-HIPped CM247LC

Test samples	as-HIP 1200 °C/150MPa/4h; as-HIP 1260 °C/150MPa/2h.
Test temperature	Room Temperature, 700 °C, 750 °C
Test piece	3 Plain & 3 notch ($K_t = 3.1$)
Test speed (strain-rate)	10^{-4}s^{-1}

The yield stress, tensile strength and total elongation to failure are shown in Table 4-4. The yield strengths of CM247LC under both HIPping conditions are not significantly affected by test temperature, while the tensile strength and ductility decrease with increase of test temperature. The samples HIPped at 1200 °C have yield strengths of the order of 860MPa over the three temperatures, about 60MPa higher than the values of samples HIPped at 1260 °C, while the ductility over the temperature range is inferior. The tensile strengths of CM247LC under the both HIPping conditions are similar over the tested temperature range.

Table 4-4 Tensile properties of as-HIPped CM247LC

Material		As-HIP 1200 °C/150MPa/4h			As-HIP 1260 °C/150MPa/2h		
Temperature (°C)		0.2%PS (MPa)	UTS (MPa)	Elong (%)	0.2%PS (MPa)	UTS (MPa)	Elong (%)
Room Temperature	Data points	860	1432	15.6	783	1436	22.1
		852	1488	19.0	790	1468	23.3
					796	1413	20.3
	Average	856	1460	17.3	790	1439	22.0
	Stdev	5	28	1.7	7	28	1.5
700	Data points	852	1157	12.4	795	1210	27.7
		782	1083	14.1	798	1154	21.8
		832	1145	14.4	796	1143	20.9
	Average	822	1128	13.6	793	1169	21.5
	Stdev	36	40	1.1	6	36	0.5
750	Data points	860	1090	9.5	795	1072	12.4
		871	1098	9.6	797	1078	12.4
		856	1106	12.5	801	1086	13.5
	Average	862	1098	10.5	798	1079	12.8
	Stdev	8	8	1.7	3	7	0.6

Notched tensile samples of HIPped CM247LC have higher tensile strengths than the plain samples as shown in Table 4-5. The NSR values calculated using the equation in Appendix 1 are also shown in Table 4-5. The samples HIPped under both conditions have similar values of the order of unity when tested at room temperature. They both increased in value when tested at 700 °C and 750 °C with 1200 °C HIPped samples demonstrating better notch ductility; its NSR values are 1.42 and 1.41 relative to 1.33 and 1.36 for the 1260 °C as-HIPped ones.

Table 4-5 Notch tensile properties of as-HIPped CM247LC, Kt=3.1

Material		As-HIP 1200 °C/150MPa/4h			As-HIP 1260 °C/150MPa/2h		
Temperature (°C)		Notch UTS (MPa)	Plain UTS (MPa)	NSR	Notch UTS (MPa)	Plain UTS (MPa)	NSR
Room Temperature	Data points	1553	1432	1.01	1459	1436	1.02
		1597	1488		1477	1468	
		1572	1157		1455	1413	
	Average	1574	1460		1464	1439	
	Stdev	22	28	12	28		
700	Data points	1583	1083	1.42	1552	1210	1.33
		1639	1145		1573	1154	
		1581	1090		1550	1143	
	Average	1601	1128		1558	1169	
	Stdev	33	40	13	36		
750	Data points	1528	1098	1.41	1456	1072	1.36
		1576	1106		1483	1078	
						1086	
	Average	1552	1098		1470	1079	
	Stdev	34	8	19	7		

The fracture surfaces of the tensile specimens were examined and showed similar features in samples HIPped at both temperatures. The fracture surfaces consist of a radial zone and shear lip zones. Radial lines converge to a point near the sample edges (Fig. 4-22 a), c), e) and Fig. 4-23 a), c), e)) indicating that the failure of all the samples was initiated near the sample surfaces. Images in views of the Fig. 4-22 b), d), e) and Fig. 4-23 b), d), e) are enlarged initiation sites on fracture surfaces. Inclusions over 30 µm in size could always be found in clusters perpendicular to the stress direction. Sometimes only part of inclusions remains in the site as in Fig. 4-22 d) and other parts could be on the other half. It appears that the crack may have been initiated by the inclusions cracking or de-bonding. The composition of the inclusions were analysed by EDS. The inclusions are mainly rich in hafnium and

oxygen (see Table 4-6), and their molar ratio is about 1: 2.

The propagation paths (radial zones) were examined and examples are shown in Fig. 4-24. The crack propagation is mostly along the prior powder boundaries in samples HIPped at 1200 °C, with single powder particles visible (see Fig. 4-24 a) and c) together with ductile dimples. The samples failed along PPBs. The propagation paths in samples HIPped at 1260 °C look ductile with no obvious de-bonding along prior powder boundaries; dimples are deeper and more frequent.

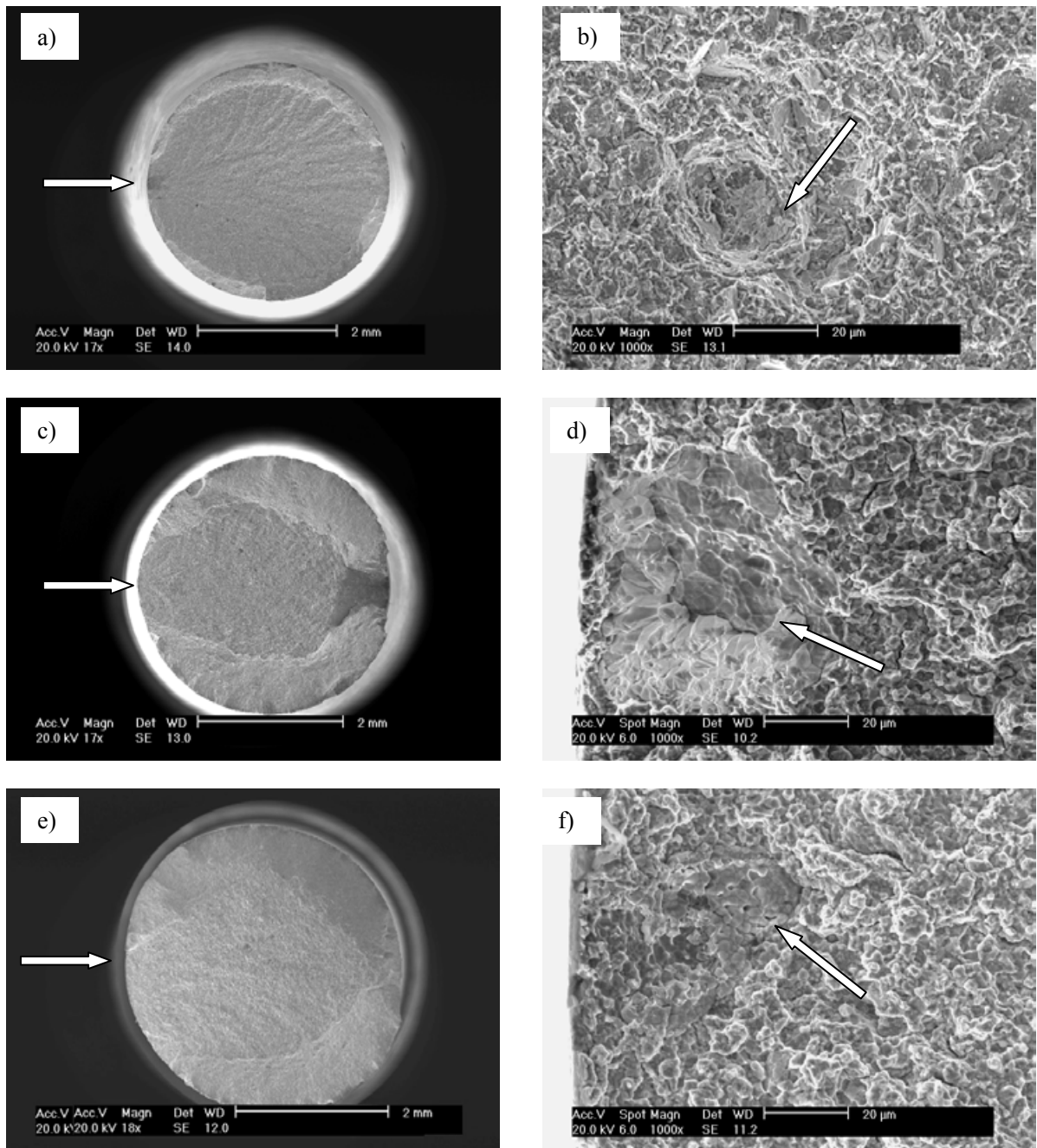


Fig.4-22 Secondary electron SEM images of fracture surfaces of failed tensile samples which had been HIPped at 1200 °C/150MPa/4h, tested a) & b) at room temperature; c) & d) at 700 °C; e) & f) at 750 °C. Arrows in a), c), e) indicate initiation sites; arrows in b), d), f) indicate inclusions.

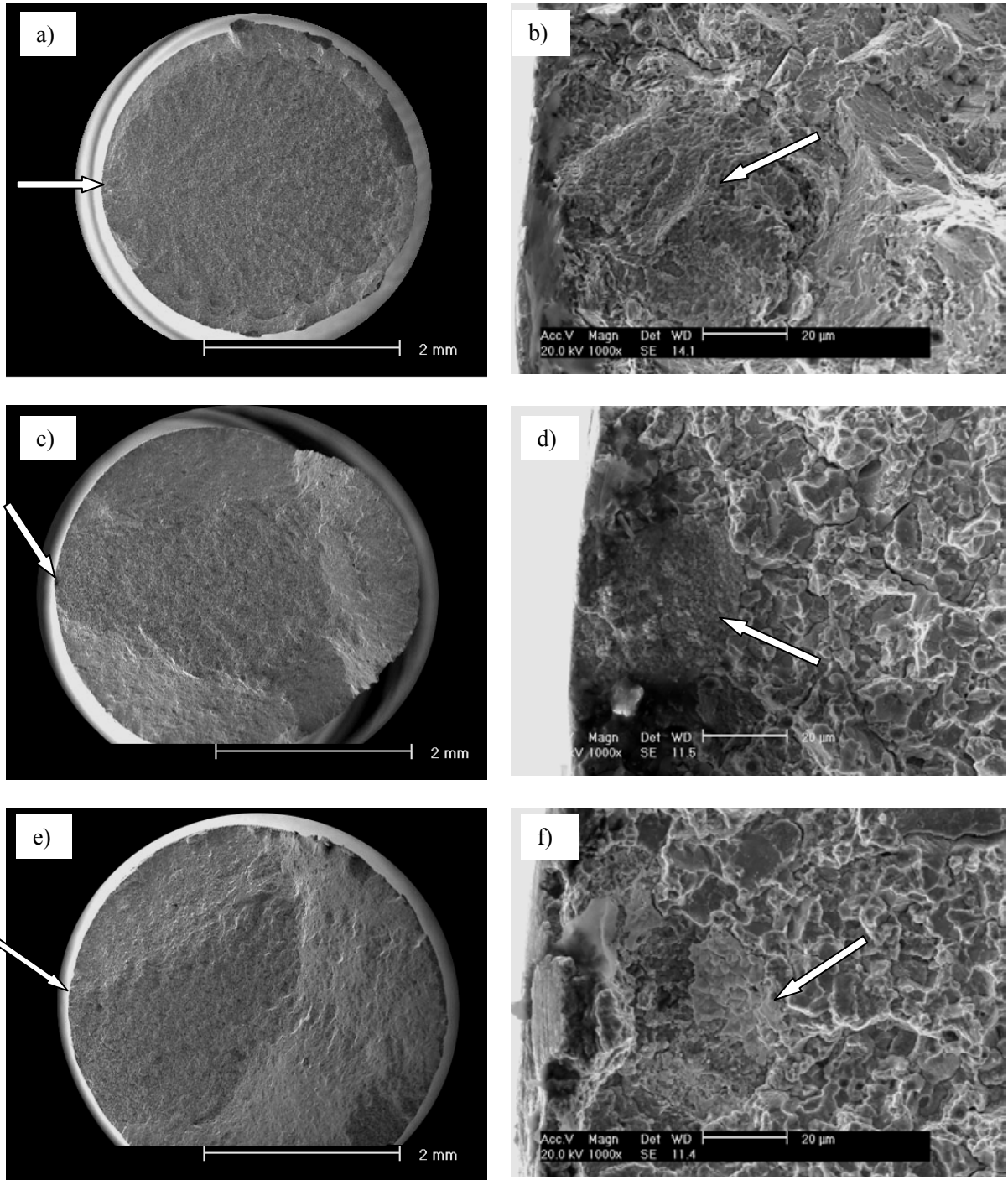


Fig.4-23 Secondary electron SEM images of fracture surfaces of failed tensile samples HIPped at 1260 °C/150MPa/2h tested a) & b) at room temperature; c) & d) at 700 °C; e) & f) at 750 °C. Arrows in a), c), e) indicate initiation sites; arrows in b), d), f) indicate inclusions.

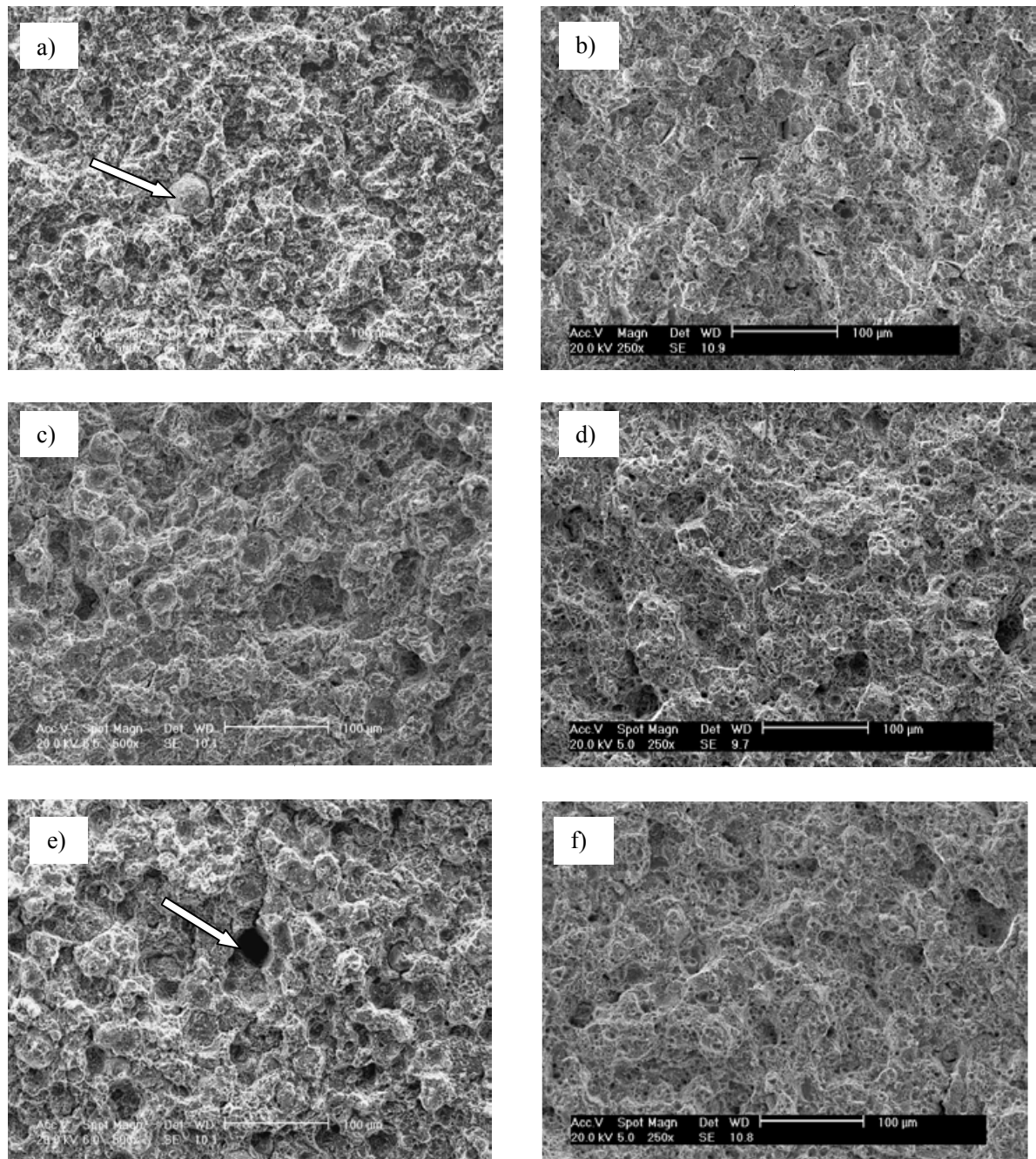


Fig. 4-24 Secondary electron SEM images of radial zones on tensile failed fracture surface. a), c), e) are samples HIPped at 1200 °C/150MPa/4h; b), d), f) are samples HIPped at 1260 °C/150MPa/2h; a),b) tested at room temperature; c), d) tested at 700 °C; e), f) tested at 750 °C. Arrows are pointing at the prior particles or the position where prior particles were present.

Table 4-6 Composition of inclusions at initiation sites

Element	Weight %	Atom %
O	19.4 ± 0.4	70
Cr	0.6 ± 0.1	0.7
Co	1.0 ± 0.1	1
Ni	5.1 ± 0.2	5.0
Hf	74.0 ± 0.5	23.9

4.2.2.3 High cycle tension-tension fatigue properties

High cycle tension-tension fatigue tests were carried out at room temperature and 750 °C on 1200 °C and 1260 °C as-HIPped CM247LC. For the plain samples, the fatigue limits are comparable between the two HIPping conditions. As shown in table 4-7, they have fatigue limits of 760MPa and 770MPa at room temperature, which are as high as 89% and 97% of their 0.2% proof strength. The fatigue limits are 650 MPa and 700 MPa at 750 °C, which are 75% and 88% of their 0.2% proof strength at the same temperature.

Notch fatigue was only conducted on 1260 °C HIPped samples to look at the notch sensitivity of the material. The notch limits of the 1260 °C as-HIPped samples are shown in Table 4-7 from which it can be seen that the fatigue limits are far lower than the plain ones at both room temperature and 750 °C. Full data of all the samples are plotted in Fig. 4-25 with notch fatigue values in the form of $K_t\sigma_n$. In Fig. 4-25 a), the notched fatigue data points almost overlap with the plain ones showing that the material is fully notch sensitive at room temperature. Surprisingly, the notched data points are higher than the plain ones when the tests are carried out at 750 °C (see Fig. 4-25 b)). This means the material gains some strength to resist the harm introduced by the notch at higher temperature (See appendix 1).

Table 4-7 fatigue limit of as-HIPped CM247LC

Temperature	HIPped at 1200 °C/150MPa/4h	HIPped at 1260 °C/150MPa/2h	HIPped at 1260 °C/150MPa/2h Notch, $K_t = 2.26$
Room Temperature	760MPa	770MPa	325MPa
750 °C	650MPa	700MPa	475MPa

Fracture surfaces are shown in Fig. 4-26 and Fig. 4-27. Inclusion clusters of about 30 μm diameter which are surrounded by facets are seen on the sample surface in both as-HIPped batches tested at room temperature, suggesting that fractures initiate at inclusions near the sample surface. In the samples tested at 750 °C, a rounded ‘river pattern’ zone was always found in every fracture surface. The edges of the zones are tangential to the sample surfaces. Inclusion clusters in size of about 30 μm can also be found in the centre of the initiation site. The EDS analysis of the inclusions shows similar result as in Table 4-6. The inclusions at the fatigue initiation sites are Hf rich oxides.

The presence of facets is consistent with the fact that the fatigue limits of the samples are lower than yield strength which is explained in next chapter. It was found that the alloys which do not give facets easily tend to have fatigue limits near the yield strength, whereas alloys in which facets are common have fatigue limits well below the yield strength [Price *et al.* 1986].

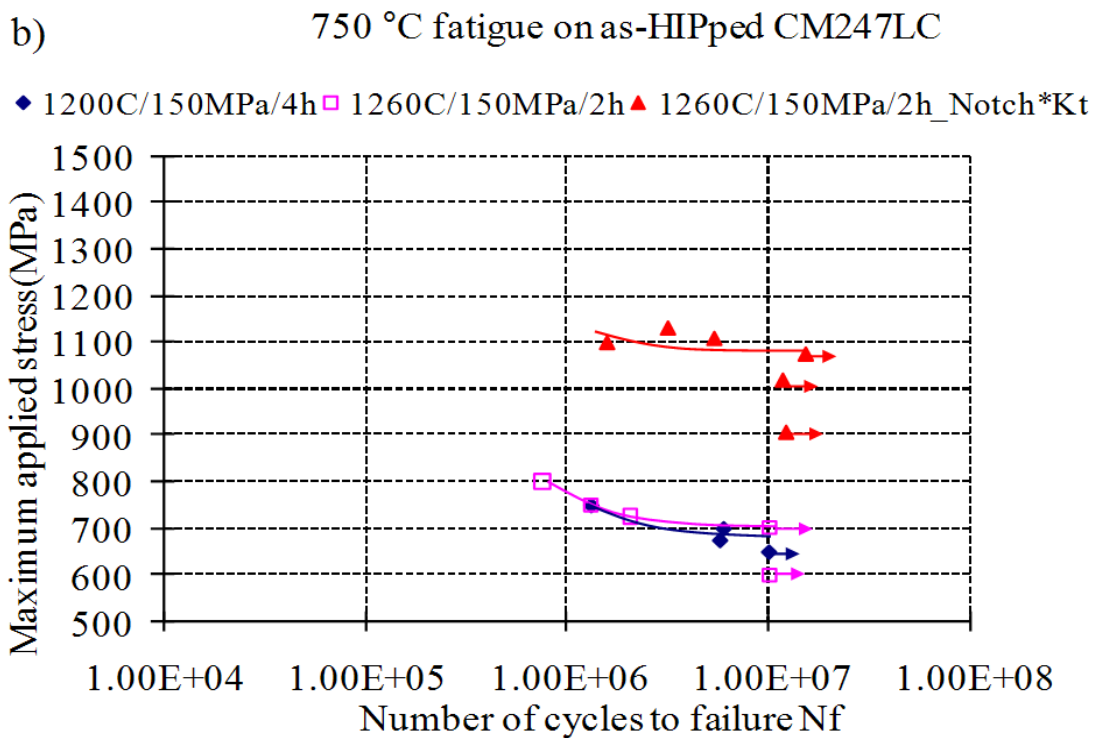
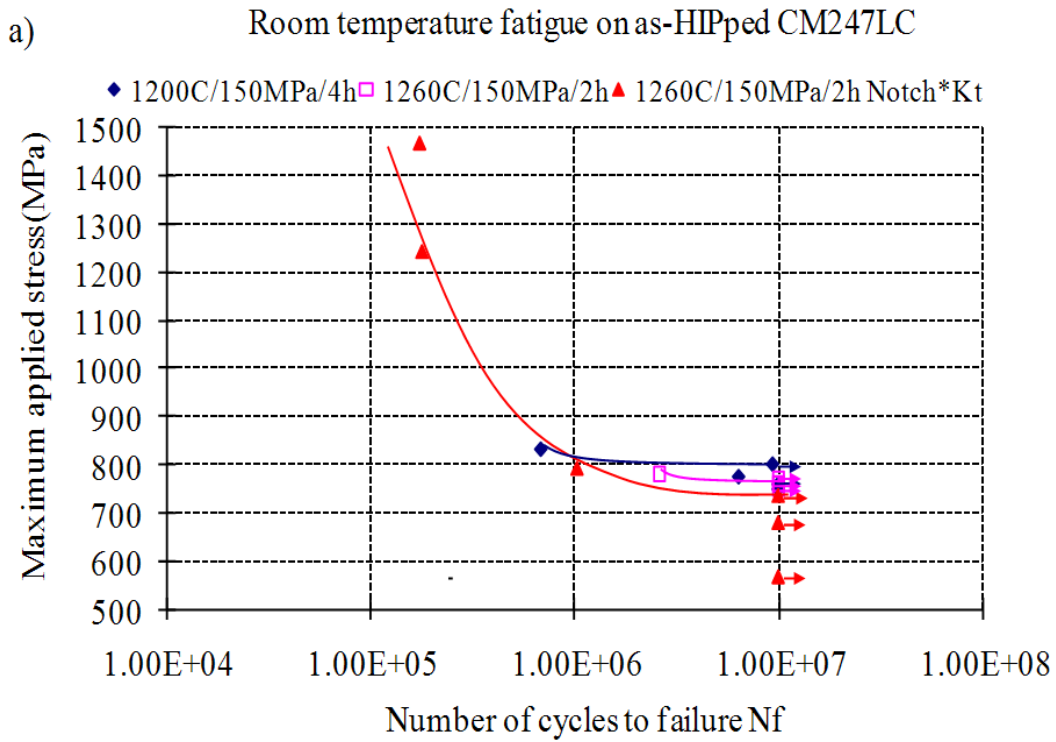


Fig. 4-25 Tension-tension fatigue of as-HIPped CM247LC.

a) Tested at room temperature; b) tested at 750 °C.

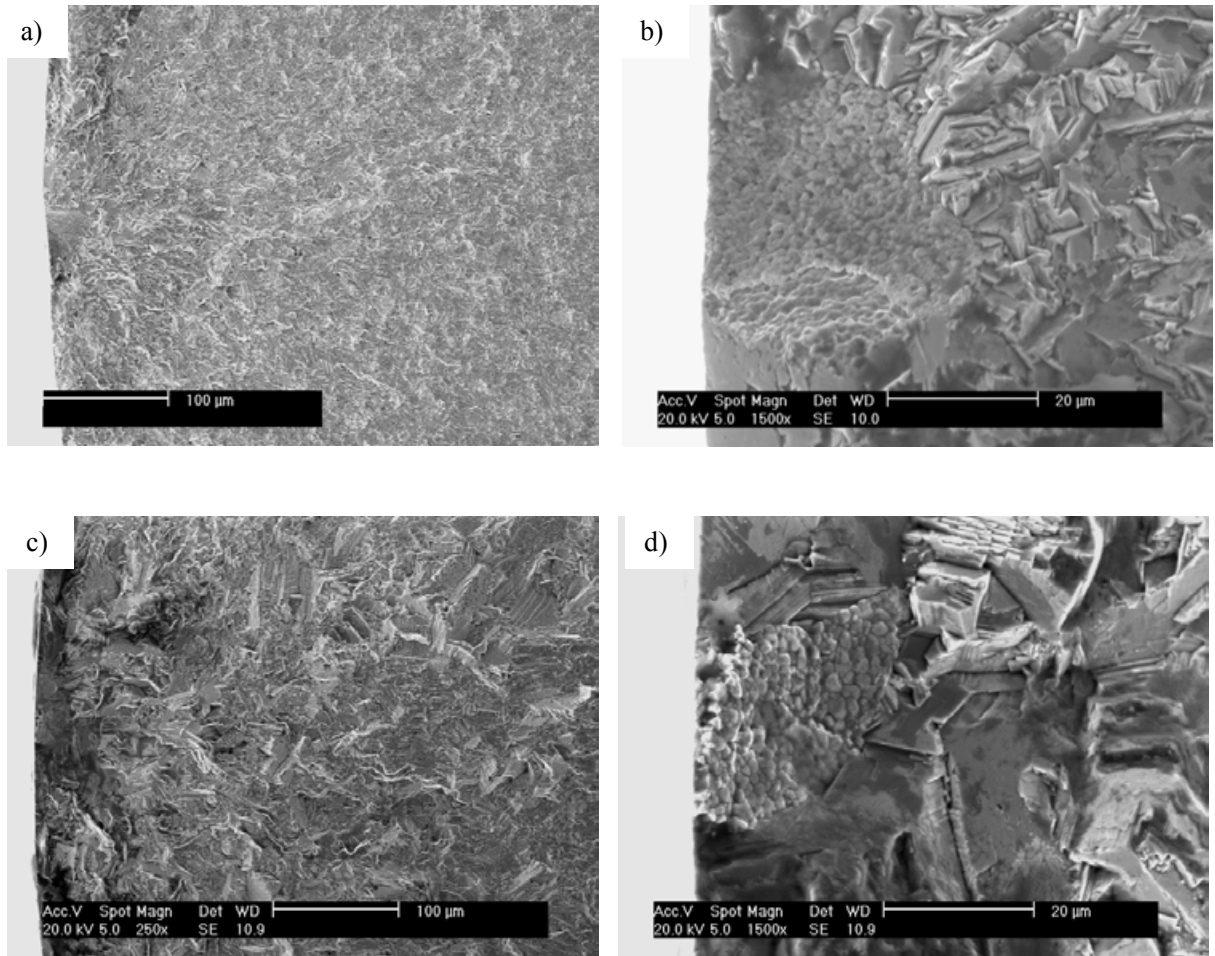


Fig.4-26 Secondary electron SEM images of fracture surface of tension-tension fatigue specimens tested at room temperature.

a), b) HIPped at 1200 °C/150MPa/4h, failed at 672900 cycles at 830MPa;

c), d) HIPped at 1260 °C/150MPa/2h, failed at 2610100 cycles at 780MPa.

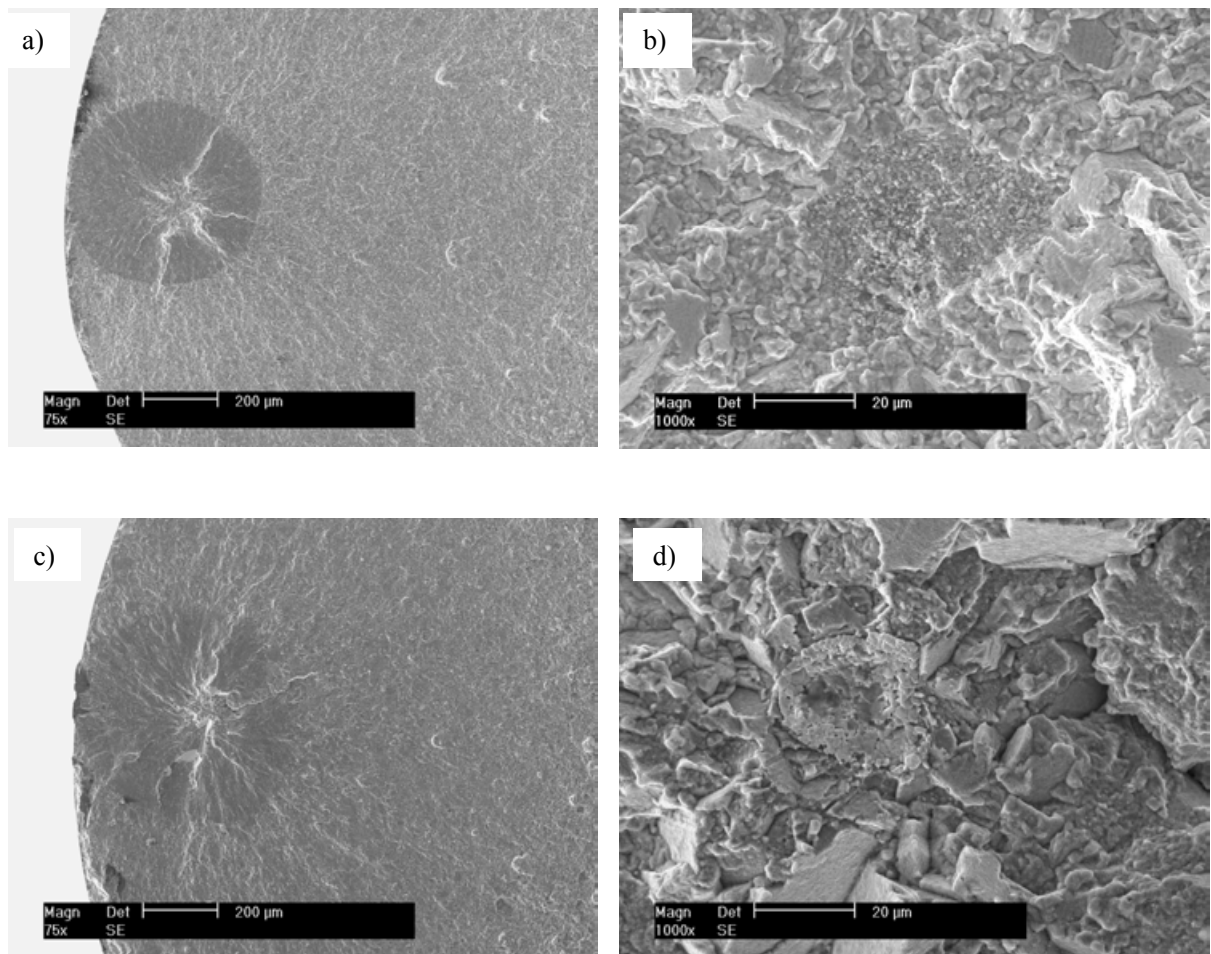


Fig.4-27 Secondary electron SEM images of fracture surface of tension-tension fatigue specimens tested at 750 °C.

a), b) HIPped at 1200 °C/150MPa/4h, failed at 5955800 cycles at 700MPa;

c), d) HIPped at 1260 °C/150MPa/2h, failed at 2038500 cycles at 725MPa.

4.2.3 Summary

Microstructure

- When CM247LC is HIPped above the γ' solvus the following microstructural changes

occur: Significant grain growth occurs; cubic γ' is formed rather than dendritic; coarse γ' forms at grain boundaries while coarse γ' forms at previous powder boundaries when HIPped below the solvus;

- Random globular particles of size up to 1 μm are found which are carbides, rich in Ta and Hf, the distribution of which does not change when HIPped above 1200 °C;
- Inclusions of size from 5 μm to ~50 μm are found in samples HIPped under all conditions. They are oxides rich in Hf.

Tensile tests

- The 0.2% proof strength and UTS are comparable for the two HIPping conditions, 1260 °C/150MPa/2h and 1200 °C/150MPa/4h while the 1260°C sample is more ductile than the 1200°C samples;
- Inclusions of over 20 μm are found in almost all initiation sites at all test temperatures;
- The 1260 °C/150MPa/2h as-HIPped CM247LC is notch ductile.

Fatigue

- At room temperature, the fatigue limits are comparable for the two HIPping conditions, of the order of 770MPa. Fatigue initiated at inclusions of about 30 μm in size at the sample surfaces;
- At 750 °C, the fatigue limits are 650MPa and 700MPa for the 1200 °C and 1260 °C as-HIPped samples. Fatigue is initiated at inclusions of about 30 μm in size near the sample surface;
- 1260 °C as-HIPped CM247LC is notch sensitive at room temperature and notch insensitive at 750 °C.

4.3 Microstructure and properties of HIP+Solution-treated+Aged CM247LC

Based on the previous section, HIPping conditions of 1260 °C at 150MPa for 2 hours were selected to investigate the influence of post-HIP treatments on the HIPped CM247LC. The as-HIPped CM247LC was solution heat treated at 1100 °C, 1200 °C and 1260 °C for 1 hour followed by forced air cooling. Primary γ' was expected to be dissolved to increasing extents as the solution temperatures were increased from below to above the solvus. All the samples were aged at 870 °C for 16 hours after solution treatment.

4.3.1 Microstructure of HIP+Solution-treated+Aged CM247LC

The microstructure of HIP + Solution-treated + Aged CM247LC, will be discussed with reference to the following aspects: grain boundary morphology, grain size, γ' morphology, carbides and defects for different solution-treatment temperatures. HIPped + Aged specimens were also examined.

4.3.1.1 Grain boundaries

The grain boundary structure of the HIP + Aged specimen shown in Fig.4-28 a) is similar to the as-HIPped sample, with coarse γ' on the grain boundaries and relatively finer γ' in grain interiors. Solution-treatment before ageing at 1100 °C for 1 hour does not change this character very much (see Fig. 4-28 b)). The amount of necklace structure along grain boundaries was reduced by certain percentage, but it was still conspicuous. The solution-treatment at 1200 °C significantly reduces the amount of γ' , but there is still some coarse γ' along grain boundaries and prior powder boundaries. When the solution temperature is above the γ' solvus at 1260 °C, no primary γ' remains.

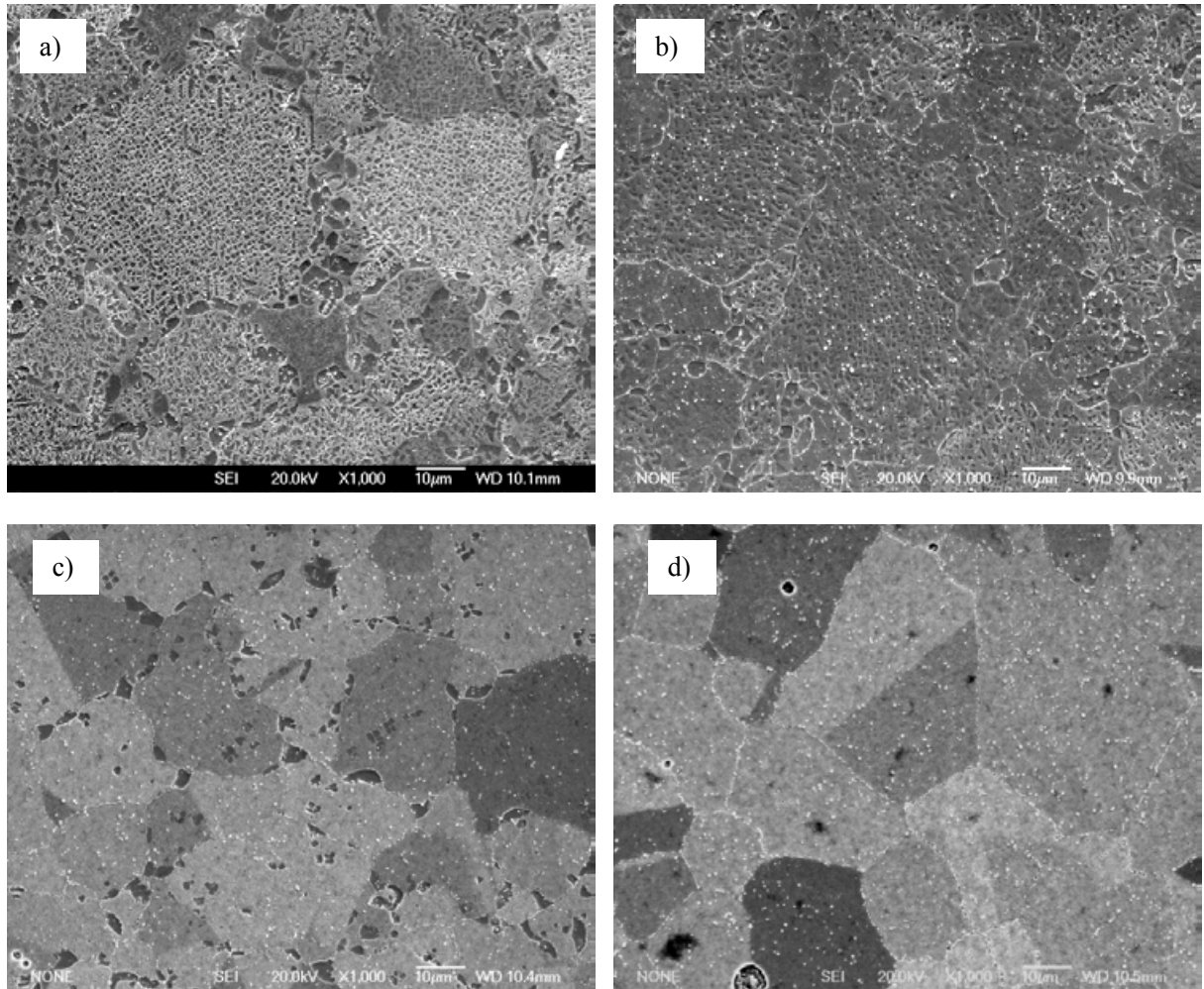


Fig. 4-28 Grain boundary morphology of HIPped + heat treated CM247LC.

a) HIPped at 1260 °C/150MPa/2h + Aged at 870 °C/16h/FC;

b) HIPped at 1260 °C/150MPa/2h + Solutioned at 1100 °C/1h/FAC+Aged at 870 °C/16h/FC;

c) HIPped at 1260 °C/150MPa/2h + Solutioned at 1200 °C/1h/FAC +Aged at 870 °C/16h/FC;

d) HIPped at 1260 °C/150MPa/2h + Solutioned at 1260 °C/1h/FAC+Aged at 870 °C/16h/FC;

4.3.1.2 Grain Size

The grain size was measured using the technique described in §4.2.1.3. The results are shown in Fig. 4-29. The average grain size of the HIPped + aged CM247LC is around 16 μm - close to the as-HIPped result (17 μm). Little grain growth was observed when solution-treated at 1100 °C and 1200 °C, with average sizes of around 18 μm , but solution-treatment at 1200 °C gives a larger range of distribution with a largest grain size of 60 μm , 10 μm larger than the maximum value in the sample treated at 1100 °C. Grains grow significantly when solution-treated at 1260 °C; the average value is 30 μm with a maximum value of 77 μm . This trend of change in grain size and distribution can be explained in terms of the depletion of γ' from grain boundaries, which is the main barrier for boundary migration. The grain boundaries became straight after 1260 °C solution treatment, because of the absence of coarse γ' particles (see Fig. 4-28 d)).

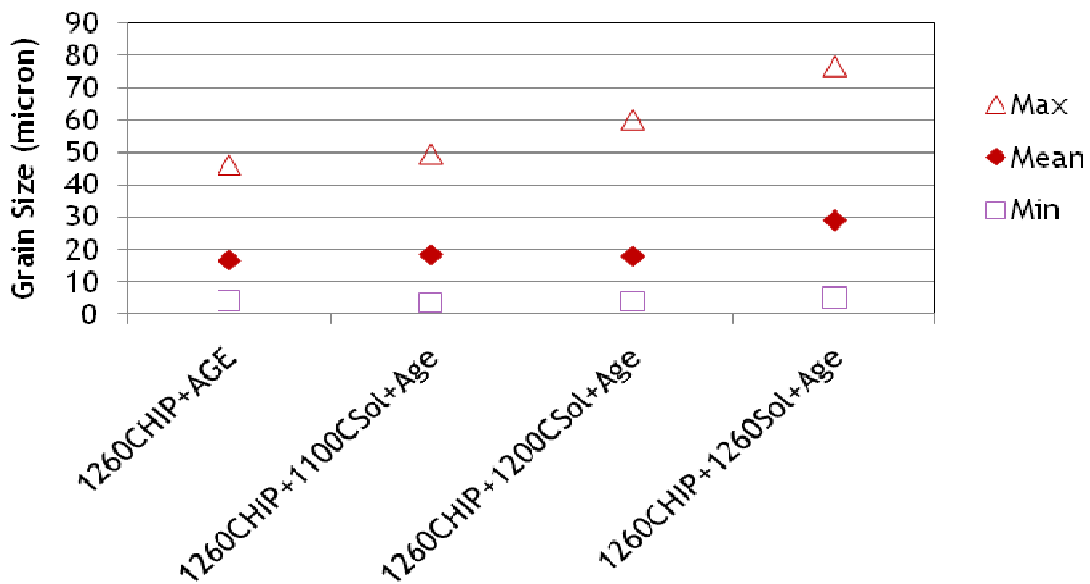


Fig. 4-29 Influence of heat treatment on grain size.

4.3.1.3 Gamma prime γ'

The morphology of γ' in the HIP + aged specimen does not change much from the as-HIPped sample. The cubic γ' formed during cooling from HIPping still remains, while a few extra fine γ' are observed in the γ channels (as shown in Fig. 4-30 a)). It is hard to say whether this fine γ' formed during aging because such fine precipitates are also observed in as-HIPped CM247LC. Fig. 4-30 b) shows a bimodal distribution of γ' , with cubic γ' up to 1 μm which is surrounded by a γ matrix, uniformly populated with nano-sized γ' . The channels between γ' are larger than in the un-aged sample and the corners of the larger γ' are rounded. The rounded γ' surrounded by ultra fine γ' structure is formed by the primary γ' partly dissolving into the matrix during the 1100 °C solution treatment. The aging process enables the nuclei formed during forced air cooling to grow in the matrix channels. Fig. 4-30 c) shows a cluster of γ' the corners of which are more rounded than those in Fig. 4-30 b) and which are bigger, because they are at prior powder boundaries where diffusion is faster. The surrounding matrix is populated by fine γ' that is much larger than those in Fig. 4-30 b). This is because most of the γ' in as-HIPped material dissolved during 1200 °C solution-treatment, providing wider γ channels for the γ' nuclei formed during forced air cooling to grow during aging. The shapes of the aging γ' particles are somewhere between cubic and spherical. Uniform fine γ' particles occupy the whole sample when solution-treated at 1260 °C and these have a similar shape to those solution-treated at 1200°C (Fig. 4-30 c). They are about 0.3 μm . No prior γ' particles remain (Fig. 4-30 d))

The volume fraction of γ' was measured to be 62% as shown in Fig. 4-31. The amount of γ' may fluctuate slightly with increasing solution temperature, but the measured change is within the error range.

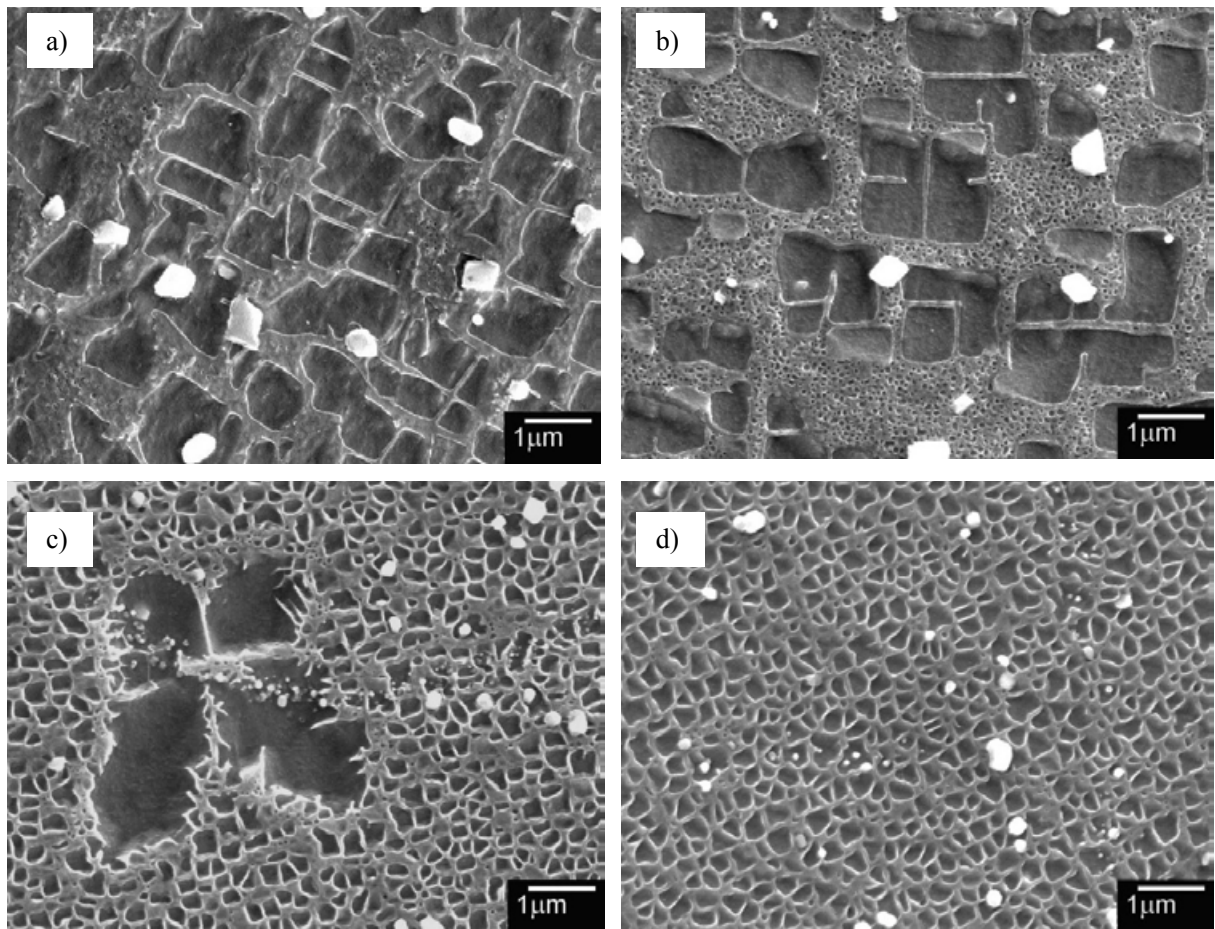


Fig. 4-30 Secondary electron SEM images of γ' morphology of HIPped + heat treated CM247LC

a) HIPped at 1260 °C/150MPa/2h + Aged at 870 °C/FC;

b) HIPped at 1260 °C/150MPa/2h +Solutioned at 1100 °C/1h/FAC+Aged at 870 °C/16h/FC;

c) HIPped at 1260 °C/150MPa/2h + Solutioned at 1200 °C/1h/FAC+Aged at 870 °C/16h/FC;

d) HIPped at 1260 °C/150MPa/2h +Solutioned at 1260 °C/1h/FAC+Aged at 870 °C/16h/FC;

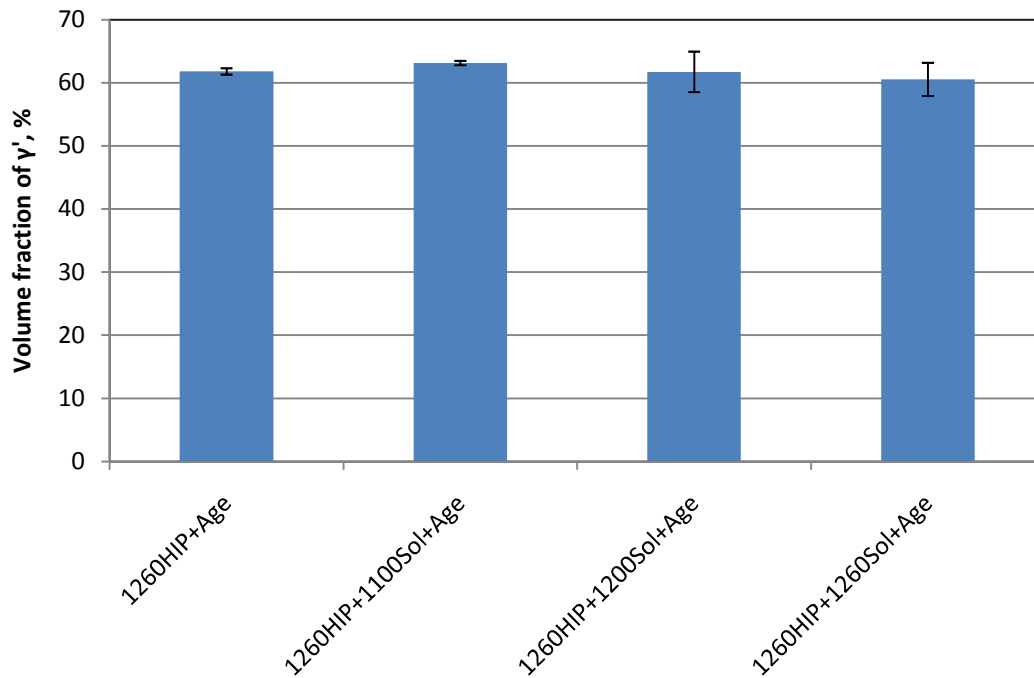


Fig.4-31 Volume fraction of γ' after different solution heat treatments

As described in Chapter 3 the influence of cooling rate from the solution temperature on the γ' size was studied via Jominy tests. An as-HIPped bar was heated to 1260 °C and held at temperature for 1 hour before being Jominy quenched and the temperatures along the bar were monitored (see Jominy curve T(t) in Appendix 2) so that the cooling rates between 900 °C and 1260 °C could be calculated. The bar was aged at 870 °C for 16 hours and the microstructure along the bar is shown in Fig. 4-32. The data of γ' particle size and cooling rate is shown in Fig. 4-33. The dependence of the two parameters fit the power law

$$\log(D_{\gamma'}) = 0.042 \log\left(\frac{dT}{dt}\right), \quad R^2 = 0.974$$

In which $D_{\gamma'}$ is in microns, dT/dt is in °C/s. (R^2 is a number from 0 to 1 that reveals how closely the estimated values for the equation correspond to the experimental data.) This

relation also agrees well with the HIP + aged sample. The size of γ' was $\sim 0.9 \mu\text{m}$, which was formed at a cooling rate of $5 \text{ }^\circ\text{C}/\text{min}$ from $1260 \text{ }^\circ\text{C}$.

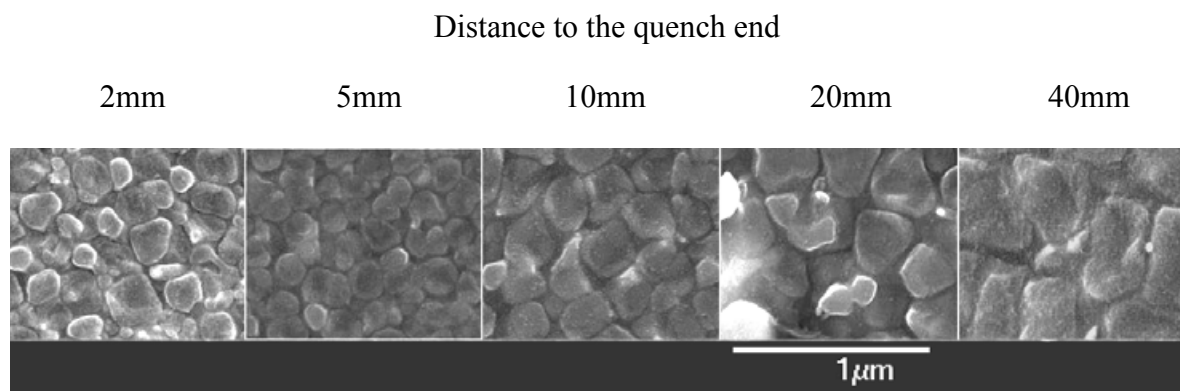


Fig. 4-32 Secondary electron SEM images of etched samples showing the morphology of γ' along the Jominy bar.

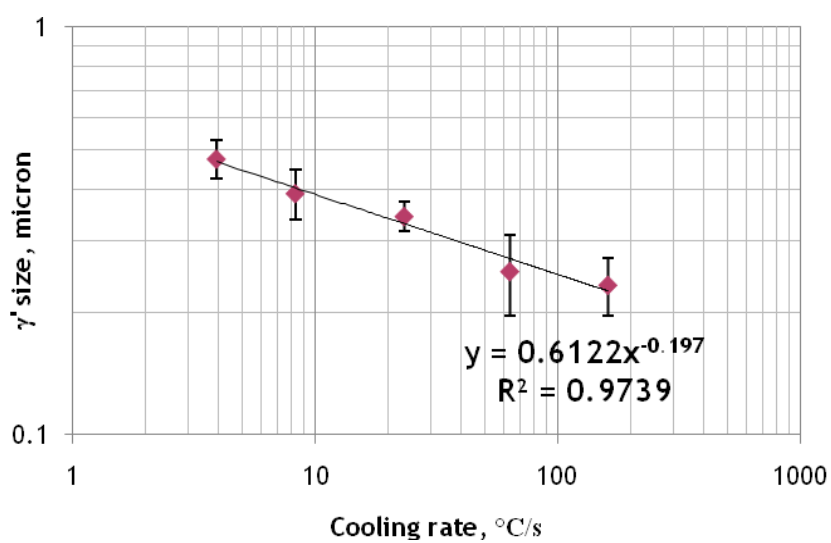


Fig. 4-33 Relationship of γ' size and cooling rate between $1260 \text{ }^\circ\text{C}$ and $900 \text{ }^\circ\text{C}$

4.3.1.4 Carbides

There are two main purposes of solution heat treatment; one is to modify the morphology of the γ' , the other is to modify the morphology of the carbides. It is reported [Sims, Stoloff *et al.* 1987] that after certain heat treatments, the MC carbides will decompose and $M_{23}C_6$ carbides (rich in Cr) will form at grain boundaries; these strengthen or weaken the grain boundaries depending on their morphology. Because of the compositional constitution, M_6C carbides (rich in Mo) are not likely to form in CM247LC [Harris, Ericson *et al.* 1982]. Fig. 4-34 shows the carbides in the heat treated CM247LC (see Fig. 4-30) which are the same shape as those in the as-HIPped samples (see Fig. 4-16 c)) and are evenly distributed over the entire sample bulk with no preference for the grain boundaries. The size and volume fraction of the carbides were measured to see if there is any influence of the solution temperature. The mean diameters of carbides (shown in Fig. 4-35 a)) do not vary for the different solution temperatures. The volume fraction of carbides (shown in Fig. 4-35 b)) decreases as the solution temperature increases. This could be an indication that some of them may break down during the solution treatment and $M_{23}C_6$ carbides formed. These would be difficult to observe in the back-scattered images as they are rich in Cr which gives a contrast close to the matrix.

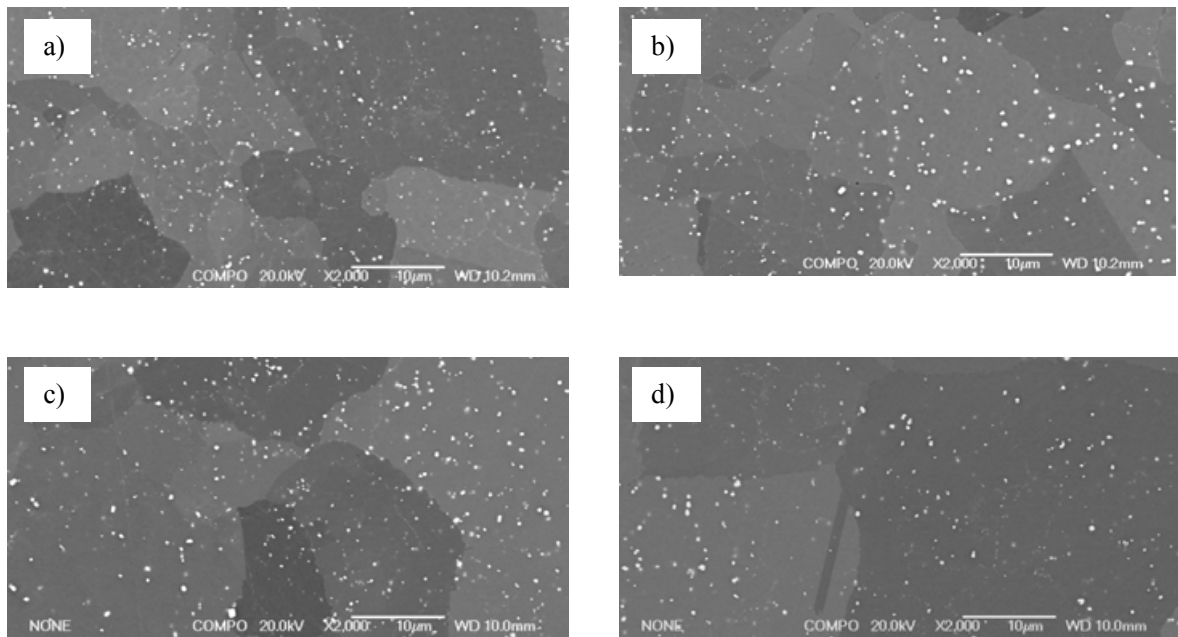


Fig.4-34 Back scattered SEM images showing the distribution of carbides in HIPped and heat treated CM247LC

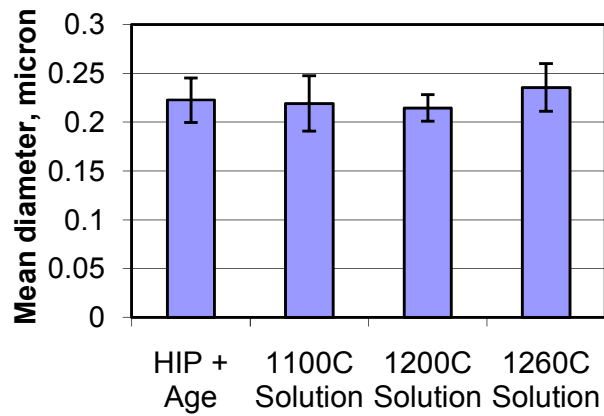
a) HIPped at 1260 °C/150MPa/2h + Aged at 870 °C/16h/FC;

b)HIPped at 1260 °C/150MPa/2h +Solutioned at 1100 °C/1h/FAC +Aged at 870 °C/16h/FC;

c)HIPped at 1260 °C/150MPa/2h +Solutioned at 1200 °C/1h/FAC +Aged at 870 °C/16h/FC;

d)HIPped at 1260 °C/150MPa/2h +Solutioned at 1260 °C/1h/FAC +Aged at 870 °C/16h/FC;

a)



b)

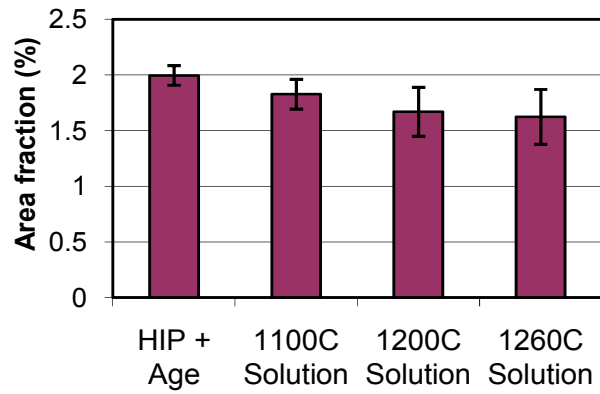


Fig. 4-35 Distribution of carbides in HIP and heat treated CM247LC (error bars stand for standard deviations of measured data).

a) Mean diameter of carbides at different solution temperatures;

b) Area fraction of carbides at different solution temperatures.

4.3.1.4 Defects

The inclusions found in as-HIPped specimens were still present in the heat treated ones. This issue will be discussed later in §4.4.

The other point to be noted is that pores are found in solution heat treated samples. There are hardly any pores in the HIP and aged samples, but as the solution temperature increases (From Fig. 4-36 a) to d)), the pores become more obvious. The pores could reach 20 μm in diameter, as shown in Fig. 4-36 d) when solution-treated above the γ' solvus at 1260 °C. These pores could be the result of the hollow powder particles that contain argon found in raw powder which are closed under the HIPping pressure. They would be expected to expand when the force associated with the expansion of the trapped argon exceeds the creep stress of the alloy under the solution temperature according to creep mechanism.

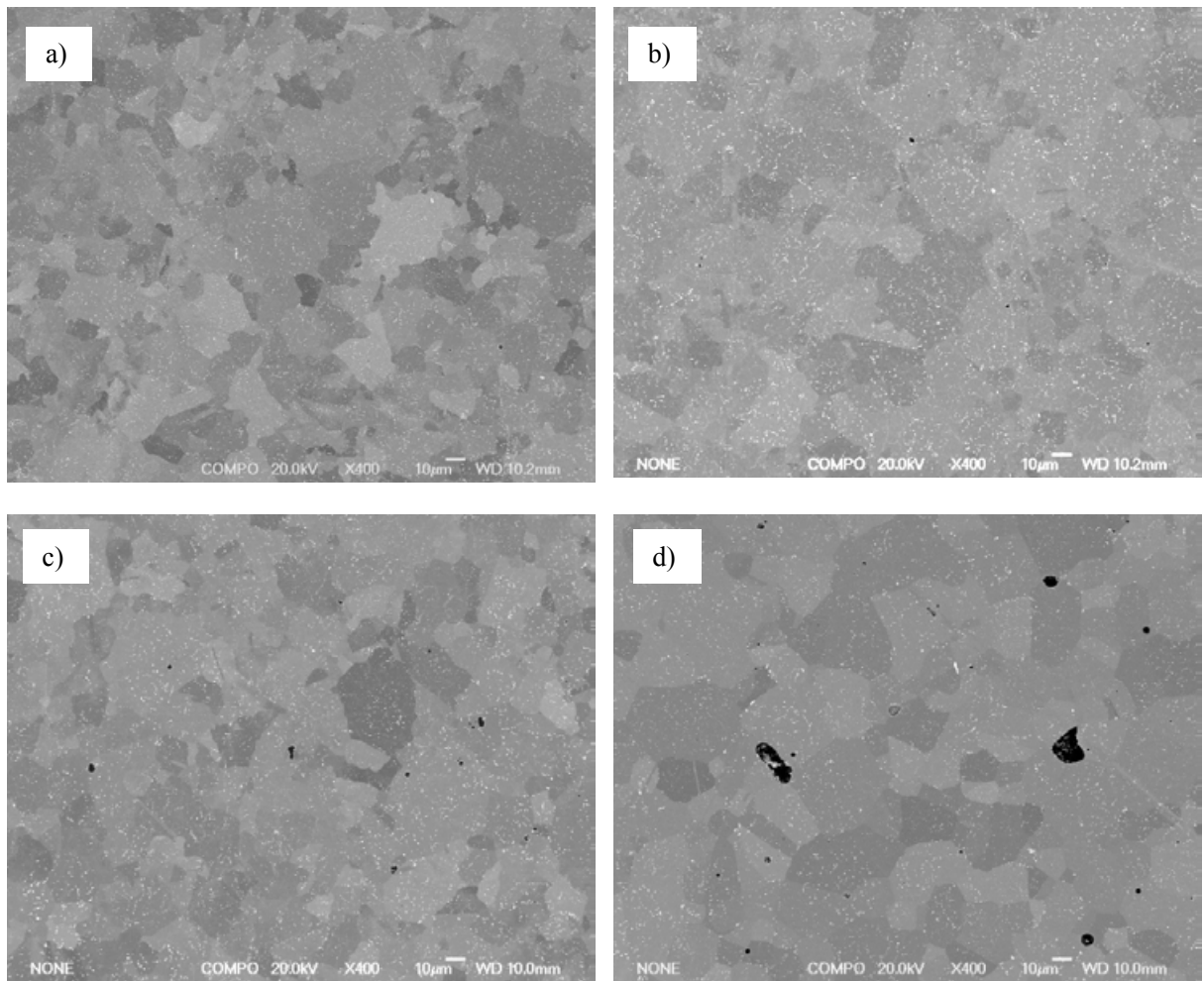


Fig. 4-36 Back scattered SEM images of pores in HIPped and heat treated CM247LC.

a) HIPped at 1260 °C/150MPa/2h + Aged at 870 °C/16h/FC;

b) HIPped at 1260 °C/150MPa/2h + Solutioned at 1100 °C/1h/FAQ + Aged at 870 °C/16h/FC;

c) HIPped at 1260 °C/150MPa/2h + Solutioned at 1200 °C/1h/FAQ + Aged at 870 °C/16h/FC;

d) HIPped at 1260 °C/150MPa/2h + Solutioned at 1260 °C/1h/FAQ + Aged at 870 °C/16h/FC;

4.3.2 Mechanical properties of HIP+Solution-treated +Aged CM247LC

1100 °C and 1260 °C solution treated samples were selected for the study of the mechanical properties. Tensile, fatigue and creep tests have been carried out. The as-HIPped properties and where available data from the literature are shown for comparison.

4.3.2.1 Tensile properties

Standard tensile tests were carried out at room temperature, 700 °C and 750 °C on both materials, other test parameters are the same as in Table 4-2. The samples which had been solution treated at 1260 °C were also tensile tested at 1050 °C and 1200 °C and the as-HIPped samples were tensile tested at 900 °C and 1050 °C. The test speed was initially controlled at 10^{-4} /s. Three test pieces were tested at each temperature for each solution condition in order to obtain some indication of the repeatability of the properties. Table 4-8 lists the 0.2% proof strength, ultimate tensile strength and elongation of the materials at different test temperatures.

At room temperature, the as-HIPped samples has the best ductility of 22% and lowest 0.2 % proof strength of 790 MPa while the 1260 °C solution treated samples show lowest ductility of 11.7 % but the highest 0.2 % proof strength of 1090 MPa. The 1100 °C solution treated samples have the highest ultimate tensile strength of 1530 MPa. At temperatures of 700 °C and 750 °C, the 1260 °C solution heat treated ones present the lowest ductility with the highest 0.2 % proof strength contrary to the as-HIPped samples. Although 1100 °C solution treated batch possesses better 0.2 % proof strength than the as-HIPped ones and better ductility than the 1260 °C solution treated ones, the tensile strength is inferior to those two.

The properties at 1050 °C are only available for the as-HIPped and the 1260 °C solution treated batches. Solution treatment at 1260°C improves the material 0.2 % proof strength and

tensile strength, but reduced the ductility.

The 0.2 % proof strength decreases as the temperature is increased with respect to that of the 1260 °C solution treated sample; the as-HIPped batch have a maximum value of 790 MPa at 750 °C while the 1100 °C solution treated sample has a maximum value of 968 MPa at 700 °C. The tensile strengths for all samples decreased as the test temperature was increased. The tensile strength of the 1100 °C solution treated batch is the most sensitive to temperature, while the 1260 °C solution treated one retains the most strength at high temperatures. Normally we would expect a steady increase of elongation with temperature. However, both the as-HIPped batch and 1260 °C solution treated batch show a trough in ductility at 900 °C and 1050 °C respectively. Although the elevated temperature ductility data is not available for the 1100 °C solution treated batch, similar behavior could be presumed. This is a common intermediate temperature property called mid range ductility minimum (MRDM) observed in many nickel-base super alloy such as Inco718, Hastelloy etc, and certain other alloy systems [Fiore 1975].

The tensile properties of cast CM247LC obtained by Huang and Koo (2004), with a grain size of 80 ~ 90 μm , are list in Table 4-9. The 1260 °C HIP plus 1260 °C solution plus 870 °C aged batch possesses better room temperature properties, while the ductility at 750 °C is inferior to the cast + HIP + heat treated but better than the HIPped CM247LC after vacuum spray forming. The room temperature properties of spray formed CM247LC are similar to the 1260 °C HIP plus 1100 °C solution plus 870 °C age treated batch in this project and they have better ductility at 760 °C.

Table 4-8 Tensile properties of HIPped CM247LC

Temperature (°C)	Material	As-HIP 1260 °C/150MPa/2h			HIP 1260 °C/150MPa/2h Solution 1100 °C/1h/FAC Age 870 °C/16h/FC			HIP 1260 °C/150MPa/2h Solution 1260 °C/1h/FAC Age 870 °C/16h/FC		
		0.2%PS (MPa)	UTS (MPa)	Elong (%)	0.2%PS (MPa)	UTS (MPa)	Elong (%)	0.2%PS (MPa)	UTS (MPa)	Elong (%)
Room Temperature	Data	783	1436	22.1	952	1525	18.1	1091	1447	13.1
	points	790	1468	23.3	952	1535	18.9	1088	1351	10.2
		796	1413	20.3						
	Average	790	1439	22.0	952	1530	18.5	1090	1399	11.7
	Stdev	7	28	1.5	1	5	0.6	2	47	2.1
700	Data	795	1210	21.7	960	1120	5.1	1056	1136	1.7
	points	798	1154	21.8	975	1125	5.6	1035	1149	2.3
		786	1143	20.9						
	Average	793	1169	21.5	968	1123	5.4	1046	1143	2.0
	Stdev	6	36	0.5	7	3	0.3	15	9	0.4
750	Data	795	1072	12.4	959	1020	3.1	1028	1061	1.5
	points	797	1078	12.4	957	1020	3.1	1030	1064	1.6
		801	1086	13.5						
	Average	798	1079	12.8	958	1020	3.1	1029	1063	1.6
	Stdev	3	7	0.6	2	1	0.1	2	2	0.1
900	Data	394	654	3.9						
	points	369	657	5.2						
		387	659	4.1	-	-	-	-	-	-
	Average	383	657	4.4						
	Stdev	13	3	0.7						
1050	Data	85	113	11.3				162	163	0.8
	points	96	128	11.5				173	174	1.0
		93	114	11.7	-	-	-			
	Average	91	118	11.5				168	169	0.9
	Stdev	6	8	0.2				8	8	0.1
1200	Data							29	30	3.4
	points							22	23	5.3
		-	-	-	-	-	-			
	Average							26	27	4.4
	Stdev							5	5	1.0

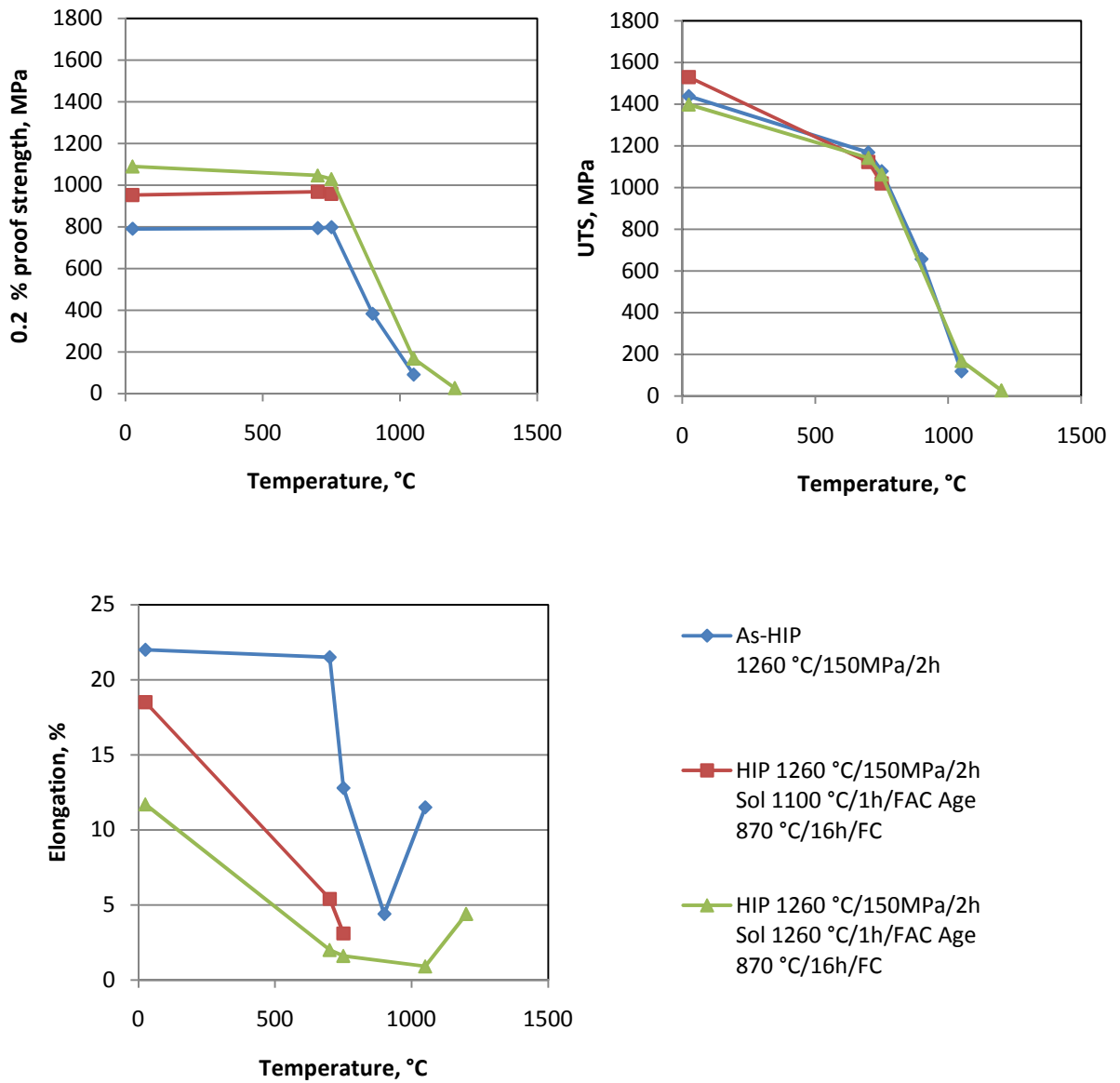


Fig. 4-37 Tensile properties of HIPped CM247LC versus testing temperature

Table 4-9 Tensile data of CM247LC manufactured by other methods

Method	As-cast CM247LC HIP at 1185 °C/173MPa/4h Solution at 1221 °C/2h/GFQ Aging at 771 °C/20h/FC <i>[Huang and Koo 2004]</i>			Vacuum Spray formed HIP at 1185 °C/172MPa/4h Solution 1260 °C/1h+1100 °C/1h/cool ≥ 40 °C min ⁻¹ 800 °C/16h <i>[Andrews 1999]</i>		
	0.2%PS (MPa)	UTS (MPa)	Elong (%)	0.2%PS (MPa)	UTS (MPa)	Elong (%)
RT	1010	1242	8.1	928	1355	17.3
760	1016	1200	8.2	900	1113	6.5

The fracture surfaces created at room temperature and 750 °C were examined by SEM. As found in the as-HIPped tensile fracture surfaces, inclusion clusters near the sample surfaces could always be found in the fracture surfaces of the 1100 °C solution treated batch (Fig.4-38 a),c)). The EDS analysis in Table 4-10 indicates again the inclusion clusters are Hf rich. The cracks propagated transgranularly, leaving a dimpled surface, indicating a ductile mode of failure (Fig.4-38 b), d)). Facets, instead of inclusion clusters, were observed in the initiation sites of 1260 °C solution-treated samples tested at room temperature (Fig.4-39 a)). The propagation path is a combined mode of failure, partly intergranular and transgranular ((Fig.4-39 b)). The strength of grain boundaries and grain interior are comparable at room temperature. No obvious initiation sites were found in the 1260 °C solution treated samples tested at 750 °C ((Fig.4-39 c)). Cracks propagated intergranularly ((Fig.4-39 d)) in a brittle mode of fracture. The bonding between grains is thus weaker than the bonding between inclusions and matrix at 750 °C.

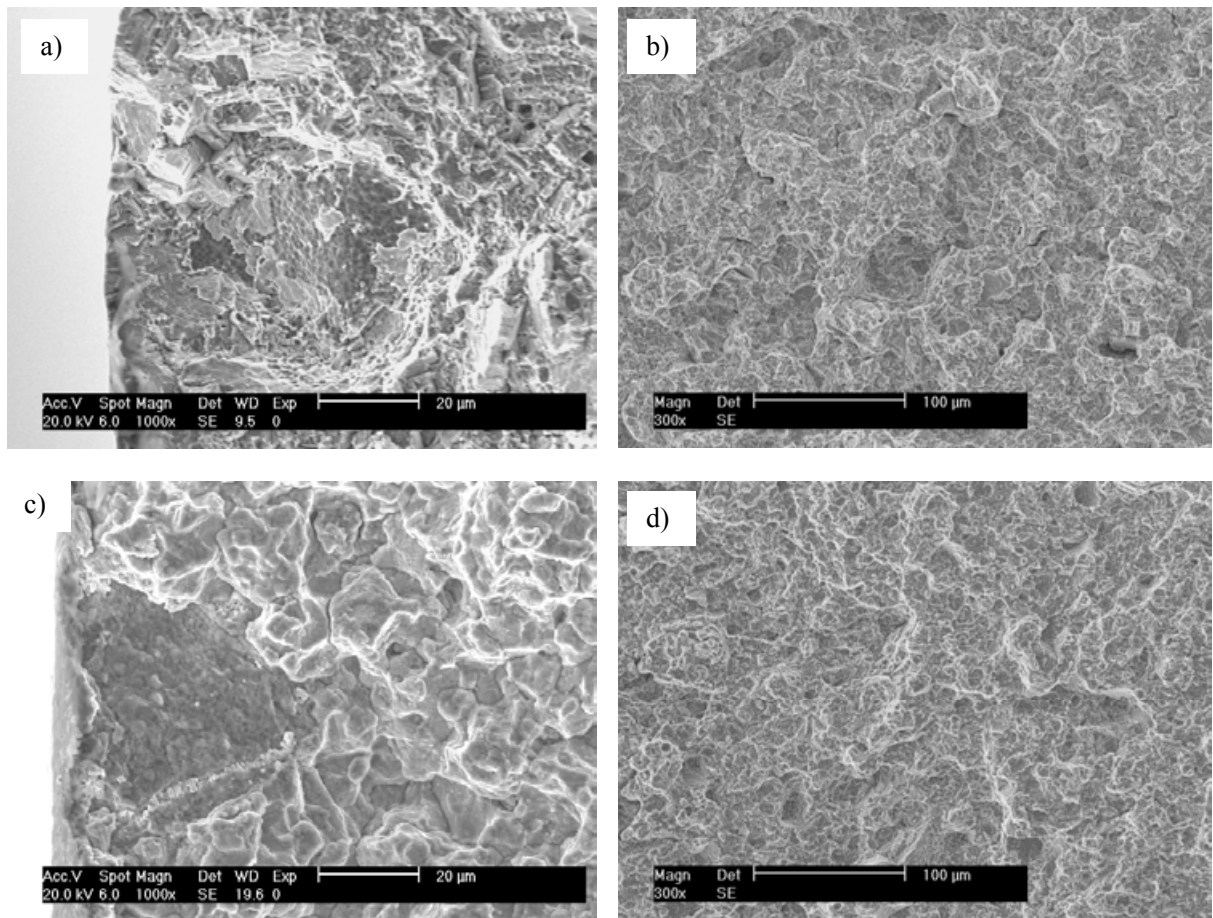


Fig. 4-38 Secondary electron SEM images of tensile fracture surface of CM247LC HIPped at 1260 °C/150MPa/2h + Solution at 1100 °C/1h/FAQ + Age at 870 °C/16h/FC

a) ,b) are initiation site and propagation path of sample tested at room temperature;
 c), d) are initiation site and propagation path of sample tested at 750 °C.

Table 4-10 EDS analysis of inclusions at initiation sites in Fig. 4-38

Element	Weight %	Atomic %
O	24.5 ± 1.7	75.2
Cr	0.7 ± 0.2	0.7
Co	1.1 ± 0.2	1.0
Ni	5.2 ± 0.3	4.3
Hf	68.5 ± 1.6	18.8

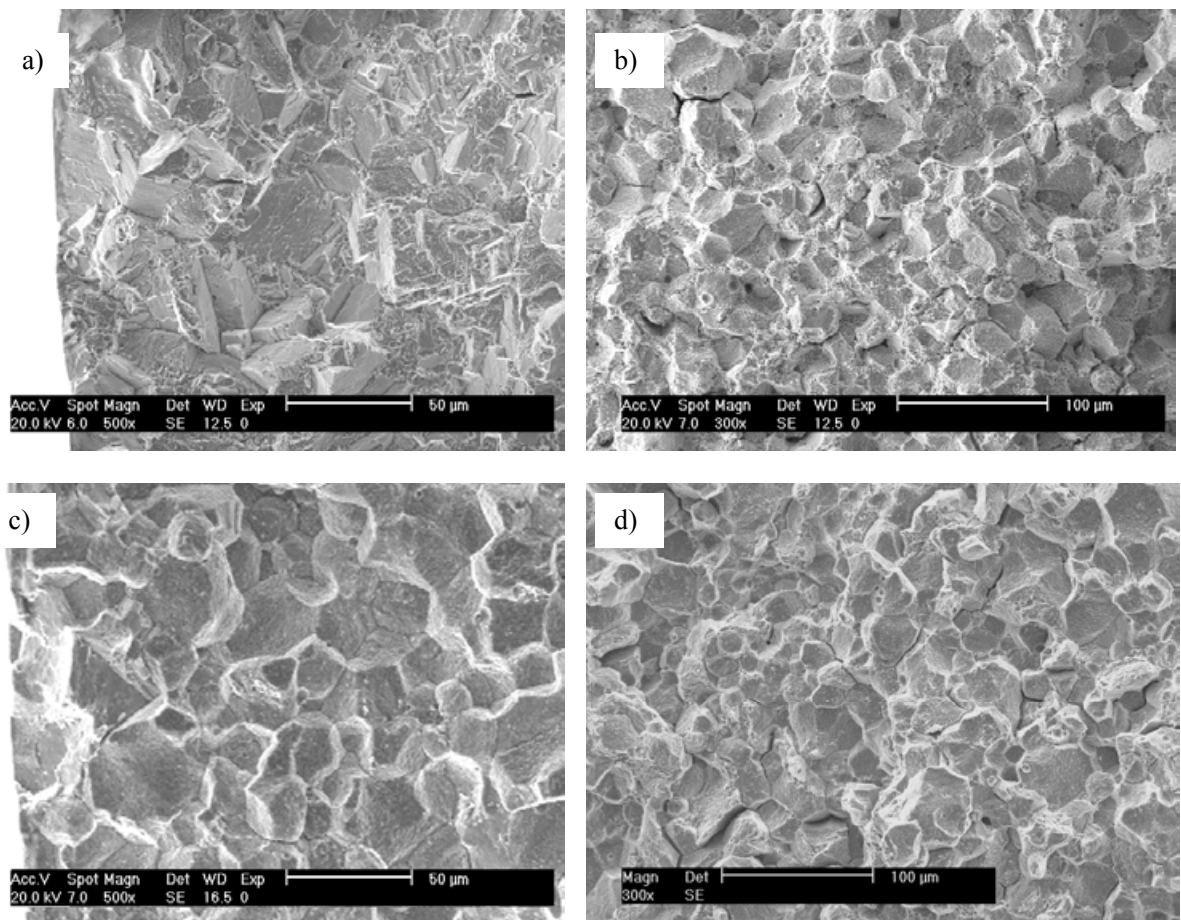


Fig. 4-39 Secondary electron SEM images of tensile fracture surface of CM247LC HIPped at 1260 °C/150MPa/2h + Solution at 1260 °C/1h/FAQ + Age at 870 °C/16h/FC

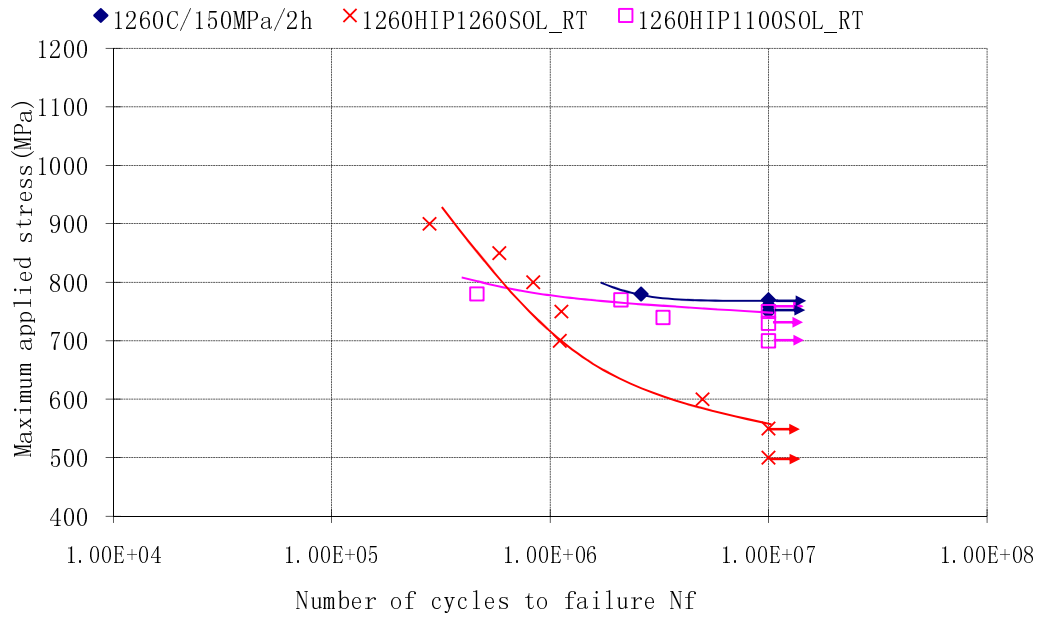
a) ,b) are initiation site and propagation path of sample tested at room temperature;

c), d) are initiation site and propagation path of sample tested at 750 °C.

4.3.2.2 High cycle tension-tension fatigue properties

High cycle tension-tension fatigue testing was conducted at room temperature and 750 °C on 1100°C and 1260 °C solution treated CM247LC. The fatigue curves are shown in Fig. 4-40, and the fatigue limits are listed in Table 4-11. The 10^7 cycle endurance limit of the 1100 °C solution treated batch is 750MPa at room temperature, 20MPa lower than that of the as-HIPped batch. The 1260 °C solution treated batch has the lowest room temperature fatigue limit of all, at 550 MPa. The fatigue limits at 750 °C are lower than those for the as-HIPped batch and the 1100 °C batch, with values of 700 MPa and 625 MPa respectively. The value of the 1260 °C solution heat treated batch decreased by 50MPa to be 500 MPa.

Room temperature fatigue on HIP+Solution+Age CM247LC



750 °C fatigue on HIP+Solution+Age CM247LC

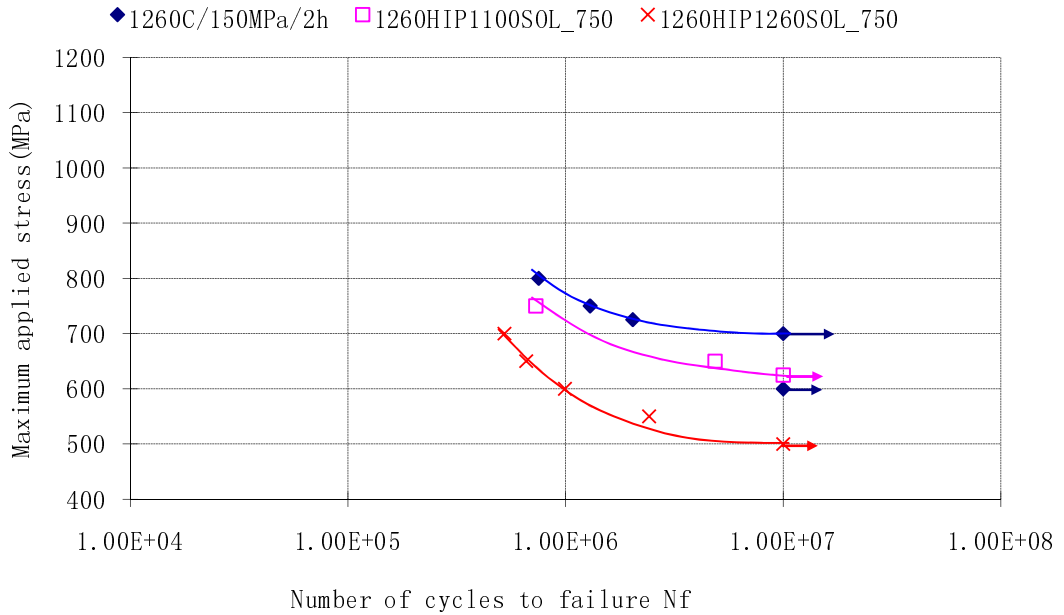


Fig.4-40 High cycle tension-tension fatigue curves of HIPped and heat treated CM247LC
 Tested at 95 Hz, R = 0.1

Table 4-11 High cycle tension-tension fatigue limits of HIPped and heat treated CM247LC

	As-HIP 1260°C/150MPa/2h	HIP 1260°C/150MPa/2h Sol 1100°C/2h/FAQ Age 870°C/16h/FC	HIP 1260°C/150MPa/2h Sol 1260°C/2h/FAQ Age 870°C/16h/FC
Room Temperature	770MPa	750MPa	550MPa
750°C	700MPa	625MPa	500MPa

At room temperature, fatigue cracks initiate at sample surfaces in both the 1100°C and 1260°C solution treated CM247LC. Inclusion clusters around 40 µm in diameter surrounded by facets can be found in most of the initiation sites in the 1100°C solution treated samples (Fig. 4-41 a)). They are still detected by EDS (see Table 4-12) to be Hf rich oxides. Only facets were observed in initiation sites of the 1260°C solution treated batch.

At 750°C, similar to the as-HIPped fracture surfaces in Fig. 4-27, a rounded ‘river pattern’ zone was found in every fracture surface in both 1100°C and 1260°C solution treated CM247LC. The edges of the zones are tangential to the sample surfaces. Hf rich inclusion clusters of about 30 µm surrounded by facets, can also be found in the centre of the initiation sites.

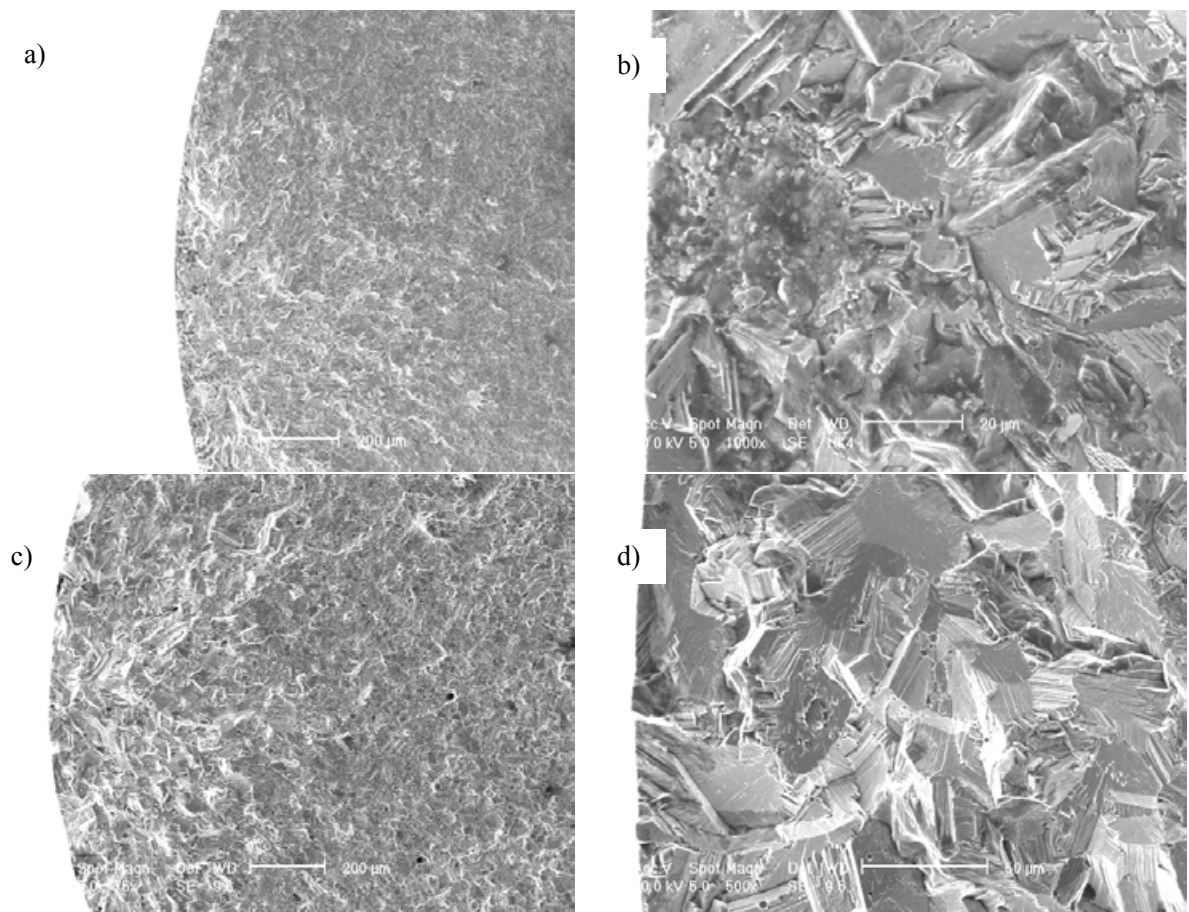


Fig. 4-41 Secondary electron SEM images of fracture surface of tension-tension fatigue specimens at room temperature. Samples were HIPped at 1260 °C/150MPa/2h and aged at 870 °C/16h/FC after solution treatment.

a), b) solution treated at 1100 °C/1h/FAQ, failed at 462000 cycles at 780MPa;

c), d) solution treated at 1260 °C/1h/FAQ, failed at 1125100 cycles at 750MPa.

Table 4-12 EDS analysis of inclusions at initiation sites in Fig. 4-41

Element	Weight %	Atomic %
O	23.9 ± 1.7	75.1
Cr	0.5 ± 0.2	0.4
Co	1.0 ± 0.2	0.8
Ni	4.5 ± 0.3	3.8
Hf	70.2 ± 1.6	19.8

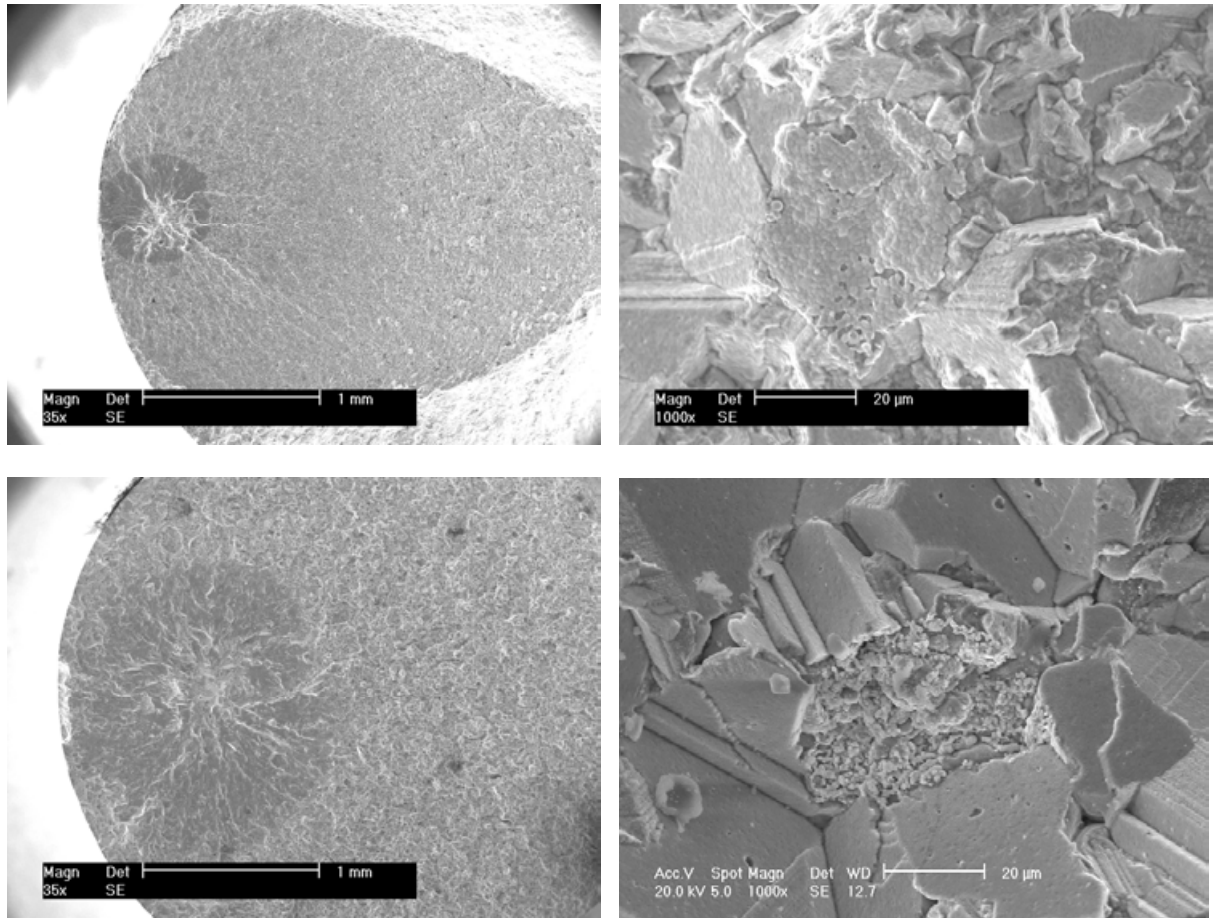


Fig. 4-42 Secondary electron SEM images of fracture surface of tension-tension fatigue specimens at 750 °C. Samples were HIPped at 1260 °C/150MPa/2h and aged at 870 °C/16h/FC after solution.

a), b) solution treated at 1100 °C/1h/FAQ, failed at 4864300 cycles at 650MPa;

c), d) solution treated at 1260 °C/1h/FAQ, failed at 993200 cycles at 600MPa.

4.3.2.3 Creep

Creep curves were obtained by a quick temperature ramping test from room temperature until significant deformation occurred, at a ramping rate of 10°C/min. The 1260°C HIPped + 1100 °C solution treated + aged batch and the 1260 °C HIPped + 1260 °C solution treated +

aged batch was investigated, the results are shown and compared with a polycrystalline MarM247(provided by NPL) in Fig. 4-43. A load of 350MPa was applied to all the samples. The polycrystalline MarM247 began to creep slowly at about 300 °C, while the strains of CM247LC batches are not significant until the temperature was over 800 °C. The 1260°C solution treated batch shows a little more creep resistance than the 1100°C solution treated one at temperatures above 900 °C. The limit of the allowable deflection was rapidly reached when the temperature approached 1000 °C for CM247LC.

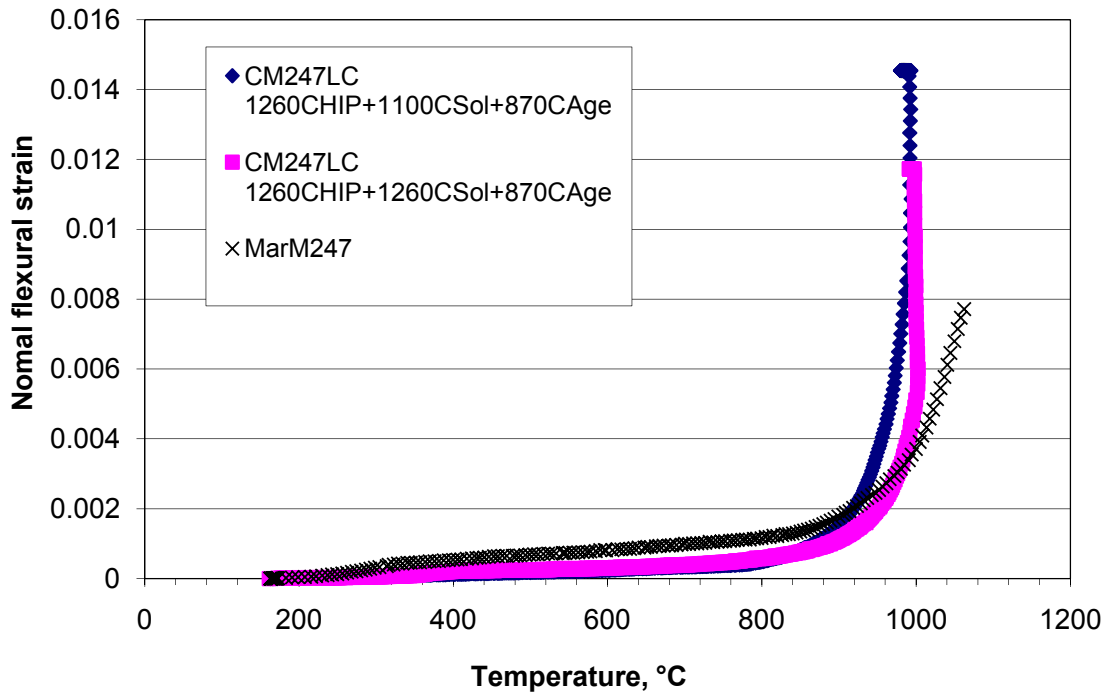


Fig. 4-43 Quick creep curves of CM247LC at 350MPa. MarM247 was polycrystalline. The temperature was increased at 10 °C/min.

Based on the creep behaviour above, step temperature tests were carried out on the two batches of CM247LC while the stress level was kept at 350MPa and temperature changes from 700 °C and 950 °C at steps of 25 °C. At each temperature step, the experiment was left

to settle long enough to be in what looked like a linear creep region. The flexural strain rates were calculated from those step-temperature curves. They are plotted in Fig. 4-44.

Step-stress tests were carried out to obtain the stress exponent. The temperature was kept at 760 °C while the stress was changed between 150MPa and 550MPa in steps of 100MPa. For each stress increment, the experiments were run long enough for the linear creep regions to appear. The flexural strain rates were calculated from the step-stress curves and are plotted in Fig. 4-45. In the step-stress tests, there is much more scatter than in the step temperature tests – there are viscoelastic effects going on during the stress changes, which can influence the measurements. [Hollenberg *et al.* 1971]

The plotted data of the test were fitted according to the general creep equation below.

$$\frac{d\varepsilon}{dt} = A\sigma^n e^{-\frac{Q}{RT}}$$

where ε is the creep strain, A is a constant, dependent on the material and the particular creep mechanism, n is stress exponent dependent on the creep mechanism, Q is the activation energy of the creep mechanism, σ is the applied stress, k is Boltzmann's constant, and T is the absolute temperature.

The 1260 °C HIPped + 1100 °C solution treated + aged CM247LC has a creep activation energy of 429.5 KJ/mol with a stress exponent of 4.12. The values for the 1260 °C HIPped + 1260 °C solution treated + aged CM247LC are slightly different with an activation energy of 403.0 KJ/mol and a stress exponent of 4.88. The 1260 °C solution treated CM247LC has better creep resistance than the 1100 °C solution treated samples over the temperature range of 700 °C to 950 °C and a stress range of 150 MPa to 550 MPa.

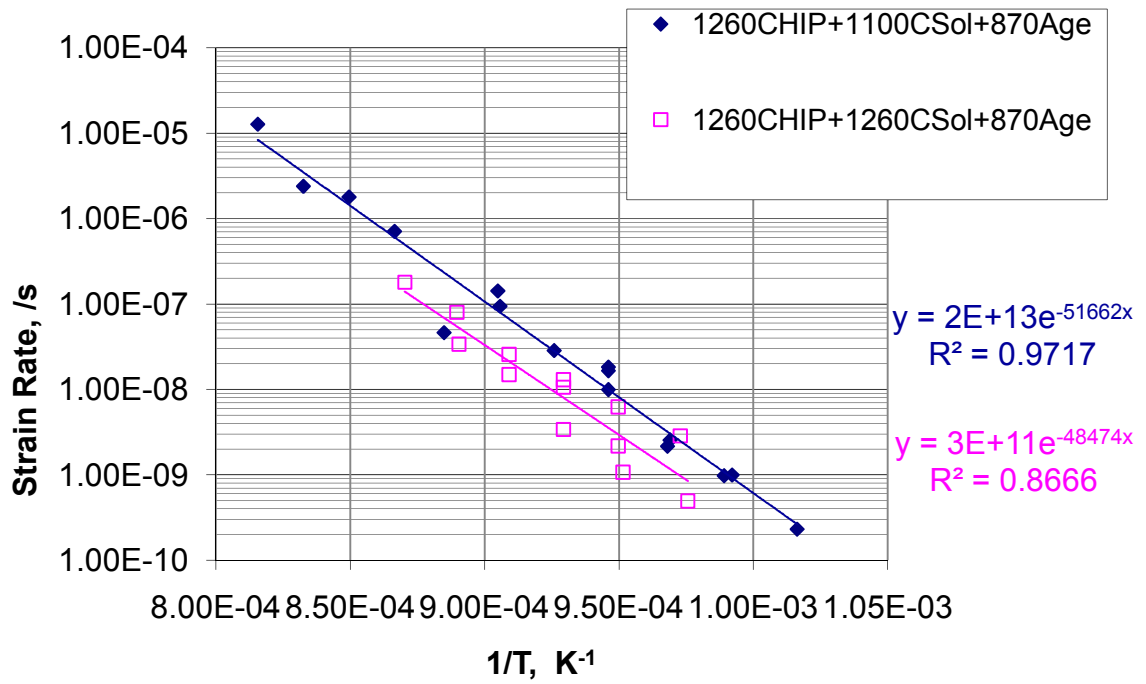


Fig. 4-44 Temperature dependence of the creep rate of HIPped CM247LC at 350MPa

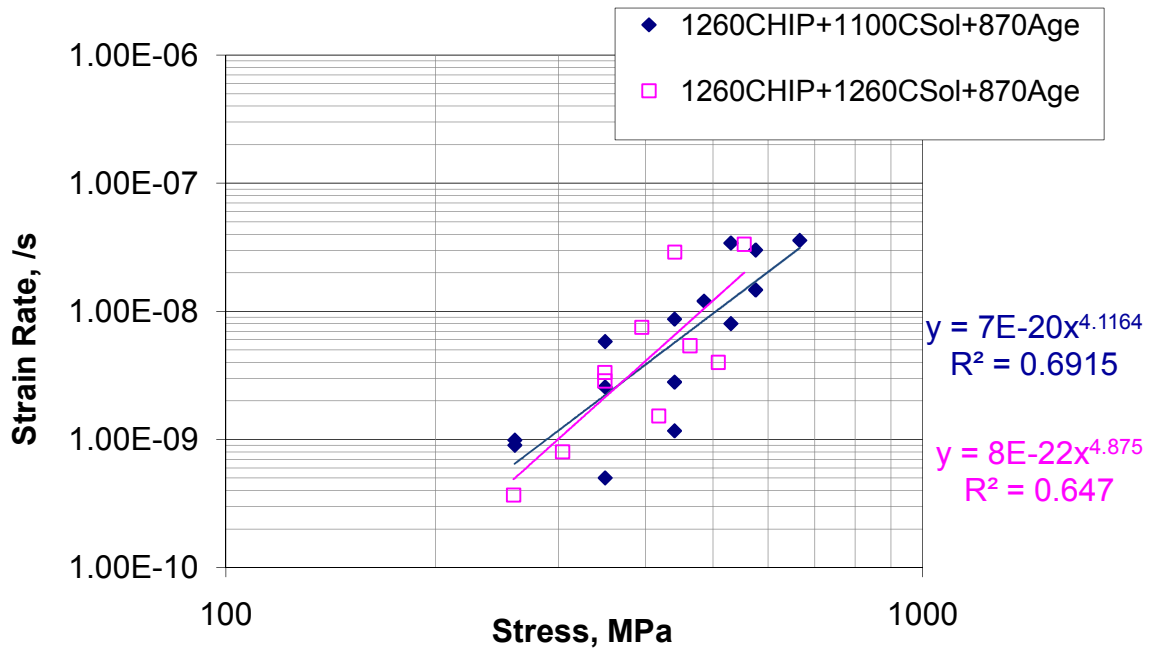


Fig. 4-45 The stress dependence of the secondary creep rate of HIPped CM247LC at 760 °C

4.3.3 Summary

Microstructure

As the solution temperature is increased, primary γ' particles are gradually dissolved, and are substituted by very fine tertiary γ' formed during cooling. When the temperature reaches 1260 °C, primary γ' is totally dissolved and the rate of grain growth increases; higher solution temperatures also presumably results in higher porosity, as trapped argon expands. The fraction and the morphology of MC carbides are relatively stable over the heat treatment. Inclusions still remain after heat treatment.

Mechanical properties

Solution treatment can increase the 0.2 % proof strength and decrease the ductility over the tested temperature range. Inclusions of over 30 μm in diameter were found at the surface failure initiation site of the 1100 °C solution treated CM247LC sample tensile tested at room temperature and at 750 °C. For the 1260 °C solution treated batch, facets were found at initiation sites at room temperature; cracks propagated intergranularly. No obvious fracture initiation sites were found in the fracture surfaces of 700 °C and 750 °C tests which showed intergranular mode of failure.

Higher solution treatment temperature does not improve the high cycle tension-tension fatigue properties. Cracks initiate at sample surfaces at room temperature. Both inclusions and facets are found at initiation sites. When tested at 750 °C, cracks initiate at inclusions below the sample surfaces to depth of about 0.5 mm. Round radial zones tangential to sample surfaces can always be found around the initiation sites. The inclusions are Hf-rich oxides.

Solution treatment above the solvus improves the creep resistance of HIPped CM247LC

over the temperature range of 700°C to 950°C and the stress range of 150 MPa to 550 MPa.

4.4 Comparison of Hf-containing and Hf-free HIPped CM247LC

It has been noted in previous sections that inclusions are found in as-HIPped (Fig. 4-20) and heat treated CM247LC. Inclusion clusters are the main initiators that cause failure in the tensile and high cycle fatigue test. From this aspect, it is worth trying to understand why these inclusions exist and their frequency in the material and whether it is possible to eliminate them. The inclusions found at initiation sites in tensile fracture surfaces were shown to be rich in hafnium (Table 4-6). Another batch of CM247LC, free of hafnium, was HIPped at 1260 °C/150MPa/4h followed by solution treatment at 1100 °C/1h/FAQ and ageing at 870 °C/ 16h/FC in order to clarify the importance of the Hf-rich inclusions in terms of properties.

4.4.1 Identification of inclusions in Hf-containing CM247LC HIPping

There are two types of inclusion observed in the HIPped CM247LC. One specific type of large inclusion was found only in the 1100 °C as-HIPped CM247LC, shown in Fig. 4-46. EDS analysis showed that these inclusions were alumina since they contained oxygen and aluminium as shown in Fig.4-46 a). The bonding between the type of inclusion and the matrix is very weak that it is hard to retain them in the sample after polishing. The site of an inclusion is commonly seen as a pore where the inclusion has been removed during specimen preparation as shown in Fig. 4-46 b). The other type of inclusion is shown in Fig. 4-46 c), which is bright and no particle-free zone is associated with them.

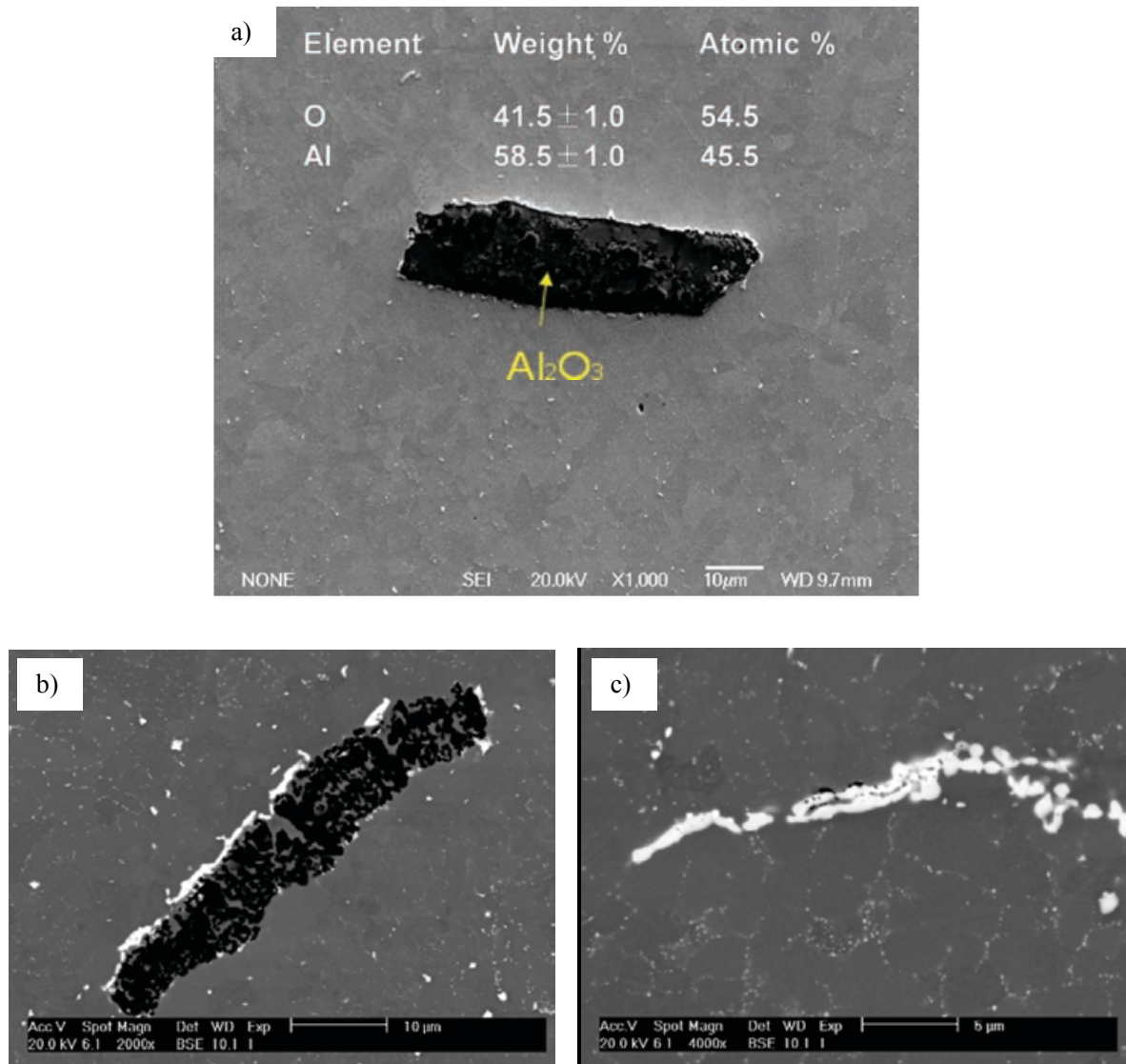


Fig. 4-46 Inclusion found in 1100 °C/150MPa/4h as-HIPped sample,

a) Secondary electron SEM image of together with EDS data;

b) Backscattered electron SEM image of a site where the inclusion was removed during polishing, surrounded by a particle free zone;

c) Backscattered electron SEM image of an inclusion, no depletion of surrounding particles is obvious.

The latter type of inclusion is more commonly found in as-HIPped CM247LC, as shown in Fig.4-47. They are bright in contrast suggesting that heavy elements are involved. Most of them are platelet shaped (Fig. 4-47 a), c), d)), but some are clusters (Fig. 4-47 b)) or blocky (Fig. 4-47 a)). It is worth noting that dark regions in inclusions are always observed in backscattered electron images. EDS plus WDS mapping of a typical particle in 1260 °C/150MPa/2h as-HIPped sample (Fig.4-48) revealed the distribution of elements in the inclusions.

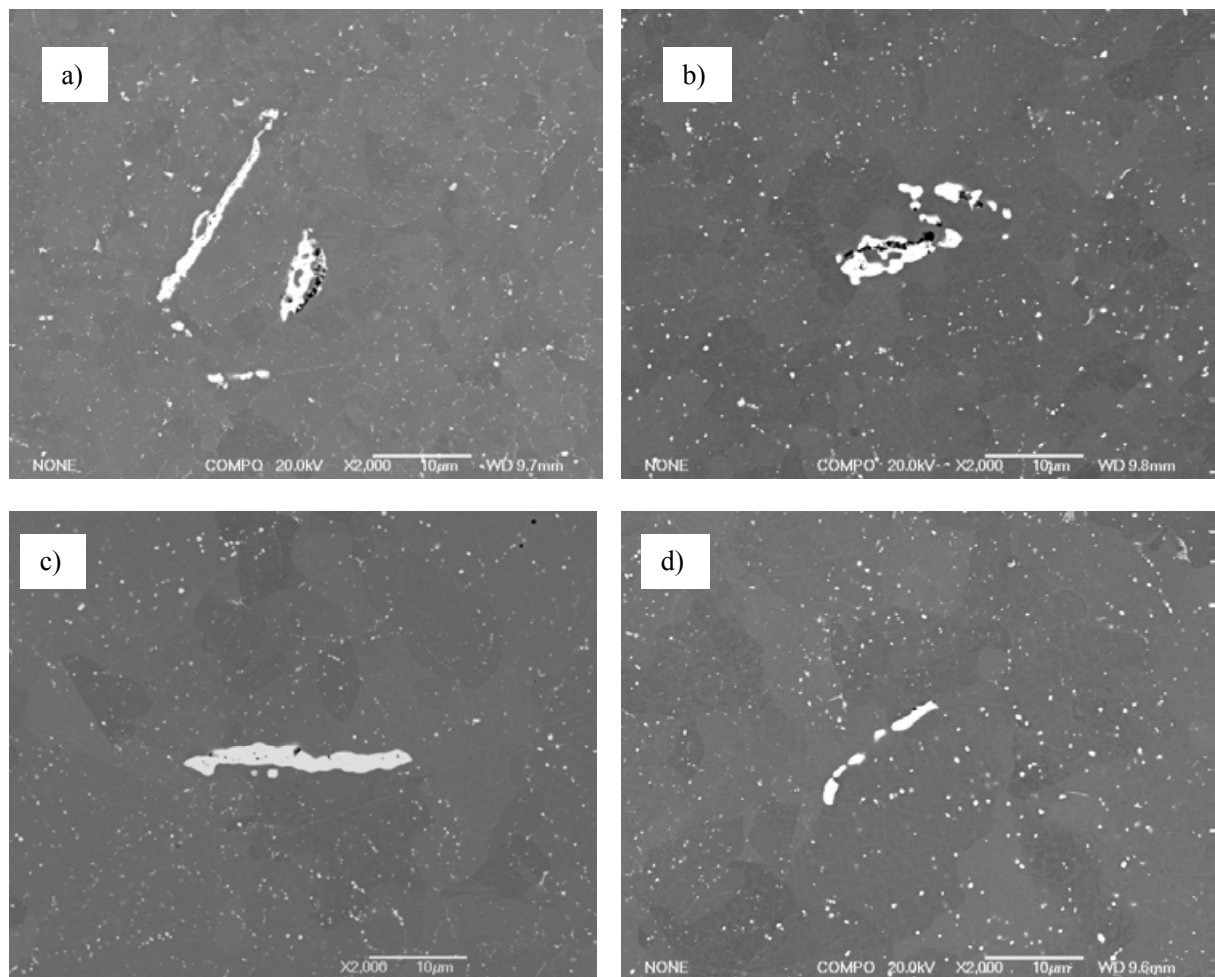


Fig.4-47 Backscattered electron SEM images of inclusions in as-HIPped CM247LC.

a) 1100°C/150MPa/4h; b) 1200°C/150MPa/4h;

c) 1260°C/150MPa/2h; d) 1320°C/150MPa/2h.

The top left hand image in fig 4-48 is a backscattered electron imaging of an inclusion which has a dark core. The other images are elemental maps, in which the brightness indicates the concentration of the selected element. The dark core which is brighter than the matrix in the Al K1 map means that Al is highly concentrated there. The bright part of the inclusion is extremely bright in the Hf M1 map but dark in Ni L1 and Al K1 maps which indicates that it mainly contains Hf and no Al or Ni. The carbon WD and oxygen WD maps illustrate that the inclusion is oxide not carbide. The same conclusion can be made from quantitative analysis result in Table 4-13. Obviously, the particles are hafnium oxide with an alumina core. Hf rich and Al-rich oxide cores size range from 2 to 5 μm was also found in MC carbides in directionally solidified MarM247[Chen, Lee et al. 1998]

Some carbide particles are seen in these elemental maps as small white particles. Thus above the inclusion particle the particles are extremely bright in Hf M1 and carbon WD maps and dark in the rest of the maps. This is a consistent with the EDS analysis in TEM (§4.2.1.4) that the carbides are mainly hafnium carbides.

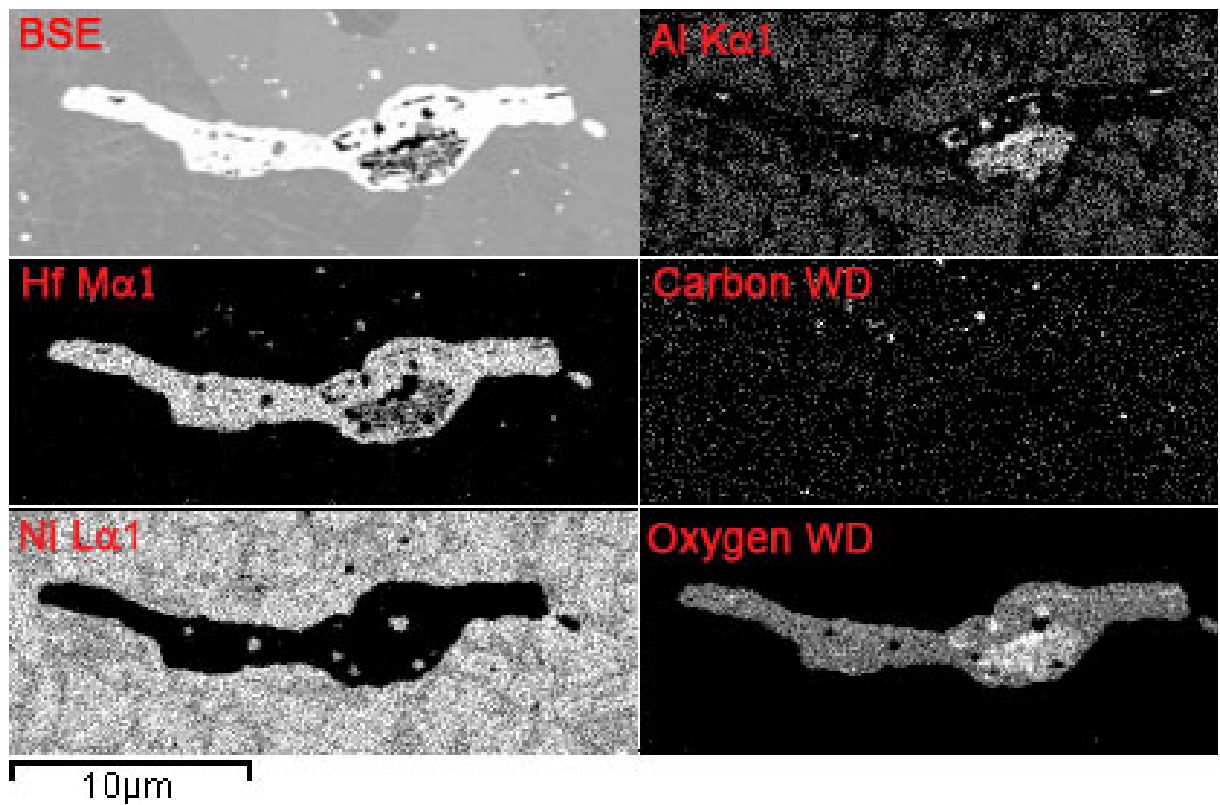


Fig.4-48 ED plus WD mapping of a typical inclusion found in 1260 °C as-HIPped CM247LC. On the top left is a backscattered electron image of the inclusion. The rest of the images are elemental maps, in which the brightness indicates the concentration of the specific element.

Table 4-13 Quantitative analysis by EDS and WDS of inclusions shown in Fig. 4-48

	Dark core		Bright part	
	Weight %	Atomic %	Weight %	Atomic %
Al_K	14.1 ± 0.5	26.1	--	
Hf_M	63.0 ± 1.0 wt %	17.7	83.9 ± 1.4 wt %	37.8
O_WD	16.6 ± 0.4 wt %	52.0	15.6 ± 0.6 wt%	66.0
C_WD	1.0 ± 0.1 wt %	4.2	0.4 ± 0.1 wt %	2.2

4.4.2 Comparison of microstructure of Hf-containing and Hf-free CM247LC

The number of inclusions is significantly decreased on removal of Hf (Fig.4-49). Meanwhile, the amount of carbon-containing particles (Fig.4-50) was also reduced as Hf is the main MC carbide former. The prior powder boundaries are decorated by extra fine dark particles when Hf is absent, instead of bright particles (Fig.4-50). The dark particles could be carbides of elements with lower atomic number than nickel. This indicates that the Hf-containing powder surfaces are rich in Hf. The necklace structure along the grain boundaries is also present in the Hf-free samples (Fig.4-51)

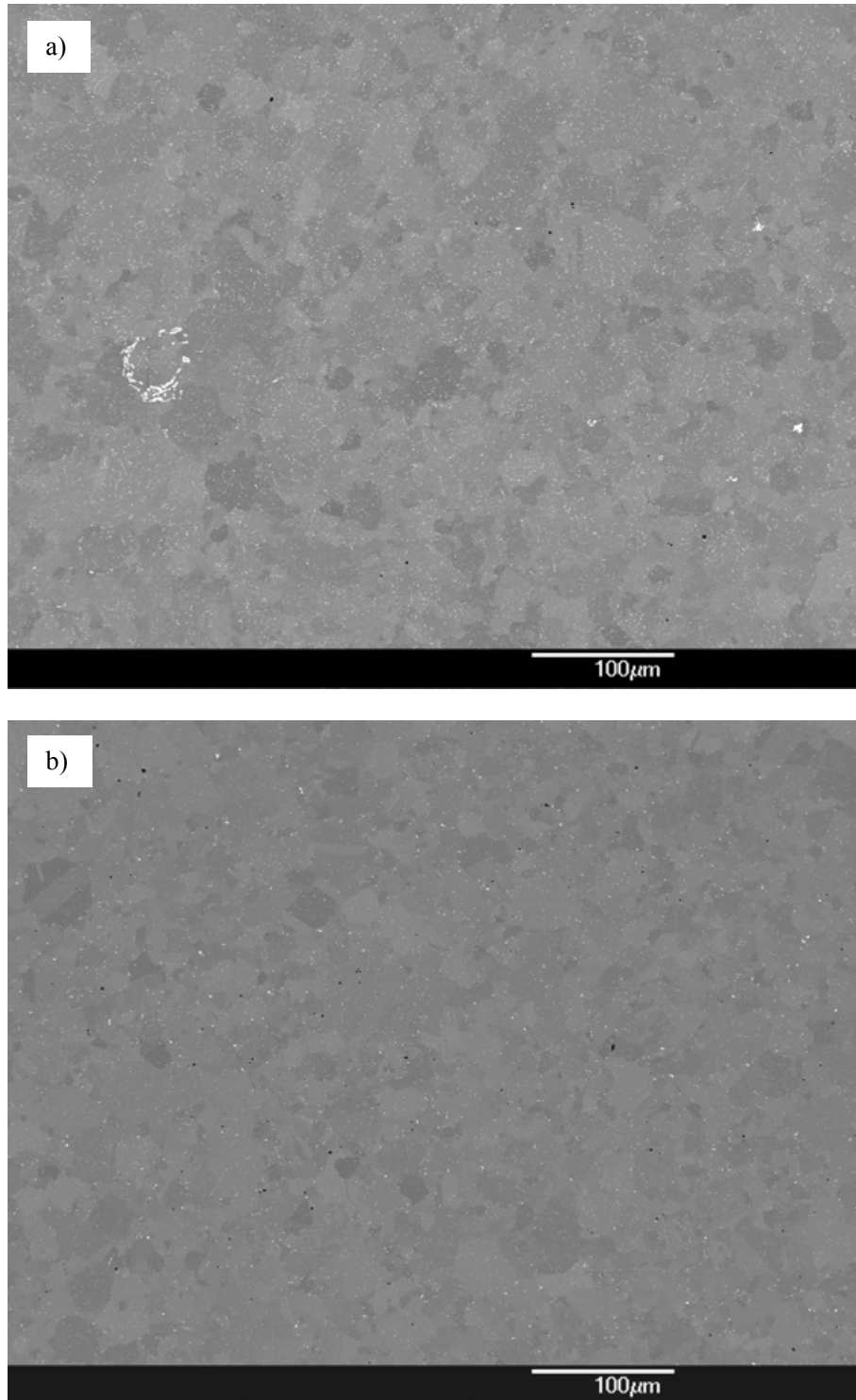


Fig. 4-49 Back scattered SEM images comparing the inclusions in Hf-containing and Hf-free CM247LC HIPed at 1260 °C/150MPa/2h + Solution at 1100 °C/1h/FAC + Age at 870 °C/16h/ FC. a) Hf containing; b) Hf free.

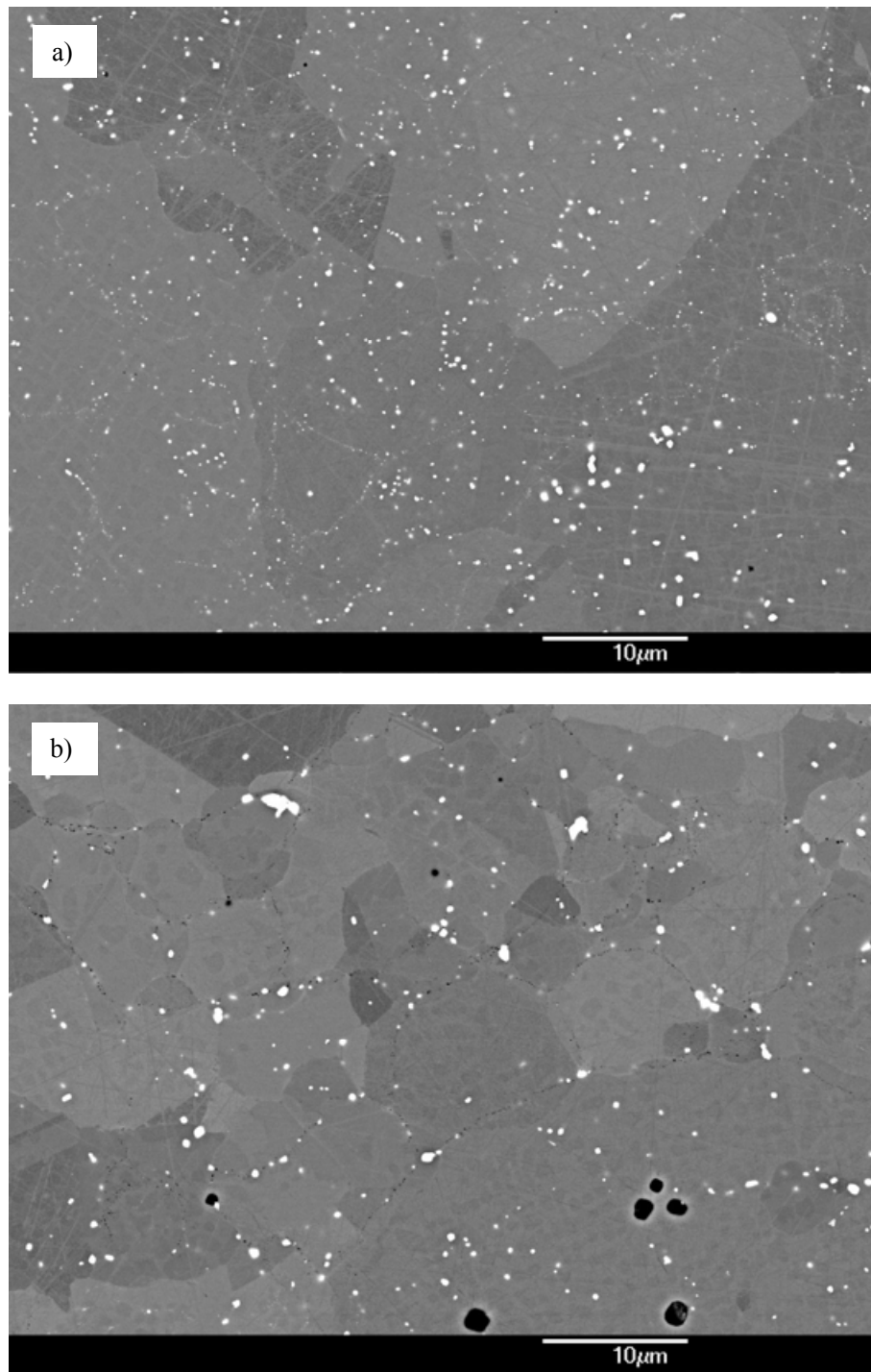


Fig. 4-50 Back scattered SEM images comparing the carbides in Hf-containing and Hf-free CM247LC HIPped at 1260 °C/150MPa/2h + Solution treated at 1100 °C/1h/FAC + Age at 870 °C/ 16h/ FC. A lower density of carbides is found in Hf-free CM247LC. When Hf is absent, PPBs are decorated by dark rather than bright dots. a) Hf containing; b) Hf free.

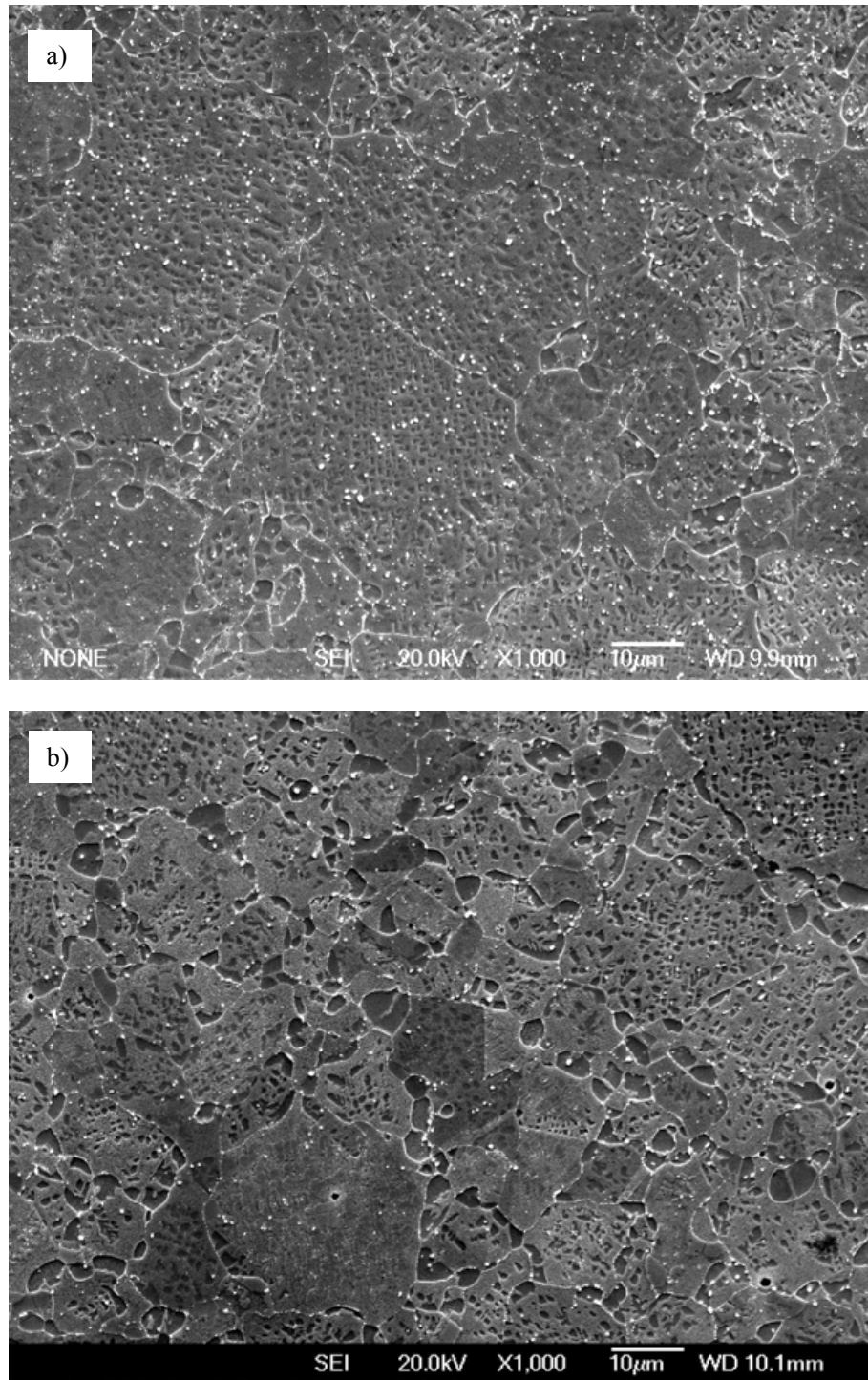


Fig. 4-51 Secondary electron SEM images of etched samples comparing the γ' morphology in Hf-containing and Hf-free CM247LC HIPped at 1260 °C/150MPa/2h + Solution at 1100 °C/1h/FAC + Age at 870 °C/ 16h/ FC. a) Hf containing; b) Hf free.

4.4.3 Quantitative analysis of defects in HIPped CM247LC

X-ray tomography scanning was done on CM247LC in the following Hf-containing samples:

- As-HIPped 1100 °C/150MPa/4h;
- HIPped 1260 °C/150MPa/2h + Solution 1100 °C/1h/FAC + Age 870 °C/16h;
- HIPped 1260 °C/150MPa/2h + Solution 1260 °C/1h/FAC + Age 870 °C/16h;

For comparison, Hf free sample HIPped at 1260 °C/150MPa/2h + Solution 1100 °C/1h/FAC + Age 870 °C/16h was scanned.

943 slides were taken for each specimen. Fig.4-52 demonstrates the typical slides chosen from each sample. They are reversed X-ray images where the brighter the image is, it is the harder for the X-ray to penetrate the sample.

Assuming a flow of 50 μm thickness (maximum size observed in SEM), the intensity of the transmitted X-ray beam can be calculated. The attenuation of the X-rays is calculated using equations in Appendix 4 to be 89.3% for a matrix particle (nickel-based alloy solution), 79.7% for an HfO_2 particle, 99.4% for an Al_2O_3 particle and 100% for a pore. Compared with the matrix, the HfO_2 particle should be brighter and the Al_2O_3 darker after processing. Pores should look as dark as the background and indistinguishable from alumina. In this case, it is clear that the bright particles are Hf-rich inclusions. The dark particles in Fig.4-52 a) are more likely to be Al_2O_3 as the alumina particles were found in this batch of material (Fig. 4-46) and hardly any pores observed in the SEM investigation; while the ones in Fig.4-52 b) are more likely to be pores since pores are frequently present during SEM observation (see Fig. 4-36 d)) and no alumina was found.

Projections are reconstructed into 3D images as shown in Fig.4-53. Particles smaller than

3 μm were not taken into the account because they could be noise. Hf-rich particles are coloured in red and Al_2O_3 or pores are coloured in yellow. The 1100 $^\circ\text{C}$ as-HIPped sample (Fig.4-53 a)) and the 1260 $^\circ\text{C}$ HIP + 1260 $^\circ\text{C}$ solution + aged sample (Fig.4-53 c)) contain both Hf-rich particles and Al_2O_3 or pores. The 1260 $^\circ\text{C}$ HIP + 1100 $^\circ\text{C}$ solution + aged sample (Fig.4-53 b)) contains Hf-rich particles only. The Hf-free CM247LC (Fig.4-53 d)) hardly contains any defects. This indicates that the presence of inclusions is associated with the presence of Hf. Some reaction might occur during the HIPping and heat treatment process. This will be discussed in Chapter 5. The fact that fewer pores are detected in Hf-free samples could be because the pores are not big enough to be detected when solution treated at 1100 $^\circ\text{C}$ (see Fig. 4-36 c)).

Table 4-14 lists the volume fraction of the defects. The 1100 $^\circ\text{C}$ as-HIPped sample has 0.006 vol% of Hf-rich inclusions and 0.007 vol% of Al_2O_3 or pores, a total of 0.013 vol% of defects. The inclusions in the 1260 $^\circ\text{C}$ HIP + 1100 $^\circ\text{C}$ solution + aged sample of 0.014 vol%, is very close to the total value of the 1100C sample. The 1260 $^\circ\text{C}$ HIP + 1260 $^\circ\text{C}$ solution + aged sample contains the same volume fraction of Hf-rich inclusions as the 1100 $^\circ\text{C}$ as-HIPped sample, but the amount of Al_2O_3 or pores is as much as 0.039 vol% - a total inclusion content of 0.045vol%, the largest among all specimens. No Hf-rich inclusions were detected in the Hf-free CM247LC, and only traces of other defects were observed.

The size distribution of defects is shown in Fig.4-54. The 1100 $^\circ\text{C}$ as-HIPped sample has the largest mean size of defects of $\sim 30 \mu\text{m}$, followed by the 1260 $^\circ\text{C}$ HIP + 1100 $^\circ\text{C}$ solution + aged sample with a value of $\sim 25 \mu\text{m}$. The 1260 $^\circ\text{C}$ HIP + 1260 $^\circ\text{C}$ solution + aged sample contains more defects than the others but their mean size is only $\sim 10 \mu\text{m}$.

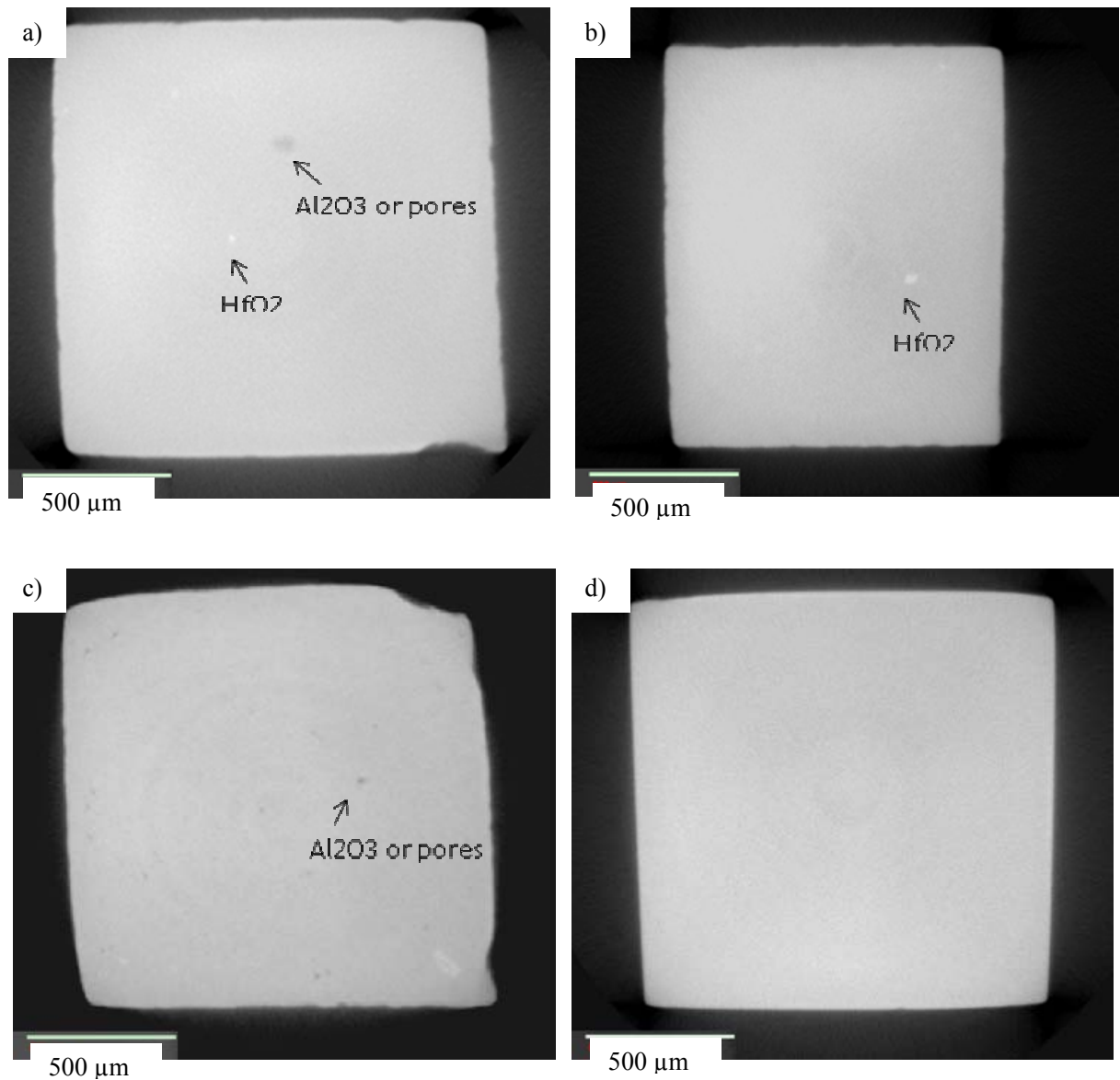


Fig.4-52 Reconstructed X-ray tomography slices of CM247LC.

- a) Hf-containing, as-HIPped 1100 °C/150MPa/4h;
- b) Hf-containing, HIP 1260 °C/150MPa/2h + Solution 1100 °C/1h/FAC + Age 870 °C/16h;
- c) Hf-containing, HIP 1260 °C/150MPa/2h + Solution 1260 °C/1h/FAC + Age 870 °C/16h;
- d) Hf-free HIP 1260 °C/150MPa/2h + Solution 1100 °C/1h/FAC + Age 870 °C/16h.

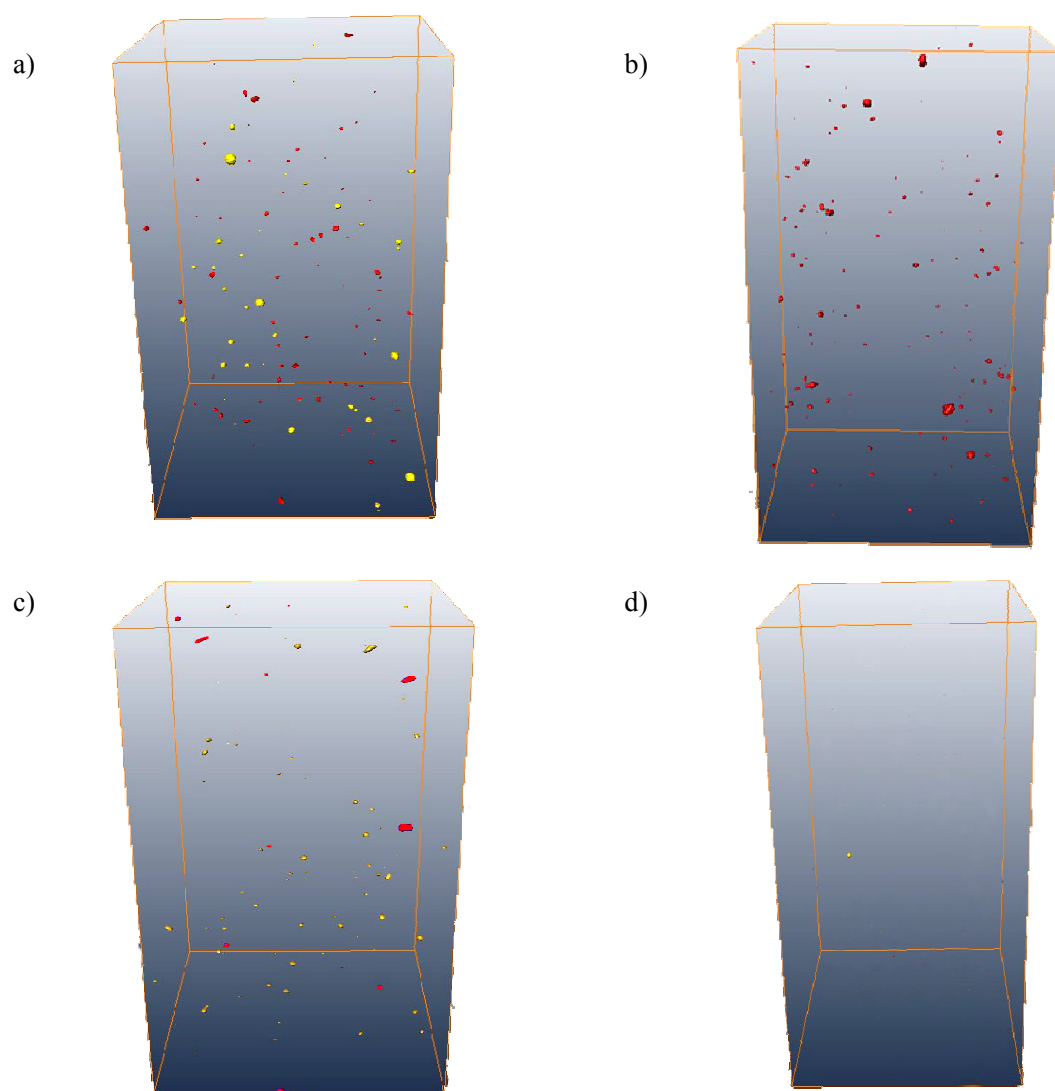


Fig. 4-53 Reconstructed 3D images of CM247LC. Red particles are Hf-rich inclusions; yellow particles are pores or alumina.

a) Hf-containing, as-HIPped 1100 °C/150MPa/4h;

b) Hf-containing, HIP 1260 °C/150MPa/2h + Solution 1100 °C/1h/FAC + Age 870 °C/16h;

c) Hf-containing, HIP 1260 °C/150MPa/2h + Solution 1260 °C/1h/FAC + Age 870 °C/16h;

d) Hf-free HIP 1260 °C/150MPa/2h + Solution 1100 °C/1h/FAC + Age 870 °C/16h.

Table 4-14 Volume fractions of defects in CM247LC

Flaw/defect type	Hf- containing 1100 °C As-HIP	Hf- containing 1260 °C HIP+ 1100 °C Sol+ Age	Hf- containing 1260 °C HIP+ 1260 °C Sol+ Age	Hf-free 1260 °C HIP+ 1100 °C Sol+ Age
Hf - rich inclusion	0.006vol%	0.014vol%	0.006vol%	0
Al- rich inclusion or Pores	0.007vol%	0	0.039vol%	Trace
Total	0.013vol%	0.014vol%	0.045vol%	0

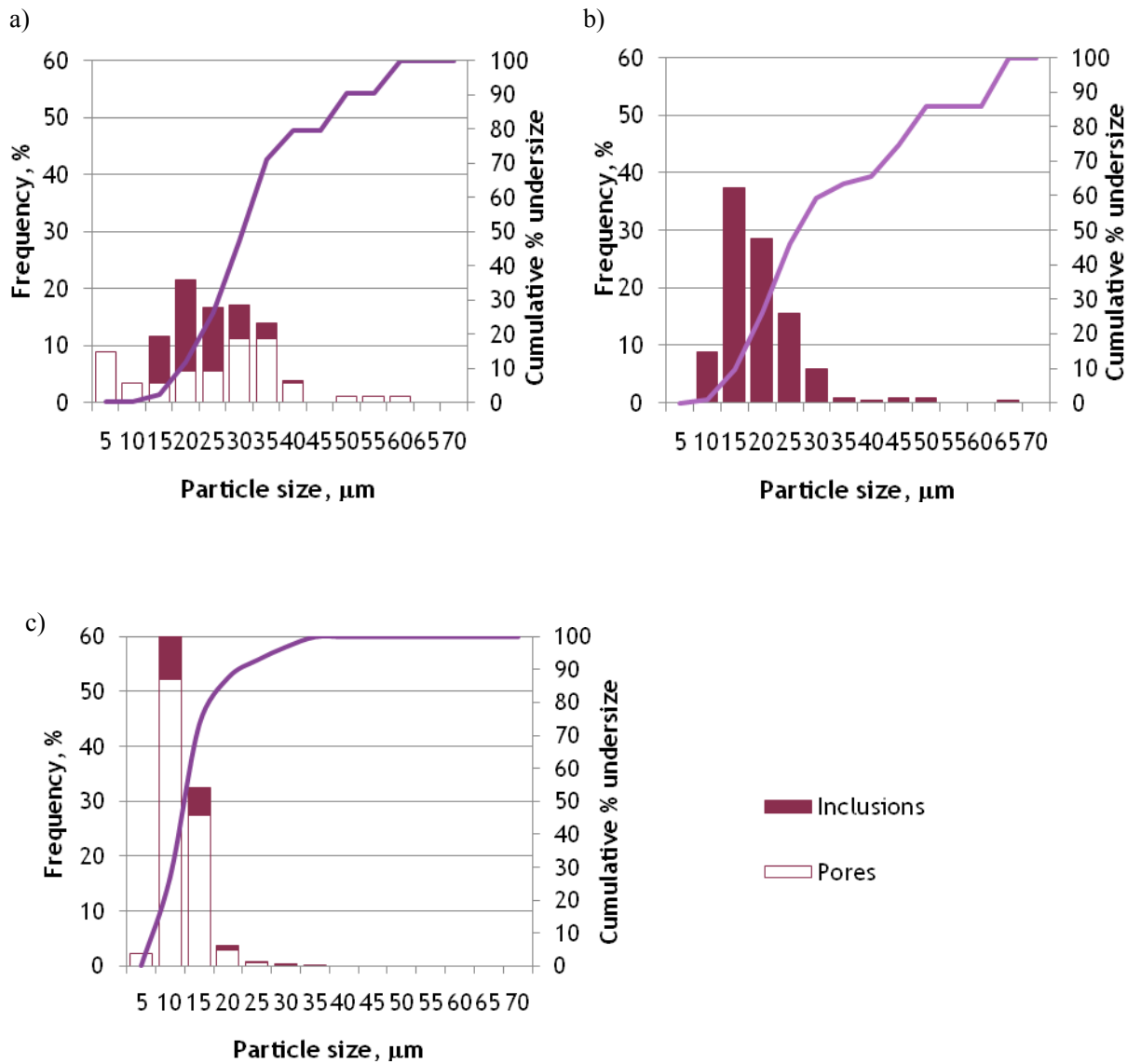


Fig.4-54 Quantitative analysis of defects in Hf-containing CM247LC (raw data are given in Appendix 2)

a) as-HIPped 1100 °C/150MPa/4h;

b) HIP 1260 °C/150MPa/2h + Solution 1100 °C/1h/FAC + Age 870 °C/16h;

c) HIP 1260 °C/150MPa/2h + Solution 1260 °C/1h/FAC + Age 870 °C/16h;

4.4.4 Comparison of mechanical properties of Hf-containing and Hf-free CM247LC

Creep measurements have been carried out to assess the influence of Hf on the high temperature properties of the CM247LC HIPped at 1260 °C + 1100 °C solution treated + aged. The tests were done under the conditions given in §4.3.2.3. The results are compared with the Hf-containing CM247LC processed using the same conditions. The quick creep curves in Fig. 4-55 do not show much difference between the two batches. The creep activation energy of Hf-free CM247LC calculated via the fitting line (Fig. 4-56) was 456 KJ/mol, and the stress exponent obtained in Fig. 4-57 was 3.74. The values of Hf-containing CM247LC are 429.5 KJ/mol and 4.11 respectively. The absence of Hf increased the creep rate over the tested temperature range and stress range.

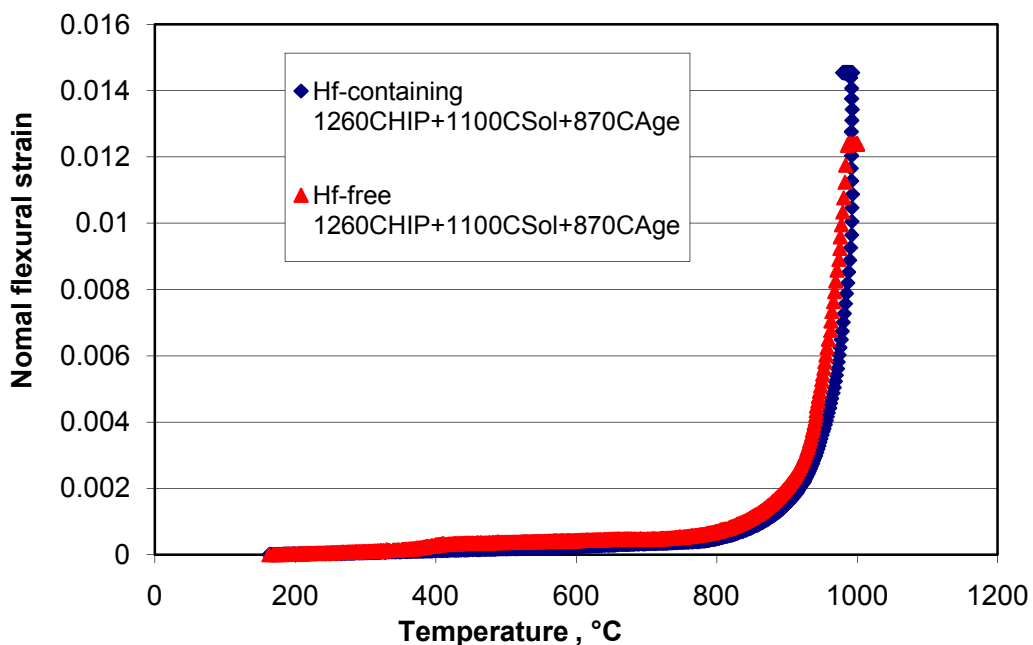


Fig. 4-55 Quick curves of Hf-containing and Hf-free CM247LC

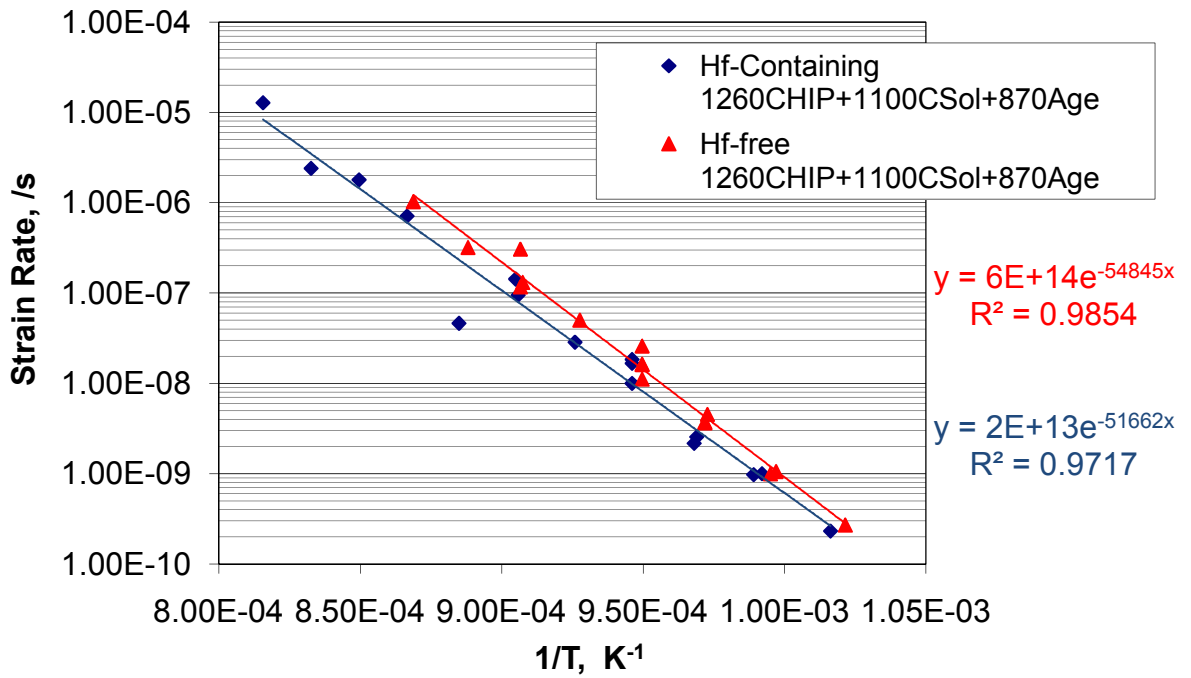


Fig. 4-56 Temperature dependence of the creep rate of HIPped CM247LC at 350MPa.

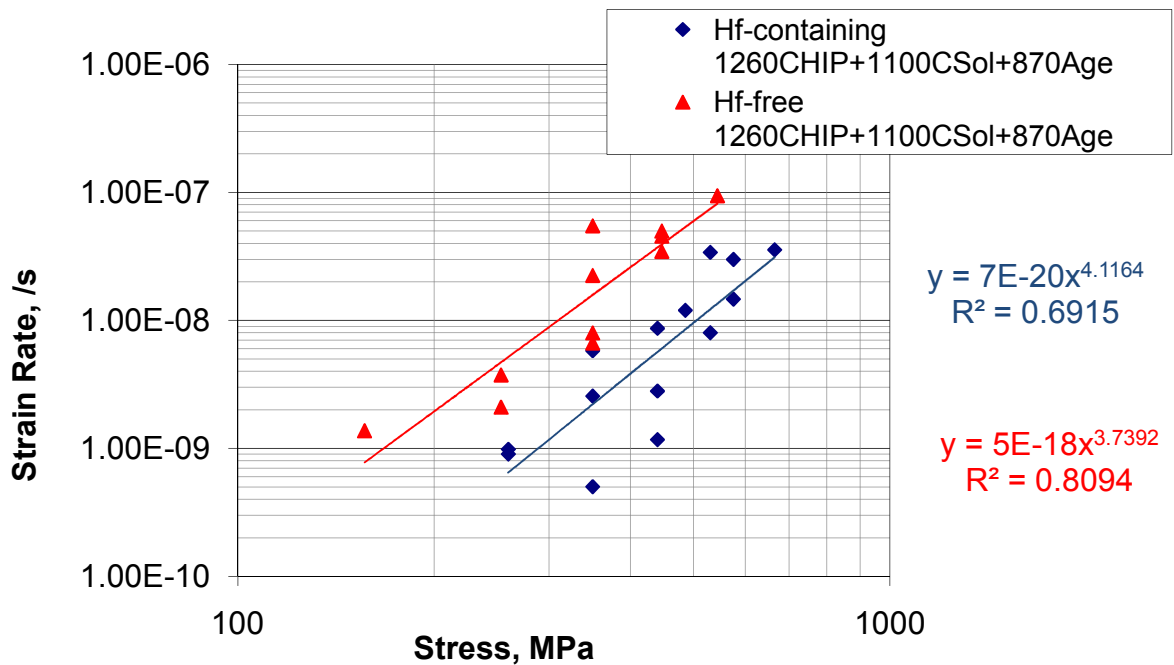


Fig. 4-57 The stress dependence of the secondary creep rate of HIPped CM247LC at 760 °C

4.4.5 Summary

Hf is the main inclusion-former in the HIPped CM247LC. The inclusions are HfO₂ with Al₂O₃ cores. This type of inclusion can be eliminated by removing Hf. Hf is more concentrated on the powder surfaces than in the powder interior in Hf-containing CM247LC.

But the removal of Hf degrades the creep resistance of HIPped CM247LC over the temperature range of 700 °C to 950 °C and the stress range of 150 MPa to 550 MPa.

Chapter 5 Discussion

The following aspects of the observations reported in Chapter 4 will be discussed in turn in this chapter: (i) The mechanism behind densification and microstructural development of CM247LC powder HIPping; (ii) the influence of HIPping temperature and solution treatment on microstructure and mechanical properties; (iii) the role of inclusions as initiators of cracks in tensile and fatigue tests; (iv) the role of Hf in CM247LC HIPping, i.e. the formation of inclusions; (v) the recommendations on powder HIPping of nickel-base superalloy.

5.1 The response of powder to HIPping

5.1.1 Densification mechanism

The process of densification in HIPping is the closing of interparticle pores under different mechanisms [Atkinson and Rickinson 1991]. For less dense material (at tap density) under the highest pressures at the beginning of the process, interparticle pore closure occurs by yielding via dislocation glide. This stage would be completed as the temperature and pressure are increased since glide is a rapid process. The material then enters the state where pore closure relies on the time-dependent process of power-law creep where the flow rate is dependent on some exponent of the applied pressure. The exponent is controlled by the material and the processing conditions. It can be as low as 3 or as high as 15. This highlights the value of reaching high pressures in the HIPping process. In the final stages, as larger densities are approached, holes are filled by diffusion. In this stage, it is important that pores should be located on grain boundaries for relatively fast diffusion.

Equations to calculate the densification rate during HIPping have been developed by earlier researchers [Swinkels *et al.* 1983; Helle, Easterling *et al.* 1985; Kang 2005]. The sintering process is commonly modelled in two stages. During the *initial stage* (Fig. 5-1 a)), while the relative density is up to 90%, the individual powder particles are still recognisable and densification is modelled by the growth of necks where the particles are in contact, and by the increase in the number of such contact points. During the *final stage* (Fig. 5-1 b)), while the relative density is between 90% and 100%, the remaining porosity is modelled as an array of spherical holes which shrink in diameter as sintering proceeds. The holes will eventually close by the diffusion of surrounding material if no gas is entrapped.

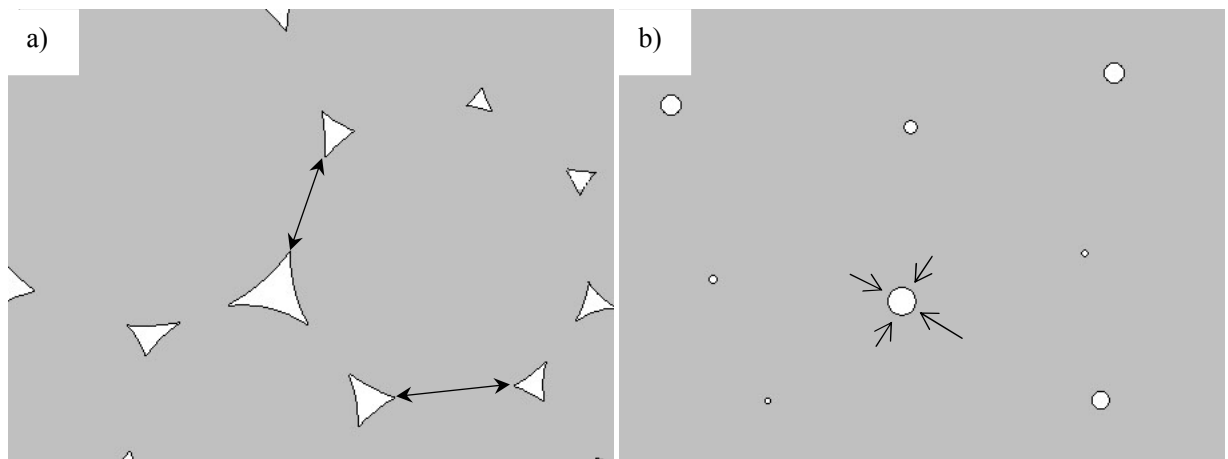


Fig. 5-1 Sketch of sintering process in modelling. a) relative density up to 90%, pore closing process by growth of necks; b) relative density between 90% to 100%, pore closing by shrinking of spherical holes.

When pressure is first applied to a powder compact, it will first deform by plastic yielding if the pressure is high enough. This causes the average contact area to grow and the effective pressure to fall until the yield stress of the material is no longer exceeded. For the initial stage of the sintering, the relation between the effective pressure and external applied

pressure is given [*Helle, Easterling et al. 1985*] by:

$$P_{eff} = \frac{P(1 - D_0)}{D^2(D - D_0)} \quad (5.1)$$

Where D is the relative density of the compact, D_0 is the tap density of powder, P is the external pressure applied. It can be noted the value of effective pressure is larger than that of the external applied pressure and decreases as the compact is densified. When D approaches 100%, the effective pressure is approximately the same as the external applied pressure.

If the external applied pressure P is large enough, the flow strength of the material is exceeded locally where particles touch. It has been modelled that the neck grows until the local effective pressure $P_{eff} \approx 3\sigma_y$ (Swinkels et al., 1983), where σ_y is the tensile yield strength of the material of the particle. Combining this criterion and equation 5.1 shows that the increase in density contributed by this process is instantaneous and can be interpreted to be [*Helle, Easterling et al. 1985*]

$$D_{yield} = \left(\frac{(1 - D_0)P}{1.3\sigma_y} + D_0^3 \right)^{1/3} \quad (5.2)$$

Where D_0 is the tap density of powder, σ_y is the yield strength of the material, P is the external pressure applied.

The compact enters final stage sintering during plastic yielding only if the pressure is high enough to cause yielding of the spherical shell surrounding each pore. The limiting pressure for yield is given by [*Helle, Easterling et al. 1985*]

$$P_{lim} = \frac{2\sigma_y}{3} \ln \left(\frac{1}{1 - D} \right) \quad (5.3)$$

In this case, the starting density for the time-dependent mechanisms is [Helle, Easterling et al. 1985]

$$D_{yield} = 1 - \exp\left(-\frac{3P}{2\sigma_y}\right) \quad (5.4)$$

In the case of this project, the external applied pressure was 150MPa for all temperatures. The yield strength of CM247LC at different HIPping temperatures can be estimated using line regression method from Fig.4-37. The effect of gas trapped in the pores is ignored. Because the volume of a gas-filled pore will be reduced by the ratio of atmospheric pressure to HIP pressure i.e. about 1500 times, so they are negligible. Then using the above equations, the density achieved by the pressure applied could be worked out. The parameters and results are listed in Table 5-1. The calculated results are plotted in Fig. 5-2 and compared with experimental results. As the model is based on powder particles of the same size, the actual value should be larger than the calculation because some densification could be caused by smaller particles being pushed into inter-particle positions early in the deformation process.

Table 5-1 Starting density of CM247LC contributed by plastic yield

HIP temperature(°C)	P (MPa)	σ_y (MPa)	D_{yield} (%)
800	150	880	71.8
900	150	590	73.1
1000	150	290	76.8
1100	150	95	90.6
1200	150	26	99.98

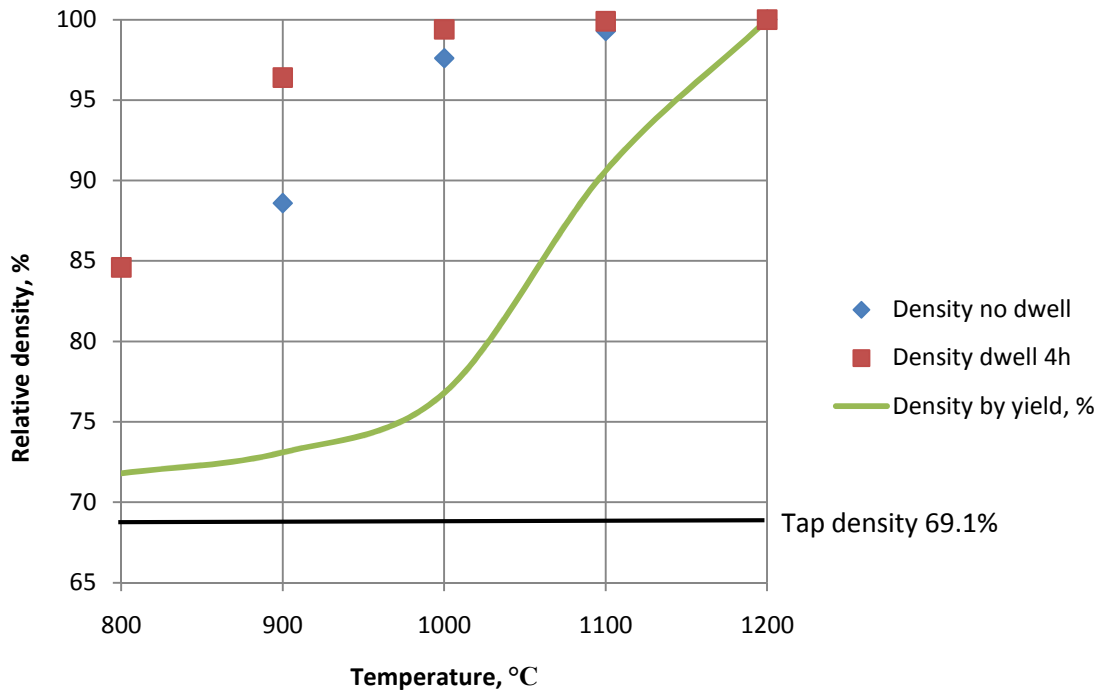


Fig. 5-2 Starting density of CM247LC contributed by plastic flow. The continuous line is the calculated density contributed by plastic flow; the discrete dots are experimental data.

It should be noted that when the temperature exceeds 1100 °C, the compact enters the final stage of sintering under a pressure of 150MPa. According to this model, when the temperature reaches 1200 °C, nearly full density could be achieved by plastic flow only. The value at this point is about the same as the experimental data. For the other temperatures, there are big gaps between the plastic yield densities and the experimental densities. This fact indicates that the time-dependent mechanisms – creep and diffusion play a significant part in the compact densification at these temperatures. The difference of densification mechanisms between samples HIPped above and below 1200 °C is the main aspect that causes the differences between their microstructures. This will be discussed in the next section.

5.1.2 Bonding behaviour of CM247LC powder

The application of temperature and pressure contributes to both the instantaneous process (plastic yielding) and the time-dependent processes (creep and diffusion), while the dwell time is essential for the time-dependent processes. Different levels of the two parameters (time, temperature) result in different microstructures of the products shown in the previous chapter.

Bonding of powder particles takes place at the same time as the densification takes place. There are two main changes to be noticed while the temperature increases, as shown in Fig.4-9. One is the increased density; the other is the change in the microstructure. Recrystallisation layers were formed at powder-particle contacting areas in samples which were cooled as soon as they reach the HIPping temperature of 1000 °C (i.e. interrupt-HIPped) with the rest of the powder particle having a similar microstructure to the sample interrupt-HIPped at 900 °C. The big particles are still spherical but the small ones are crushed and squeezed into the inter-particle pores (Fig. 4-9 c) d)). The density increase compared to the 900 °C sample is actually due to the crushing and squeezing of the small particles into pores (Fig. 4-8 b)). The grain size in the contact area and the crushed particle area is obviously much smaller than in the interior of the larger powder particles. This indicates that these sites are the preferred site for recrystallisation which is associated with plastic deformation. The effective stress levels in the particles during the initial stage of the HIPping process have been previously simulated[DeLo *et al.* 1999], see Fig. 5-3; it was found that the part near the contact area of a particle experienced higher stresses than the central part of the same particle causing more deformation at the contact area. Furthermore, the smaller particles experienced higher stresses than the larger particles causing them to experience more deformation. The deformation of the smaller particle accommodated the rigid body motion

of the larger particles which in turn increased the packing efficiency and relative density.

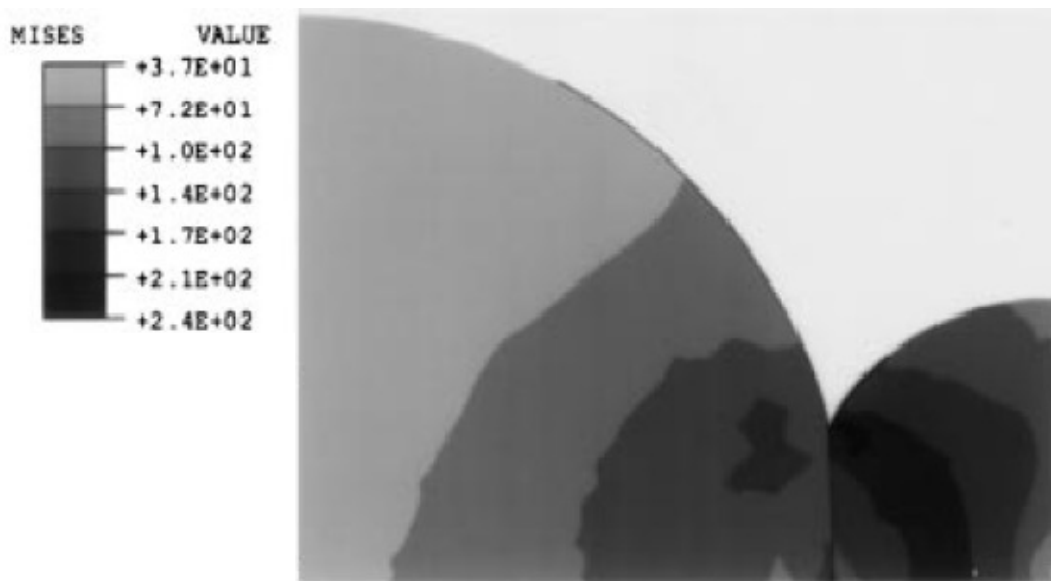


Fig. 5-3 FEM interparticle contact analysis showing relative particle deformation and effective stress levels resulting from contact deformation by plasticity and creep. Loading is compressive parallel to the 2 direction. Stress units are MPa. Taken from [DeLo and Piehler 1999]

As the temperature is increased to 1100 °C, the sample is almost fully densified (Fig. 4-8 c)). Only large original powder particles can be seen, around which a layer of smaller grains are observed (Fig. 4-9 e) f)). The data in Fig.5-3 suggests that this could be a result of the smaller powder particles being crushed and filling the pores; part of the big particles is also deformed. The recrystallisation layer is thicker than that formed at 1000°C and the recrystallised grains are also observed to pass prior particle boundaries, indicating good bonding took place. Recrystallisation may also occur in large powder interiors but not as rapidly as in the more highly deformed sites.

The 4 hour dwell time allows the recrystallisation layer also designated “necklace” structure elsewhere to grow at 1100 °C (Fig. 4-12 a) b)). The ‘necklace’ in other researcher’s work was found to be along grain boundaries in hot worked nickel-base alloys or Ni₃Al forged at certain temperatures and a specific extent of deformation [Jeandin 1982; Jeandin, Bartout et al. 1986; Aretz et al. 1992; Ponge et al. 1998], which occurs during dynamic recrystallisation. The preferred nucleation site at grain boundaries is associated with the higher stored energy in the vicinity of the grain boundaries [Bee, Jones et al. 1980]. The recrystallised new layer in Fig. 4-12 b) does not penetrate the whole particle at this temperature either because the deformation energy at the recrystallisation front is not adequate and/or that the time is not sufficient to achieve equilibrium.

At the temperature of 1200 °C, it is obvious that both the deformation rate of the powder particles and the diffusion of atoms are faster than at 1100°C. Compare Fig. 4-12 c) and d); it seems that the recrystallisation layers grow from the powder boundaries toward the powder particle centre after 4 hours’ dwell time. The compact is then fully recrystallised and no prior particle boundaries can be seen.

The formation of carbides was also accelerated by the deformation and recrystallisation. The solvus of carbides in CM247 is reported to be 1342 °C, which is very close to the incipient melting temperature [Zhang and Singer 2002] so that carbide precipitation would be expected at all temperatures. Fig. 4-6 a) taken from the as-received powder shows no obvious carbides whereas HIPped samples show carbide formation at 1100 °C and above. The role of deformation is clear from Fig. 4-6 c) and Fig. 4-9 e). Both samples were processed at 1100 °C with the former one heat treated in vacuum and the latter one under 150 MPa pressure. Carbide particles can be seen in the latter sample, especially in the vicinity of prior particle boundaries, while the former one remains in a similar state to the as-

received powder particle. This feature of carbide precipitation is more obvious in etched samples shown in Fig. 4-12 a) and b). As the temperature reaches 1200 °C, the distribution of carbides becomes uniform, i.e. the particle boundaries area was no longer the preferred site for carbide precipitation (Fig. 4-12 c) and d)). The precipitation of carbides is also preferred to be at prior particle boundaries as it is assisted by deformation and recrystallisation and also at grain boundaries. The data in Fig. 4-19 suggests that the number of carbides is greater when HIPped at 1100 °C than at higher temperatures which is reasonable since 1100 °C is further below the solvus. It is also possible that some carbides are precipitated during cooling after HIPping.

5.2 The influence of HIPping temperature on microstructure and mechanical properties

5.2.1 The influence of HIPping temperature on microstructure of CM247LC

The morphology of γ' in as-HIPped CM247LC is determined by the HIPping temperature. Comparison of samples HIPped above and below the solvus show more cubic morphology matrix gamma prime in the higher temperature HIP (Fig. 4-16), reflecting a slow cool through the solvus. The gamma prime morphology of the lower temperature HIP samples is not as cuboidal, probably due to non-equilibrium nucleation and growth of existing gamma prime [Podob 1977]. The position of the 'necklace' structure was changed from prior particle boundaries to grain boundaries when HIPped above the solvus (Fig.4-13). This can be due to the mechanisms of their formation. The formation of prior particle boundary 'necklace' is associated with the concentrated local stress during HIPping as mentioned

previously, and this layer can grow at higher temperature and over time (Fig. 4-12). The formation of grain boundary ‘necklace’ can be due to the higher diffusion rate of γ' forming atoms along the grain boundaries when the sample is slowly cooled through the solvus, so larger γ' particles can be precipitated at grain boundaries rather than in the grain interior. This will be explained in detail via the development of the microstructures in the following paragraphs.

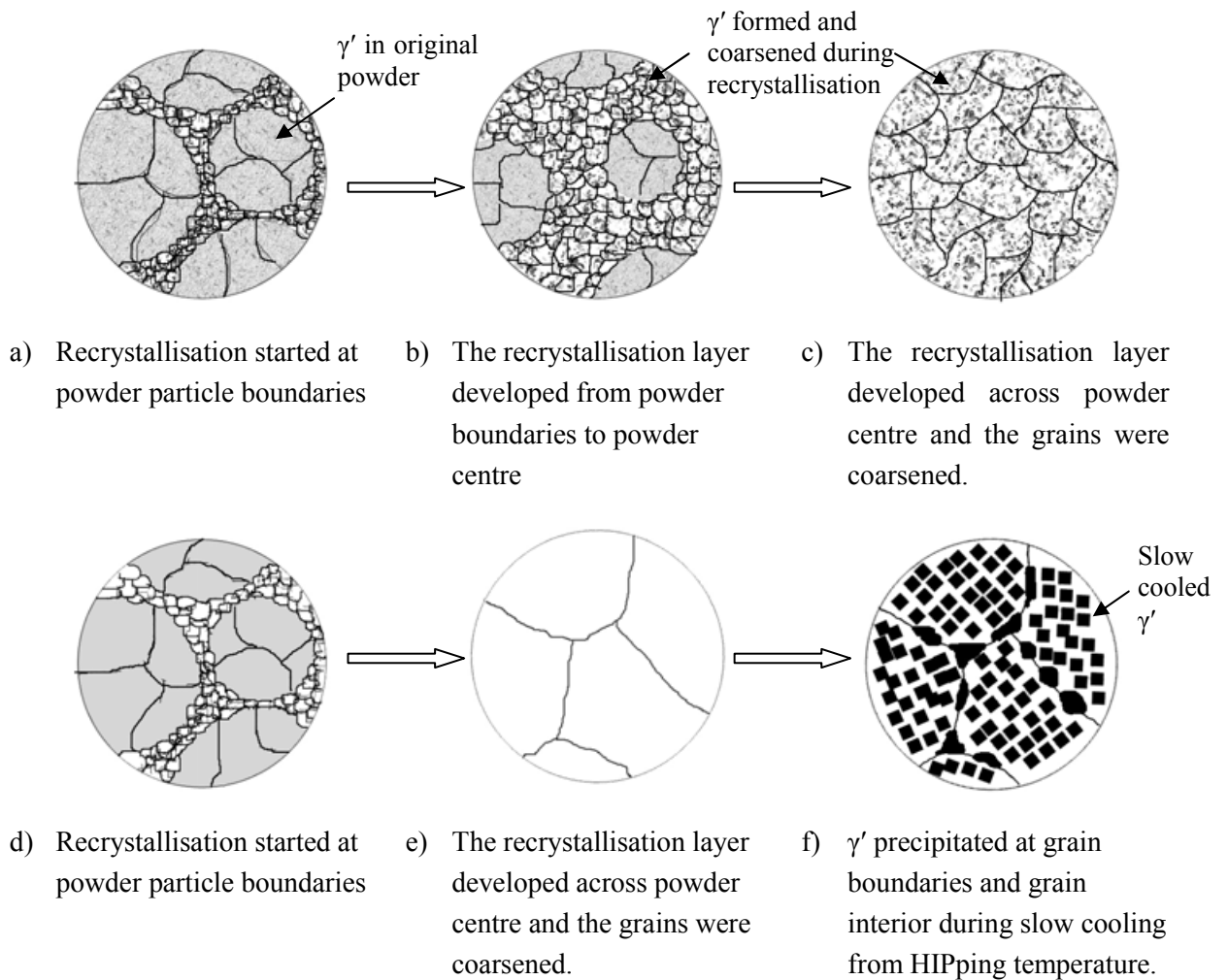


Fig. 5-4 Sketch of microstructural development during HIPping. a)-b)-c) is the route HIPped below γ' solvus; d)-e)-f) is the route HIPped above γ' solvus. Smaller grains are recrystallisation layers in a), b), and d). Black dots are γ' particles in a), b), c) and f).

The microstructural development of CM247LC HIPped above 1100 °C is sketched in Fig. 5-4. Carbides will be discussed later and are not taken into consideration here. As discussed in the previous section, the density of the CM247LC compact reaches almost 100% when the temperature is over 1100 °C. When the temperature is below the γ' solvus, the microstructure changes along the route of a) – b) – c) shown in Fig. 5-4. The recrystallisation layer starts to form and grow as small grains around prior particles when the temperature and pressure are ramping up, which is shown in Fig. 5-4 a). This layer becomes wider during the dwell period, in which the prior particles still remain (see Fig. 5-4 b)). If the time and temperature are high enough, the material can be fully recrystallised and no prior particles can be observed as shown in Fig. 5-4 c). As the temperature is kept below the γ' solvus, γ' particles precipitate at the same time as grain growth in the whole HIPping process. Experimental evidence for the route for samples HIPped below the γ' solvus is shown in Fig. 4-12 and Fig. 4-13 a) and b).

The microstructural development of CM247LC HIPped above the γ' solvus could follow d) – e) – f) route in Fig. 5-4. The microstructure should be the same as Fig. 5-4 a) when the temperature is ramping up but has not yet reached the solvus. Once the temperature is over the γ' solvus, the existing γ' particles or nuclei (could be formed during fast cool from liquid) begin to dissolve (see Fig. 5-4 d)). This could happen in a very short time as the existing γ' particles are very small. The recrystallisation layer of the samples HIPped above solvus grows much faster than those HIPped below solvus in Fig.5-4 a) b) c), not only because it gets more energy to grow at higher temperature but also because of the absence of γ' particles retarding boundary migration. A γ matrix of large grains is produced after the dwell period above the γ' solvus as shown in Fig. 5-4 e). The strengthening γ' particles are all produced by slow cooling from the above the γ' solvus temperature (see Fig.5-4 f)). Thus the

morphology of the γ' particles develop following the sequence of spheres-cuboids-cubical arrays-dendrites [Ricks, Porter et al. 1983]. Large irregular γ' particles are formed on the grain boundaries because of the higher diffusion rate of γ' -forming elements along grain boundaries [Henry, Yoo et al. 1993]. The irregular shape is because the γ' particles are growing into surrounding grains of different orientations and these grain boundaries have different mobility. The actual samples HIPped above the solvus Fig. 4-13 c) and d) demonstrate the same final structures as in Fig.5-4. The morphology in Fig. 5-4 d) and e) is interpreted from the existing observation (of microstructure of recrystallisation behaviour in Fig. 4-12) and calculation (in Fig. 5-2 that the density achieves 100% by plastic flow only above 1200 °C). Interrupt quench from 1260 °C HIPping needs to be done to support this interpretation about the microstructural development during HIPping above the solvus as shown in Fig. d) and e).

The carbides are not dissolved during HIPping but will tend to achieve equilibrium from the non-equilibrium status resulting from the rapid cooling during gas atomising. Apart from the 1100°C HIP, the carbide morphology of the samples HIPped at 1200°C, 1260° and 1320°C are similar (Fig. 4-18 and Fig. 4-19). This indicates that the equilibrium statuses of carbides are similar during HIPping at 1200°C, 1260° and 1320 °C.

5.2.2 The influence of HIPping temperature on mechanical properties of CM247LC

Different HIPping conditions produce different microstructures, thus the mechanical properties of the specimens are different. The fracture surfaces of hammer impact tests reveal the prior particle boundaries of the 1100 °C HIP in which the recrystallised layer does not grow across all the original particles, i.e. the crack propagates along the path of this layer

along prior particle boundaries (Fig. 4-21 a)). Particles in size similar to the coarse carbides in the vicinity of prior particle boundaries are found in the particle-shaped dimples (Fig. 4-21 c)), this suggests they debond from the matrix under the impact. The 1200 °C HIPped CM247LC showed more ductile and even fracture surfaces than those HIPped at 1100°C (Fig. 4-21 b)), no particular features found (Fig. 4-21d)). This homogeneity is in agreement with its microstructure of fracture surface appearance (Fig. 4-13 b)).

The 1200 °C HIPped CM247LC showed a mixed mode of fracture surface in tensile tests. The cracks were observed to propagate mostly along grain boundaries but they did also propagate through grain interiors. However, some prior particles can still be seen on fracture surfaces (Fig. 4-24 a),c) and e)), but the morphology of prior particle boundaries on the fracture surface is not as obvious as in the hammer-tested samples which had been HIPped at 1100 °C. It is likely that the sintering state after 1200 °C HIP should be as the sketch shown in Fig. 5-4 b) rather than Fig. 5-4 c). The recrystallisation layer does not actually grow across the centre of the original powders.

The fracture surfaces of the samples which were super-solvus HIPped at 1260 °C showed ductile modes of fracture over all the test temperatures. The topology of the surfaces is somewhat similar to the 1200 °C HIP, but no obvious prior particles are found and there are also more dimples which tended to be deeper. This is in agreement with the ductility data of the materials – those HIPped at 1260 °C were more ductile than those HIPped at 1200 °C.

As with many other γ' -strengthened nickel-base superalloys, the 0.2% proof strength of powder HIPped CM247LC increases as the test temperature increases (Table 4-4). This is due to the 0.2% yield strength versus temperature behaviour of the ordered L_{12} structure γ' (Fig. 2-8) which is associated with cross slip onto $\{100\}$ planes of $\frac{1}{2}\langle 110 \rangle$ dislocations

which become locked [Kear et al. 1974]. The superior 0.2% proof strength of the samples HIPped at 1200 °C to those HIPped at 1260 °C could be associated with the smaller grain size according to Hall-Petch relationship. In this case, the ductility of the samples HIPped at 1200 °C should be also better than those HIPped at 1260 °C, but the fact is opposite. Other factors may control the strength and/or ductility such as the carbide morphology and γ' distribution. As the carbide morphology is stable above 1200 °C HIP, the different distribution of γ' particles could be the more important factor. Since the γ' volume fraction is almost the same after the two HIP treatments, the coarse γ' particles along grain boundaries will lead to a decrease in the amount of fine γ' available to enhance the yield strength of the alloy. Hence, compared to the sample HIPped at 1200 °C, the sample HIPped at 1260 °C will not be strengthened to the same extent. It had been stated that a high strength alloy will favour grain boundary cracking and a low strength alloy will favour grain deformation [Pearcey et al. 1967]. Thus, the grains in the sample HIPped at 1260 °C are easier to deform and the coarse γ' strengthened grain boundaries are harder to debond than those in the sample HIPped at 1200 °C.

The initiation of fatigue crack is mainly by debonding of inclusions from the matrix and the initial propagation by glide plane decohesion along $\{111\}$ active slip planes (Fig. 4-26 and 4-27). Facets are conspicuous in all fracture surfaces. The different size of facets corresponds to different grain size. For most metals, smaller grains yield longer fatigue lives but for the condition of this project, the samples with larger grains yield longer fatigue lives at the same stress level. The grain size is less important in the HIPped CM247LC since the gamma prime controls deformation behaviour. It is reported by Fine and Ritchie in 1979 that fine grains with high strength benefit the resistance to fatigue crack initiation and propagation of micro cracks, whereas coarse grains with lower strength benefit the resistance to crack propagation.

For this work, all the fatigue cracks initiate at inclusions at or near specimen surfaces, resistance to crack propagation is then the main aspect to determine the fatigue life, and samples HIPped at 1260 °C with larger grain size plus the grain boundaries strengthened by γ' particles therefore yield longer fatigue lives.

5.2.3 The influence of heat treatment on microstructure of HIPped CM247LC

The purpose of heat treatment has already been stated in Chapter 2. The volume fraction of γ' is not affected by the solution treatment (Fig.4-31), whereas the morphology of γ' is very sensitive to the solution temperature when it is close to the solvus (Fig.4-28, Fig. 4-30) as can be understood from the phase diagram. The composition of CM247LC can be equivalent to the dashed line on the nickel-aluminium binary diagram (Fig. 5-5). According to the lever law, the fraction of γ' can be roughly worked out to be of the order of 50% and 20% at 1100 °C and 1200 °C respectively. Although not accurate, the value is consistent with the amount of the remaining primary γ' in Fig.4-28 and Fig.4-30. The HIP + Aged samples demonstrate little difference from the as-HIPped structure indicating that the as-HIPped structure is already very close to equilibrium during slow cooling through 870 °C. The matrix is not supersaturated for γ' to grow when heating up to 870 °C. For the other samples, they went through a dwell period at a solution temperature so that primary γ' partly or totally dissolved into the matrix. This dwell was followed by fast cooling, giving no time for equilibrium to be reached (as the composition of the matrix remains at A, B and C for solution at 1260 °C, 1200 °C and 1100 °C respectively). The matrix is supersaturated with γ' -forming elements, with remaining γ' and/or quenched γ' nuclei. Once heated up again to a

sufficient temperature, the quenched γ' or γ' nuclei grow until equilibrium at 870 °C (D-D') is reached.

The grain boundary morphology is affected by the behaviour of γ' against solution temperatures, as is the grain size. The grain boundaries are straightened by the total dissolution of the coarse γ' particles after super solvus treatment at 1260 °C (Fig. 4-28). The grains can grow when no coarse γ' particles are present pinning the grain boundaries (Fig. 4-29). The morphology of carbides is relatively stable over the heat treatment so that the change of pinning effect of carbides on grain boundaries over different solution temperatures is negligible compared to the effect of coarse γ' (Fig. 4-34, Fig. 4-35).

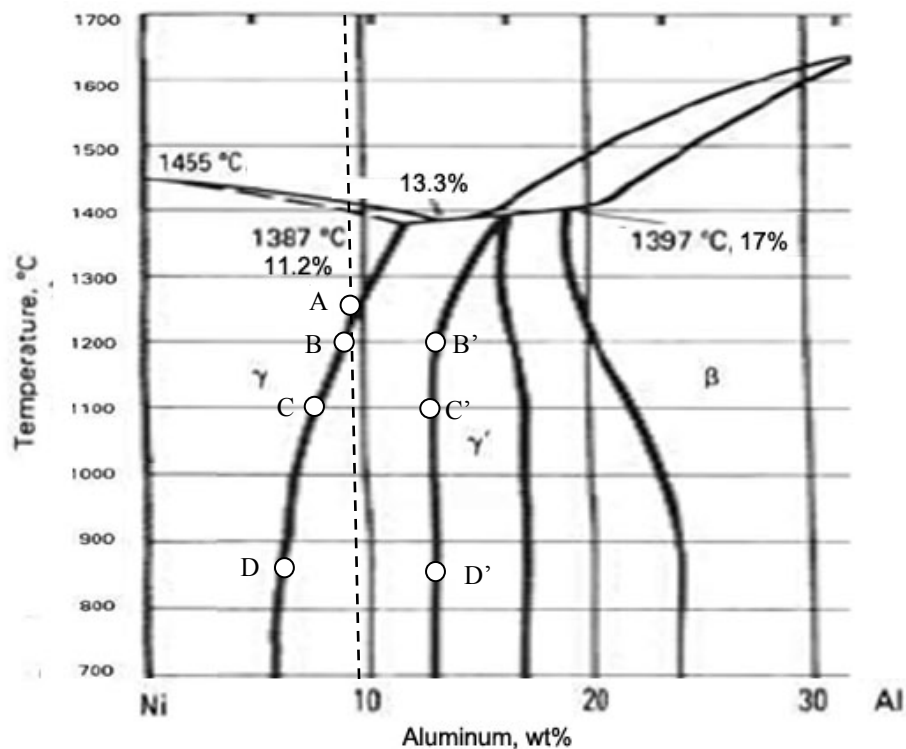


Fig. 5-5 A corner of nickel-aluminium binary phase diagram [Davis 1997]. The dashed line indicates the equivalent composition of CM247LC on the binary system. A, B-B', C-C' and D-D' are equilibrium state of the γ - γ' at 1260 °C, 1200 °C, 1100 °C and 870 °C.

5.2.4 The influence of heat treatment on mechanical properties of HIPped CM247LC

(i) Room temperature tensile

The 0.2 % proof strength and ductility are highly influenced by different heat treatment conditions while the ultimate tensile strength is not as sensitive (Fig. 4-37). The ultimate tensile strength may depend on the volume fraction of the γ' and is influenced by the work-hardening behaviour of the alloy. The samples with necklace structure (the as-HIP and the 1100 °C solution treated) yield inferior yield strength to the necklace-free samples (the 1260 °C solution treated), but better ductility. As the total volume fraction of γ' is constant under different heat treatment conditions (because cooling is slow enough to precipitate all γ') the more coarse particles precipitates there are along grain boundaries, the smaller the volume fraction of γ' remains to strengthen the grain interior. Under the same stress level, dislocations are easier to move in grains that are surrounded by coarse γ' particles, thus the 0.2% proof strength is lower. When the applied stress is further increased, dislocations pile up at grain boundaries where the coarse γ' particles cause the formation of serrated grain boundaries in the 1100 °C solution treated samples. The dislocations may tangle around the coarser grain boundary γ' particles (which is harder to cut through) and the internal stress is then accommodated by the further deformation of the grains and finally the cracks initiate and coalesce at weakest sites which is the inclusion-matrix interface in this case, and propagate intragranularly (Fig.4-38 a) and b)). For the 1260 °C solution-treated samples, although the fine γ' particles improve yield strength of the material, they are more easily cut through by dislocations due to their small size. Once dislocations are piled up along the

active slip planes, cracks will initiate at these planes and propagate intergranularly as no grain boundary strengtheners are present in this batch of samples (Fig. 4-39 a) and b)).

The ductility decreases with solution treatment temperature. When solution treated at 1260 °C the crack is propagated along the faceted grain boundaries suggesting that the boundaries have been weakened by dissolution of boundary γ' particles. The composition of grain boundaries could change during solution treatment and the concentration of grain boundary strengtheners could be reduced. This could be investigated by using WDX to measure the grain boundary composition on samples prepared using a focussed ion beam (FIB) to prepare a thinned sample which contain a grain boundary [Wu *et al.* 2006]. At the lower solution temperatures the ductility appears to be limited by inclusions which are seen to nucleate failure. This will be discussed below in §5.3.

(ii) Elevated temperature tensile

The change of tensile properties at high temperature over solution treatment temperature is similar to the change of room temperature properties over solution treatment temperature which is associated with the morphology of γ' as discussed above. The higher strength and lower ductility of 1260 °C solution-treated samples is due to the fine distributed γ' and absence of grain boundary strengtheners. The initiation of cracks in 1100 °C solution treated samples still occurs at inclusions which will be discussed later.

A ductility trough was observed at testing temperature of 900 °C (Fig. 4-37). According to Fiore [Fiore 1975], there are a number of reasons which can cause ductility minima of alloys at intermediate temperatures. The most important factors in the case of superalloys are: 1) embrittlement of grain boundaries by carbide particles or enrichment with trace elements or oxygen; 2) deformation mechanisms which lead to strain localization and 3) instability of γ'

particles during exposure to high temperatures. Depending on the circumstances, one or several mechanisms may be operating simultaneously. Although not studied in this project, extensive work has been done to characterise the mechanism of this phenomenon in other γ' strengthened nickel-base superalloys [He et al. 2004; Sajjadi, Nategh et al. 2004; Lian et al. 2008; Chu et al. 2010]. Similar conclusions were drawn; namely that the temperature dependence of the elongation was controlled mainly by the slip character within the γ/γ' microstructure. The dominant deformation is cutting of γ' at low temperatures and is bypassing of γ' at high temperatures, the two mechanisms were both observed at intermediate temperatures. In principle it was found that whenever a new deformation mechanism started to operate a decrease of ductility occurred simultaneously [Bettge 1995]. Thus at ductility minima temperatures, high densities of dislocations are found at γ/γ' interfaces and many of them tangle. The operation of multiple slip systems creates dislocation debris and thus produces more barriers for cross-slip. Most importantly, lots of stacking faults exist that also create barriers for cross-slip. The work hardening rate is then very high because of the cube cross-slip producing many sessile dislocations and barriers to further slip and the flow stress quickly reaches the fracture stress at small strains.

(iii) Fatigue at room temperature

The fatigue properties and crack surfaces of the 1100 °C solution treated samples are very similar to the as-HIPped samples because they have similar microstructures. The 1260 °C solution treated sample yields lower fatigue strength. The fracture surface of this sample (Fig. 4-41 and Fig. 4-42) suggests that the propagation of the fatigue crack gives a more faceted surface than seen in the sample solution treated at a lower temperature. This is perhaps associated with the formation of persistent slip bands which are caused by the localisation of deformation during fatigue which is characteristic of precipitate-hardened

alloys and would thus be more likely in the 1260 °C sample where the γ' precipitates are all smaller and there is no coarse gamma prime to block dislocations. It should be noted that initiation of fatigue failure was associated with inclusions in the as-HIPped and in the sample solution-treated at 1100 °C. This will be discussed later.

(iv) Fatigue at elevated temperature

The fatigue strength at elevated temperature decreases from the as-HIPped sample to lower values as the solution temperature is increased. This is in contrast to the proof stress which increases with increase of solution treatment temperature. This suggests that the mechanism of crack propagation is not controlled by the factors that control tensile strength. The crack surface in the region where slow crack growth is occurring appears to be more faceted in the sample solution treated at 1260 °C than in the 1100 °C solution treated sample suggesting that persistent slip bands are formed during slip (because of the smaller gamma prime) and thus that the fatigue is linked more to this aspect of the microstructure. Note that the fatigue fracture surface of 750 °C tested samples is not like the tensile tested one, the cracks propagated intragranularly rather than along the grain boundaries. Initiation of the fatigue failure is again always associated with inclusions but the inclusions may be subsurface. Again the role of inclusions will be discussed later.

(v) Creep behaviour

1260 °C solution treated CM247LC presents better creep resistance over the tested temperature range and stress range. The creep of the samples at the testing range can be identified as dislocation creep as the stress exponent is in the range of 3~10, while for the diffusion-controlled creep, the stress exponent would be 1. The activation energy of dislocation creep is normally equal to self diffusion energy of elements in matrix. The tested

value is around 400 KJ/mol, it can be considered as an average value of the self diffusion energy of compositional elements (W exhibit slowest diffusivity in nickel at 571KJ/mol[Chaudhuri 1969], Al, Ti and Ni have self diffusion energy at about 270 KJ/mol, 257 KJ/mol and 280 KJ/mol respectively [Zhao, Xie et al. 2004]). The creep of CM247LC has grain size dependence at chosen test conditions (760 °C/350MPa) which is consistent with creep behaviour reported previously [Nabarro et al. 1995] .

5.3 The role of inclusions on initiation of failure

As noted above, the samples tested in tension and fatigue failed at inclusions for virtually all conditions. It is not usual for inclusions to nucleate failure in tensile tests and in this section the role of inclusions will be discussed. It has been reported that brittle second phases or inclusions reduce the fracture strain of several types of steel and some nickel-base superalloys [Nazmy and Singer 1985]. They normally act as stress concentrators that initiate failure. The literature shows that the mechanisms of crack formation at constituent particles are dependent on the slip characteristics of the matrix, the relative properties of the inclusion and the matrix, the inclusion size and the strength of the particle-matrix interface.

5.3.1 The role of inclusions on initiation of failure in tensile

Cracks are frequently found to initiate at inclusions beneath the sample surface in tensile test samples which are as-HIPped and HIP + 1100 °C solution treated + aged (Fig. 4-23, Fig.4-38). Inclusions are obviously sites of stress concentration, which explains their role in the fracture nucleation process. Their bonds with the rest of the matrix are weaker than the bonds between grain boundaries; therefore, fracture is likely to be nucleated at the inclusion-matrix interfaces. Assuming the inclusions are spherical in shape, the possible location of

inclusions in a test piece could be as shown in Fig. 5-6 where it is indicated that for a particle which intersects the surface the weakened zone will be smaller. With the same dimension, the ones in a subsurface zone introduce a large weakened zone at the samples surface, thus the inclusions at this location are preferred crack initiation sites. The fact that inclusions are the source of failure in tensile tests suggests that there is a very high density of such inclusions in these samples. However inclusions do not nucleate fracture in the tensile test samples of HIP + 1260 °C solution treated + aged. The inclusions in this sample are smaller than those in other samples (Table 4-14 and Fig. 4-54) and this could make the inclusions less likely to act as crack initiators, as suggested above. The fact that the proof stress of these samples is higher than for those samples solution treated at 1100 °C would make failure at inclusions more likely and it appears that the reduction in size is more important.

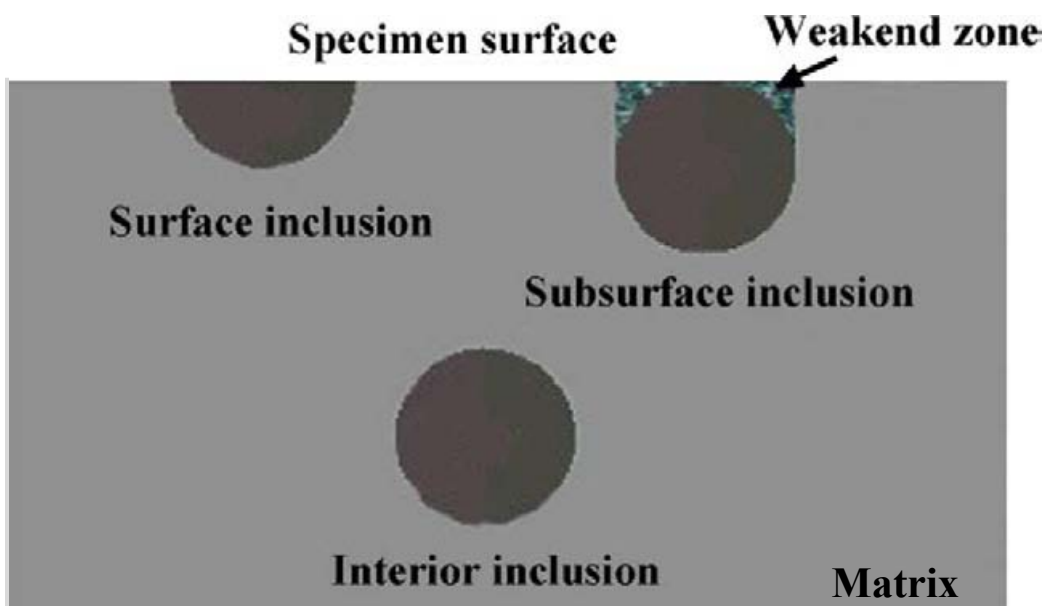


Fig. 5-6 Three types of inclusion locations in a test piece.

5.3.2 The role of inclusions on initiation of failure in fatigue

Nonmetallic inclusions are important defects influencing the fatigue properties of materials [Broek 1973; Luyckx 1975; Kumar et al. 1984; Laz et al. 1998]. At certain applied fatigue stress amplitude, it is assumed that only when the size of an inclusion is greater than a critical value the inclusion may act as the crack initiation site; otherwise fatigue cracking will not occur or will take place at other type of defects. This critical value is defined as the 'critical inclusion size' (CIS). Accurate identification of this value is very important to the quality control and life prediction of the material.

Experimentally, the CIS is generally obtained from extrapolation method, as shown in Fig. 5-7. First, a figure giving the relationship between the size (inclusion diameter, \emptyset , μm) and location (the distance from the inclusion to surface, D , μm) of inclusions at which the fatigue crack initiated is obtained from experimental measurements. Then, the lowest line is drawn by passing through two data points, below which no other data point exists. The line is extended to intersect the ordinate at $D = 0 \mu\text{m}$ (i.e. the specimen surface). The intercept is considered as the CIS of steel investigated. Apparently, it is assumed that the lowest CIS should be for an inclusion which is located on the specimen surface. However, it is obvious that in this method a large number of fractured specimens are required to define the line below which no points lie. For the present study, it is not possible to determine CIS using this method not only because the number of samples tested is small but also because all samples failed at surface inclusions.

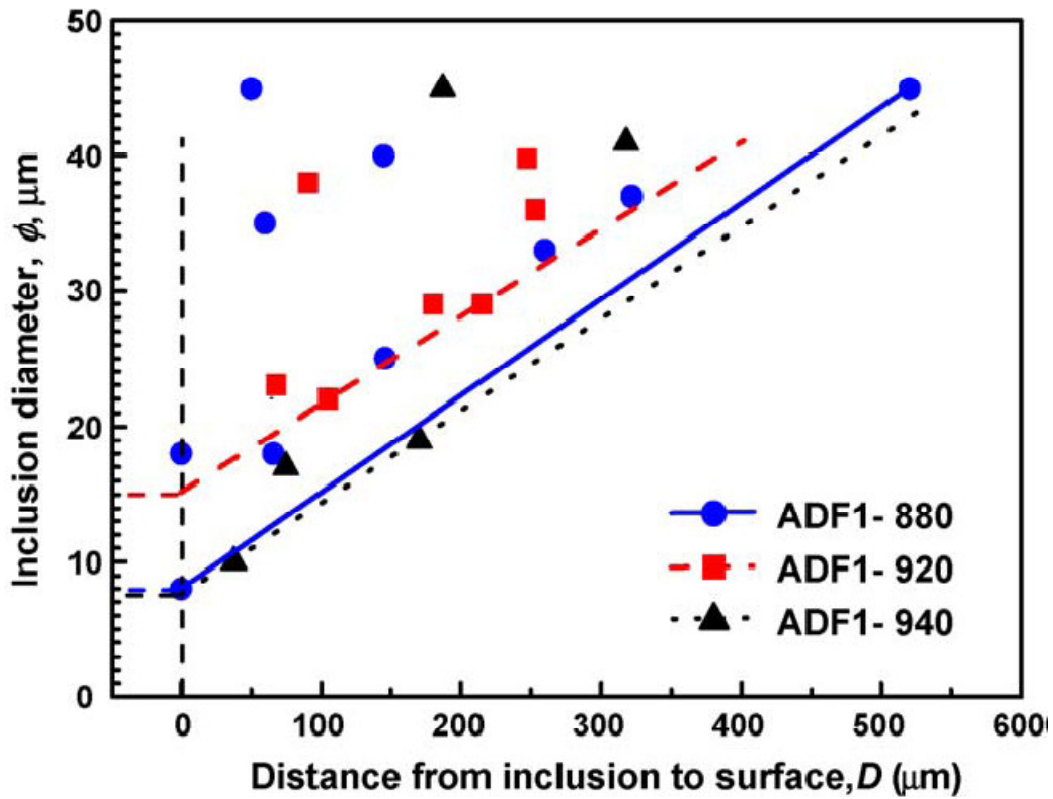


Fig. 5-7 Extrapolation for the determination of CIS. Picture shows the relationship between inclusion diameter and distance from inclusion to surface in three ADF1 steels. Taken from [Yang et al. 2006]

Models predicting the effects of defects, inclusions on fatigue strength of metals are reviewed by Murakami and Endo [Murakami et al. 1994]. They also proposed a model based on fracture mechanisms and experimental data of steels. The fatigue strength σ_w determined by a nonmetallic inclusion is given by

$$\sigma_w = \frac{C(H_v + 120)}{(\sqrt{\text{area}})^{1/6}} \times \left(\frac{1-R}{2}\right)^\alpha \quad (5.5)$$

Where $\alpha = 0.226 + H_v \times 10^{-4}$, C is location constant for surface and internal inclusions equal to 1.43 and 1.56 respectively; H_v is Vickers hardness in MPa; R is the stress ratio; \sqrt{area} in μm , is geometric parameter of a defect, which is defined as the square root of the area obtained by projecting a defect or a crack onto the plane perpendicular to the maximum tensile stress. This equation is valid with an error less than $\sim 15\%$ when the value of \sqrt{area} is up to $1000 \mu\text{m}$ and $H_v = 100 \sim 740$.

For the condition of this project, $R = 0.1$ and the inclusion size at initiation sites is of the order of $20 \mu\text{m}$, thus the predicted life is calculated to be 549 MPa to 587MPa in the valid hardness range. The predicted life is lower than the tested value of 770 MPa. In the other way, the \sqrt{area} value needed to maintain the stress limit at 770 MPa is calculated to be up to $4\mu\text{m}$. Murakami and Endo also stated that if the predicted value of σ_w for a \sqrt{area} exceeds the ideal upper bound of fatigue limit σ_{wu} ($\approx 1.6 H_v$), the defect having such a small \sqrt{area} should be regarded as non-detrimental. Thus the CIS value could be determined via the above equation to be between $17.9 \mu\text{m}$ and $0.3\mu\text{m}$ if H_v value varies in the valid range of 100 to 740 (Fig. 5-8). The Vickers hardness of HIPped CM247LC is of the order of 350 to 400 (not shown in the results), thus the CIS of CM247LC could be of the order of $1 \mu\text{m}$. It can be noted that the values calculated here are smaller than the experimental data of CM247LC the actual CIS should be larger than $1 \mu\text{m}$. Because the above empirical formula was obtained based on experimental data of ferrous materials, it is by no means clear if it can be applied to nickel alloys and it is not surprising that the predictions differ from the observations. The more important conclusion is that since the failure of these powder HIPped samples is dominated by inclusions it is essential that the inclusion density and their size is reduced as discussed below.

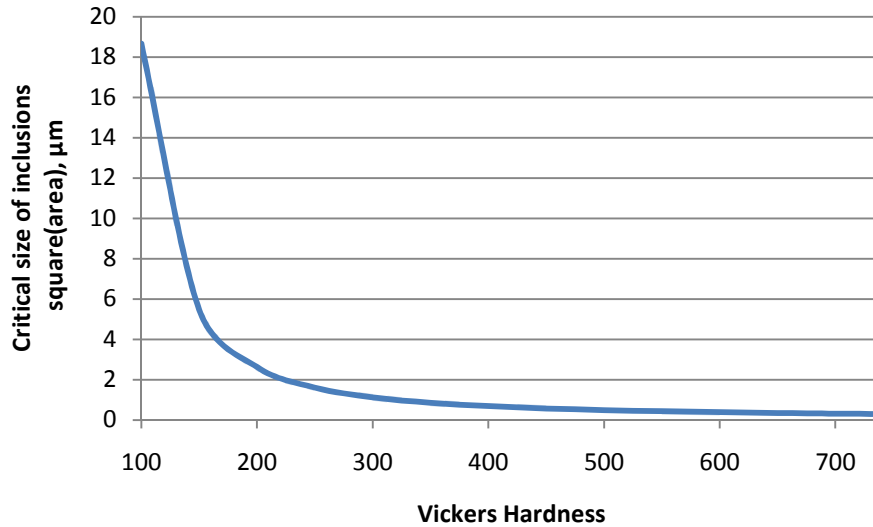


Fig. 5-8 Calculated critical inclusion size vs. Vickers hardness of the matrix.

5.3.3 The formation of inclusions in CM247LC powder HIPping

As the inclusions are so frequently found as crack initiators during tensile and fatigue tests, the inclusions are analysed in detail in the previous chapter. The results show that the inclusions consist of hafnia and most have an alumina core. Thus the role of Hf, the main element which forms inclusions is investigated in this section and the possible mechanism of the formation of this kind of inclusion is also proposed.

In the late 1960s, Hf was added to some cast nickel-base superalloys in order to solve the problem of low ductility at intermediate temperatures [Lund, Hockin et al. 1972]. It is also found to benefit the resistance to grain boundary cracking during solidification in directional solidification (DS). However, Hf is such a reactive element with oxygen that it may cause reactions with the mould and formation of brittle Hf-containing inclusions. Hf shows little or

no strength advantage at all compared with the same alloy without Hf modification in the equiaxed condition of cast CM247LC and IN792 [Zhang and Singer 2002].

In the HIPped CM247LC, Hf was found to be take part in the formation of two types of particles – carbides and inclusions. HfC is very stable, compared with other carbides, therefore, its formation is strongly favoured by thermodynamics, especially when the Hf content is more than 1% [McLean 1983]. The inclusions in the HIPped structure are identified in the previous chapter to be oxides rich in Hf and Al. They could be formed at any point of the route of the manufacture when alumina is present. The standard Gibbs free energy ΔG° is -203.3 kJ/ (mol of O₂) at 1027 °C for the reaction $3\text{Hf} + 2\text{Al}_2\text{O}_3 \rightarrow 3\text{HfO}_2 + 4\text{Al}$ [Ronald et al. 2004], the absolute value would be more negative when the temperature is higher according to the Ellingham diagram [McBride 1963]. The most likely moment at which the Hf could be oxidised could be when the alloy was melted and gas atomized. Reactions between Hf and alumina crucibles or nozzles may take place at the melting temperature of the alloy. It is also possible that the alumina particles dropped in the as-atomized powders at some stage and the above reaction took place during the HIPping process. Fig. 4-46 a) shows an inclusion particle that is mainly Al₂O₃. It is surrounded by a layer of ‘bright particle-free zone’; meanwhile its boundary is decorated by bright particles. Fig. 4-46 c) shows an inclusion particle that is mainly bright with no particle-free zone around. It seems that whether the particle-free zone is present or not depends on the size and shape of alumina core; the blocky ones tend to have a particle-free zone while the script shaped ones do not. For example, the script-shaped inclusion on the upper left in Fig. 4-47 a), the ones in Fig.4-47 c) and d), do not have particle-free zones; the blockier shaped ones in the middle of Fig. 4-47 a) and the one in Fig. 4-47 b), are surrounded by particle-free zone, and there are more dark areas in this type of inclusion. A typical inclusion particle (Fig. 4-48)

which had an upper part which is script with distributed carbide particles and the lower part was blocky with dark zone with no particles below it, was chosen for chemical analysis. The results (Fig. 4-48 and Table 4-13) show that it consists of hafnium oxide and aluminium oxide only. This indicates that the above reaction took place between the alumina particle and Hf in the matrix during HIPping; hafnium was depleted in the surrounding matrix and generated a carbide-free zone. The hafnium oxide of the upper part of the inclusion may exist before HIPping so no reaction took place during HIPping.

The possible evolution of inclusions during HIPping is explained as follows. It is likely that several types of particles exist in the CM247LC powder before HIPping. They could be alumina only or alumina with hafnia or hafnia that was generated during powder manufacturing, as schematically shown in the upper part of Fig.5-7. (The fact to be noted during gas atomisation of the batch of the powder employed in this project is that the Hf level was found lower than the specification when Osprey was preparing the melt for atomisation. Thus some pure Hf was added in the liquid to solve this problem. It could be this amount of pure Hf that reacted with the ceramic components during atomisation.)

During the HIPping process, the alumina reacts with the matrix while the hafnia is stable and no reactions take place. The different resulting morphologies are shown schematically in the lower part of Fig.5-7. The carbide particle-free zone always exists around inclusions which originally contains alumina. The quantitative analysis of defects in HIPped CM247LC using X-ray tomography (Table 4-14) shows the overall volume fraction of the alumina and hafnia in the 1100 °C as-HIPped sample is similar to the volume fraction of the hafnia in the 1260°C HIP + 1100 °C solution treated sample. The two batches also have similar particle size distribution (Fig. 4-54). It is likely that HIPping at 1100 °C for 4 hours is not sufficient to transform alumina to hafnia while HIPping at 1260 °C is. Once the 1260 °C as-HIPped

sample was subjected to 1260 °C solution treatment, the amount and size of the inclusions seems to decrease. They may dissolve into the matrix. There is not enough evidence to prove this assumption about the development of inclusions in HIPping as the quantitative analysis was based on one sample each. The results may not be representative. Examination on more samples is needed in future work.

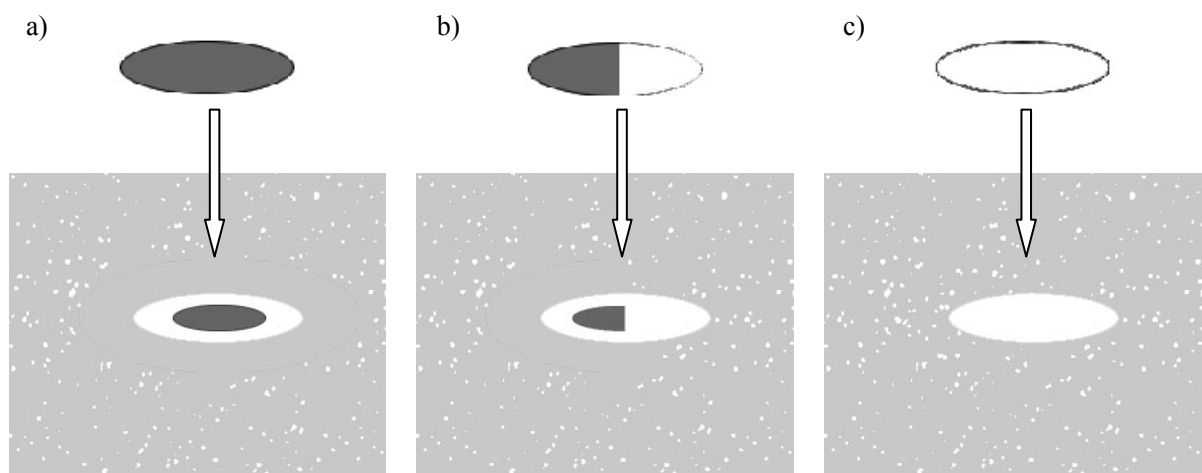


Fig. 5-7 Sketch of reactions between inclusions and matrix. a) alumina inclusion before and after HIPping ; b) alumina+ hafnia inclusion before and after HIPping; c) hafnia inclusion before and after HIPping; Particle free zone presents around inclusions which originally contains alumina.

The removal of Hf from the material proved to be an effective way to remove inclusions from the material (Fig.4-49, Fig 4-52, Fig.4-53 and Table 4-14). Little change was observed in microstructure (Fig.4-50, Fig. 4-51). The creep strength of the Hf-free samples is comparable with the Hf-containing one. Although the creep activation energy of the Hf-free samples is larger than the Hf-containing ones, they present larger creep rate when subjected to the same stress level. Further mechanical tests such as tensile and fatigue are needed to

understand whether the removal of Hf benefits the mechanical properties or not. Since there are no inclusions in the Hf-free samples it is highly likely that the tensile behaviour will be different.

5.4 Recommendations on powder HIPping of nickel-base alloys

Based on the findings of this project combined with literature review (§2.2.5), several recommendations on powder HIPping of nickel-base alloys are given as follows. Over and above all else methods must be found to reduce the overall sizes and numbers of inclusions.

(i) Choice of alloys

HIPping in this project is employed as an alternative fabrication method to making components by casting. The carbon level is relatively high in cast alloys because it benefits the castability, but HIPped products, made from alloys with high carbon, form carbide networks along the PPBs. The low carbon version is preferred if the material is going to be processed by powder HIPping and the work reported here shows that the properties are not downgraded by the reduction in C-level.

Alloys with strong carbide formers such as Ta, Nb, Hf are preferred for powder HIPping, as they get any remaining carbon to form carbides homogeneously in the matrix rather than at PPBs. However, Hf is found in this work to be a main inclusion former. Although it is reported to enhance many properties of many nickel-base superalloys such as DS CM247 and RR1000, and suppress the carbide networks along PPBs during HIPping, the detrimental effect in producing inclusions which nucleate failure strongly suggests that Hf should not be added to CM247LC.

(ii) Choice of HIPping parameters

If large grains are required after HIPping, temperatures above the γ' solvus for HIPping are recommended for three reasons. Firstly, the super - solvus material is fully recrystallised, the internal stress caused by inhomogeneities in the material could be minimized. Secondly, slow cool from temperatures above the γ' solvus produces a necklace structure along the grain boundaries, which results in serrated boundaries. This type of morphology is found to enhance mechanical properties of the material. Thirdly, large grains can be obtained in one run; the grain growth heat treatment can be saved. Finally the higher the HIP temperature that is used the less likely are gas pores to be able to expand when samples are heated to high temperatures during any subsequent heat treatments.

Quality control of powder is vital for powder HIPping. Apart from contamination by foreign particles, oxidation should be avoided at any point of the process. This includes the oxygen level control during the gas atomization, the powder storage and the leak testing of cans before HIPping.

(iii). Choice of heat treatment conditions

For the super-solvus as-HIPped material, a solution treatment, part of which is carried out below the γ' solvus is preferred to the super-solvus solution. Although solution above the solvus promotes grain growth which enhances creep resistance, there are several detrimental effects on microstructure and properties of the material. Firstly, solution above the solvus dissolves all the γ' obtained after HIPping, and provides a material with very strong grains strengthened by uniform fine γ' particles but relatively weak and straight grain boundaries. The morphology of γ' is sensitive to the temperature when the alloy is at temperatures

Chapter 5 Discussion

approaching the solvus. The desired distribution of γ' can be obtained by careful control of sub-solution temperature and cooling rate. Secondly, for powders produced by the method where gas is involved, as in the gas-atomised powders used here, solution above the γ' solvus faces higher risk that the entrapped gas in the original particles, that closed during HIPping, may reopen and expand to a catastrophic level.

Chapter 6 Conclusions and Future Work

The work carried out in this project was focused on optimising the properties of powder HIPped CM247LC. Different HIPping conditions and heat treatments were covered in this work and the resultant microstructures correlated with the mechanical properties. The main findings are summarised in §6.1. In the light of the findings, the most necessary future work is suggested in §6.2.

6.1 Conclusions

- The optimised powder HIPping condition and heat treatment condition were found to be HIP at 1260 °C, 150MPa for 2 hours followed by solution treatment at 1100 °C for two hours and forced air quench plus aging at 870 °C for 16 hours and furnace cool.
- This process-route produces a microstructure with grain size up to 50 μm, coarse γ' particles in a “necklace structure” decorating serrated grain boundaries, with fine γ' in size about 1 μm in the matrix; carbides distributed homogeneously in the matrix of particle size up to 0.25 μm, together with Hf-rich inclusions.
- The properties of optimally processed samples were 952MPa, 1530MPa and 18.5% for the 0.2% proof strength, tensile strength and elongation at room temperature respectively; 958MPa, 1020MPa and 3.1% for the 0.2% proof strength, tensile strength and elongation at 750 °C respectively.
- CM247LC produced using the optimised process results in the production of serrated grain boundaries (necklace structure). This structure enhances tensile and high cycle

fatigue properties at both room temperature and 750 °C

- Super-solvus solution treatment at 1260 °C results in larger grain size which enhances creep resistance at 760 °C/ 350MPa. But ductility and high cycle fatigue limit are inferior to the sub-solvus treatment.
- Inclusions are found at most initiation sites of failure. They consist of alumina and hafnia which may be inherited from the powder or formed during the HIPping process. Removal of Hf effectively reduces the volume fraction of inclusions. Creep properties of Hf-free specimen are inferior to the Hf-containing alloy.
- Pores with entrapped gas observed in as-received powder close during HIPping, but they reopen when the specimen is subjected to solution treatment above or close to the HIPping temperature. No detrimental effect of the reopened pores was noticed in this study.
- Despite the fact that inclusions dominate the fracture behaviour of the standard Hf-containing CM247LC the tensile, fatigue and creep properties of samples processed by the optimized condition are comparable with those of thermo-mechanically processed samples.

6.2 Future work

- The failed tensile and fatigue samples to be examined using TEM to confirm mechanisms suggested for governing strength and ductility of the HIPped CM247LC.
- The fracture behaviour of 1260 °C HIPped + 1260 °C Solution treated + Aged samples was found to be intergranular whereas it was intragranular in other batches. It is possible that this grain boundary failure is associated with a difference in composition of grain

boundaries in samples solution treated at 1100 °C and 1260 °C. This possibility could be checked by FIBed TEM samples using WDX.

- As the inclusions are the main crack initiators for tensile and fatigue test in Hf-containing CM247LC and the removal of Hf can successfully remove the inclusions. Tensile and fatigue behaviour need to be investigated on Hf-free HIPped CM247LC in order to further determine the effect of the removal of Hf on the properties.
- If the properties of Hf-free HIPped CM247LC are not superior to the current Hf-containing (inclusion-bearing) properties, some work should be carried out on ultra-clean Hf-containing powder in order to assess the tensile and fatigue properties of material which is hopefully free from inclusions such as alumina.
- The influence of the diffusion layer between HIPped material and mild steel can on the mechanical properties of the material since this is important in net shape HIPped samples.

Appendices

Appendix 1 Notch test

Notch tensile test

Ductility measurements on standard smooth tensile specimens do not always reveal metallurgical or environmental changes that lead to reduced local ductility. The tendency for reduced ductility in the presence of a triaxial stress field and steep stress gradients (such as occur at a notch) is called notch sensitivity. A common way of evaluating notch sensitivity is a tensile test using a notched specimen. [Davis 2004] The notch tensile test has been used extensively for investigating the properties of high-strength steels, for studying hydrogen embrittlement in steels and titanium, and for investigating the notch sensitivity of high-temperature alloys.

Because of the plastic constraint at the notch, this value will be higher than the tensile strength of an unnotched specimen if the material possesses some ductility. Therefore, the common way of detecting notch brittleness (or high notch sensitivity) is by determining the notch-strength ratio, NSR:

$$NSR = \frac{\delta_n(\text{for notched specimen at maximum load})}{\delta_u(\text{tensile strength for unnotched specimen})} \quad (1)$$

If the NSR is less than unity, the material is notch brittle. This property is of interest in engineering applications as most components have features of geometric discontinuity that causes stress amplification. As strength, hardness, or some metallurgical variable restricting plastic flow increases, the metal at the root of the notch is less able to flow, and fracture becomes more likely. Notch brittleness may be considered to begin at the strength level

where the notch strength begins to fall or, more conventionally, at the strength level where the NSR becomes less than unity.

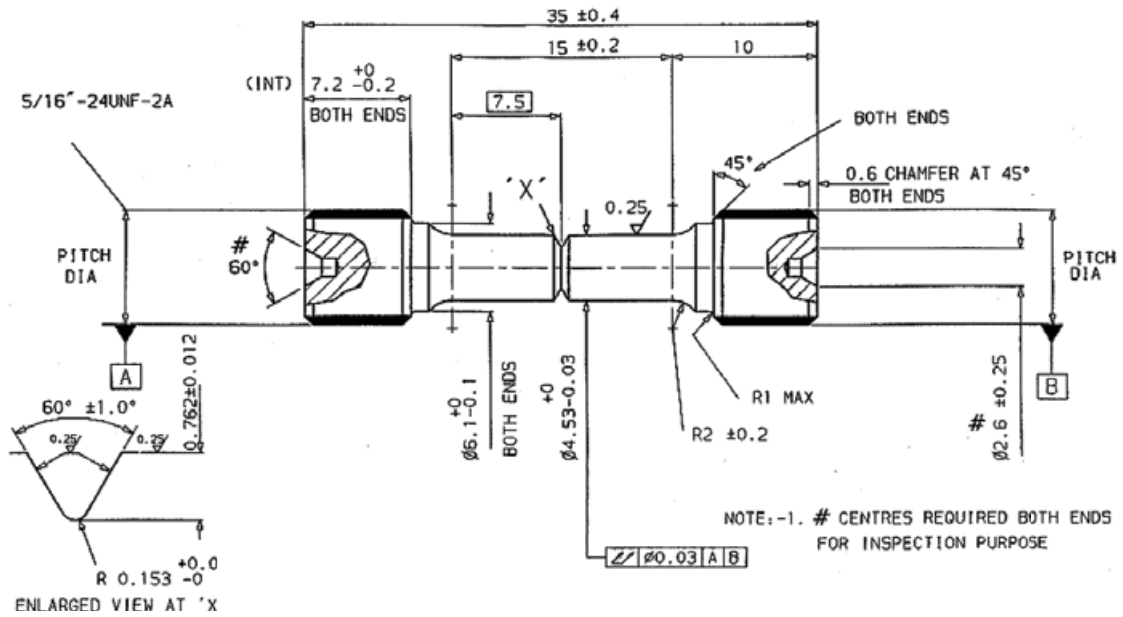


Fig. 1 dimensions for round notched tensile test pieces. Stress concentration factor $K_t=3.1$

Notch fatigue test

As mentioned previously, very few components or structural members are of uniform cross-section; most contain a change in cross-section resulting from a discontinuity such as, for example, a fillet, a hole, or an external groove or notch. Examples of components which have failed in service as a consequence of cyclic loadings, reveals that in many cases, the cause of failure has been the initiation of a fatigue crack at some point on the boundary of a notch. A crack forms here because the cyclic stresses at and near the notch boundary are higher than the nominal cyclic stresses remote from the notch.

An important difference between the behaviour of a statically-loaded notched member and a

Appendices

cyclically-loaded notched member of similar geometry and material may be illustrated by considering a cylindrical ductile metal bar containing a hole drilled transversely through a diameter. If subjected to a static tensile load, which gives rise to a nominal stress on the minimum cross-sectional area of, say, 80 percent of the 0.1 percent proof stress of the metal, the bar will not break, even though the metal in the highly stressed regions at and near the hole boundary will have deformed plastically. On the other hand, if the bar is subjected to a cyclic load such that the nominal stress range on the minimum cross-section is equal to 80 percent of the plain fatigue limit of the metal, fatigue cracks will form at the hole boundary on the plane of minimum cross-sectional area because the local stress range here will be greater than the fatigue limit of the metal. Once formed in these highly stressed regions, cracks will propagate across the cross-section of the bar under the action of the nominal applied stress range and eventually cause complete fracture of the bar. Thus, in the former case, local stresses at the notch boundary higher than the yield stress merely cause plastic deformation but not necessarily catastrophic failure, whereas in the latter case, local stress ranges at the notch boundary greater than the plain fatigue limit initiate fatigue cracks which in many cases will continue growing under the cyclic nominal stresses remote from the notch, until they cause catastrophic failure.

The need to provide data for the safe, yet economic, design of notched components has led to fatigue tests being carried out on notched specimens. Just as it is possible to estimate the plain fatigue limit (or strength at a given endurance) of a batch of plane specimens of a given material, so it is possible to determine the fatigue limit (or strength at a given endurance) of a batch of nominally identical notched specimens. The ratio of the plain fatigue limit to the corresponding notched fatigue limit is called the fatigue strength reduction factor, and is commonly denoted by K_f .

$$K_f = \frac{\sigma_u(\text{Endurance limit of a notch - free specimen})}{\sigma_n(\text{Endurance limit of a notched specimen})} \quad (2)$$

The notch, of course, may be of any shape, for example, a hole, a keyway, a fillet, or a circumferential groove, but generally the notch introduced into a laboratory specimen is either a hole or a circumferential V-groove. The drawing of the notched samples used in this project is shown in Fig. 2. They are carefully machined, that means the same surface finish of the test piece at notch with plane samples was guaranteed

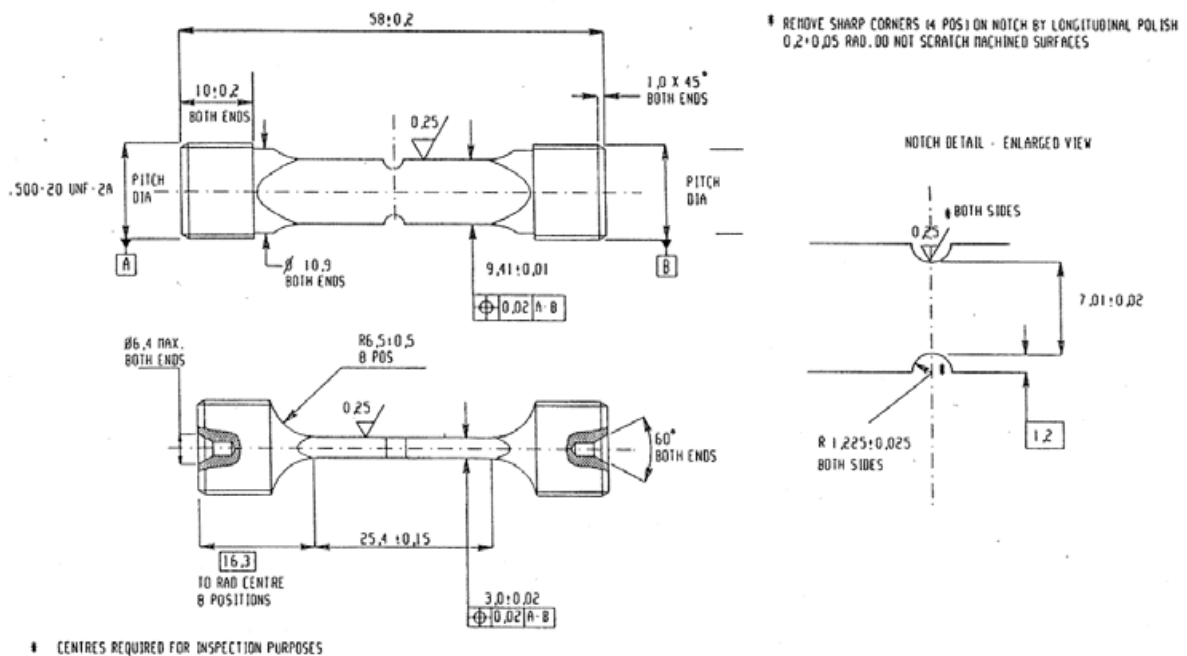


Fig. 2 dimensions for notched tension-tension fatigue test pieces. $K_t=2.26$

Because the conventional notched fatigue limits of some materials are greater than the corresponding plain fatigue limits divided by K_t , whereas those of other materials are either equal to or are not far removed from the corresponding plain fatigue limits divided by K_t , the former materials are sometimes referred to as notch insensitive and the latter as notch sensitive. It has been argued that this difference in behaviour arises because the former

Appendices

materials have the ability to deform plastically each cycle (presumably without leading to cracking), so reducing the maximum stress range at the notch root to a value less than the calculated elastic value. In addition, it has been suggested that the ratio of the increase of the actual stress range over the nominal stress range to the increase of the theoretical elastic stress range over the nominal stress range could be considered as a material constant. Thus if the nominal stress at the notched fatigue limit is σ_n

$$\frac{K_f \sigma_n - \sigma_n}{K_t \sigma_n - \sigma_n} = \frac{K_f - 1}{K_t - 1} = q \quad (3)$$

where q is termed the notch sensitivity index of a material. If $K_f=K_t$, $q=1$ and the material is said to be fully notch sensitive whereas, if $K_f=1$, $q=0$ and the material is said to be fully notch insensitive. However it is clear from the experimental data that q depends not only on material but also on specimen size and notch geometry. [Frost, Marsh et al. 1974]

Interpreted from equation (3), the fatigue stress concentration factor can be in the range of

$$1 \leq K_f \leq K_t$$

Replace the value of K_f by equation (2)

$$1 \leq \frac{\sigma_u}{\sigma_n} \leq K_t \text{ Or } \sigma_n \leq \sigma_u \leq K_t \sigma_n$$

The notch fatigue limit times the geometric stress concentrate factor $K_t \sigma_n$ can be treated as the theoretical maximum stress at the notch root assuming the value is still in the elastic range of the material. If the notch fatigue limit σ_n is equal to un-notched fatigue limit σ_u , the material is fully notch insensitive; or if $K_t \sigma_n$ is equal to the un-notched fatigue limit, then the material is fully notch sensitive.

Appendix 2 Diffusion layer

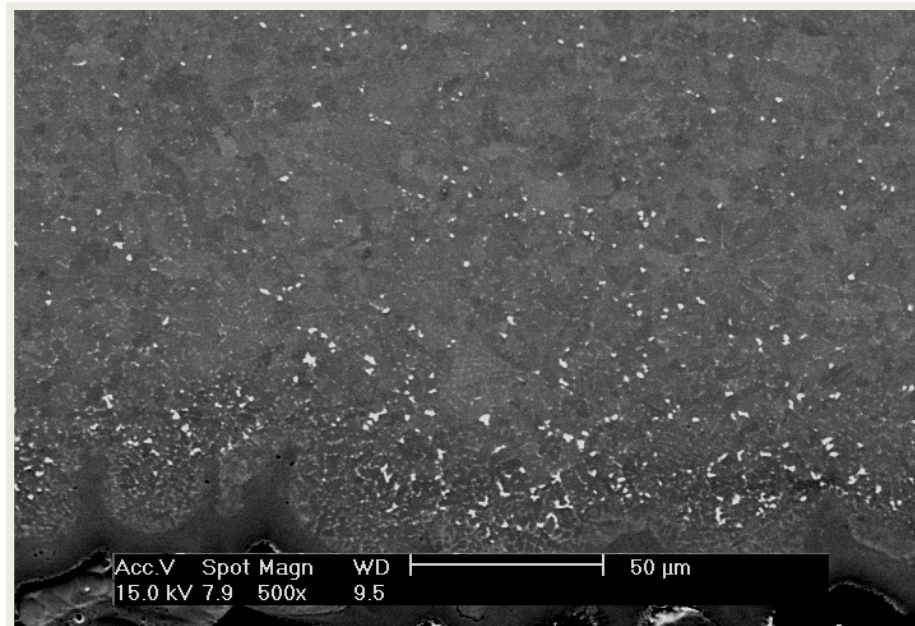


Fig.1 Diffusion layer between mild steel can and CM247LC HIPped at 1100 °C/150MPa/ 4h.

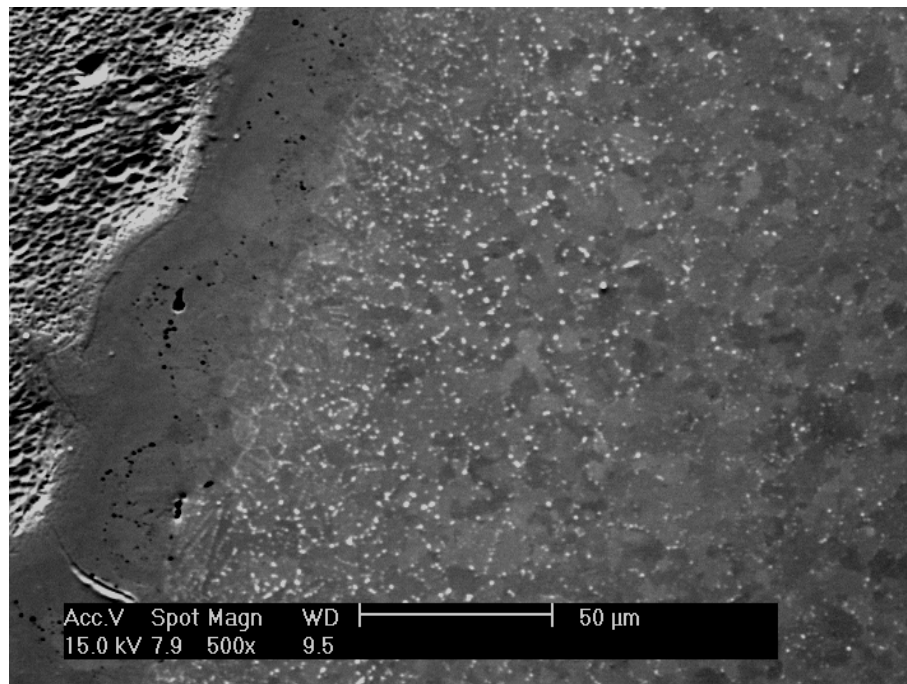


Fig.2 Diffusion layer between mild steel can and CM247LC HIPped at 1200 °C/150MPa/ 4h.

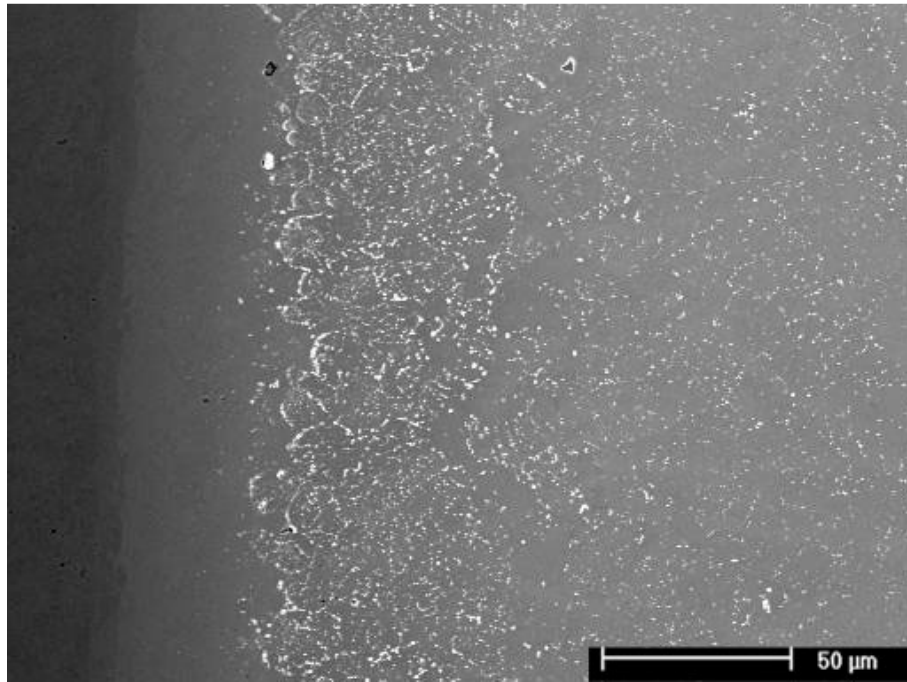
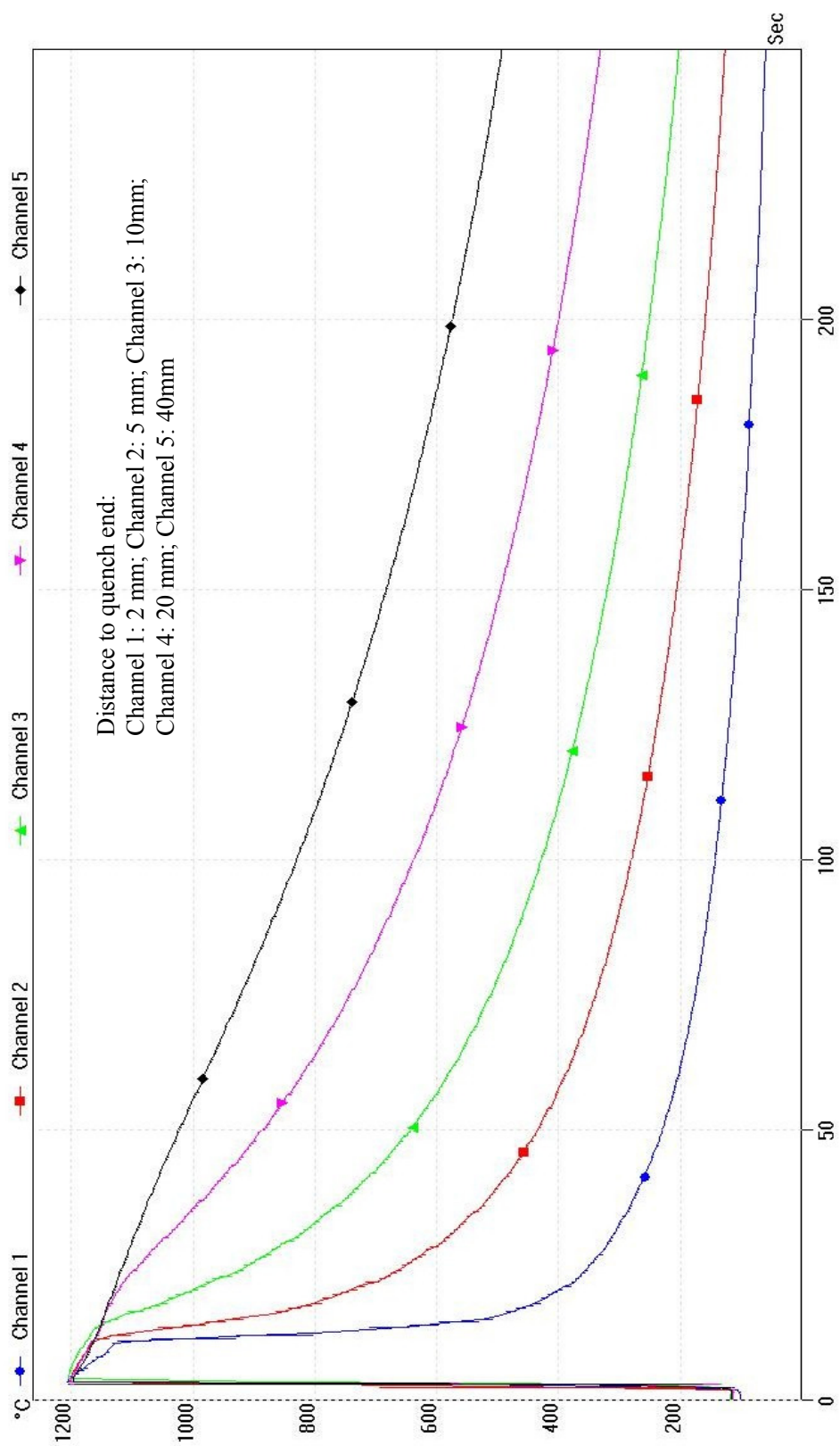


Fig.3 Diffusion layer between mild steel can and CM247LC HIPped at 1260 °C/150MPa/ 2h.

Appendix 3 Jominy Curve T (t)



Appendix 4 X-ray tomography

The relative penetration can be calculated by the exponential attenuation law

$$\frac{I}{I_0} = \exp [-(\mu/\rho)x]$$

Which means a narrow beam of mono energetic photons with an incident intensity I_0 , penetrating a layer of material with mass thickness x and density ρ , emerges with intensity I .

μ/ρ is the mass attenuation coefficient. The value of each element can be found on the NIST website. The value for mixture and compounds can be obtained according to simple additivity

$$\mu/\rho = \sum_i w_i(\mu/\rho)_i$$

Where w_i is the weight percentage of element i .

The raw tomography data of defects in CM247LC

1. *Hf-containing As-HIPped 1100 °C/150MPa/4h;*

- Count (voxel) of matrix: 674617088
- Count (voxel) of particles brighter than matrix: 39089

Index	Count (voxel)	EqDiameter3d	Diameter (micron)
1	234	7.6455	18.15424
2	119	6.10262	14.49067
3	306	8.36067	19.85241
4	137	6.39599	15.18728
5	576	10.32305	24.51208
6	679	10.90495	25.8938
7	1166	13.0587	31.00788
8	386	9.03364	21.45038

9	619	10.57379	25.10746
10	276	8.078	19.18121
11	148	6.56278	15.58332
12	482	9.72784	23.09876
13	51	4.60105	10.92519
14	101	5.77796	13.71977
15	160	6.73556	15.99359
16	937	12.14079	28.82831
17	294	8.24992	19.58944
18	289	8.20288	19.47774
19	1277	13.46059	31.96217
20	56	4.74675	11.27116
21	324	8.52149	20.23428
22	71	5.13752	12.19904
23	145	6.51813	15.4773
24	346	8.71016	20.68227
25	536	10.07834	23.93102
26	398	9.1263	21.6704
27	153	6.63587	15.75687
28	343	8.68491	20.62232
29	887	11.92088	28.30613
30	583	10.3647	24.61098
31	387	9.04144	21.4689
32	154	6.65029	15.79111
33	180	7.00527	16.63401
34	509	9.90619	23.52225
35	835	11.68322	27.74181
36	549	10.15917	24.12295
37	292	8.23117	19.54491
38	321	8.49511	20.17164
39	304	8.34241	19.80905
40	596	10.44117	24.79256
41	376	8.95495	21.26353
42	74	5.20888	12.36849
43	500	9.84745	23.38277
44	175	6.93979	16.47853
45	671	10.86196	25.79172
46	235	7.65637	18.18005
47	1078	12.72155	30.20732
48	160	6.73556	15.99359
49	480	9.71436	23.06675
50	434	9.39357	22.30503
51	276	8.078	19.18121
52	105	5.85325	13.89854

Appendices

53	360	8.82608	20.95753
54	71	5.13752	12.19904
55	200	7.25567	17.22859
56	100	5.75883	13.67434
57	386	9.03364	21.45038
58	111	5.96268	14.15838
59	67	5.03917	11.96551
60	191	7.14516	16.96618
61	74	5.20888	12.36849
62	1054	12.62644	29.98148
63	121	6.13662	14.5714
64	713	11.08401	26.31898
65	1363	13.75622	32.66414
66	918	12.05817	28.63212
67	46	4.44549	10.55582
68	216	7.44421	17.67628
69	892	11.94324	28.35922
70	1288	13.49913	32.05368
71	656	10.78041	25.59808
72	67	5.03917	11.96551
73	830	11.65986	27.68634
74	97	5.70065	13.53619
75	189	7.12013	16.90675
76	231	7.61269	18.07633
77	154	6.65029	15.79111
78	203	7.29176	17.31428
79	227	7.56849	17.97138
80	227	7.56849	17.97138
81	78	5.30109	12.58744
82	374	8.93904	21.22575
83	338	8.6425	20.52162
84	233	7.63459	18.12833
85	413	9.23954	21.93929
86	197	7.2192	17.14199
87	290	8.21233	19.50018
88	233	7.63459	18.12833
89	331	8.58242	20.37896
90	1388	13.83982	32.86265
91	169	6.85956	16.28803
92	223	7.52377	17.86519
93	167	6.83239	16.22351
94	1747	14.94279	35.48165
95	97	5.70065	13.53619
96	233	7.63459	18.12833

97	756	11.3025	26.83779
	39089		

- Count (voxel) of particles darker than matrix: 49003

Index	Count (voxel)	EqDiameter3d	Diameter (micron)
1	87	5.49761	13.05407
2	1294	13.52006	32.10338
3	3743	19.26374	45.74175
4	1717	14.85676	35.27738
5	670	10.85656	25.7789
6	1724	14.87692	35.32525
7	1338	13.6716	32.46321
8	291	8.22176	19.52257
9	223	7.52377	17.86519
10	271	8.02892	19.06467
11	171	6.88651	16.35202
12	966	12.26478	29.12272
13	5799	22.29042	52.9286
14	984	12.34049	29.30249
15	1482	14.14545	33.58837
16	714	11.08919	26.33128
17	657	10.78588	25.61107
18	1361	13.74949	32.64816
19	755	11.29751	26.82594
20	2342	16.47642	39.12326
21	382	9.00233	21.37603
22	604	10.48768	24.903
23	1617	14.56254	34.57875
24	864	11.81694	28.05932
25	1446	14.02997	33.31416
26	371	8.91508	21.16886
27	852	11.76198	27.92882
28	479	9.70761	23.05072
29	1372	13.78643	32.73588
30	1298	13.53398	32.13644
31	355	8.78503	20.86005
32	1068	12.68209	30.11362
33	826	11.6411	27.64179
34	17	3.19019	7.575106
35	1	1.2407	2.946042

Appendices

36	1	1.2407	2.946042
37	9	2.58076	6.128015
38	2	1.56319	3.711795
39	3	1.7894	4.24893
40	1	1.2407	2.946042
41	1	1.2407	2.946042
42	1	1.2407	2.946042
43	10	2.67301	6.347062
44	1	1.2407	2.946042
45	8384	25.20486	59.84894
46	126	6.22001	14.76941
47	1160	13.03627	30.95462
48	170	6.87306	16.32008
49	113	5.99828	14.24292
50	880	11.88944	28.23148

49003

2. *Hf-containing HIPped 1260 °C/150MPa/2h + Solution 1100 °C/1h/FAC + Age 870 °C/16h;*

- Count (voxel) of matrix: 502785714
- Count (voxel) of particles brighter than matrix: 70390

Index	Count (voxel)	EqDiameter3d	Diameter (micron)
1	263	7.94912	18.87519
2	114	6.01592	14.2848
3	250	7.81593	18.55893
4	369	8.89903	21.13075
5	432	9.37911	22.2707
6	27	3.7221	8.838126
7	81	5.3682	12.74679
8	467	9.62586	22.8566
9	166	6.81873	16.19107
10	183	7.04397	16.72591
11	27	3.7221	8.838126
12	472	9.66009	22.93788
13	104	5.83461	13.85428
14	93	5.62119	13.34752
15	699	11.01099	26.1456

16	141	6.45764	15.33367
17	125	6.20351	14.73023
18	314	8.4329	20.02392
19	66	5.01397	11.90567
20	514	9.93852	23.59902
21	200	7.25567	17.22859
22	224	7.535	17.89186
23	198	7.2314	17.17096
24	3236	18.35522	43.58447
25	309	8.3879	19.91707
26	122	6.15348	14.61144
27	115	6.03346	14.32645
28	60	4.85718	11.53337
29	66	5.01397	11.90567
30	128	6.25274	14.84713
31	157	6.6932	15.893
32	157	6.6932	15.893
33	515	9.94496	23.61431
34	254	7.85739	18.65737
35	657	10.78588	25.61107
36	27	3.7221	8.838126
37	10049	26.77813	63.58467
38	36	4.09671	9.727638
39	155	6.66466	15.82524
40	69	5.08882	12.0834
41	36	4.09671	9.727638
42	533	10.0595	23.88628
43	57	4.77484	11.33786
44	281	8.12648	19.29633
45	80	5.34602	12.69412
46	645	10.71981	25.45419
47	103	5.81585	13.80974
48	36	4.09671	9.727638
49	803	11.53203	27.38281
50	57	4.77484	11.33786
51	772	11.38168	27.0258
52	51	4.60105	10.92519
53	93	5.62119	13.34752
54	3915	19.55773	46.43983
55	59	4.83005	11.46895
56	840	11.7065	27.79708
57	170	6.87306	16.32008
58	57	4.77484	11.33786
59	354	8.77678	20.84046

Appendices

60	36	4.09671	9.727638
61	103	5.81585	13.80974
62	96	5.68099	13.48951
63	36	4.09671	9.727638
64	610	10.5223	24.9852
65	63	4.93682	11.72248
66	374	8.93904	21.22575
67	74	5.20888	12.36849
68	254	7.85739	18.65737
69	94	5.64127	13.3952
70	110	5.94472	14.11574
71	445	9.47227	22.49191
72	54	4.68956	11.13536
73	133	6.33312	15.03799
74	228	7.57959	17.99774
75	45	4.41304	10.47876
76	495	9.81452	23.30458
77	207	7.33935	17.42729
78	391	9.07248	21.5426
79	132	6.31721	15.00022
80	457	9.55666	22.69229
81	60	4.85718	11.53337
82	93	5.62119	13.34752
83	27	3.7221	8.838126
84	60	4.85718	11.53337
85	136	6.38038	15.15021
86	45	4.41304	10.47876
87	27	3.7221	8.838126
88	108	5.90847	14.02966
89	262	7.93903	18.85123
90	63	4.93682	11.72248
91	69	5.08882	12.0834
92	51	4.60105	10.92519
93	149	6.57753	15.61834
94	54	4.68956	11.13536
95	1395	13.86636	32.92567
96	272	8.03878	19.08808
97	157	6.6932	15.893
98	154	6.65029	15.79111
99	136	6.38038	15.15021
100	1017	12.48101	29.63616
101	107	5.89018	13.98623
102	186	7.08225	16.8168
103	137	6.39599	15.18728

104	108	5.90847	14.02966
105	804	11.53681	27.39416
106	145	6.51813	15.4773
107	51	4.60105	10.92519
108	51	4.60105	10.92519
109	69	5.08882	12.0834
110	27	3.7221	8.838126
111	114	6.01592	14.2848
112	55	4.71833	11.20367
113	77	5.27834	12.53342
114	87	5.49761	13.05407
115	546	10.14063	24.07893
116	435	9.40077	22.32213
117	104	5.83461	13.85428
118	152	6.62138	15.72247
119	264	7.95918	18.89907
120	27	3.7221	8.838126
121	161	6.74957	16.02685
122	167	6.83239	16.22351
123	258	7.89842	18.7548
124	430	9.36462	22.23629
125	36	4.09671	9.727638
126	669	10.85115	25.76606
127	138	6.41151	15.22413
128	552	10.17764	24.16681
129	66	5.01397	11.90567
130	122	6.15348	14.61144
131	240	7.7103	18.30811
132	146	6.53308	15.5128
133	128	6.25274	14.84713
134	718	11.10986	26.38036
135	267	7.98922	18.9704
136	134	6.34895	15.07558
137	400	9.14157	21.70666
138	371	8.91508	21.16886
139	139	6.42696	15.26082
140	286	8.1744	19.41011
141	27	3.7221	8.838126
142	71	5.13752	12.19904
143	45	4.41304	10.47876
144	57	4.77484	11.33786
145	77	5.27834	12.53342
146	74	5.20888	12.36849
147	275	8.06823	19.15801

Appendices

148	340	8.65951	20.56201
149	376	8.95495	21.26353
150	116	6.0509	14.36786
151	446	9.47936	22.50874
152	45	4.41304	10.47876
153	309	8.3879	19.91707
154	63	4.93682	11.72248
155	82	5.3902	12.79903
156	437	9.41516	22.3563
157	83	5.41203	12.85087
158	27	3.7221	8.838126
159	958	12.23083	29.04211
160	250	7.81593	18.55893
161	67	5.03917	11.96551
162	1328	13.64088	32.39027
163	448	9.49351	22.54234
164	340	8.65951	20.56201
165	116	6.0509	14.36786
166	141	6.45764	15.33367
167	507	9.8932	23.4914
168	1706	14.82786	35.20875
169	63	4.93682	11.72248
170	380	8.98659	21.33866
171	135	6.36471	15.113
172	57	4.77484	11.33786
173	182	7.03112	16.69539
174	87	5.49761	13.05407
175	255	7.86769	18.68183
176	72	5.16153	12.25605
177	46	4.44549	10.55582
178	57	4.77484	11.33786
179	233	7.63459	18.12833
180	81	5.3682	12.74679
181	166	6.81873	16.19107
182	36	4.09671	9.727638
183	861	11.80325	28.02682
184	117	6.06824	14.40904
185	163	6.7774	16.09294
186	77	5.27834	12.53342
187	127	6.23642	14.80838
188	45	4.41304	10.47876
189	96	5.68099	13.48951
190	150	6.59221	15.6532
191	310	8.39694	19.93853

192	36	4.09671	9.727638
193	445	9.47227	22.49191
194	489	9.7747	23.21003
195	150	6.59221	15.6532
196	3103	18.10038	42.97935
197	51	4.60105	10.92519
198	102	5.79696	13.76488
199	75	5.23224	12.42395
200	36	4.09671	9.727638
201	3814	19.38816	46.03719
202	257	7.88821	18.73055
203	192	7.1576	16.99572
204	372	8.92308	21.18785
205	200	7.25567	17.22859
206	151	6.60683	15.68792

70390

- Count (voxel) of particles darker than matrix: 0

3. *Hf-containing HIPped 1260 °C/150MPa/2h + Solution 1260 °C/1h/FAC + Age 870 °C/16h;*

- Count (voxel) of matrix: 838948544
- Count (voxel) of particles brighter than matrix: 52584

Index	Count(voxel)	EqDiameter	Diameter (micron)
1	1392	13.85	16.81
2	408	9.20	11.17
3	1344	13.69	16.61
4	280	8.12	9.85
5	176	6.95	8.44
6	120	6.12	7.43
7	128	6.25	7.59
8	768	11.36	13.79
9	608	10.51	12.75
10	176	6.95	8.44
11	272	8.04	9.75

Appendices

12	3288	18.45	22.39
13	312	8.41	10.21
14	256	7.88	9.56
15	48	4.51	5.47
16	48	4.51	5.47
17	392	9.08	11.02
18	184	7.06	8.56
19	304	8.34	10.12
20	280	8.12	9.85
21	1592	14.49	17.58
22	328	8.56	10.38
23	272	8.04	9.75
24	176	6.95	8.44
25	216	7.44	9.03
26	128	6.25	7.59
27	7472	24.26	29.43
28	272	8.04	9.75
29	424	9.32	11.31
30	96	5.68	6.89
31	96	5.68	6.89
32	224	7.54	9.14
33	128	6.25	7.59
34	480	9.71	11.79
35	296	8.27	10.03
36	160	6.74	8.17
37	56	4.75	5.76
38	328	8.56	10.38
39	208	7.35	8.92
40	224	7.54	9.14
41	200	7.26	8.80
42	104	5.83	7.08
43	432	9.38	11.38
44	88	5.52	6.70
45	440	9.44	11.45
46	944	12.17	14.77
47	64	4.96	6.02
48	304	8.34	10.12
49	704	11.04	13.39
50	48	4.51	5.47
51	56	4.75	5.76
52	272	8.04	9.75
53	680	10.91	13.24
54	144	6.50	7.89
55	136	6.38	7.74

56	7064	23.81	28.89
57	88	5.52	6.70
58	312	8.41	10.21
59	768	11.36	13.79
60	360	8.83	10.71
61	152	6.62	8.03
62	64	4.96	6.02
63	112	5.98	7.26
64	784	11.44	13.88
65	64	4.96	6.02
66	688	10.95	13.29
67	200	7.26	8.80
68	176	6.95	8.44
69	872	11.85	14.38
70	328	8.56	10.38
71	336	8.63	10.47
72	456	9.55	11.59
73	464	9.61	11.66
74	72	5.16	6.26
75	136	6.38	7.74
76	456	9.55	11.59
77	304	8.34	10.12
78	224	7.54	9.14
79	152	6.62	8.03
80	320	8.49	10.30
81	232	7.62	9.25
82	728	11.16	13.54
83	128	6.25	7.59
84	40	4.24	5.15
85	312	8.41	10.21
86	168	6.85	8.31
87	80	5.35	6.49
88	376	8.95	10.87
89	200	7.26	8.80
90	184	7.06	8.56
91	168	6.85	8.31
92	152	6.62	8.03
93	1128	12.92	15.67
94	496	9.82	11.92
95	128	6.25	7.59
96	2304	16.39	19.88
97	80	5.35	6.49
98	376	8.95	10.87
99	176	6.95	8.44

Appendices

100	1560	14.39	17.46
101	40	4.24	5.15

52584

- Count (voxel) of particles darker than matrix: 309160

Index	Count (voxel)	EqDiameter3d	Diameter (micron)
1	88	5.51858	6.696521
2	32	3.93898	4.779755
3	32	3.93898	4.779755
4	408	9.2021	11.16629
5	64	4.9628	6.02211
6	64	4.9628	6.02211
7	88	5.51858	6.696521
8	144	6.50312	7.891211
9	112	5.98054	7.257086
10	80	5.34602	6.487128
11	80	5.34602	6.487128
12	232	7.62366	9.25093
13	80	5.34602	6.487128
14	376	8.95496	10.8664
15	64	4.9628	6.02211
16	416	9.26186	11.2388
17	16	3.12638	3.793706
18	432	9.37912	11.38109
19	168	6.846	8.307279
20	32	3.93898	4.779755
21	32	3.93898	4.779755
22	184	7.05678	8.56305
23	264	7.95918	9.658067
24	10936	27.53934	33.41761
25	24	3.5788	4.342695
26	96	5.681	6.893609
27	136	6.38038	7.742272
28	152	6.62138	8.034714
29	64	4.9628	6.02211
30	216	7.4442	9.033164
31	672	10.86736	13.187
32	96	5.681	6.893609
33	32	3.93898	4.779755

34	208	7.35114	8.920241
35	48	4.509	5.471446
36	304	8.34242	10.12311
37	336	8.62542	10.46652
38	144	6.50312	7.891211
39	40	4.24314	5.148838
40	64	4.9628	6.02211
41	112	5.98054	7.257086
42	48	4.509	5.471446
43	216	7.4442	9.033164
44	136	6.38038	7.742272
45	32	3.93898	4.779755
46	56	4.74676	5.759956
47	560	10.22656	12.40942
48	160	6.73556	8.173265
49	288	8.19342	9.942305
50	248	7.79504	9.458891
51	120	6.11966	7.425901
52	320	8.48628	10.29768
53	160	6.73556	8.173265
54	72	5.16152	6.263246
55	696	10.99522	13.34215
56	40	4.24314	5.148838
57	48	4.509	5.471446
58	16	3.12638	3.793706
59	104	5.8346	7.079995
60	112	5.98054	7.257086
61	32	3.93898	4.779755
62	128	6.25274	7.587387
63	40	4.24314	5.148838
64	128	6.25274	7.587387
65	40	4.24314	5.148838
66	240	7.7103	9.356064
67	248	7.79504	9.458891
68	200	7.25566	8.804381
69	72	5.16152	6.263246
70	224	7.535	9.143346
71	72	5.16152	6.263246
72	312	8.41496	10.21113
73	192	7.1576	8.68539
74	296	8.26858	10.03351
75	392	9.08022	11.01839
76	1216	13.24276	16.06943
77	1112	12.85392	15.59759

Appendices

78	928	12.1018	14.68493
79	64	4.9628	6.02211
80	184	7.05678	8.56305
81	128	6.25274	7.587387
82	40	4.24314	5.148838
83	128	6.25274	7.587387
84	104	5.8346	7.079995
85	224	7.535	9.143346
86	56	4.74676	5.759956
87	72	5.16152	6.263246
88	40	4.24314	5.148838
89	544	10.12824	12.29011
90	144	6.50312	7.891211
91	40	4.24314	5.148838
92	1096	12.79198	15.52243
93	176	6.95298	8.437094
94	88	5.51858	6.696521
95	384	9.01802	10.94292
96	312	8.41496	10.21113
97	176	6.95298	8.437094
98	152	6.62138	8.034714
99	80	5.34602	6.487128
100	136	6.38038	7.742272
101	112	5.98054	7.257086
102	80	5.34602	6.487128
103	128	6.25274	7.587387
104	112	5.98054	7.257086
105	248	7.79504	9.458891
106	152	6.62138	8.034714
107	448	9.4935	11.51989
108	88	5.51858	6.696521
109	48	4.509	5.471446
110	144	6.50312	7.891211
111	360	8.82608	10.71001
112	128	6.25274	7.587387
113	368	8.89098	10.78876
114	296	8.26858	10.03351
115	72	5.16152	6.263246
116	104	5.8346	7.079995
117	64	4.9628	6.02211
118	664	10.82406	13.13446
119	112	5.98054	7.257086
120	104	5.8346	7.079995
121	216	7.4442	9.033164

122	64	4.9628	6.02211
123	3248	18.3741	22.29605
124	592	10.41776	12.64143
125	40	4.24314	5.148838
126	72	5.16152	6.263246
127	472	9.6601	11.72205
128	392	9.08022	11.01839
129	416	9.26186	11.2388
130	144	6.50312	7.891211
131	56	4.74676	5.759956
132	96	5.681	6.893609
133	224	7.535	9.143346
134	136	6.38038	7.742272
135	744	11.24238	13.64207
136	352	8.76022	10.63009
137	184	7.05678	8.56305
138	232	7.62366	9.25093
139	208	7.35114	8.920241
140	32	3.93898	4.779755
141	80	5.34602	6.487128
142	208	7.35114	8.920241
143	96	5.681	6.893609
144	184	7.05678	8.56305
145	120	6.11966	7.425901
146	216	7.4442	9.033164
147	56	4.74676	5.759956
148	128	6.25274	7.587387
149	24	3.5788	4.342695
150	128	6.25274	7.587387
151	168	6.846	8.307279
152	72	5.16152	6.263246
153	16	3.12638	3.793706
154	152	6.62138	8.034714
155	320	8.48628	10.29768
156	16	3.12638	3.793706
157	24	3.5788	4.342695
158	192	7.1576	8.68539
159	208	7.35114	8.920241
160	32	3.93898	4.779755
161	304	8.34242	10.12311
162	104	5.8346	7.079995
163	2216	16.17548	19.62814
164	168	6.846	8.307279
165	24	3.5788	4.342695

Appendices

166	112	5.98054	7.257086
167	128	6.25274	7.587387
168	232	7.62366	9.25093
169	104	5.8346	7.079995
170	160	6.73556	8.173265
171	584	10.37062	12.58423
172	216	7.4442	9.033164
173	112	5.98054	7.257086
174	96	5.681	6.893609
175	80	5.34602	6.487128
176	40	4.24314	5.148838
177	16	3.12638	3.793706
178	336	8.62542	10.46652
179	312	8.41496	10.21113
180	48	4.509	5.471446
181	224	7.535	9.143346
182	120	6.11966	7.425901
183	120	6.11966	7.425901
184	152	6.62138	8.034714
185	144	6.50312	7.891211
186	144	6.50312	7.891211
187	360	8.82608	10.71001
188	192	7.1576	8.68539
189	80	5.34602	6.487128
190	240	7.7103	9.356064
191	784	11.44034	13.88228
192	248	7.79504	9.458891
193	72	5.16152	6.263246
194	24	3.5788	4.342695
195	152	6.62138	8.034714
196	200	7.25566	8.804381
197	64	4.9628	6.02211
198	88	5.51858	6.696521
199	144	6.50312	7.891211
200	232	7.62366	9.25093
201	40	4.24314	5.148838
202	192	7.1576	8.68539
203	280	8.11684	9.849379
204	80	5.34602	6.487128
205	112	5.98054	7.257086
206	80	5.34602	6.487128
207	48	4.509	5.471446
208	248	7.79504	9.458891
209	200	7.25566	8.804381

210	224	7.535	9.143346
211	8	2.4814	3.011055
212	256	7.87796	9.559511
213	88	5.51858	6.696521
214	216	7.4442	9.033164
215	72	5.16152	6.263246
216	112	5.98054	7.257086
217	128	6.25274	7.587387
218	112	5.98054	7.257086
219	200	7.25566	8.804381
220	168	6.846	8.307279
221	184	7.05678	8.56305
222	600	10.46448	12.69812
223	296	8.26858	10.03351
224	112	5.98054	7.257086
225	280	8.11684	9.849379
226	72	5.16152	6.263246
227	112	5.98054	7.257086
228	288	8.19342	9.942305
229	240	7.7103	9.356064
230	168	6.846	8.307279
231	552	10.17764	12.35006
232	240	7.7103	9.356064
233	216	7.4442	9.033164
234	144	6.50312	7.891211
235	392	9.08022	11.01839
236	200	7.25566	8.804381
237	64	4.9628	6.02211
238	88	5.51858	6.696521
239	264	7.95918	9.658067
240	240	7.7103	9.356064
241	400	9.14156	11.09283
242	272	8.03878	9.754658
243	424	9.32086	11.3104
244	984	12.34048	14.97456
245	280	8.11684	9.849379
246	16	3.12638	3.793706
247	176	6.95298	8.437094
248	88	5.51858	6.696521
249	528	10.02794	12.1684
250	120	6.11966	7.425901
251	160	6.73556	8.173265
252	280	8.11684	9.849379
253	752	11.28254	13.6908

Appendices

254	272	8.03878	9.754658
255	248	7.79504	9.458891
256	288	8.19342	9.942305
257	96	5.681	6.893609
258	128	6.25274	7.587387
259	112	5.98054	7.257086
260	136	6.38038	7.742272
261	336	8.62542	10.46652
262	72	5.16152	6.263246
263	160	6.73556	8.173265
264	64	4.9628	6.02211
265	680	10.9103	13.2391
266	248	7.79504	9.458891
267	320	8.48628	10.29768
268	160	6.73556	8.173265
269	424	9.32086	11.3104
270	360	8.82608	10.71001
271	240	7.7103	9.356064
272	272	8.03878	9.754658
273	64	4.9628	6.02211
274	104	5.8346	7.079995
275	208	7.35114	8.920241
276	760	11.3224	13.73917
277	144	6.50312	7.891211
278	528	10.02794	12.1684
279	40	4.24314	5.148838
280	40	4.24314	5.148838
281	80	5.34602	6.487128
282	88	5.51858	6.696521
283	176	6.95298	8.437094
284	120	6.11966	7.425901
285	64	4.9628	6.02211
286	96	5.681	6.893609
287	192	7.1576	8.68539
288	64	4.9628	6.02211
289	56	4.74676	5.759956
290	96	5.681	6.893609
291	256	7.87796	9.559511
292	440	9.43666	11.45092
293	200	7.25566	8.804381
294	72	5.16152	6.263246
295	56	4.74676	5.759956
296	104	5.8346	7.079995
297	440	9.43666	11.45092

298	168	6.846	8.307279
299	992	12.37384	15.01504
300	120	6.11966	7.425901
301	96	5.681	6.893609
302	344	8.69334	10.54893
303	88	5.51858	6.696521
304	160	6.73556	8.173265
305	160	6.73556	8.173265
306	40	4.24314	5.148838
307	296	8.26858	10.03351
308	152	6.62138	8.034714
309	96	5.681	6.893609
310	240	7.7103	9.356064
311	72	5.16152	6.263246
312	64	4.9628	6.02211
313	152	6.62138	8.034714
314	280	8.11684	9.849379
315	152	6.62138	8.034714
316	520	9.97704	12.10664
317	160	6.73556	8.173265
318	432	9.37912	11.38109
319	160	6.73556	8.173265
320	176	6.95298	8.437094
321	128	6.25274	7.587387
322	544	10.12824	12.29011
323	160	6.73556	8.173265
324	568	10.27504	12.46825
325	344	8.69334	10.54893
326	848	11.74354	14.2502
327	120	6.11966	7.425901
328	216	7.4442	9.033164
329	216	7.4442	9.033164
330	192	7.1576	8.68539
331	224	7.535	9.143346
332	64	4.9628	6.02211
333	32	3.93898	4.779755
334	88	5.51858	6.696521
335	88	5.51858	6.696521
336	208	7.35114	8.920241
337	144	6.50312	7.891211
338	576	10.32306	12.52652
339	160	6.73556	8.173265
340	88	5.51858	6.696521
341	296	8.26858	10.03351

Appendices

342	448	9.4935	11.51989
343	408	9.2021	11.16629
344	288	8.19342	9.942305
345	1344	13.692	16.61456
346	48	4.509	5.471446
347	392	9.08022	11.01839
348	144	6.50312	7.891211
349	720	11.12016	13.49376
350	184	7.05678	8.56305
351	40	4.24314	5.148838
352	416	9.26186	11.2388
353	416	9.26186	11.2388
354	216	7.4442	9.033164
355	144	6.50312	7.891211
356	152	6.62138	8.034714
357	72	5.16152	6.263246
358	192	7.1576	8.68539
359	120	6.11966	7.425901
360	1472	14.11356	17.1261
361	536	10.07834	12.22956
362	344	8.69334	10.54893
363	864	11.81694	14.33927
364	216	7.4442	9.033164
365	192	7.1576	8.68539
366	456	9.54968	11.58806
367	120	6.11966	7.425901
368	72	5.16152	6.263246
369	280	8.11684	9.849379
370	128	6.25274	7.587387
371	496	9.82112	11.91744
372	88	5.51858	6.696521
373	400	9.14156	11.09283
374	384	9.01802	10.94292
375	88	5.51858	6.696521
376	712	11.07884	13.44362
377	368	8.89098	10.78876
378	224	7.535	9.143346
379	296	8.26858	10.03351
380	144	6.50312	7.891211
381	248	7.79504	9.458891
382	448	9.4935	11.51989
383	48	4.509	5.471446
384	296	8.26858	10.03351
385	1224	13.27174	16.10459

386	176	6.95298	8.437094
387	128	6.25274	7.587387
388	2472	16.7758	20.35659
389	736	11.20194	13.59299
390	160	6.73556	8.173265
391	104	5.8346	7.079995
392	120	6.11966	7.425901
393	440	9.43666	11.45092
394	240	7.7103	9.356064
395	88	5.51858	6.696521
396	216	7.4442	9.033164
397	1576	14.4384	17.52028
398	104	5.8346	7.079995
399	216	7.4442	9.033164
400	184	7.05678	8.56305
401	560	10.22656	12.40942
402	456	9.54968	11.58806
403	176	6.95298	8.437094
404	56	4.74676	5.759956
405	208	7.35114	8.920241
406	360	8.82608	10.71001
407	520	9.97704	12.10664
408	104	5.8346	7.079995
409	136	6.38038	7.742272
410	144	6.50312	7.891211
411	120	6.11966	7.425901
412	112	5.98054	7.257086
413	576	10.32306	12.52652
414	40	4.24314	5.148838
415	640	10.69204	12.97426
416	56	4.74676	5.759956
417	640	10.69204	12.97426
418	256	7.87796	9.559511
419	512	9.92562	12.04424
420	32	3.93898	4.779755
421	232	7.62366	9.25093
422	296	8.26858	10.03351
423	104	5.8346	7.079995
424	352	8.76022	10.63009
425	128	6.25274	7.587387
426	832	11.66922	14.16002
427	128	6.25274	7.587387
428	112	5.98054	7.257086
429	48	4.509	5.471446

Appendices

430	376	8.95496	10.8664
431	272	8.03878	9.754658
432	128	6.25274	7.587387
433	248	7.79504	9.458891
434	168	6.846	8.307279
435	160	6.73556	8.173265
436	56	4.74676	5.759956
437	344	8.69334	10.54893
438	104	5.8346	7.079995
439	520	9.97704	12.10664
440	368	8.89098	10.78876
441	512	9.92562	12.04424
442	72	5.16152	6.263246
443	96	5.681	6.893609
444	168	6.846	8.307279
445	696	10.99522	13.34215
446	128	6.25274	7.587387
447	128	6.25274	7.587387
448	480	9.71436	11.78789
449	240	7.7103	9.356064
450	88	5.51858	6.696521
451	72	5.16152	6.263246
452	472	9.6601	11.72205
453	136	6.38038	7.742272
454	264	7.95918	9.658067
455	760	11.3224	13.73917
456	128	6.25274	7.587387
457	168	6.846	8.307279
458	152	6.62138	8.034714
459	280	8.11684	9.849379
460	784	11.44034	13.88228
461	248	7.79504	9.458891
462	64	4.9628	6.02211
463	336	8.62542	10.46652
464	80	5.34602	6.487128
465	240	7.7103	9.356064
466	104	5.8346	7.079995
467	320	8.48628	10.29768
468	280	8.11684	9.849379
469	112	5.98054	7.257086
470	608	10.51078	12.75431
471	200	7.25566	8.804381
472	208	7.35114	8.920241
473	296	8.26858	10.03351

474	192	7.1576	8.68539
475	264	7.95918	9.658067
476	240	7.7103	9.356064
477	440	9.43666	11.45092
478	160	6.73556	8.173265
479	264	7.95918	9.658067
480	176	6.95298	8.437094
481	488	9.76804	11.85303
482	224	7.535	9.143346
483	48	4.509	5.471446
484	168	6.846	8.307279
485	80	5.34602	6.487128
486	272	8.03878	9.754658
487	408	9.2021	11.16629
488	312	8.41496	10.21113
489	72	5.16152	6.263246
490	248	7.79504	9.458891
491	80	5.34602	6.487128
492	896	11.96106	14.51415
493	1128	12.91528	15.67205
494	808	11.55592	14.02253
495	1368	13.77302	16.71287
496	64	4.9628	6.02211
497	520	9.97704	12.10664
498	136	6.38038	7.742272
499	312	8.41496	10.21113
500	232	7.62366	9.25093
501	376	8.95496	10.8664
502	392	9.08022	11.01839
503	168	6.846	8.307279
504	208	7.35114	8.920241
505	384	9.01802	10.94292
506	112	5.98054	7.257086
507	160	6.73556	8.173265
508	168	6.846	8.307279
509	168	6.846	8.307279
510	280	8.11684	9.849379
511	168	6.846	8.307279
512	256	7.87796	9.559511
513	176	6.95298	8.437094
514	328	8.55642	10.38279
515	200	7.25566	8.804381
516	248	7.79504	9.458891
517	464	9.6052	11.65543

Appendices

518	208	7.35114	8.920241
519	368	8.89098	10.78876
520	296	8.26858	10.03351
521	680	10.9103	13.2391
522	272	8.03878	9.754658
523	384	9.01802	10.94292
524	888	11.92536	14.47083
525	1128	12.91528	15.67205
526	392	9.08022	11.01839
527	392	9.08022	11.01839
528	1672	14.72582	17.86905
529	216	7.4442	9.033164
530	264	7.95918	9.658067
531	504	9.87364	11.98117
532	232	7.62366	9.25093
533	208	7.35114	8.920241
534	232	7.62366	9.25093
535	192	7.1576	8.68539
536	272	8.03878	9.754658
537	456	9.54968	11.58806
538	440	9.43666	11.45092
539	192	7.1576	8.68539
540	120	6.11966	7.425901
541	448	9.4935	11.51989
542	120	6.11966	7.425901
543	272	8.03878	9.754658
544	368	8.89098	10.78876
545	64	4.9628	6.02211
546	80	5.34602	6.487128
547	256	7.87796	9.559511
548	176	6.95298	8.437094
549	136	6.38038	7.742272
550	200	7.25566	8.804381
551	208	7.35114	8.920241
552	64	4.9628	6.02211
553	176	6.95298	8.437094
554	232	7.62366	9.25093
555	408	9.2021	11.16629
556	24	3.5788	4.342695
557	136	6.38038	7.742272
558	160	6.73556	8.173265
559	392	9.08022	11.01839
560	224	7.535	9.143346
561	96	5.681	6.893609

562	176	6.95298	8.437094
563	304	8.34242	10.12311
564	232	7.62366	9.25093
565	832	11.66922	14.16002
566	808	11.55592	14.02253
567	264	7.95918	9.658067
568	136	6.38038	7.742272
569	144	6.50312	7.891211
570	472	9.6601	11.72205
571	264	7.95918	9.658067
572	688	10.95292	13.29082
573	632	10.6473	12.91997
574	272	8.03878	9.754658
575	152	6.62138	8.034714
576	168	6.846	8.307279
577	192	7.1576	8.68539
578	1080	12.72942	15.44651
579	632	10.6473	12.91997
580	1440	14.01054	17.00109
581	368	8.89098	10.78876
582	200	7.25566	8.804381
583	208	7.35114	8.920241
584	160	6.73556	8.173265
585	344	8.69334	10.54893
586	224	7.535	9.143346
587	136	6.38038	7.742272
588	168	6.846	8.307279
589	360	8.82608	10.71001
590	96	5.681	6.893609
591	240	7.7103	9.356064
592	256	7.87796	9.559511
593	184	7.05678	8.56305
594	208	7.35114	8.920241
595	352	8.76022	10.63009
596	424	9.32086	11.3104
597	328	8.55642	10.38279
598	184	7.05678	8.56305
599	224	7.535	9.143346
600	224	7.535	9.143346
601	328	8.55642	10.38279
602	120	6.11966	7.425901
603	384	9.01802	10.94292
604	352	8.76022	10.63009
605	248	7.79504	9.458891

Appendices

606	160	6.73556	8.173265
607	192	7.1576	8.68539
608	144	6.50312	7.891211
609	368	8.89098	10.78876
610	184	7.05678	8.56305
611	616	10.55668	12.81
612	264	7.95918	9.658067
613	152	6.62138	8.034714
614	40	4.24314	5.148838
615	832	11.66922	14.16002
616	136	6.38038	7.742272
617	440	9.43666	11.45092
618	664	10.82406	13.13446
619	472	9.6601	11.72205
620	256	7.87796	9.559511
621	408	9.2021	11.16629
622	864	11.81694	14.33927
623	176	6.95298	8.437094
624	736	11.20194	13.59299
625	168	6.846	8.307279
626	184	7.05678	8.56305
627	408	9.2021	11.16629
628	280	8.11684	9.849379
629	96	5.681	6.893609
630	344	8.69334	10.54893
631	256	7.87796	9.559511
632	264	7.95918	9.658067
633	152	6.62138	8.034714
634	80	5.34602	6.487128
635	1024	12.50548	15.17477
636	432	9.37912	11.38109
637	176	6.95298	8.437094
638	224	7.535	9.143346
639	360	8.82608	10.71001
640	1216	13.24276	16.06943
641	280	8.11684	9.849379
642	320	8.48628	10.29768
643	480	9.71436	11.78789
644	976	12.30696	14.93388
645	1056	12.63442	15.33124
646	200	7.25566	8.804381
647	760	11.3224	13.73917
648	856	11.78036	14.29488
649	216	7.4442	9.033164

650	520	9.97704	12.10664
651	528	10.02794	12.1684
652	376	8.95496	10.8664
653	88	5.51858	6.696521
654	200	7.25566	8.804381
655	40	4.24314	5.148838
656	152	6.62138	8.034714
657	304	8.34242	10.12311
658	608	10.51078	12.75431
659	456	9.54968	11.58806
660	48	4.509	5.471446
661	240	7.7103	9.356064
662	48	4.509	5.471446
663	488	9.76804	11.85303
664	680	10.9103	13.2391
665	200	7.25566	8.804381
666	1984	15.59006	18.91776
667	352	8.76022	10.63009
668	168	6.846	8.307279
669	184	7.05678	8.56305
670	2408	16.62976	20.17938
671	392	9.08022	11.01839
672	216	7.4442	9.033164
673	296	8.26858	10.03351
674	864	11.81694	14.33927
675	480	9.71436	11.78789
676	216	7.4442	9.033164
677	256	7.87796	9.559511
678	216	7.4442	9.033164
679	264	7.95918	9.658067
680	328	8.55642	10.38279
681	96	5.681	6.893609
682	672	10.86736	13.187
683	184	7.05678	8.56305
684	392	9.08022	11.01839
685	896	11.96106	14.51415
686	248	7.79504	9.458891
687	48	4.509	5.471446
688	768	11.36198	13.78719
689	328	8.55642	10.38279
690	472	9.6601	11.72205
691	184	7.05678	8.56305
692	424	9.32086	11.3104
693	160	6.73556	8.173265

Appendices

694	472	9.6601	11.72205
695	360	8.82608	10.71001
696	128	6.25274	7.587387
697	848	11.74354	14.2502
698	320	8.48628	10.29768
699	96	5.681	6.893609
700	104	5.8346	7.079995
701	384	9.01802	10.94292
702	432	9.37912	11.38109
703	336	8.62542	10.46652
704	552	10.17764	12.35006
705	984	12.34048	14.97456
706	248	7.79504	9.458891
707	384	9.01802	10.94292
708	744	11.24238	13.64207
709	304	8.34242	10.12311
710	728	11.1612	13.54356
711	320	8.48628	10.29768
712	224	7.535	9.143346
713	112	5.98054	7.257086
714	600	10.46448	12.69812
715	184	7.05678	8.56305
716	184	7.05678	8.56305
717	320	8.48628	10.29768
718	160	6.73556	8.173265
719	448	9.4935	11.51989
720	240	7.7103	9.356064
721	312	8.41496	10.21113
722	1080	12.72942	15.44651
723	488	9.76804	11.85303
724	120	6.11966	7.425901
725	624	10.60218	12.86522
726	1208	13.21366	16.03412
727	264	7.95918	9.658067
728	368	8.89098	10.78876
729	136	6.38038	7.742272
730	256	7.87796	9.559511
731	248	7.79504	9.458891
732	192	7.1576	8.68539
733	200	7.25566	8.804381
734	608	10.51078	12.75431
735	104	5.8346	7.079995
736	456	9.54968	11.58806
737	384	9.01802	10.94292

738	464	9.6052	11.65543
739	296	8.26858	10.03351
740	1024	12.50548	15.17477
741	400	9.14156	11.09283
742	176	6.95298	8.437094
743	72	5.16152	6.263246
744	176	6.95298	8.437094
745	2384	16.57434	20.11213
746	96	5.681	6.893609
747	432	9.37912	11.38109
748	384	9.01802	10.94292
749	952	12.20524	14.81045
750	48	4.509	5.471446
751	152	6.62138	8.034714
752	128	6.25274	7.587387
753	320	8.48628	10.29768
754	1120	12.88466	15.63489
755	120	6.11966	7.425901
756	128	6.25274	7.587387
757	104	5.8346	7.079995
758	1432	13.98454	16.96954
759	296	8.26858	10.03351
760	152	6.62138	8.034714
761	280	8.11684	9.849379
762	288	8.19342	9.942305
763	376	8.95496	10.8664
764	2128	15.95846	19.36479
765	176	6.95298	8.437094
766	280	8.11684	9.849379
767	232	7.62366	9.25093
768	152	6.62138	8.034714
769	1096	12.79198	15.52243
770	384	9.01802	10.94292
771	472	9.6601	11.72205
772	152	6.62138	8.034714
773	120	6.11966	7.425901
774	248	7.79504	9.458891
775	480	9.71436	11.78789
776	80	5.34602	6.487128
777	216	7.4442	9.033164
778	144	6.50312	7.891211
779	120	6.11966	7.425901
780	88	5.51858	6.696521
781	576	10.32306	12.52652

Appendices

782	344	8.69334	10.54893
783	336	8.62542	10.46652
784	160	6.73556	8.173265
785	160	6.73556	8.173265
786	696	10.99522	13.34215
787	144	6.50312	7.891211
788	384	9.01802	10.94292
789	472	9.6601	11.72205
790	544	10.12824	12.29011
791	408	9.2021	11.16629
792	656	10.7804	13.08148
793	360	8.82608	10.71001
794	152	6.62138	8.034714
795	280	8.11684	9.849379
796	2768	17.42032	21.13869
797	184	7.05678	8.56305
798	184	7.05678	8.56305
799	360	8.82608	10.71001
800	176	6.95298	8.437094
801	480	9.71436	11.78789
802	144	6.50312	7.891211
803	104	5.8346	7.079995
804	224	7.535	9.143346
805	280	8.11684	9.849379
806	1096	12.79198	15.52243
807	376	8.95496	10.8664
808	104	5.8346	7.079995
809	144	6.50312	7.891211
810	144	6.50312	7.891211
811	536	10.07834	12.22956
812	608	10.51078	12.75431
813	264	7.95918	9.658067
814	72	5.16152	6.263246
815	616	10.55668	12.81
816	384	9.01802	10.94292
817	168	6.846	8.307279
818	312	8.41496	10.21113
819	984	12.34048	14.97456
820	1160	13.03626	15.81885
821	256	7.87796	9.559511
822	416	9.26186	11.2388
823	144	6.50312	7.891211
824	576	10.32306	12.52652
825	952	12.20524	14.81045

826	248	7.79504	9.458891
827	576	10.32306	12.52652
828	552	10.17764	12.35006
829	272	8.03878	9.754658
830	256	7.87796	9.559511
831	368	8.89098	10.78876
832	360	8.82608	10.71001
833	280	8.11684	9.849379
834	176	6.95298	8.437094
835	584	10.37062	12.58423
836	232	7.62366	9.25093
837	104	5.8346	7.079995
838	32	3.93898	4.779755
839	2024	15.69414	19.04405
840	288	8.19342	9.942305
841	240	7.7103	9.356064
842	240	7.7103	9.356064
843	440	9.43666	11.45092
844	512	9.92562	12.04424
845	720	11.12016	13.49376
846	304	8.34242	10.12311
847	88	5.51858	6.696521
848	584	10.37062	12.58423
849	584	10.37062	12.58423
850	896	11.96106	14.51415
851	792	11.47912	13.92934
852	728	11.1612	13.54356
853	472	9.6601	11.72205
854	208	7.35114	8.920241
855	240	7.7103	9.356064
856	200	7.25566	8.804381
857	72	5.16152	6.263246
858	144	6.50312	7.891211
859	296	8.26858	10.03351
860	664	10.82406	13.13446
861	400	9.14156	11.09283
862	336	8.62542	10.46652
863	168	6.846	8.307279
864	432	9.37912	11.38109
865	96	5.681	6.893609
866	800	11.51766	13.9761
867	176	6.95298	8.437094
868	184	7.05678	8.56305
869	256	7.87796	9.559511

Appendices

870	792	11.47912	13.92934
871	616	10.55668	12.81
872	168	6.846	8.307279
873	288	8.19342	9.942305
874	2712	17.30204	20.99516
875	176	6.95298	8.437094
876	912	12.03184	14.60004
877	880	11.88944	14.42724
878	552	10.17764	12.35006
879	568	10.27504	12.46825
880	992	12.37384	15.01504
881	576	10.32306	12.52652
882	496	9.82112	11.91744
883	408	9.2021	11.16629
884	112	5.98054	7.257086
885	472	9.6601	11.72205
886	864	11.81694	14.33927
887	808	11.55592	14.02253
888	736	11.20194	13.59299
889	296	8.26858	10.03351
890	544	10.12824	12.29011
891	568	10.27504	12.46825
892	520	9.97704	12.10664
893	104	5.8346	7.079995
894	1640	14.63126	17.7543
895	152	6.62138	8.034714
896	296	8.26858	10.03351
897	512	9.92562	12.04424
898	64	4.9628	6.02211
899	128	6.25274	7.587387
900	152	6.62138	8.034714
901	432	9.37912	11.38109
902	184	7.05678	8.56305
903	800	11.51766	13.9761
904	104	5.8346	7.079995
905	280	8.11684	9.849379
906	224	7.535	9.143346
907	72	5.16152	6.263246
908	816	11.59392	14.06864
909	256	7.87796	9.559511
910	264	7.95918	9.658067
911	352	8.76022	10.63009
912	320	8.48628	10.29768
913	568	10.27504	12.46825

914	992	12.37384	15.01504
915	376	8.95496	10.8664
916	112	5.98054	7.257086
917	152	6.62138	8.034714
918	896	11.96106	14.51415
919	288	8.19342	9.942305
920	472	9.6601	11.72205
921	536	10.07834	12.22956
922	176	6.95298	8.437094
923	264	7.95918	9.658067
924	304	8.34242	10.12311
925	192	7.1576	8.68539
926	144	6.50312	7.891211
927	152	6.62138	8.034714
928	96	5.681	6.893609
929	112	5.98054	7.257086

309160

References

- Allen, M. M., R. L. Athey and J. B. Moore (1975). "Nickel-base superalloy powder metallurgy -state-of-the-art." Progress in Powder Metallurgy **31**: 243-268.
- Andrews, P. (1999). "Spray formed and HIP'ed CM247LC-Evaluation of tensile, fatigue and creep properties". Rolls-Royce Ltd. Report DNS64458.
- Ardell, A. J. (1968). "An application of the theory of particle coarsening: The γ' precipitate in Ni-Al alloys." Acta Metallurgica **16**(4): 511-516.
- Aretz, W., D. Ponge and G. Gottstein (1992). "Evolution of necklace structures during hot compression of Ni₃Al+B." Scripta Metallurgica et Materialia **27**(11): 1593-1598.
- Atkinson, H. and S. Davies (2000). "Fundamental aspects of hot isostatic pressing: An overview." Metallurgical and Materials Transactions A **31**(12): 2981-3000.
- Atkinson, H. V. and B. A. Rickinson (1991). Hot isostatic processing, Bristol : Adam Hilger.
- Aubin, C., J. P. Trottier and J. H. Davidson (1980). "The influence of powder particle surface composition on the properties of a nickel-based superalloy produced by Hot Isostatic Pressing." Superalloys 1980; Champion; PA ,TMS: 345-354.
- Balikci, E., A. Raman and R. A. Mirshams (1997). "Influence of various heat treatments on the microstructure of polycrystalline IN738LC." Metallurgical and Materials Transactions A - Physical Metallurgy and Materials Science **28A**(10): 1993-2003.
- Bee, J., A. Jones and P. Howell (1980). "The development of the "necklace" structure in a powder-produced nickel-base superalloy." Journal of Materials Science **15**(2): 337-344.
- Bettge, D. O., W; Ziebs, J (1995). "Temperature dependence of yield strength and elongation of the nickel-base superalloy IN 738 LC and the corresponding microstructural evolution" Zeitschrift für Metallkunde **86**(3): 190-197.
- Bhadeshia, H. K. D. H. (1997). "Recrystallisation of practical mechanically alloyed iron-base and nickel-base superalloys." Materials Science and Engineering: A **223**(1-2): 64-77.

- Bhadeshia, H. K. D. H. (2003). "Nickel based superalloys." Retrieved 04/05, 2010. <http://www.msm.cam.ac.uk/phase-trans/2003/Superalloys/superalloys.html>.
- Blackburn, M. J. and R. A. Sprague (1977). "Production of components by hot isostatic pressing of nickel-base superalloy powders." Metals Technology **4**(pt 8): 388-395.
- Bor, H. Y., C. G. Chao and C. Y. Ma (1997). "Influence of magnesium on carbide characteristics and creep behaviour of the Mar-M247 superalloy." Scripta Materialia **38**(2): 329-335.
- Bor, H. Y., C. N. Wei, R. R. Jeng and P. Y. Ko (2008). "Elucidating the effects of solution and double ageing treatment on the mechanical properties and toughness of MAR-M247 superalloy at high temperature." Materials Chemistry and Physics **109**(2-3): 334-341.
- Broek, D. (1973). "The role of inclusions in ductile fracture and fracture toughness." Engineering Fracture Mechanics **5**(1): 55-56, IN1-IN6, 57-66.
- Brown, A. M. and M. F. Ashby (1980). "Correlations for diffusion constants." Acta Metallurgica **28**(8): 1085-1101.
- Caron, P. (2000). "High γ' solvus new generation nickel-based superalloys for single crystal turbine blade applications." Superalloys 2000, Champion, Pennsylvania, TMS: 246.
- Chang, S. H. (2009). "Optimization of pressure and soaking time of HIP treatment on 713LC cast superalloy." Materials Transactions **50**(4): 909-916.
- Chaudhuri, A. (1969). ""On the activation energy for creep of nickel-base high-temperature alloys." Metal Science **3**: 159-160.
- Chellman, D. J. and A. J. Ardell (1976). "Precipitation hardening of Ni-Al single crystals containing bimodal distributions of the gamma prime precipitate." Int Conf on the Strength of Metals and Alloys, 4th, Proc, Aug 30-Sep 3 1976 Ed by Lab de Phys du Solide ENSMIM. **1**: 219-223.
- Chen, J., J. H. Lee, C. Y. Jo, S. J. Choe and Y. T. Lee (1998). "MC carbide formation in directionally solidified MAR-M247 LC superalloy." Materials Science And Engineering A-Structural Materials Properties Microstructure And Processing **247**(1-2): 113-125.

References

- Chu, Z., J. Yu, X. Sun, H. Guan and Z. Hu (2010). "Tensile property and deformation behavior of a directionally solidified Ni-base superalloy." Materials Science and Engineering: A **527**(12): 3010-3014.
- Clement, N., A. Couret and D. Caillard (1991). "An in-situ study of cube glide in the gamma'-phase of a superalloy – the controlling mechanism." Philosophical Magazine a-Physics of Condensed Matter Structure Defects and Mechanical Properties **64**(3): 669-695.
- Cornish, L. A., R. Suss, A. Douglas, L. H. Chown and L. Glaner (2009). "The platinum development initiative: platinum-based alloys for high temperature and special applications: Part I" Platinum Metals Review **53**(1): 2-10.
- Craw, D. A. and W. G. Henry (1956). "A laboratory scale chill-casting vacuum induction furnace." Journal of Scientific Instruments **33**(1): 22.
- Dahlén, M., N. G. Ingesten and H. Fischmeister (1981). "Parameters influencing particle boundary precipitation in superalloy powders." Modern developments in powder metallurgy, Princeton, NJ, Metal Powder Industries Federation. **14**:3-14.
- Danflou, H. L., M. Macia, T. H. Sanders and T. Khan (1996). "Mechanisms of formation of serrated grain boundaries in nickel base superalloys", Superalloys 1996; Proceedings of the Eighth International Symposium on Superalloys 1992, Warrendale, PA, USA, TMS.119-127.
- Danflou, H. L., M. Marty and A. Walder (1992). "Formation of serrated grain-boundaries and their effect on the mechanical-properties in a P/M nickel-base superalloy." Superalloys 1992; Proceedings of the Seventh International Symposium on Superalloys 1992, Warrendale, PA, USA, TMS. 63-72.
- Davis, J. R. (1997). Heat resistant materials, ASM International.
- Davis, J. R. (2004). Tensile testing. Materials Park, Ohio, ASM International.
- Daymond, M. R., M. Preuss and B. Clausen (2007). "Evidence of variation in slip mode in a polycrystalline nickel-base superalloy with change in temperature from neutron diffraction strain measurements." Acta Materialia **55**(9): 3089-3102.
- Decker, R. F. (1973). Nickel-based and Cobalt-based superalloys: present and future

- potential. The symposium on high-temperature materials in gas turbines, Baden, Switzerland, Brown, Boveri & company limited.
- Decker, R. F. and J. R. Mihalisin (1969). "Coherency strains in gamma hardened nickel alloys (Elements substitution for Al in gamma prime of Ni-Al alloy to change aged hardness by gamma prime mismatch and coherency strains)." ASM Transactions Quarterly **62**: 481-489.
- DeLo, D. P. and H. R. Piehler (1999). "Early stage consolidation mechanisms during hot isostatic pressing of Ti-6Al-4V powder compacts." Acta Materialia **47(9)**: 2841-2852.
- Doi, M., T. Miyazaki and T. Wakatsuki (1984). "The effect of elastic interaction energy on the morphology of [gamma]'precipitates in nickel-based alloys." Materials Science and Engineering **67(2)**: 247-253.
- Engler-Pinto, C. C., C. Nosedo, M. Y. Nazmy and F. Rezai-aria (1996). "Interaction between creep and thermo-mechanical fatigue of CM247LC-DS." Superalloys 1996 : proceedings of the Eighth International Symposium on Superalloys, Champion, Pennsylvania Warrendale.PA **22-26**:319-325
- Fairbank, G. B. (2003). "The development of platinum alloys for high temperature service." Materials science and metallurgy. Cambridge, University of Cambridge. **Ph.D.**
- Fine, M. E. and R. O. Ritchie (1979). "Fatigue-crack initiation and near-threshold crack growth." Fatigue and microstructure; Proceedings of the Materials Science Seminar, **St**: 245-278.
- Fiore, N. F. (1975). "Mid-range ductility minimum in Ni-base superalloys." Review of High Temperature Materials, **2**: 373-408.
- Fost, H. J. and M. F. Ashby (1982). Deformation-mechanism maps: The plasticity and creep of metals and ceramics. Oxford, Pergamon Press.
- Frost, N. E., K. J. Marsh and L. P. Pook (1974). Metal fatigue. Oxford, Claren Press.
- Gabb, T. P., J. Gayda, J. Telesman and A. Garg (2008). "The effects of heat treatment and microstructure variations on disk superalloy properties at high temperature," Superalloys 2008, Champion, PA, United states, Minerals, Metals and Materials Society

References

- Gao, Q., S. Zhang, B. Hu and H. Li (1996). "Development of necklace structure in P/M Rene'95 superalloys." Acta Metallurgica Sinica **32**(10): 1019-22.
- Gasko, K. L., G. M. Janowski and B. J. Pletka (1988). "The influence of γ - γ' eutectic on the mechanical properties of conventionally cast Mar-M247." Materials Science & Engineering, A: Structural Materials: Properties, Microstructure and Processing **104**: 1-8.
- Gell, M. and G. R. Leverant (1968). "The characteristics of stage I fatigue fracture in a highstrength nickel alloy." Acta Metallurgica **16**(4): 553-561.
- Harada, H. (2001). Design of Ni-base superalloys. Warrendale, Minerals, Metals & Materials Soc.
- Harris, K., G. L. Ericson and S. R.E. (1984). "Mar M 247 derivations - CM247 LC DS alloy CMSX single crystal alloys properties & performance." Superalloys 1984; Proceedings of the Fifth International Symposium, Champion, PA; United States: 221-230.
- Harris, K., G. L. Ericson and R. E. Schwer (1982). "Development of a high creep strength, high ductility, cast superalloy for integral turbine wheels - CM Mar-M-247 LC" TMS High temperature Alloys Committee Sponsored Session on Fatigue and Fracture of Superalloys AMIE Annual Meeting, Dallas, Texas.
- He, L. Z., Q. Zheng, X. F. Sun, G. C. Hou, H. R. Guan and Z. Q. Hu (2004). "Low ductility at intermediate temperature of Ni-base superalloy M963." Materials Science and Engineering A **380**(1-2): 340-348.
- Helle, A. S., K. E. Easterling and M. F. Ashby (1985). "Hot-isostatic pressing diagrams: New developments." Acta Metallurgica **33**(12): 2163-2174.
- Henry, M. F., Y. S. Yoo, D. Y. Yoon and J. Choi (1993). ""The dendritic growth of γ' precipitates and grain boundary serration in a model nickel-base superalloy." Metallurgical Transactions A (Physical Metallurgy and Materials Science) **24A**(8): 1733-1743.
- Hohmann, M. and S. Jönsson (1990). "Modern systems for production of high quality metal alloy powder." Vacuum **41**(7-9): 2173-2176.

- Hollenberg, G. W., G. R. Terwilliger and R. S. Gordon (1971). "Calculation of Stresses and Strains in Four-Point Bending Creep Tests." Journal of the American Ceramic Society **54**(4): 196-199.
- Hou, J. S., J. T. Guo, Y. X. Wu, L. Z. Zhou and H. Q. Ye (2010). "Effect of hafnium on creep behavior of a corrosion resistant nickel base superalloy." Materials Science and Engineering: A **527**(6): 1548-1554.
- Huang, A., D. Hu, M. H. Loretto, J. Mei and X. Wu (2007). "The influence of pressure on solid-state transformations in Ti-46Al-8Nb." Scripta Materialia **56**(4): 253-256.
- Huang, H. E. and C. H. Koo (2004). "Characteristics and Mechanical Properties of Polycrystalline CM 247 LC Superalloy Casting." Materials Transactions **45**(2): 562-568.
- Huda, Z. and B. Ralph (1990). "Mechanism of grain growth and intergranular precipitation of γ' in a nickel base superalloy." Praktische Metallographie **27**(2): 64-74.
- Ingesten, N. G., R. Warren and L. Winberg (1982). "Nature and origin of previous particle boundary precipitates in P/M superalloys." High Temperature Alloys for Gas Turbines 1982. Liege, Belg, D. Reidel Publ Co: 1013-1027.
- Janowski, G., R. Heckel and B. Pletka (1986). "The effects of tantalum on the microstructure of two polycrystalline nickel-base superalloys: B-1900 + Hf and MAR-M247." Metallurgical and Materials Transactions A **17**(11): 1891-1905.
- Jeandin, M. (1982). "Necklace structure obtained by forging Astroloy supersolidus-sintered preforms." Journal of Materials Science **17**(10): 2902-10.
- Jeandin, M., J. D. Bartout, Y. Bienvenu and F. Grillon (1986). "Advanced microstructural observations of the 'necklace' structure of a P/M nickel-based superalloy." Metallurgical Society of AIME, Fall Meeting, Orlando, FL; United States; 5-9 Oct.
- Johnson, J. (1967). "Sigma phase formed in a nickel-base UDIMET 700." Journal of the Institute of Metals **95**: 379.
- Kakehi, K. (1999). "Influence of precipitate size and crystallographic orientation on strength of a single crystal Ni-base superalloy." JIM, Materials Transactions **40**(2): 159-167.
- Kang, S. L. (2005). Sintering: densification, grain growth & microstructure. Oxford, Elsevier

References

Butterworth-Heinemann.

- Kear, B. H. and J. M. Oblak (1974). "Deformation modes in gamma-prime precipitation hardened nickel-base alloys." (Societe Francaise de Physique and Societe Europeenne de Physique, Colloque sur la Dissociation des Dislocations, Beaune, France, Sept 35: C7-45.
- Kendall, J. M., L. Grabowski, K. E. King and D. Rolls-Royce Ltd (1989). "Microstructural design for fatigue crack growth resistance in Ni-base alloy." Rolls-Royce Ltd. Report. PNR90632.
- Kim, I. S., B. G. Choi, S. M. Seo, D. H. Kim and C. Y. Jo (2008). "Influence of heat treatment on microstructure and tensile properties of conventionally cast and directionally solidified superalloy CM247LC." Materials Letters 62(6-7): 1110.
- Koehler, J. S. and F. Seitz (1947). "Proposed experiments for further study of the mechanism of plastic deformation." Journal of Applied Mechanics-Transactions of the Asme 14(3): A217-A224.
- Komazaki, S., T. Shoji and M. Sato (2000). "Creep life prediction of Ni-base superalloy used in advanced gas turbine blades by electrochemical method." Asme International Journal Series A-Solid Mechanics and Material Engineering 43(2): 156-165.
- Kortovitch, C. S. and H. E. Collins (1971). "Superalloy P/M materials for 1800/2000F temperature applications." Vestec 1971 Conference, L. A. California.
- Kotval, P. S., J. D. Venables and R. W. Calder (1972). "The role of hafnium in modifying the microstructure of cast nickel-base superalloys." Metallurgical and Materials Transactions B 3(2): 457-462.
- Koul, A. K. and D. D. Morphy (1983). "Serrated grain boundary formation in nickel-base superalloys", Microstructural Science 11:79-88
- Kumar, A. N. and R. K. Pandey (1984). "Effect of inclusions and states of stress on the mechanics of fracture in a quenched and tempered Ni-Cr-Mo steel." Materials Science and Engineering 63(1): 121-136.
- Lall, C., S. Chin and D. P. Pope (1979). "Orientation and temperature-dependence of the yield stress of Ni₃(Al, Nb) single-crystals." Metallurgical Transactions a-Physical

Metallurgy and Materials Science **10**(9): 1323-1332.

- Larker, R. (1999). "Diffusion bonding of CMSX-4 to UDIMET 720 using PVD-coated interfaces and HIP." Journal of Engineering for Gas Turbines and Powder-Transactions of the ASME **121**(3): 489-493.
- Larson, J. M. (1976). "Carbide morphology in p/m IN-792." Metallurgical and Materials Transactions A **7**(10): 1497 -1502.
- Laz, P. J. and B. M. Hillberry (1998). "Fatigue life prediction from inclusion initiated cracks." International Journal of Fatigue **20**(4): 263-270.
- Lefebvre, A. H. (1983). Gas turbine combustion. Washington, Hemisphere Pub. Corp.
- Lian, Z. W., J. J. Yu, X. F. Sun, H. R. Guan and Z. Q. Hu (2008). "Temperature dependence of tensile behavior of Ni-based superalloy M951." Materials Science and Engineering: A **489**(1-2): 227-233.
- Lund, C. H., J. Hockin and M.J.Woulds (1972). Casting process for nickel base alloys. U. S. Patent, Martin Marietta Corporation, New York. **3677331**.
- Luyckx, S. B. (1975). "Role of inclusions in the fracture initiation process in WC-Co alloys." Acta Metallurgica **23**(1): 109-115.
- Lvov, G. (2004). "Mechanism of primary MC carbide decomposition in Ni-base superalloys." Metallurgical and Materials Transactions: A **35A**(6): 1669-1679.
- Ma, S., D. Brown, M. A. M. Bourke, M. R. Daymond and B. S. Majumdar (2005). "Microstrain evolution during creep of a high volume fraction superalloy." Materials Science and Engineering: A **399**(1-2): 141.
- Ma, W., Y. Han and S. Li (2007). "Effect of Ru on Microstructure of a single crystal nickel-base superalloy." Materials Science Forum **546-549**: 1195-1200.
- MacKay, R. A. and M. V. Nathal (1990). " γ' coarsening in high volume fraction nickel-base alloys." Acta Metallurgica et Materialia **38**(6): 993-1005.
- Maldini, M., M. Marchionni, M. Nazmy, M. Staubli and G. Osinkolu (1996). "Creep and fatigue properties of a directionally solidified nickel base superalloy at elevated temperature." Superalloys 1996; 8th International Symposium on Superalloys, Champion, Pa, Minerals, Metals & Materials Soc: 327-334.

References

- Matthews, S. J. (1976). "Thermal stability of solid solution strengthened high performance alloys" Superalloys: Metallurgy and manufacture; Proceedings of the Third International Symposium, United States, Seven Springs, Pa: 215-226.
- McLean, M. (1983). Directionally solidified materials for high temperature service. London, The Metals Society.
- Menzies, R. G., R. H. Bricknell and A. J. Craven (1980). "STEM microanalysis of precipitates and their nuclei in a nickel-base superalloy." Philosophical Magazine A: Physics of Condensed Matter, Structure, Defects and Mechanical Properties **41**(4): 493-508.
- Menzies, R. G., G. J. Davies and J. W. Edington (1982). "Effect of heat treatment on superplastic response of powder-consolidated nickel-base superalloy IN 100." Metal Science **16**(7): 356-62.
- Miner, R. V. (1977). "Effects of C and Hf concentration on phase relations and microstructure of a wrought powder-metallurgy superalloy " Metallurgical and Materials Transactions A **8**(2): 259-263.
- Mishra, R. S., S. p. Singh, A. M. Sriramamurthy and M. C. Pandey (1995). "Effect of grain boundary orientation on creep behaviour of directionally solidified nickel base superalloy(CM247LC alloy)." Materials Science and Technology **11**(4): 341-345.
- Mitchell, R. J., H. Y. Li and Z. W. Huang (2009). "On the formation of serrated grain boundaries and fan type structures in an advanced polycrystalline nickel-base superalloy." Journal of Materials Processing Technology **209**(2): 1011-1017.
- Mitchell, R. J., M. Preuss, S. Tin and M. C. Hardy (2008). "The influence of cooling rate from temperatures above the γ' solvus on morphology, mismatch and hardness in advanced polycrystalline nickel-base superalloys." Materials Science and Engineering: A **473**(1-2): 158-165.
- Murakami, Y. and M. Endo (1994). "Effects of defects, inclusions and inhomogeneities on fatigue strength." International Journal of Fatigue **16**(3): 163-182.
- Nabarro, F. R. N. and H. L. Villiers (1995). The Physics of Creep. London, Taylor & Francis.
- Nazmy, M. Y. and R. F. Singer (1985). "Effect of inclusions on tensile ductility of a nickel-

- base oxide dispersion strengthened superalloy." Scripta Metallurgica **19**(7): 829-832.
- Nganbe, M. and M. Heilmaier (2004). "Modelling of particle strengthening in the γ' and oxide dispersion strengthened nickel-base superalloy PM3030." Materials Science and Engineering A **387-389**: 609-612.
- Nganbe, M. and M. Heilmaier (2009). "High temperature strength and failure of the Ni-base superalloy PM 3030." International Journal of Plasticity **25**(5): 822-837.
- Okazaki, M. (2003). "Undesirable effect of local cellular transformation in microstructurally-controlled Ni-base superalloys subjected to previous damage on high temperature fatigue strength and the prevention: For recoating and refurbishment technology." Materials Science Research International **9**(1): 55-60.
- Osinkolu, G. A., M. Maldini and M. Marchionni (1999). "Creep deformation and rupture of nickel base superalloy CM247LC under variable loading." Materials Science and Technology **15**: 1395.
- Pearcey, B. J. and B. E. Terkelsen (1967). "The effect of unidirectional solidification on the properties of cast nickel-base superalloys (Unidirectional solidification of cast nickel-base superalloys, effect on creep behaviour, stress- rupture properties and thermal shock resistance)." AIME, Transactions **239**: 1143-1150.
- Podob, M. T. (1977). "Effect of heat treatment and slight chemistry variations on the physical metallurgy of hot isostatically pressed low carbon Astroloy powder." Modern Developments in Powder Metallurgy-Proceedings of the Fifth International Powder Metallurgy Conference, Chicago, Ill ; United States. **11**:25-44.
- Ponge, D. and G. Gottstein (1998). "Necklace formation during dynamic recrystallization: mechanisms and impact on flow behaviour." Acta Materialia **46**(1): 69-80.
- Prakash, T. L., Y. N. Chari, E. S. Bhagiradha Rao and R. Thamburaj (1983). "Microstructures and mechanical properties of hot isostatically pressed powder metallurgy alloy APK-1." Metallurgical Transactions a-Physical Metallurgy and Materials Science **14A**: 733-742.
- Preuss, M., J. Q. da Fonseca, B. Grant, E. Knoche, R. Moat and M. Daymond (2008). "The effect of gamma' particle size on the deformation mechanism in an advanced polycrystalline nickel-base superalloy." Superalloys 2008, Warrendale, Minerals,

References

- Metals & Materials Soc: 405-414.
- Price, C. E. and R. Kunc (1986). "Occurrence of faceted fatigue fractures in nickel." Metallography **19**(3): 317-326.
- Price, P. E., R. Widmer and J. C. Runkle (1977). "Effects of hot isostatic pressing process variables on properties of consolidated superalloy powders." Modern developments in powder metallurgy-Proceedings of Fifth International Powder Metallurgy Conference, Chicago, United States. **11**:45-62.
- Qin, X. Z., J. T. Guo, C. Yuan, C. L. Chen, J. S. Hou and H. Q. Ye (2008). "Decomposition of primary MC carbide and its effects on the fracture behaviors of a cast Ni-base superalloy." Materials Science and Engineering: A **485**(1-2): 74-79.
- Rao, G. A., M. Srinivas and D. S. Sarma (2006). "Influence of modified processing on structure and properties of hot isostatically pressed superalloy inconel 718." Materials Science and Engineering: A **418**(1-2): 282-291.
- Reed, R. C. (2006). The superalloys: fundamentals and applications. Cambridge, Cambridge University Press.
- Reppich, B., W. Kuhlein, G. Meyer, D. Puppel, M. Schulz and G. Schumann (1986). "Duplex gamma' particle hardening of the superalloy Nimonic PE-16." Materials Science and Engineering **83**(1): 45-63.
- Ricks, R. A., A. J. Porter and R. C. Ecob (1983). "The growth of gamma'-precipitates in nickel-base superalloys." Acta Metallurgica **31**(1): 43-53.
- Rifai, M. A., M. A. Abdou, G. M. Ali and M. A. Bayoumi (1985). "Effect of particle size of precipitate on the strength of gamma prime- hardened alloys." Modelling, simulation & control. B **2**(1): 51-63.
- Ronald, E. L. and G. K. Paul (2004). "Spectral Imaging Analysis of Interfacial Reactions and Microstructures in Brazing of Alumina by a Hf-Ag-Cu Alloy." Journal of the American Ceramic Society **87**(1): 55-59.
- Sajjadi, S. A., S. Nategh, M. Isac and S. M. Zebarjad (2004). "Tensile deformation mechanisms at different temperatures in the Ni-base superalloy GTD-111." Journal of Materials Processing Technology **155-156**: 1900-1904.

- Schweikert, W. and P. G. Bailey (1980). "New method for cast superalloy frames - Segmented mold and HIP utilized." ManTech Journal **5**(3): 28-32.
- Seliverstov, D., V. Samarov and E. Kratt (1999). "Development and manufacturing of 'net shape' critical rotating parts for rocket propulsion systems from Ni-base superalloy." AIAA/ASME/SAE/ASEE Joint Propulsion Conference and Exhibit, 35th, Los Angeles, CA; United States; 20-24 June 1999: 2898.
- Shah, D., L. Lin and D. Duhal (1980). "Orientation dependence of yield strength in Ni-base super-alloy single-crystal." Journal of Metals **32**(8): 62-62..
- Shamblen, C. E. and D. R. Chang (1985). "Effect of inclusions on LCF life of HIP plus heat-treated powder metal Rene 95." Metallurgical Transactions B **16**(4): 775-784.
- Sharpe, H. J. (2007). "Effect of microstructure on high-temperature mechanical behaviour of nickel-base superalloys for turbine disc applications." Dissertation Abstracts International **68**.
- Sims, C. T., N. S. Stoloff and W. C. Hagel (1987). Superalloys II. United States, Wiley-Interscience, New York, NY.
- Stantonbevan, A. E. and R. D. Rawlings (1975). "Deformation behaviour of single-crystal Ni₃(Al, Ti)." Physica Status Solidi A-Applied Research **29**(2): 613-622.
- Swinkels, F. B., D. S. Wilkinson, E. Arzt and M. F. Ashby (1983). "Mechanisms of hot-isostatic pressing." Acta Metallurgica **31**(11): 1829-1840.
- Taunt, R. J. and B. Ralph (1974). "Observations of fine-structure of super dislocations in Ni₃Al by field-ion microscopy." Philosophical Magazine **30**(6): 1379-1394.
- Thornton, P. H., R. G. Davies and T. L. Johnston (1970). "Temperature dependence of flow stress of gamma' phase based upon Ni₃Al." Metallurgical Transactions **1**(1): 207.
- Tian, S. G., D. Xia, T. Li, F. L. Meng, M. G. Wang and X. F. Yu (2008). "Influence of element W and microstructure evolution on lattice parameters and misfits of nickel-base superalloys." Journal of Aeronautical Materials **28**(4): 12-16.
- Tien, J. K. and T. E. Howson (1982). Advances in P/M and ODS superalloys. Advances in Powder Technology, Papers presented at the 1981 ASM Materials Science Seminar. Louisville, KY, USA, ASM, Metals Park, Ohio, USA: 155-187.

References

- Wang, H.Y., Y. Chen, Y.W. Liu, F. Li, J.H. Liu, G.R. Peng and W.K. Wang. (2009). "Pressure Effects on Solid State Phase Transformation of Aluminium Bronze in Cooling Process." Chinese Physics Letters **26**(10): 106201.
- Williams, D. L. (1977). "Hot isostatically pressed alloy APK1 a nickel-base superalloy." Powder Metallurgy **2**: 84-89.
- Wu, X., J. Del Prado, Q. Li, A. Huang, D. Hu and M. H. Loretto (2006). "Analytical electron microscopy of C-free and C-containing Ti-15-3." Acta Materialia **54**(20): 5433-5448.
- Yang, Z. G., J. M. Zhang, S. X. Li, G. Y. Li, Q. Y. Wang, W. J. Hui and Y. Q. Weng (2006). "On the critical inclusion size of high strength steels under ultra-high cycle fatigue." Materials Science and Engineering: A **427**(1-2): 167-174.
- Youdelis, W. V. and O. Kwon (1983). "Carbide phases in nickel base superalloy: nucleation properties of MC type carbide." Metal Science **17**(8): 385-388.
- Yu, H. C. (2009). "The influence of inclusion on high cycle fatigue behavior of an advanced P/M superalloy." Transferability and Applicability of Current Mechanics Approches: 279-284.
- Zhang, J. and R. F. Singer (2002). "Hot tearing of nickel-based superalloys during directional solidification." Acta Materialia **50**(7): 1869-1879.
- Zhang, J. X., J. C. Wang, H. Harada and Y. Koizumi (2005). "The effect of lattice misfit on the dislocation motion in superalloys during high-temperature low-stress creep." Acta Materialia **53**(17): 4623-4633.
- Zhao, S., X. Xie, G. D. Smith and S. J. Patel (2004). "Gamma prime coarsening and age-hardening behaviors in a new nickel base superalloy." Materials Letters **58**(11): 1784.
- Zhao, X. M. (2009). "The effect of hot isostatic pressing on crack healing, microstructure, mechanical properties of Rene88DT superalloy prepared by laser solid forming." Materials Science and Engineering A **504**(1-2): 129-134.
- Zhou, X.M., W.X. Wang, X.Q. Wang, D.Z. Tang and M.G. Yan (2006). "Effect of SiO₂ non-metallic inclusion on micro-mechanical behavior of nickel-base P/M superalloy." Hangkong Cailiao Xuebao (Journal of Aeronautical Materials) **26**(3): 1-6.